Liquid-Feed Flame Spray Pyrolysis Synthesized Active Material Nanopowders: Toward Co-free, High-Energy Density, and Low-Cost Li-Ion Batteries

by

Taylor G. Brandt

A dissertation submitted in partial fulfillment
of the requirements for the degree of
Doctor of Philosophy
(Materials Science and Engineering)
in the University of Michigan
2024

Doctoral Committee:

Professor Richard M. Laine, Chair
Professor John T. Heron
Professor Yiyang Li
Professor Nirala Singh

Taylor G. Brandt

tgbrandt@umich.edu

ORCID iD: 0000-0003-3471-3124

Dedication

To my family, BMs and friends.

Proverbs 25:2

Acknowledgements

I would like to thank my dissertation committee chair and advisor, Professor Richard M. Laine, and my committee members, Professors John T. Heron, Yiyang Li, and Nirala Singh for their valuable guidance and insightful feedback during my graduate studies.

Additionally, I would like to offer my thanks to current and past colleagues in the Laine group: Dr. Eleni Temeche, Dr. Xinyu Zhang, Mengjie Yu, and Phil Yong Kim. I must acknowledge contributions from undergraduate researcher colleagues, especially Andrew R. Tuokkola, Dylan A. Edelman, Charlie Cappelletti, Erik D. Flaspohler, Marie C. Taylor, Joseph Shangraw, and Jaime Minarro-May for their support and contributions. I would also like to thank Professor Sylvio Indris, Hang Li, Dr. Angela Dial, and Dr. Kai Sun for their collaborations.

While I have spent my longest tenure at the University of Michigan, I would not be in the position to acknowledge anyone in this dissertation without the positive influence of professors and mentors at my previous institutions. I would like to thank Prof. Guozhong Cao and Dr. Zachary Neale at the University of Washington for getting me started in materials science and battery research. I would also like to thank and acknowledge Prof. Gerard Fasel, Prof. John Mann, Prof. David Green, and Prof. Katie Frye at Pepperdine University for their guidance and influence, in and out of the classroom.

I would like to extend special thanks to my former colleagues Tim McGuire, Johnson Mark, Bryann Morgan, and - especially - Dr. Tobias Glossmann for their continued encouragement and support in applying my graduate studies outside academia.

Finally, I would like to acknowledge the financial support from Department of Energy, National Science Foundation, and especially Mercedes-Benz Research & Development, North America.

Table of Contents

List of Tables

List of Figures

List of Abbreviations

- A.V. → Average potential
- AAM → anode active material
- Abb → abbreviation
- APS → Average particle size
- BET → Brunauer–Emmett–Teller Analysis
- BEV → Battery electric vehicle
- C.S. → Crystal structure
- CAM → cathode active material
- CCCV → Constant current, constant voltage
- CEI → cathode-electrolyte interphase
- Ch → Charge
- CMC → carboxymethyl cellulose
- CoNMFT → $(CoNiMnFeTi)_3O_4$
- CoP → Cobalt propionate
- CuB → Copper isobutyrate
- CuNMFT → $(CuNiMnFeTi)_3O_4$
- CV → Cyclic voltammetry
- CY → Ceramic yield

- DC → Direct current
- DCh → Discharge
- DOE → Department of Energy
- DRX → Disordered rock salt
- EDS → Energy dispersive X-ray spectroscopy
- EM → Entropy metric
- ESO → Entropy stabilized oxide
- ESP → Electrostatic precipitator
- EtOH → Ethanol
- EW → Extended cycling window
- FeB → Iron isobutyrate
- FFT → Fast Fourier transform
- FSP → Flame spray pyrolysis
- FTIR → Fourier transform infrared spectroscopy
- GCPL → Galvanostatic cycling, potential limited
- HAADF S/TEM → High annular dark-field scanning transmission electron microscopy
- HEO → High entropy oxide
- HEP → High entropy phosphate
- HV → High voltage
- ICP-MS → Inductively coupled plasma mass spectroscopy
- L → layered
- LCV → Lower cutoff voltage

- LF-FSP → Liquid feed-flame spray pyrolysis
- LFP → $Li_1Fe_1PO_4$
- LiBOB → Lithium bis(oxalate)borate
- LIB → Lithium-ion battery
- LMFP → $Li_1Fe_xMn_yPO_4$ where x+y=1
- LTO → $Li_4Ti_5O_{12}$
- M → monoclinic
- M-LMO → m-$Li_2Mn_2O_3$
- MEO → Medium entropy oxide
- MnB → Manganese isobutyrate
- NiB → Nickel isobutytate
- NMC622 → $Li_1Ni_{0.6}Mn_{0.2}Co_{0.2}O_2$
- NMC811 → $Li_1Ni_{0.8}Mn_{0.1}Co_{0.1}O_2$
- NMP → n-methyl pyrrolidone
- NMR → Nuclear magnetic resonance spectroscopy
- NP → Nanoparticle
- NSP → Nebulized spray pyrolysis
- NTO → Nb_2TiO_7
- O → Olivine
- PSA → Particle size analysis
- PVDF → Polyvinylidene difluoride
- Q → Capacity

- S → Spinel
- s-LMNO → s-$Li_1Mn_{1.5}Ni_{0.5}O_4$
- s-LMO → s-$Li_1Mn_2O_4$
- S.G. → Space Group
- SBR → Styrene butadiene rubber
- SEI → solid-electrolyte interphase
- SEM → Scanning electron microscopy
- SSA → Specific surface area
- st-LMNO → s-$Li_1Mn_{1.5}Ni_{0.5}O_4$ + t-$Li_2Mn_{1.5}Ni_{0.5}O_4$
- SW → Standard cycling window
- T → tetragonal
- T-LMNO → t-$Li_2Mn_{1.5}Ni_{0.5}O_4$
- TEA → Triethanolamine
- TGA → thermogravimetric analysis
- TiG → Titanatrane glycolate
- TM → Transition metal
- UCV → Upper cutoff voltage
- XPS → X-ray photoelectron spectroscopy
- XRD → X-ray diffraction
- ZnB → Zinc isobutyrate
- ZnNMFT → $(ZnNiMnFeTi)_3O_4$

Abstract

High energy density batteries are enabling electrification on a global scale in almost every facet of life. Batteries that power electric vehicles contain a wide array of materials with rigorous performance exigencies as defined by the consumer – inexpensive, fast charging, and long range. Active materials represent the largest cost fraction (cathode ~50%) and specify the upper performance limit. High energy density cathodes, materials that can enable long range EV batteries, represent the greatest fraction of total battery cell materials cost due to the typical compositions containing mined transition metals such as Co, Ni, Mn, and Fe.

There is a growing need for alternatives to commercialized high-energy-density cathode active materials (CAMs) for Li-ion batteries with chemistries less dependent on Co and Ni and, in the past decade, particular attention has been placed on Mn- and/or Fe-based cathodes. Additionally, optimization of anode active materials (AAMs), typically composed of graphite and/or Si-based materials, is vital to high energy density cell realization. High entropy oxides (HEOs) are potential anode candidates for applications demanding high volumetric capacity; however, transition metals require careful consideration to minimize cost while maintaining performance.

In this dissertation, we investigate the design, synthesis, characterization, and resulting performance of nano active materials synthesized via liquid feed-flame spray pyrolysis (LF-FSP). LF-FSP provides a high-throughput method (> kg h^{-1}) for nanoparticle (<100 nm APS) synthesis with a high level of compositional control facilitated by metalloorganic precursors. The synthesized materials demonstrate progress towards Co-free, low cost, and high energy density batteries.

We studied the LF-FSP synthesis and characterization of two Co- and Cr-free, novel HEO compositions - replacing Co [$(CoNiMnFeTi)_3O_4$] with Zn [$(ZnNiMnFeTi)_3O_4$] and Cu [$(CuNiMnFeTi)_3O_4$] - for use as next generation AAMs. The goal of Cu/Zn as potential substitutes for Co is to lower cost while maintaining or improving electrochemical performance from either a material perspective or per cost basis. Compared to industry standard graphite, ZnNMFT showed gravimetric (480 mAh g_{HEO}^{-1} vs. 372 mAh $g_{graphite}^{-1}$) and volumetric (2460 mAh cm_{HEO}^{-3} vs. 820 mAh $cm_{graphite}^{-3}$) capacity gains. A decrease in performance was expected by replacing Co in favor of Zn/Cu; however, galvanostatic cycling results show improved performance for ZnNMFT (~2x) compared to both CoNMFT and CuNMFT on a lower cost basis.

On the cathode side, we examined Li- and Mn-rich CAMs with spinel-based nanocomposite structures having stoichiometries $Li_xMn_{1.5}Ni_{0.5}O_4$ (x=0.45-1.50) synthesized via liquid-feed flame spray pyrolysis. Initially amorphous and crystalline spinel phases transform to nanocomposites composed of spinel and monoclinic/layered phases post calcination (800ºC/6h/O_2). With increasing Li content, monoclinic phase content increases at the expense of the base spinel phase. When cycled from 4.9 – 2.4 V, $Li_xMn_{1.5}Ni_{0.5}O_4$ (x=1.26, 1.50) exhibited energy densities greater than 1000 Wh kg_{CAM}^{-1} (~300 mAh g^{-1}) coupled with a green, aqueous binder.

We studied the electrochemical performance of LFP and LFP-type materials synthesized using an alternative, scalable method – using metal carboxylate precursors via liquid feed-flame spray pyrolysis (LF-FSP). Four $LiTMPO_4$ (TM = Fe, Mn, and/or Ni) nanoparticle systems with varying degrees of Fe substitution - $LiFePO_4$, $LiMn_{1/3}Fe_{2/3}PO_4$, $LiMn_{2/3}Fe_{1/3}PO_4$, and $LiNi_{1/3}Mn_{1/3}Fe_{1/3}PO_4$ - were synthesized. As-produced materials exhibited spherical morphology (~100 nm APS) and amorphous phase but provided the target olivine phase after calcination. In electrochemical studies, practical energy density was maximized with 1:2 Mn:Fe ratio ($LiMn_{1/3}Fe_{2/3}PO_4$) compared

to LFP (491±9 vs 464±3 Wh kg^{-1} at 1.0C) while maintaining excellent capacity retention after 100 cycles (~96%).

Chapter 1 Introduction

1.1 Batteries in Recent History

The focus of this dissertation is materials for energy storage, specifically active materials for Li-ion batteries (LIBs); however, this branch of research is relativity new in the scope of science as we know it. Since the first rechargeable battery (lead-acid) invented by Gaston Planté in 1859, the growth and improvement of secondary batteries has been rapid and increasingly consequential [1–10]. While a derivative of Planté's lead-acid battery is pervasive to this day, for the last 30 years the world has focused on LIBs as the workhorse of rechargeable electrochemical storage.

In recognition of the tremendous effort in designing modern LIBs, the 2019 Nobel prize in chemistry was awarded to three pioneers: John B. Goodenough, M. Stanley Whittingham, and Akira Yoshino [11]. The development by these laureates, and continued research by many others, has enabled large societal changes including, but not limited to, the global electrification of transportation. Substantial progress has been realized since the first $LiCoO_2$/petroleum coke cells were assembled by Asahi Kasei Corporation [12,13].

The work of the three Nobel prize winners has continued in both academia and industry alike. In academia, evidence of the continued research push can be easily observed in the number of publications on LIBs over time. The trend of publications using the keywords "lithium" or "battery" has grown exponentially since 2000 (<500 research publications in 2000, ~9000 research publications in 2019) [14]. In tandem, industry has devoted vast resources to the development of LIBs from material to cell to automotive manufacturers, and important progress has been demonstrated. Simple evidence of this can be seen in the increase in number of battery electric

vehicles (BEVs) on the road today and the number of models available from almost every automotive company in the world [4,15].

While industry spends a significant amount on research in the private sector and academia, governments such as the United States have increasingly pledged financial resources to varying levels of electrochemical storage research. The U.S. Department of Energy's (DOE's) Vehicle's Technology Office provided funding for the Battery500 Consortium with grant recipients including key scientists and engineers in industry and academia alike [16]. Programs like the DOE's Battery500 show common goals especially the need for energy densities higher than traditional graphite anode LIBs. Along with targets for increased energy densities, academia and industry agree on the importance of a diverse battery material portfolio [4,15]. Well-documented price volatility of critical resources and the vulnerability of supply chains over the past decade further amplify the need for cathodes with diverse compositions while maintaining high performance [1,8,17–19]. The definition of high performance is constantly changing as materials and processes improve. Automotive manufacturers, such as Tesla, have used diverse cathode chemistries based on factory location, market, material price, and desired performance [3,19–21]. This push for a variety of chemistries shows the inherent value in studying novel battery materials, as greater options for manufacturers will lead to better consumer products and further facilitate the electrification of transportation.

1.2 Electrochemical Storage

For the purposes of this dissertation, electrochemical energy storage refers to a single battery cell using liquid electrolyte. A wide range of materials are required for LIBs with high energy density and long cycle life. Current state-of-the-art cells have energy densities of 270 Wh kg^{-1} (650 Wh L^{-1}) at the cell level, which represents a 2x improvement over commercialized cells from Sony

in 1991, 120 Wh kg^{-1} (264 Wh L^{-1}) [1]. Four main components of LIBs can be defined as: 1) active material (cathode and anode), 2) binder, 3) conductive additive, and 4) electrolyte. Each of these components is discussed in detail in Chapters 3-5. Other components such as separators and current collectors play important roles but are not examined further in this body of work.

Active materials including CAMs and AAMs, determine the maximum electrochemical energy that can be stored in a given cell. The theoretical capacity (Q_t), or how much charge (number of electrons) can be stored in a material, can be determined using the simple equation, Equation 1 [22,23]:

$$Q_t = \frac{nF}{3.6*M} \quad (1)$$

Where n is the number of electrons, F is Faraday's constant, and M is the molar mass. The factor of 3.6 is the ratio of Faraday's constant in C mol^{-1} (96,485) to mAh mol^{-1} (26,801), and typical capacity figures are described in mAh instead of C. In applications such as BEVs, energy density is considered as, or possibly more, important than strict capacity. Energy density [Wh kg^{-1} or Wh L^{-1}] depends on capacity [mAh g^{-1}] and the potential at which capacity is obtained. The working potential of a LIB half-cell (active material and Li metal) is determined by the difference between the Fermi energy of the active material and that of Li metal [22,23]. Generally, LIB redox potentials are stated with reference to Li/Li^+. This reference is important to note because the half-cell and full cell redox potentials will vary due to the additional active material and its intrinsic Fermi level, or electrode electrochemical potential. The thermodynamically stable open circuit potential (V_{oc}) can be determined from Equation 2 [22,23]:

$$V_{oc} = \frac{\mu_A - \mu_C}{e} \quad (2)$$

Where μ_A and μ_C represent the anode and cathode electrochemical potential, respectively, and e is the magnitude of the electron charge. To maximize the redox potential, and therefore energy

density, of a full cell, materials with high μ_C should be coupled with materials with low μ_A. The μ of a given material is intricately dependent on several factors such as the Fermi energy of an itinerant-electron band (graphite) or a redox couple of a transition metal-cation (cathodes) [22,23].

The redox couple of a transition metal (TM) will depend on the current state of the TM (valence state), electron configuration, and intrinsic crystallographic properties such as ionic/covalent bonding character and counter cations [22,23]. With increased V_{oc}, the energy of each electron in the battery increases, therefore improving the energy density of the battery, providing the impetus to use high-potential active materials. The rationalization of redox potentials for a given active material is beyond the scope of this work; however, it is important to note that each composition and associated crystal structure determines the observed redox potentials.

1.3 Cathode Active Material (CAM)

CAMs not only represent the greatest limiting factor in practical full cell capacity but also the greatest cost percentage [4,15,19,21,24]. In 2019, Wentker et al.[24] estimated that CAMs make up 30-50% of the total cell cost: 20-65 \$ kWh^{-1}. While the two characteristics may appear to be unrelated, a common factor is the generic composition of CAMs: TM oxides or phosphates. The typical molar mass of TMs, and the associated oxides and phosphates, are much greater than common anode materials such as graphite or Si, therefore decreasing possible gravimetric capacity. In addition to greater mass, the cost of TMs is greater than carbonaceous or Si-based materials. While some CAM transition metals are considered low-cost like global commodities (Fe, Mn), others suffer from high cost and strained supply chains (Co, Ni). These four TMs (Fe, Mn, Co, Ni) are present in the three main CAMs used in applications such as BEVs: $LiFePO_4$ (LFP), $LiNi_xMn_yCo_zO_2$ (NMC xyz where x+y+z=1), and $LiMn_2O_4$ (LMO) or $LiMn_{1.5}Ni_{0.5}O_4$ (LMNO) [4,15,19,21].

On a material level, the three main CAMs can be distinguished by characteristic crystal symmetry: olivine (LFP), layered (NMC), and spinel (LMO). The dimensionality of ion mobility is also distinct between the typical crystal symmetry from 1D to 3D Li^+ diffusion pathways: 1D (olivine), 2D (layered), and 3D (spinel). A brief comparison of the capacities, energy densities, cost of each system and select derivatives is shown in Table 1.1. Section 4.2. examines select CAMs further.

Table 1.1: Summary of CAMs.

CAM	Abb.	Crystal Structure	Typical Capacity [mAh g^{-1}]	Average DCh Potential [V]	Relative cost per energy	Ref.
$LiFePO_4$	LFP	Olivine	160	3.4	$	[4,15]
$LiMn_{0.5}Fe_{0.5}PO_4$	LMFP	Olivine	160	3.7	$$	[25]
$LiNi_{0.6}Mn_{0.2}Co_{0.2}O_2$	NMC622	Layered	175	3.8	$$$$	[17,23]
$LiNi_{0.8}Mn_{0.1}Co_{0.1}O_2$	NMC811	Layered	200	3.8	$$$$$	[17,23]
$LiMn_2O_4$	LMO	Spinel	120	4.1	$$	[3]
$LiMn_{1.5}Ni_{0.5}O_4$	LMNO	Spinel	130	4.7	$$	[26]

While NMC materials have the highest energy density in Table 1.1, there is a tradeoff in cost compared to materials like LMFP and LMNO. The cost difference is due primarily to the NMC Co-content and associated supply chain issues, depending on the exact composition [8,17–19]. Co prices are subject to volatility, as well as the documented issues with labor in Co mining [8,17–19]. Design of low cost and high energy density CAMs should focus on materials with high Fe and Mn contents.

As discussed in Section 1.2, energy density depends on both gravimetric capacity and redox potential. Focusing on the latter, high-voltage CAMs (μ_C >4.5 V vs. Li/Li^+) are good candidates for increasing practical energy density [6,7]. While there is an obvious connection between increased redox potential and increased energy density, high-voltage CAMs are not without inherent challenges. The major challenge is pairing high-voltage CAMs with a stable electrolyte,

such as an electrolyte that forms a stable solid-electrolyte interphase (SEI), or more specifically a cathode-electrolyte interphase (CEI) [27,28].

A stable CEI allows for the transport of Li^+ in and out of the electrode without increases in thickness (continuing to grow) over time. Common inorganic solvents and salts such as ethylene carbonate and lithium hexafluorophosphate have limited stability in cycling windows that include an upper cutoff voltage > 4.5 V vs. Li/Li^+. Careful selection of electrolyte additives such as LiBOB can aid in the formation of a stable CEI; however, the stability that can be achieved is often less than other commercial cathodes such as LFP [22,29–31]. Accessing high potentials to maximize energy density can also lead to oxygen redox activity and often oxygen loss.

This is a risk when the target transition metal (for example $Co^{4+/3+}$ in $LiCoO_2$) has a Fermi energy that overlaps with that of oxygen (O^{2-}). In a liquid electrolyte cell, this reaction is typically irreversible and results in gaseous oxygen evolution leading to oxidation of electrolyte [22,23]. Despite the challenges, academia and industry alike are keen to develop high voltage CAMs. Cathode manufacturers are developing high voltage CAMs such as LMNO for use in full cells. In 2023, Toshiba announced plans to use Co-free LMNO in a new high energy density cell design that outperformed comparable LFP cell in cycle life metrics (6,000 vs 3,000 cycles).

1.4 Anode Active Material (AAM)

Predominantly, the anode used in BEV cells is graphite based – the evolution of seminal work by Akira Yoshino [11]. Optimization of graphite anodes has resulted in stable SEI and therefore stable cycling; however, graphite anodes are limited by gravimetric (376 mAh g^{-1}) and/or volumetric capacity (820 mAh cm^{-3}) [32]. The utility of AAMs is quantified via capacity compared to energy density for CAMs. This difference is due to the desire to minimize μ_A which in turn maximizes working redox potentials. The current industrial thrust is to incorporate Si (Si, SiO_x,

SiC, Si-C) into graphite, based on its high theoretical capacity that is ~10x higher than graphite (376 vs 4200 mAh g^{-1}). The introduction of Si presents unique challenges compared to graphite: significant volume expansion with de/lithiation (~400%) that challenges electrode design and long-term cycling stability.

There are a few commercialized alternatives to graphite and Si, such as spinel oxides $Li_4Ti_5O_{12}$ (LTO) and Nb_2TiO_7 (NTO). The primary benefit of these alternate materials is fast charging capabilities. Fast charging is possible with LTO and NTO due to three main factors: 1) the stability of the spinel structure during de/lithiation, 2) higher redox potential (~1.4 V vs. Li/Li^+) prevents dendrite formation, and 3) no true SEI is formed due to the relatively high redox potential [33]. Applications that require high power would favor materials like LTO and NTO over industry standard graphite. Spinel oxides (4.3-3.5 g cc^{-1}) are ~2x denser than graphite (2.2 g cc^{-1}) resulting in higher volumetric energy densities: a metric that is vital for mobile applications such as BEVs. A brief comparison of commercialized anode materials is presented in Table 1.2. An additional anode substitute, HEO, was recently discovered by reexamining thermodynamic vs. kinetic phase stability and the classical Gibbs free energy equation.

Table 1.2: Summary of AAMs.

AAM	Typical Capacity [mAh g^{-1}]	Density [g/cc]	Volume change [%]	Power capability	Cost per capacity	Ref
Graphite	370	2.2	10	Low	$	[34]
Si-based (Si, SiO_x, SiC)	>800	2.3	400	Medium	$	[35]
$Li_4Ti_5O_{12}$ (LTO)	175	3.5	<1	High	$$$	[36]
Nb_2TiO_7 (NTO)	230	4.3	7	High	$$$$	[33]

HEOs are a relatively new class of materials (2015) that have been demonstrated as a possible candidate for next generation LIB anodes [32,37]. Classical thermodynamics would predict

multiple phases when mixing two or more binary oxides due to the high enthalpic mixing penalties, dominating the Gibbs free energy ΔG, Equation 3 [38].

$$\Delta G = \Delta H - T\Delta S \tag{3}$$

Configurational entropy can be simply calculated based on a solid solution model with dependence on each constituent mole fraction X_i in Equation 4 [39]:

$$S_{SS}^{Config} = -R\sum_i X_i \ln(X_i) = -R * ln(n) \tag{4}$$

Where R is the universal gas constant and n is the number of constituents in an equimolar TM oxide. The sum term in S_{SS}^{Config} simplifies to ln(n) when the constituents are equimolar. Typically, HEOs are defined as materials with configurational entropy, ΔS_{config}, >1.5R. Initial studies showed that a five-component TM system heated to 1000˚C and quickly quenched formed a solid solution (ΔS_{config} = 1.51R) while systems with fewer components, or non-equimolar compositions, showed multiple phases [40].

Multiple phases also presented when the sample was cooled slowly, showing that the formation of the single solution is an enantiotropic phase transformation (dependent on and reversible with temperature) [40]. There is a breakdown of the simple quantification of ΔS_{config} in systems with multiple cationic sublattices, i.e. spinel [32]. To remedy this issue, the entropy metric (EM) term, Equation 7, was devised by Dippo et al. [39] to normalize the sublattice model S_{SL}^{Config} such that a comparison could be made between materials with varying crystal types and compositions.

This distinction is important to note as it can be easy to assume the configurational entropy of a given system strictly based on the number of constituents; however, the configurational entropy, or better yet the EM, requires knowledge of the crystal structure before reasonable conclusions can be drawn.

Although high entropy alloys were demonstrated as early as 2004, Rost et al. [40] reported the first single phase HEOs in 2015 Since then, HEOs have found use in numerous applications including catalysis, thermal insulation, dielectric material, and - of special interest to this dissertation - anodes. Sarkar et al. [37] demonstrated that the rock salt seminal composition presented by Rost, $Mg_{0.2}Co_{0.2}Ni_{0.2}Cu_{0.2}Zn_{0.2}O$, could be successfully used as a LIB anode. The Li reaction during de/lithiation for HEOs differs from typical graphite or LTO/NTO. Instead of intercalation (typical cathode mechanism), HEOs undergo a conversion reaction typical of metal oxide anodes such as MnO_2, Fe_3O_4, or Co_3O_4 [41]. The generic conversion reaction can be described by Equation 5 [41].

$$TM_xA_y + (y+z)Li^+ + (y+z)e^- \rightleftharpoons xTM^0 + yLi_z^+A \quad (5)$$

TM is a transition metal and *A* is an anionic species such as O, S, F, P, or N. The conversion reaction typically results in significantly higher gravimetric and volumetric capacities, than intercalation counterparts (up to ~5x); however, poor cyclability and high irreversible capacity loss limit real world application [41,42]. A common theme in HEO applications is that observed properties exhibit a synergistic effect, such that the observed properties are greater than the sum of the parts [43]. This phenomenon has been demonstrated in dielectric, mechanical, and electrochemical properties and subsequently provides additional impetus to study and develop this class of material [44,45].

As new HEO compositions are developed for LIBs, one must consider similar design parameters to CAMs: e.g. cost. The compositional landscape for HEOs is vast; however, the area that includes TMs that are electrochemically active, low-cost, abundant, and nontoxic is quite limited. An unfortunate trend, regarding cost and toxicity, in HEO anode compositions is to rely upon Cr or Co for redox activity. The inclusion of TMs in HEOs, as well as LTO and NTO,

introduces, additional cost compared to carbonaceous and Si-based AAMs. Compounding the problem is the use of Co for redox activity, which is already an issue in CAM composition. Alternatives to Cr and/or Co will significantly improve the appeal of HEO anodes for use in next generation LIBs.

1.5 A Question of Scale

Detailed studies have examined particle size effects for both cathodes and anodes on their respective electrochemical properties. In terms of Li^+ diffusion, smaller average particle sizes (APSs) result in higher specific surface areas (SSAs) with increased number of surface (vs. bulk) sites and shorter average diffusion lengths. In principle, high SSAs should lead to superior charge transfer kinetics and shorter Li^+ diffusion paths on average. Increased interfacial contact area between active material and electrolyte means more Li^+ diffusion pathways and potential for rapid Li^+ diffusion in and out of the active material [24,46–48]. Characteristic migration times of Li^+ within the interior of a cathode particle during intercalation can be derived from Fick's law; Equation 6 [49].

$$\tau = \frac{L^2}{4\pi D^*} \tag{6}$$

Here τ is the characteristic time (or Li^+ migration time), L is the mean free path, and D^* is the chemical diffusion coefficient of Li^+ in the host lattice. The decrease in τ from micro- to nanoparticles can be as much as a factor of 10^6 [49]. Greater access to Li^+ should in theory lead to higher capacity at higher C-rates and subsequently higher power [49].

Additionally, increased SSAs in CAMs offer other benefits that require consideration. Kuppan et al.[46] found that the strain release mechanism for (de)lithiation is influenced by the state of

(de)lithiation and particle size. LMNO particles with APSs < 1 μm resist fracture during (de)lithiation [46].

Unfortunately, the strict minimization of APS is not a perfect design parameter. In layered $LiCoO_2$, it was shown that APSs < 20 nm can result in electronic distortions that decrease redox potential and capacity while increasing capacitive behavior [22]. Even if the ideal design parameter is modified to an APS range of 20 nm to 1μm, the advantage of smaller particles is hindered by increased surface reactions with increases in SSA that can result in excessive SEI formation or in some cases TM dissolution.

A common failure mechanism for Mn-based cathode materials, such as LMNO, is Mn^{2+} dissolution into the electrolyte. This inherent disadvantage is exacerbated by increased SSA [24,50,51]. The disproportionation reaction is triggered by acids such as HF, a common byproduct of PF_6 decomposition in the presence of unwanted moisture and CEI formation [31,50–53]. Newly formed Mn^{2+} dissolves easily in the electrolyte, effectively accelerating cell aging and reducing practical capacity.

AAMs can also benefit from nanoscale APSs. Nanoscale, Si-based materials have shown increased performance compared to mesoscale counterparts. Conversion-type AAMs also benefit from nanostructured morphologies as a mitigation scheme for deleterious volume expansion; however, excessive SEI formation remains a concern with increased SSAs.

As discussed, designing a single, perfect APS for LIB active materials is quite difficult. As is a common theme in active materials, each design choice must exploit targeted advantages and attenuate unavoidable disadvantages – including the synthesis method. There are a considerable number of options for synthesizing active materials which broadly includes solid, liquid, or gaseous methods. Generally, liquid (co-precipitation, sol-gel, solvo/hydrothermal, solution

combustion) and gaseous (flame spray pyrolysis, nebulized spray pyrolysis, liquid feed-flame spray pyrolysis) can produce nanoscale materials. Solid state synthesis can also reduce APSs to nanoscale via post processing (ball milling); though, this process can be costly in terms of time, energy, and equipment milling at scale.

Liquid-based synthesis methods characteristically have high yields and uniform particle morphologies, but the as-produced particles often require high temperature calcination to achieve the desired phase. Gaseous synthesis methods often result in a high yield; however, flame spray pyrolysis (FSP) typically relies on chloride-based precursors and produces HCl gas during synthesis. In addition to unwanted by-products, particle morphologies of FSP-synthesized materials often feature nano sized primary particles with micron size aggregates. LF-FSP offers synthesis that combines the advantages of both liquid and gaseous methods: high purity with high yield and excellent stoichiometry control. Kinetic phases, a consequence of high flame temperature (~1500 K) and rapid quenching, not typically accessible by other synthesis methods are possible via LF-FSP and have been demonstrated previously.

1.6 Scope of Dissertation

As discussed above, active material remains a critical component, driving the development of high energy density batteries and, in a larger sense global electrification such as BEVs. The synthesis of nanoparticles as CAMs and AAMs via LF-FSP is the focus of the work presented here.

Chapter 2 describes typical experimental techniques and parameters for nanoparticle synthesis. Additionally, electrochemical and material characterization techniques are described including scanning electron microscopy (SEM), energy dispersive spectroscopy (EDS), thermogravimetric analysis (TGA), Fourier transform infrared spectroscopy (FTIR), particle size

analysis (PSA), specific surface area analysis via Brunauer-Emmett-Teller (BET) theory, X-ray diffraction (XRD), and X-ray photoelectron spectroscopy (XPS).

Chapter 3 describes the synthesis and characterization of three HEO nanoparticle systems for use as next generation AAMs. Two novel compositions were produced, replacing Co $(CoNiMnFeTi)_3O_4$ with Zn $(ZnNiMnFeTi)_3O_4$ and Cu $(CuNiMnFeTi)_3O_4$. ZnNMFT showed gravimetric and volumetric capacity improvement over industry standard graphite due to high density of spinel HEOs (>5 g cm^{-3}). A brief economic analysis showcased the effect of exchanging high cost for lower cost materials on the overall raw materials price, while also factoring in respective performance. ZnNMFT showed improvement over CoNMFT in capacity per cost by 2x.

Chapter 4 details the synthesis and characterization of Li-, Mn-rich CAMs using LF-FSP with stoichiometries Li_xMNO with x = 0.45-1.50. Initially amorphous and crystalline spinel phases transformed to nanocomposites composed of spinel and monoclinic/layered phases post calcination, with increasing phase content as Li content increases (800ºC/6h/O_2). In electrochemical testing, energy densities greater than 1000 Wh kg_{CAM}^{-1} (~300 mAh g^{-1}) were observed using a green, aqueous binder for $Li_{1.26}MNO$ and $Li_{1.50}MNO$ cycled between 4.9 – 2.4 V.

Chapter 5 focuses on the synthesis and characterization of LFP-type cathode materials by LF-FSP with varying ratios of Fe:Mn ($LiFePO_4$, $LiMn_{1/3}Fe_{2/3}PO_4$, and $LiMn_{2/3}Fe_{1/3}PO_4$) and with addition of Ni ($LiNi_{1/3}Mn_{1/3}Fe_{1/3}PO_4$). Electrochemical performance of synthesized materials was demonstrated in half-cell format with varying C-rates. An increase in practical energy density was obtained with 1/3 Mn substitution ($LiMn_{1/3}Fe_{2/3}PO_4$) compared to LFP, 491±9 vs 464±3 Wh kg^{-1} at 1.0C, respectively.

Chapter 6 provides general conclusions for the work detailed in this dissertation with recommendations for follow-up studies and new directions.

References

[1] J.T. Frith, M.J. Lacey, U. Ulissi, A non-academic perspective on the future of lithium-based batteries, Nat Commun 14 (2023). https://doi.org/10.1038/s41467-023-35933-2.

[2] N. Nitta, F. Wu, J. Lee, G. Yushin, Li-ion battery materials: present and future, Materials Today 18 (2015). https://doi.org/10.1016/j.mattod.2014.10.040

[3] D. Andre, S.J. Kim, P. Lamp, S.F. Lux, F. Maglia, O. Paschos, B. Stiaszny, Future generations of cathode materials: An automotive industry perspective, J Mater Chem A Mater 3 (2015) 6709–6732. https://doi.org/10.1039/c5ta00361j.

[4] M.S.E. Houache, C.H. Yim, Z. Karkar, Y. Abu-Lebdeh, On the Current and Future Outlook of Battery Chemistries for Electric Vehicles—Mini Review, Batteries 8 (2022). https://doi.org/10.3390/batteries8070070.

[5] N. Tolganbek, Y. Yerkinbekova, S. Kalybekkyzy, Z. Bakenov, A. Mentbayeva, Current state of high voltage olivine structured LiMPO4 cathode materials for energy storage applications: A review, J Alloys Compd 882 (2021) 160774. https://doi.org/10.1016/j.jallcom.2021.160774.

[6] S. Ghosh, U.B. charjee, S. Bhowmik, S.K. Martha, A Review on High-Capacity and High-Voltage Cathodes for Next-Generation Lithium-ion Batteries, Journal of Energy and Power Technology 4 (2021) 1–1. https://doi.org/10.21926/jept.2201002.

[7] W. Li, B. Song, A. Manthiram, High-voltage positive electrode materials for lithium-ion batteries, Chem Soc Rev 46 (2017) 3006–3059. https://doi.org/10.1039/c6cs00875e.

[8] Y. Kim, W.M. Seong, A. Manthiram, Cobalt-free, high-nickel layered oxide cathodes for lithium-ion batteries: Progress, challenges, and perspectives, Energy Storage Mater 34 (2021) 250–259. https://doi.org/10.1016/j.ensm.2020.09.020.

[9] M. Wang, X. Chen, H. Yao, G. Lin, J. Lee, Y. Chen, Q. Chen, Research Progress in Lithium-excess Disordered Rock-salt Oxides Cathode, Energy & Environmental Materials (2022) 1139–1154. https://doi.org/10.1002/eem2.12413.

[10] P. Kurzweil, Gaston Planté and his invention of the lead-acid battery-The genesis of the first practical rechargeable battery, J Power Sources 195 (2010) 4424–4434. https://doi.org/10.1016/j.jpowsour.2009.12.126.

[11] P. V. Kamat, Lithium-Ion Batteries and Beyond: Celebrating the 2019 Nobel Prize in Chemistry - A Virtual Issue, ACS Energy Lett (2019) 2757–2759. https://doi.org/10.1021/acsenergylett.9b02280.

[12] A. Yoshino, K. Sanechika, T. Nakajima, Secondary Battery, JP 1989293, 1985.

[13] K. Mizushima, P.C. Jones, P.J. Wiseman, J.B. Goodenough, Li_xCoO_2 (0<x<-1): A new cathode material for batteries of high energy density, Mater Res Bull 15 (1980) 783–789. https://doi.org/10.1016/0025-5408(80)90012-4.

[14] N.T.M. Balakrishnan, A. Das, N.S. Jishnu, L.R. Raphael, J.D. Joyner, J.-H. Ahn, M.J. Jabeen Fatima, R. Prasanth, The Great History of Lithium-Ion Batteries and an Overview on Energy Storage Devices BT - Electrospinning for Advanced Energy Storage Applications, in: N.T.M. Balakrishnan, R. Prasanth (Eds.), Springer Singapore, Singapore, 2021: pp. 1–21. https://doi.org/10.1007/978-981-15-8844-0_1.

[15] R.M. Salgado, F. Danzi, J.E. Oliveira, A. El-Azab, P.P. Camanho, M.H. Braga, The latest trends in electric vehicles batteries, Molecules 26 (2021) 1–41. https://doi.org/10.3390/molecules26113188.

[16] P. Liu, S. Meng, Battery500 Consortium: Development of High Capacity Cathodes and Robust Solid Electrolytes, Pittsburgh, PA, and Morgantown, WV (United States), 2022. https://doi.org/10.2172/1838452.

[17] W.E. Gent, G.M. Busse, K.Z. House, The predicted persistence of cobalt in lithium-ion batteries, Nat Energy 2 (2022) 1132–1143. https://doi.org/10.1038/s41560-022-01129-z.

[18] R. Amin, N. Muralidharan, R.K. Petla, H. Ben Yahia, S.A. Jassim Al-Hail, R. Essehli, C. Daniel, M.A. Khaleel, I. Belharouak, Research advances on cobalt-free cathodes for Li-ion batteries - The high voltage $LiMn_{1.5}Ni_{0.5}O_4$ as an example, J Power Sources 467 (2020) 228318. https://doi.org/10.1016/j.jpowsour.2020.228318.

[19] H.H. Ryu, H.H. Sun, S.T. Myung, C.S. Yoon, Y.K. Sun, Reducing cobalt from lithium-ion batteries for the electric vehicle era, Energy Environ Sci 14 (2021) 844–852. https://doi.org/10.1039/d0ee03581e.

[20] Tesla, Tesla Shareholder Deck Q3 2020, Palo Alto, CA, 2020.

[21] Y. Miao, P. Hynan, A. Von Jouanne, A. Yokochi, Current li-ion battery technologies in electric vehicles and opportunities for advancements, Energies (Basel) 12 (2019) 1–20. https://doi.org/10.3390/en12061074.

[22] C. Liu, Z.G. Neale, G. Cao, Understanding electrochemical potentials of cathode materials in rechargeable batteries, Materials Today 19 (2016) 109–123. https://doi.org/10.1016/j.mattod.2015.10.009.

[23] J.B. Goodenough, Y. Kim, Challenges for rechargeable Li batteries, Chemistry of Materials 22 (2010) 587–603. https://doi.org/10.1021/cm901452z.

[24] M. Wentker, M. Greenwood, J. Leker, A bottom-up approach to lithium-ion battery cost modeling with a focus on cathode active materials, Energies (Basel) 12 (2019) 1–18. https://doi.org/10.3390/en12030504.

[25] S. Oukahou, M. Maymoun, A. Elomrani, K. Sbiaai, A. Hasnaoui, Enhancing the Electrochemical Performance of Olivine LiMnPO4as Cathode Materials for Li-Ion Batteries by Ni-Fe Codoping, ACS Appl Energy Mater 5 (2022) 10591–10603. https://doi.org/10.1021/acsaem.2c01319.

[26] T.G. Brandt, E. Temeche, A.R. Tuokkola, H. Li, S. Indris, D.A. Edelman, K. Sun, R.M. Laine, A. Materials, D.A. Edelman, R.M. Laine, Nanocomposite Li- and Mn-Rich Spinel Cathodes Characterized with a Green, Aqueous Binder System, Chemical Engineering Journal 479C (2024) 147419. https://doi.org/https://doi.org/10.1016/j.cej.2023.147419.

[27] E.A. Wu, S. Banerjee, H. Tang, P.M. Richardson, J.-M. Doux, J. Qi, Z. Zhu, A. Grenier, Y. Li, E. Zhao, G. Deysher, E. Sebti, H. Nguyen, R. Stephens, G. Verbist, K.W. Chapman, R.J. Clément, A. Banerjee, Y.S. Meng, S.P. Ong, A stable cathode-solid electrolyte composite for high-voltage, long-cycle-life solid-state sodium-ion batteries, Nat Commun 12 (2021) 1256. https://doi.org/10.1038/s41467-021-21488-7.

[28] S. Chen, K. Wen, J. Fan, Y. Bando, D. Golberg, Progress and future prospects of high-voltage and high-safety electrolytes in advanced lithium batteries: From liquid to solid electrolytes, J Mater Chem A Mater 6 (2018) 11631–11663. https://doi.org/10.1039/c8ta03358g.

[29] S. Dalavi, M. Xu, B. Knight, B.L. Lucht, Effect of added LiBOB on high voltage ($LiNi_{0.5}Mn_{1.5}O_4$) spinel cathodes, Electrochemical and Solid-State Letters 15 (2012) 1–5. https://doi.org/10.1149/2.015202esl.

[30] A. Hofmann, A. Höweling, N. Bohn, M. Müller, J.R. Binder, T. Hanemann, Additives for Cycle Life Improvement of High-Voltage LNMO-Based Li-Ion Cells, ChemElectroChem 6 (2019) 5255–5263. https://doi.org/10.1002/celc.201901120.

[31] X. Fan, C. Wang, High-voltage liquid electrolytes for Li batteries: Progress and perspectives, Chem Soc Rev 50 (2021) 10486–10566. https://doi.org/10.1039/d1cs00450f.

[32] T.G. Brandt, A.R. Tuokkola, M. Yu, R.M. Laine, Liquid-feed flame spray pyrolysis enabled synthesis of Co- and Cr-free, high-entropy spinel oxides as Li-ion anodes, Chemical Engineering Journal 474 (2023) 145495. https://doi.org/10.1016/j.cej.2023.145495.

[33] K.J. Griffith, Y. Harada, S. Egusa, R.M. Ribas, R.S. Monteiro, R.B. Von Dreele, A.K. Cheetham, R.J. Cava, C.P. Grey, J.B. Goodenough, Titanium Niobium Oxide: From Discovery to Application in Fast-Charging Lithium-Ion Batteries, Chemistry of Materials 33 (2021) 4–18. https://doi.org/10.1021/acs.chemmater.0c02955.

[34] M. Yu, E. Temeche, S. Indris, R.M. Laine, Sustainable SiC Composite Anodes, Graphite Accelerated Lithium Storage, J Electrochem Soc 170 (2023) 070504. https://doi.org/10.1149/1945-7111/ace132.

[35] M. Yu, E. Temeche, S. Indris, W. Lai, R.M. Laine, Silicon carbide (SiC) derived from agricultural waste potentially competitive with silicon anodes, Green Chemistry 1 (2022) 4061–4070. https://doi.org/10.1039/d2gc00645f.

[36] E. Temeche, E. Buch, X. Zhang, T. Brandt, A. Hintennach, R.M. Laine, Improved Electrochemical Properties of $Li_4Ti_5O_{12}$ Nanopowders (NPs) via Addition of $LiAlO_2$ and Li_6SiON Polymer Electrolytes, Derived from Agricultural Waste, ACS Appl Energy Mater 4 (2021) 1894–1905. https://doi.org/10.1021/acsaem.0c02994.

[37] A. Sarkar, L. Velasco, D. Wang, Q. Wang, G. Talasila, L. de Biasi, C. Kübel, T. Brezesinski, S.S. Bhattacharya, H. Hahn, B. Breitung, High entropy oxides for reversible energy storage, Nat Commun 9 (2018). https://doi.org/10.1038/s41467-018-05774-5.

[38] J.W. Gibbs, A Method of Geometrical Representation of the Thermodynamic Properties of Substances by Means of Surfaces, Transactions of the Connecticut Academy of Arts and Sciences (1873) 382–404.

[39] O.F. Dippo, K.S. Vecchio, A universal configurational entropy metric for high-entropy materials, Scr Mater 201 (2021) 113974. https://doi.org/10.1016/j.scriptamat.2021.113974.

[40] C.M. Rost, E. Sachet, T. Borman, A. Moballegh, E.C. Dickey, D. Hou, J.L. Jones, S. Curtarolo, J.P. Maria, Entropy-stabilized oxides, Nat Commun 6 (2015). https://doi.org/10.1038/ncomms9485.

[41] S.H. Yu, X. Feng, N. Zhang, J. Seok, H.D. Abruña, Understanding Conversion-Type Electrodes for Lithium Rechargeable Batteries, Acc Chem Res 51 (2018) 273–281. https://doi.org/10.1021/acs.accounts.7b00487.

[42] M.D. Bhatt, J.Y. Lee, High capacity conversion anodes in Li-ion batteries: A review, Int J Hydrogen Energy 44 (2019) 10852–10905. https://doi.org/10.1016/j.ijhydene.2019.02.015.

[43] B.L. Musicó, D. Gilbert, T.Z. Ward, K. Page, E. George, J. Yan, D. Mandrus, V. Keppens, The emergent field of high entropy oxides: Design, prospects, challenges, and opportunities for tailoring material properties, APL Mater 8 (2020). https://doi.org/10.1063/5.0003149.

[44] A. Sarkar, Q. Wang, A. Schiele, M.R. Chellali, S.S. Bhattacharya, D. Wang, T. Brezesinski, H. Hahn, L. Velasco, B. Breitung, High-Entropy Oxides: Fundamental Aspects and Electrochemical Properties, Advanced Materials 31 (2019). https://doi.org/10.1002/adma.201806236.

[45] A. Sarkar, B. Breitung, H. Hahn, High entropy oxides: The role of entropy, enthalpy and synergy, Scr Mater 187 (2020) 43–48. https://doi.org/10.1016/j.scriptamat.2020.05.019.

[46] S. Kuppan, Y. Xu, Y. Liu, G. Chen, Phase transformation mechanism in lithium manganese nickel oxide revealed by single-crystal hard X-ray microscopy, Nat Commun 8 (2017). https://doi.org/10.1038/ncomms14309.

[47] Q. Tian, Z. Zhang, L. Yang, Y. Xiang, Improving the lithium storage properties of $Li_4Ti_5O_{12}$ anodes by facile two-phase formation and nanostructure engineering strategy, J Alloys Compd 705 (2017) 638–644. https://doi.org/10.1016/j.jallcom.2017.02.175.

[48] C. Julien, A. Mauger, K. Zaghib, H. Groult, Optimization of layered cathode materials for lithium-ion batteries, Materials 9 (2016). https://doi.org/10.3390/MA9070595.

[49] G. Gabrielli, M. Marinaro, M. Mancini, P. Axmann, M. Wohlfahrt-Mehrens, A new approach for compensating the irreversible capacity loss of high-energy $Si/C|LiNi_{0.5}Mn_{1.5}O_4$ lithium-ion batteries, J Power Sources 351 (2017) 35–44. https://doi.org/10.1016/j.jpowsour.2017.03.051.

[50] R. Benedek, Role of Disproportionation in the Dissolution of Mn from Lithium Manganate Spinel, Journal of Physical Chemistry C 121 (2017) 22049–22053. https://doi.org/10.1021/acs.jpcc.7b05940.
[51] M. Yu, T.G. Brandt, E. Temeche, R.M. Laine, Stabilizing High-Voltage Cathodes via Ball-Mill Coating with Flame-Made Nanopowder Electrolytes, ACS Appl Mater Interfaces 14 (2022) 49617–49632. https://doi.org/10.1021/acsami.2c09284.
[52] S. Zhang, N.S. Andreas, R. Li, N. Zhang, C. Sun, D. Lu, T. Gao, L. Chen, X. Fan, Mitigating irreversible capacity loss for higher-energy lithium batteries, Energy Storage Mater 48 (2022) 44–73. https://doi.org/10.1016/j.ensm.2022.03.004.

Chapter 2 Experimental

This chapter discusses experimental techniques and characterization tools utilized throughout the course of this dissertation. Synthesis of precursors and subsequent nanopowders are detailed in the following sections. Unique experimental techniques and methodologies can be found in their respective chapters.

2.1 Precursor Synthesis

Two primary types of metalloorganic precursors were used to synthesis nanoparticles via LF-FSP in this work. The first group is broadly metal carboxylates including metal propionates and isobutyrates. The second group is metal-atranes such as titanatrane glycolate. Typically, metal carboxylate synthesis begins with the associated carboxylic acid reacting with a metal organic or inorganic compound such as a metal acetate, hydroxide, or nitrate. Details of the reaction can be found in Chapter 2.1.1 Generally, metal-atrane precursors begin by reacting a metal alkoxide with triethanolamine (TEA). Details of the reaction can be found in Chapter 2.1.2.

All TM precursors were synthesized in the Laine lab before forming a precursor solution used in LF-FSP synthesis.

2.1.1 Nickel Isobutyrate (NiB)

{$[Ni(OH)_2]$, 102 g, 1.1 mol} was reacted with $[(CH_3)_2CHCOOH$, 300 mL, 3.3 mol] at a molar ratio of 1:3, in a 500 mL three neck round bottom flask using a distillation setup to form $\{Ni[O_2CCH(CH_3)_2]_2\}$. The solution was stirred using a magnetic stir bar and heated to 135˚C under

N_2 flow until a solid product was obtained. Upon cooling the solid was removed from the flask. Excess isobutyric acid was removed via vacuum drying at 100˚C, 30 in Hg. Ceramic yield (CY) of the collected precursor was determined by TGA to be 27%, lower than the theoretical CY 32%. This discrepancy is attributed to excess, unreacted isobutyric acid. Yield of NiB precursor reaction was 69%, while purity was determined to be 84%.

2.1.2 Titanatrane Glycolate (TiG)

[$Ti(OiPr)_4$, 1150 ml, 3.80 mole] was reacted with [$N(CH_2CH_2OH)_3$, 1010 ml, 7.60 mole] to form at a molar ratio of 1:2 in a 3 L vessel under N_2 flow to form {$Ti(OCH_2CH_2)_3N[OCH_2CH_2N(CH_2CH_2OH)_2]$}, following previous studies [1]. [$N(CH_2CH_2OH)_3$] was added slowly via addition funnel while the mixture was stirred constantly over a 12 h period. The resulting titanatrane glycolate, dissolved in byproduct isopropanol, had a TGA determined ceramic yield of 13%.

2.2 Nanopowder Synthesis via LF-FSP

The Laine Group developed the LF-FSP synthesis method at the University of Michigan during the 1990's and has since remained at the forefront of LF-FSP enabled synthesis of fine nanopowders. The working principle of LF-FSP is a combination of liquid and vapor methods; alcohol solution containing metalloorganic precursors is aerosolized with oxygen and subsequently combusted. Gas phase evolution of ceramic nanoparticles first includes particle nucleation, which occurs when vapors react to form oxo ions that condense into clusters that eventually form nanosized particles via coagulation [2–4]. The rate of particle growth can be modeled using a Brownian collision-coalescence growth model that depends on several time-based variables that are typically less than 1 ms [3–6].

In-depth description of the LF-FSP process has previously been detailed elsewhere [1,7–12]. Typical LF-FSP syntheses begin with a 3 wt.% ceramic yield solution composed of metalloorganic precursors dissolved in anhydrous EtOH. Thermogravimetric analyses are performed on each precursor to calculate the proper precursor quantities. An accurate ceramic yield, with predicted decomposition product(s), is vital to forming a precursor solution that will result in the target composition. In some cases, additional precursor will be added to the solution for elements that are known to be especially volatile (i.e. Li) [1,7,9–11,13–15]. Early studies of phase diagrams demonstrated the level of compositional control possible when using the LF-FSP as a synthesis method. After combustion in an oxygen-rich environment, synthesized nanoparticles are collected downstream in aluminum tubes acting as electrostatic precipitators (10 kV DC potential) and can be removed manually from the system post-synthesis. After collection, a supernatant solution is formed using the as-produced nanopowders (5-25 g), a polar solvent (i.e. 100-500 mL EtOH), and a polymeric dispersant (i.e. 1-4% Bicine). The nanopowders are dispersed via ultrasonication of the supernatant solution using an ultrasonic horn for 10 min at 50 W. The solution is left to settle (3-6 h) and then decanted to remove unwanted and undispersed material. Excess solvent is removed and the dispersed nanopowder can be calcined or directly used in a slurry for thin film or electrode studies.

2.3 Material Characterization

X-Ray Diffraction (XRD) was performed (SmartLab XRD, Rigaku, Japan) operating at 40kV and 45mA with a scan rate of 8º 2Θ min^{-1} and step size of 0.01 2Θ in Bragg-Brentano geometry. Lattice parameters were calculated using Rietveld refinement using the appropriate target phase. XRD allows for the identification of primary and secondary crystalline phases, as well as

amorphous content. Rietveld refinement allows for quantification of phase content and unit cell dimensions.

Fourier transform infrared (FTIR) spectroscopy was performed from 400 to 4000 cm^{-1} (Nicolet 6700 FTIR, Thermo Scientific, Waltham, MA, United States) under N_2. FTIR studies allow the identification of characteristic functional groups, phases, and other bonds.

Inductively coupled plasma mass spectrometry (ICP-MS) studies were performed (iCAP quadrupole ICP-MS, Thermo Scientific) using diluted samples digested in aqua regia solution. ICP-MS is a method to determine sample composition with high resolution.

Thermogravimetric analysis (TGA) was run under N_2 (60 mL min^{-1}) at ramp rate of 5˚C min^{-1} (SDT Q600, TA Instruments, Newcastle, DE, United States) unless otherwise stated. TGA studies are used to determine the ceramic yield of a sample under a particular atmosphere.

Brunauer–Emmett–Teller Analysis (BET) specific surface area (SSAs) analyses were performed on the as-shot and heated NPs (ASAP 2020, Micromeritics Instruments Corp, Norcross, GA, United States). The powders were degassed at 400˚C/5 h before nitrogen adsorption and desorption analysis was conducted, unless otherwise stated. The temperature and time used for these materials is standard for metal oxide testing. BET studies are used to quantify the SSA of nanoparticles via nitrogen gas de/adsorption, and the particle size can be estimated from the SSA.

Scanning Electron Microscopy (SEM) and Energy Dispersive Spectroscopy (EDS) was conducted using JSM-IT300HR In Touch Scope scanning electron microscope (JEOL USA, Inc.) to acquire the microstructure images and EDS maps. SEM allows for determination of particle morphology. When combined with EDS, material composition maps can be generated to determine composition homo- or heterogeneity.

Particle size analysis (PSA) was performed (LS 13 320 Particle Size Analyzer Beckman Coulter, Indianapolis, IN, United States) using a liquid module, where NPs were dispersed in DI water with sonication for size measurement. Data was taken from the average of 10 measurements of 90 s each using a Fraunhofer optical model. PSA is another method to determine the APS of a sample. While BET offers a single APS, PSA provides a histogram of particle sizes with concentration.

X-ray photoelectron spectroscopy (XPS) was performed (Kratos Axis Ultra, Kratos Analytical) to analyze the element oxidation states of the HEOs. Measurements were conducted at room temperature under $3.1\times10-8$ Pa using monochromatic Al source. Core level scans were recorded at 14 kV and 8 mA. The binding energies of all the elements were calibrated relative to C 1s at 284.8 eV. Deconvolution analysis was performed using CasaXPS. XPS is a surface characterization method to determine elemental composition and chemical state of a sample.

2.4 Electrochemical Sample Preparation

In a typical electrode study for electrochemical analysis, the dispersed nanopowders require calcination to 1) remove dispersant and 2) crystallize or increased crystallinity. As-produced powders are pressed into pellets and placed between alumina disks for calcination in a tube furnace with controlled gas flow (i.e. O_2, Ar). The calcination conditions including ramp rate and calcination temperature are dependent on the starting material and target phase. Typically, calcined materials are ground via mortar and pestle to reduce average particle size increases due to particle sintering. Particle size can be further reduced via low intensity ball milling (20 rpm). Details of slurry preparation for each study can be found in the corresponding materials and methods section.

Typically, electrode discs were punched out using a 13- (cathode) or 16-mm (anode) diameter handheld punch. The electrode discs were calendared between two Mylar sheets (50 μm thickness)

using a uniaxial press at 4.5 ksi/1 min/55˚C. Theoretical 1C capacity value of a pressed electrode is calculated based on the mass of the electrode, mass of the bare current collector, % active material in the electrode, and the theoretical capacity of the active material. Coin cells using the processed electrodes were assembled with Li-metal anodes to form a half-cell.

References

[1] E. Yi, W. Wang, S. Mohanty, J. Kieffer, R. Tamaki, R.M. Laine, Materials that can replace liquid electrolytes in Li batteries: Superionic conductivities in $Li_{1.7}Al_{0.3}Ti_{1.7}Si_{0.4}P_{2.6}O_{12}$. Processing combustion synthesized nanopowders to free standing thin films, J Power Sources 269 (2014) 577–588. https://doi.org/10.1016/j.jpowsour.2014.07.029.

[2] J. Azurdia, Processing and synthesis of multi-metallic nano oxide ceramics via liquid-feed flame spray pyrolysis, University of Michigan, 2009.

[3] M.S. Wooldridge, Gas-phase combustion synthesis of particles, Prog Energy Combust Sci 24 (1998) 63–87.

[4] S.E. Pratsinis, Flame aerosol synthesis of ceramic powders, Prog Energy Combust Sci 24 (1998) 197–219. https://doi.org/10.1016/S0360-1285(97)00028-2.

[5] G.D. Ulrich, B.A. Milnes, N.S. Subramanian, Particle Growth in Flames. II: Experimental Results for Silica Particles, Combustion Science and Technology 14 (1976) 243–249. https://doi.org/10.1080/00102207608547532.

[6] N.J. Taylor, Liquid-Feed Flame Spray Pyrolysis Synthesis of Oxide Nanopowders for the Processing of Ceramic Composites, University of Michigan, 2015.

[7] E. Temeche, E. Buch, X. Zhang, T. Brandt, A. Hintennach, R.M. Laine, Improved Electrochemical Properties of $Li_4Ti_5O_{12}$ Nanopowders (NPs) via Addition of $LiAlO_2$ and Li_6SiON Polymer Electrolytes, Derived from Agricultural Waste, ACS Appl Energy Mater 4 (2021) 1894–1905. https://doi.org/10.1021/acsaem.0c02994.

[8] E. Temeche, E. Yi, V. Keshishian, J. Kieffer, R.M. Laine, Liquid-feed flame spray pyrolysis derived nanopowders (NPs) as a route to electrically conducting calcium aluminate ($12Ca_{O.7}Al_2O_3$) films, J Eur Ceram Soc (2019). https://doi.org/10.1016/j.jeurceramsoc.2018.11.051.

[9] E. Yi, W. Wang, J. Kieffer, R.M. Laine, Key parameters governing the densification of cubic-$Li_7La_3Zr_2O_{12}$ Li+ conductors, J Power Sources (2017). https://doi.org/10.1016/j.jpowsour.2017.03.126.

[10] E. Temeche, S. Indris, R.M. Laine, $LiAlO_2/LiAl_5O_8$ Membranes Derived from Flame-Synthesized Nanopowders as a Potential Electrolyte and Coating Material for All-Solid-State Batteries, ACS Appl Mater Interfaces 12 (2020) 46119–46131. https://doi.org/10.1021/acsami.0c13021.

[11] E. Yi, W. Wang, J. Kieffer, R.M. Laine, Flame made nanoparticles permit processing of dense, flexible, Li+ conducting ceramic electrolyte thin films of cubic-$Li_7La_3Zr_2O_{12}$ (c-

LLZO), J Mater Chem A Mater 4 (2016) 12947–12954. https://doi.org/10.1039/c6ta04492a.

[12] E. Yi, E. Temeche, R.M. Laine, Superionically conducting beta"-Al_2O_3 thin films processed using flame synthesized nanopowders, J Mater Chem A Mater 6 (2018) 12411–12419. https://doi.org/10.1039/c8ta02907e.

[13] W. Wang, E. Yi, A.J. Fici, R.M. Laine, J. Kieffer, Lithium Ion Conducting Poly(ethylene oxide)-Based Solid Electrolytes Containing Active or Passive Ceramic Nanoparticles, Journal of Physical Chemistry C 121 (2017) 2563–2573. https://doi.org/10.1021/acs.jpcc.6b11136.

[14] T.G. Brandt, E. Temeche, A.R. Tuokkola, H. Li, S. Indris, D.A. Edelman, K. Sun, R.M. Laine, A. Materials, D.A. Edelman, R.M. Laine, Nanocomposite Li- and Mn-Rich Spinel Cathodes Characterized with a Green, Aqueous Binder System, Chemical Engineering Journal 479C (2024) 147419. https://doi.org/https://doi.org/10.1016/j.cej.2023.147419.

[15] M. Yu, T.G. Brandt, E. Temeche, R.M. Laine, Stabilizing High-Voltage Cathodes via Ball-Mill Coating with Flame-Made Nanopowder Electrolytes, ACS Appl Mater Interfaces 14 (2022) 49617–49632. https://doi.org/10.1021/acsami.2c09284.

Chapter 3 Liquid-Feed Flame Spray Pyrolysis Enabled Synthesis of Co- and Cr-Free, High-Entropy Spinel Oxides as Li-Ion Anodes.

3.1 Summary

Typically, high-entropy oxide (HEO) and medium-entropy oxide (MEO) electrochemical studies rely on Co and/or Cr for high capacity; however, for safety and cost issues this is not ideal for large scale application. To this end, we report the synthesis and characterization of two Co-free, novel HEO compositions, replacing Co [$(CoNiMnFeTi)_3O_4$] with Zn [$(ZnNiMnFeTi)_3O_4$] and Cu [$(CuNiMnFeTi)_3O_4$], for use as next generation anode active materials. The distinction between HEO and MEO is calculated based on an entropy metric via the sublattice model due to the two cationic sublattices in the spinel structure. XRD results indicate a single phase was maintained for all synthesized samples, and SEM/EDX showed uniform elemental distribution for each synthesized nanomaterial. While the best performing nanomaterial (ZnNMFT) showed some gravimetric capacity improvement over the industry standard graphite "Gr" (480 mAh g_{HEO}^{-1} vs. 372 mAh g_{Gr}^{-1}), there is a clear gain in volumetric capacity (2460 mAh cm_{HEO}^{-3} vs. 820 mAh cm_{Gr}^{-3}). A decrease in performance was expected by replacing Co in favor of Zn/Cu; however, galvanostatic cycling results show improved performance for ZnNMFT compared to both CoNMFT and CuNMFT when using high loading electrodes (>1 mAh cm^{-2}). While performance alone is critical for industrial applications, cost can also act as an enabling or limiting factor. To this end, a brief economic analysis was undertaken showcasing the effect of exchanging high cost for lower cost materials on both the raw materials prices, but also factoring in respective

performance. By including observed discharge capacity, ZnNMFT showed improvements in capacity per cost by 2x over CoNMFT.

The study detailed in this chapter was primarily conducted by myself with specialized characterization performed by Mengjie Yu (XPS) and Andrew Tuokkola (PSA). The remaining author – Prof. Richard M. Laine– contributed to this work via other mechanisms such as funding acquisition and manuscript revisions. This work is published in a journal article entitled "Liquid-Feed Flame Spray Pyrolysis Enabled Synthesis of Co- and Cr-Free, High-Entropy Spinel Oxides as Li-Ion Anodes" in Chemical Engineering Journal, 2023, Vol 474C, page 145495 [1]. The text and figures in this chapter were adapted from that article by retained copyright of the author.

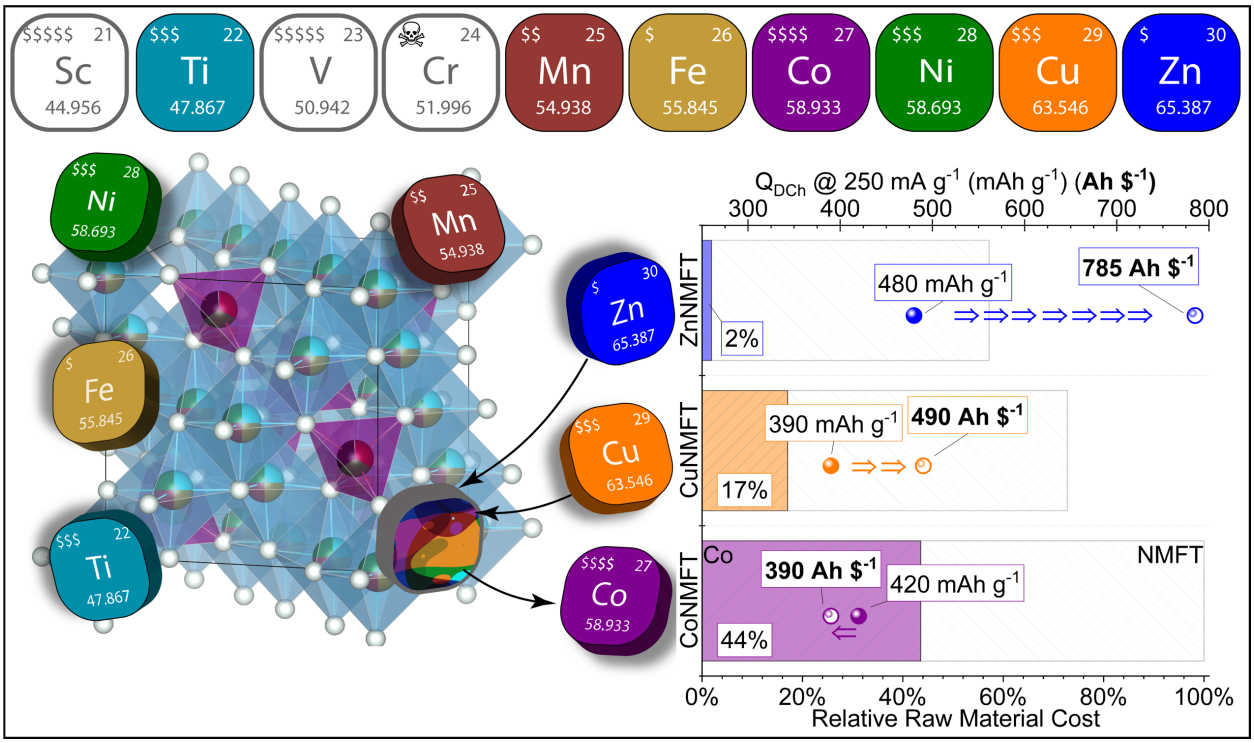

Figure 3.1: Graphical abstract detailing structure, composition, cost, and performance of synthesized high entropy oxide nanoparticles.

3.2 Introduction

Anode active material (AAM) optimization is critical to the success of electric vehicles (EVs). The near-term EV market is slowly introducing Si-additives ($Q_{Si\text{-}theoretical}$ = 3590 mAh g^{-1}) to well-

understood graphite ($Q_{Gr\text{-}theoretical}$ = 372 mAh g^{-1}) [2,3]. The primary limitation of Si-Gr (graphite) composite anodes is catastrophic volumetric expansion on lithiation (~370% Si component), which in turn inhibits high Si contents unless cell designs can accommodate or minimize this expansion [3]. Li-metal ($Q_{Li\text{-}theoretical}$ = 3860 mAh g^{-1}) seems to be an obvious choice; however, there are well known challenges with respect to cycle life and dendrite formation, which leads to safety concerns [2]. The next generation of AAMs will require significant improvement from standard Gr, which can feasibly be achieved by continued optimization of Si-Gr composites – or an alternate material. Next-generation AAMs, especially for EVs, should improve on gravimetric (372 mAh g^{-1}) and volumetric Gr capacities (841 mAh cm^{-3}, un-lithiated) [4]. Among possible candidates, HEOs and MEOs make up a relatively new class of material with interesting properties.

Entropy-stabilized oxides (ESOs), first reported by Rost et al.[5] in 2015, rely on entropic stabilization to form a single-phase oxide. Thermodynamics of mixtures can be simply described by the Gibbs free energy equation $\Delta G = \Delta H - T\Delta S$, where T is absolute temperature (K) and ΔG, ΔH, and ΔS are the changes in Gibbs free energy, enthalpy, and entropy, respectively [6]. Mixing two or three binary metal oxide systems often results in multiple phases due to a large positive enthalpy of mixing penalty, ΔH_{mixing} [5,7]. In ESO materials, large configurational entropy allows ΔS to overcome ΔH_{mixing} penalties. Configurational entropy can be described using the sublattice model, shown in Equation 7 below [8].

$$S_{SL}^{config} = \frac{-R\Sigma_s\Sigma_i a^s X_i^s \ln(X_i^s)}{\Sigma_s a^s} \quad (7)$$

Here a^s is the number of available sites on the s sublattice and X_i^s is the fraction of element species i randomly distributed on the s sublattice (site fraction) [8]. Typically, the configurational entropy of ESOs or high-entropy oxides (HEOs) is calculated using a solid-solution model, which can be derived from Equation **1** using a single sublattice. When considering structures with a single

cation sublattice such as rock salt, configurational entropy calculation via the solid solution model is appropriate; however, when the solid solution method is applied to structures with multiple cation sublattices (i.e. spinel) the calculated configurational entropy will be inaccurate or misleading.

To standardize these calculations, Dippo et. al [8] proposed a method to distinguish between high-, medium-, and low-entropy oxides using a modified sublattice model [9]. Entropy metric (EM) is a modification of the configurational entropy calculated via the sublattice model (Equation 7) by multiplying by L/R where L is the number of sublattices and R is universal gas constant [8]. Based on this proposal, materials with EM >1.5 and 1.0 >EM >1.5 are referred to as HEO and MEO, respectively [9]. In the case of a crystal structure with multiple cation sublattices (i.e. spinel) assuming a solid solution of 5 unique cations will result in $\Delta S = 1.61R$ (where R is the ideal gas constant), whereas considering multiple sublattices could result in EM values that reflect medium entropy (EM = 1.00-1.50).

Spinel materials, with the general composition $(A)[B_2]O_4$, have a total of three sublattices: two cationic and one anionic. The calculated EM depends on the total number of unique cations per sublattice, and the total number of sites per sublattice [8]. It can be difficult to calculate the correct EM values solely based on the elemental composition – the relative sublattice location(s) of each component can be the difference between high and medium EM. Previous theoretical studies which consider configurational entropy and Entropy Metric often assume cations which wholly select one site over another, such that none of the constituent elements are shared between sites. Experimentally, this level of selectivity is difficult to control, and quantify, given that many transition metals have preference for both octahedral and tetrahedral sites, or the inverse spinel structure [10]. To maximize the EM of a five cation $(A)[B_2]O_4$ structure, all five cations should be

shared between the (A) and [B] sites with a molar ratio of (1):[2] between (A):[B] sites, i.e. $(a_{0.33}b_{0.33}c_{0.33}d_{0.33}e_{0.33})$ $[a_{0.67}b_{0.67}c_{0.67}d_{0.67}e_{0.67}]O_4$ for cations a, b, c, d, and e. The EM of this system can be calculated to 2.07, which is much higher than the EM value using the solid solution model (1.61) for the same number of cations. While the sublattice model results in a higher EM than the solid solution model for this system, the EM will decrease as constituent elements increase preference for a particle site/sublattice. Additionally, there are site preference limitations based on stoichiometry following the (A):[B] ratio. For example, systems with one element in either the (A) or [B] site with the remaining elements located in the other site are not stoichiometrically possible given an equimolar composition. These cases would result in (A):[B] ratios of 4.00 and 0.25, respectively. Assuming equimolar ratio of five cations, the lowest possible EM (1.42) is calculated from a configuration where only one cation is shared between the A (tetrahedral) and B (octahedral) sites, one cation is only in tetrahedral, and three cations are only in octahedral. Most equimolar configurations result in an EM in the high entropy range. Select scenarios are presented in Figure 3.2 and Table 3.1 specifying the quantity and location of unshared cations with the maximum calculated EM. The surface shown in Figure 3.2 is an extension of possible EMs from a system with 3 shared cations (1A1B), and one unshared cation in each of the sublattices. A surface can be constructed in three-dimensional space as there are three concentration variables but the third is a function of the first two. In this scenario, only near the bounds of low concentration does the EM dip into the medium entropy range – therefore it is likely that a material with this composition is a high-entropy material.

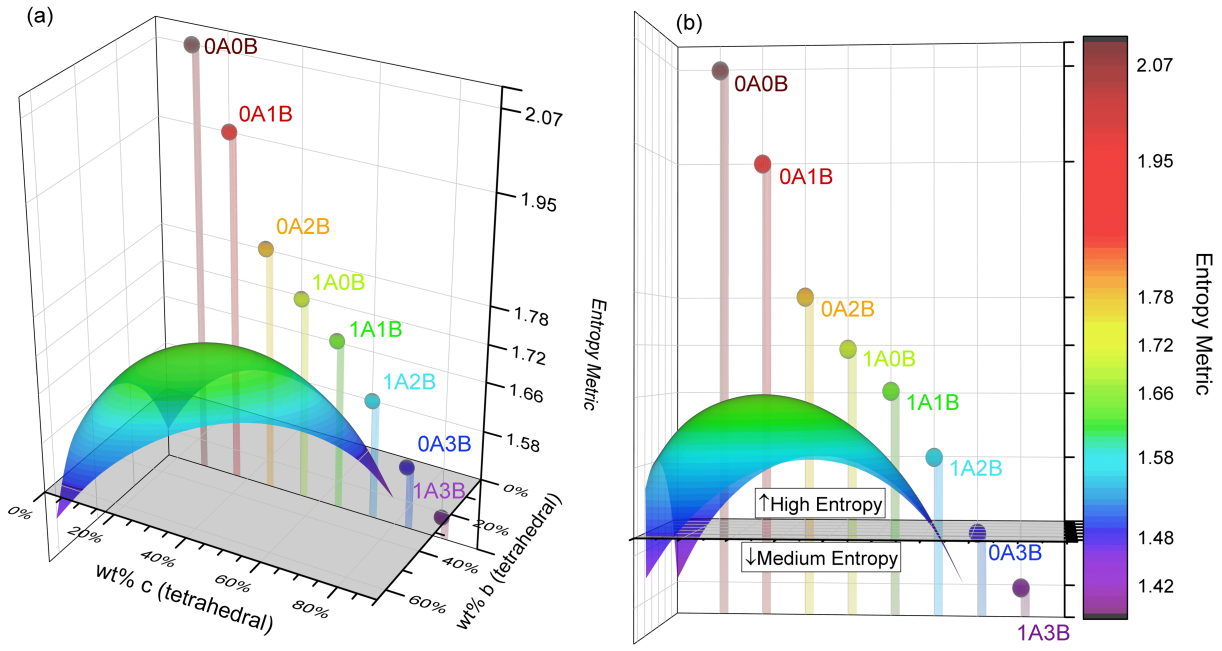

Figure 3.2: Calculated Entropy Metrics for five cation spinel systems with varying site preference. Spheres labeled as number of exclusive A and B site elements are referenced in Table 3.1.

Table 3.1: Summary of calculated Entropy Metrics using five cation, equimolar spinel structure and example cation location by mol%.

Sample	Composition	Example cations in $(A)[B_2]O_4$ (mol%)				EM
		(A)	(A) shared	[B] shared	[B]	
0A0B	$(a_{0.33}b_{0.33}c_{0.33}d_{0.33}e_{0.33})[\ a_{0.67}b_{0.67}c_{0.67}d_{0.67}e_{0.67}]O_4$	-	$(abcde)_{0.33}$	$[abcde]_{0.67}$	-	2.07
0A1B	$(a_{0.42}b_{0.42}c_{0.42}d_{0.42})[\ a_{0.58}b_{0.58}c_{0.58}d_{0.58}e]O_4$	-	$(abcd)_{0.42}$	$[abcd]_{0.58}$	e	1.95
0A2B	$(a_{0.55}b_{0.55}c_{0.55})[\ a_{0.45}b_{0.45}c_{0.45}de]O_4$	-	$(abc)_{0.55}$	$[abc]_{0.45}$	de	1.78
0A3B	$(a_{0.83}b_{0.83})[\ a_{0.17}b_{0.17}cde]O_4$	-	$(ab)_{0.83}$	$[ab]_{0.17}$	cde	1.48
1A0B	$(ab_{0.17}c_{0.17}d_{0.17}e_{0.17})[\ b_{0.83}c_{0.83}d_{0.83}e_{0.83}]O_4$	a	$(bcde)_{0.17}$	$[bcde]_{0.83}$	-	1.72
1A1B	$(ab_{0.22}c_{0.22}d_{0.22})[\ b_{0.78}c_{0.78}d_{0.78}e]O_4$	a	$(bcd)_{0.22}$	$[bcd]_{0.78}$	e	1.66
1A2B	$(ab_{0.33}c_{0.33})[\ b_{0.67}c_{0.67}de]O_4$	a	$(bc)_{0.33}$	$[bc]_{0.67}$	de	1.58
1A3B	$(ab_{0.67})[\ b_{0.33}cde]O_4$	a	$(b)_{0.67}$	$[b]_{0.33}$	cde	1.42

In this work, materials without EM calculations will be referred to as a compositionally complex. It is important to note that high configurational entropy materials do not necessarily qualify as entropy stabilized, and vice versa. Entropy stabilization is a property that is generally demonstrated experimentally, whereas configurational entropy can be calculated theoretically, see Equation 7. HEOs and MEOs both take advantage of having many constituent cations, which

allows for compositional flexibility, and subsequent tailoring of material properties based on compositional design.

Sarkar et al.[11] were the first to employ HEOs in electrochemical applications as an AAM using the rock salt $Mg_{0.2}Ni_{0.2}Cu_{0.2}Co_{0.2}Zn_{0.2}O$ (rock salt, RS-1) composition. This study, and an analogous study using spinel structures, emphasized the importance of entropy stabilization, such that samples with only 4 TMs showed significantly worse capacity and capacity retention compared to the material with 5 TMs [11,12]. The electrochemical contribution of each constituent element in RS-1 has been studied extensively [11,13–17]. The RS-1 lithiation mechanism is best described as a combination of conversion and alloying [11,16,17]. For the RS-1 composition, operando XAS and XRD studies combined with cyclic voltammetry reveal that Co, Ni, and Cu undergo irreversible conversion during the initial discharge, resulting in high capacity. Zn was shown to undergo reversible de/alloying through cycling. Importantly, the original single phase is not maintained after the initial cycle, but instead a mixed phase consisting of metal and metal oxides is produced.

Since this initial work, there have been numerous studies on additional rock salt derivatives in addition to spinel structured materials with a wide range of configurational entropies [12,18]. The large number of required constituent elements to form HEOs and MEOs results in many possible combinations of TMs. For large-scale applications such as the EV market, cost is an unavoidable requirement [19,20]. While many of the studied materials offer promising performance, most of the compositions contain either Co or Cr [12,18,21–41]. These TMs present well-documented challenges in supply chain risk, cost, and safety [42]. A similar issue exists on the opposite side of the battery, where there are widespread efforts to eliminate Co use in high energy density cathode

materials [43,44]. Avoiding high-cost metals and focusing on inexpensive, commodity TMs is a crucial design consideration if H/MEOs are to be used on an industrial scale.

Additionally, the electrochemical impact of each constituent element should be considered. Most reported HEO anodes undergo some level of conversion during initial lithiation. The Ni, Cu, and Co components in RS1 and Mn, Ni, Co, Fe, Cr within typical spinel compositions have all shown conversion behavior upon de/lithiation, while Zn typically shows alloying behavior [12,22,23,36,37,39–41,45]. Chen et. al [12] demonstrated a compositionally complex oxide $(NiCoMnFeTi)_3O_4$ that showed strong performance as an Li-ion anode. The demonstrated stability of this AAM is attributed to the formation of $LiTi_2O_4$ maintaining anode crystallinity as other constituents undergo conversion and de/alloying reactions with Li, which are accompanied by phase transformations and volume expansion [12]. While this system is notable for its impressive electrochemical performance, its use of Co remains a challenge for potential use at a large scale.

One challenge for H/MEOs is synthesis – both time and temperature. The first HEOs were synthesized via physical mixing of the constituent binary oxides and transformed at high temperature through solid-state reaction to target products. Calcination temperatures and times can vary from 900° to 1350˚C for 6 to 36 h [12,27,36,37,40]. These calcination requirements represent a tremendous amount of energy presenting not only practical challenges, but also economic problems. Rapid synthesis techniques such as nebulized spray pyrolysis (NSP) and flame spray pyrolysis (FSP) drastically reduce synthesis time while still producing crystalline powder [11,46–48]. While NSP and FSP methods have been used for HEO anode syntheses, the target structures have been rock salt only – not spinel [11,46–48].

The Laine group has used liquid-feed flame spray pyrolysis (LF-FSP) to synthesize phase pure, unaggregated ceramic nanopowders (NPs), which have been explored in electrochemical

applications as solid electrolyte and AAM [49–60]. LF-FSP has not been extensively explored as an AAM synthesis method with current studies limited to $Li_4Ti_5O_{12}$ (LTO). Compared to other aerosol technologies such as FSP, LF-FSP offers the benefit of synthesis without HCl byproduct [61]. Detailed LF-FSP procedures have previously been reported [49–56,58–60]. LF-FSP syntheses, at laboratory scales, can range from 10 to 300 g h^{-1}, while commercial scale syntheses reach kg h^{-1} in a continuous process [61–63]. LF-FSP offers the benefits of controlled morphology, phase purity, high yield, and relatively low cost [49,59]. Due to the nature of high temperature synthesis followed by rapid quenching, LF-FSP can often access metastable, kinetically-driven phases not produced by standard calcination reactions [49–51,60].

Herein we report the LF-FSP synthesis and characterization of two Co- and Cr-free, novel HEO compositions, replacing Co [$(CoNiMnFeTi)_3O_4$] with Zn [$(ZnNiMnFeTi)_3O_4$] and Cu [$(CuNiMnFeTi)_3O_4$], for use as next generation anode active materials. Removal of Co from the CoNMFT system is critical due to negative economical and supply chain implications; however, Co has been demonstrated to be a key component of high-performance HEO anode materials. The role of Cu and Zn as potential substitutes for Co would be to 1) lower the cost and supply chain impact on the overall material and 2) to maintain or improve electrochemical performance from either the material perspective or a per cost basis.

3.3 Materials and Methods

3.3.1 Precursor Synthesis

3.3.1.1 Manganese Isobutyrate (MnB) {$Mn[O_2CCH(CH_3)_2]_2$}

{$(CH_3COO)_2Mn{\bullet}4H_2O$, 267 g, 1.1 mol} was reacted with [$(CH_3)_2CHCOOH$, 300 mL, 3.3 mol] at a molar ratio of 1:3, in a 500 mL three neck round bottom flask using a distillation setup. The

solution was stirred using a magnetic stir bar and heated to 135˚C under N_2 flow until a transparent liquid was obtained. Upon cooling the solution crystalized and the solid was removed from the flask. Excess isobutyric acid was removed via vacuum drying at 100˚C, 30 in Hg. Ceramic yield of the collected precursor was determined by TGA to be 35.8%, higher than the theoretical CY 34.4% (assuming Mn_2O_3 product). This discrepancy is attributed to a mixture of Mn_2O_3 and MnO_2 forming via decomposition. Based on the mixed decomposition products, yield of MnB was 45%, while purity was determined to be 98%.

3.3.1.2 Iron Isobutyrate (FeB) {$Fe[O_2CCH(CH_3)_2]_2$}

{$[Fe(NO_3)_3 \bullet 9H_2O]$, 267 g, 0.66 mol} was reacted with [$(CH_3)_2CHCOOH$, 300 mL, 3.3 mol] at a molar ratio of 1:3, in a 500 mL three neck round bottom flask using a distillation setup. The solution was stirred using a magnetic stir bar and heated to 135˚C under N_2 flow until a solid product was obtained. The solid was then cooled and removed from the flask. Excess isobutyric acid was removed via vacuum drying at 100˚C, 30 in Hg. Ceramic yield of the collected precursor was determined by TGA to be 24.8%, lower than the theoretical CY 31%. This discrepancy is attributed to excess, unreacted isobutyric acid. Yield of FeB precursor reaction was 38%, while purity was determined to be 80%.

3.3.1.3 Zinc Isobutyrate (ZnB) {$Zn[O_2CCH(CH_3)_2]_2$}

{$[Zn(OAc)_2 \bullet 2H_2O]$, 302 g, 1.38 mol} was reacted with [$(CH_3)_2CHCOOH$, 375 mL, 4.13 mol] at a molar ratio of 1:3, in a 500 mL three neck round bottom flask using a distillation setup. The solution was stirred using a magnetic stir bar and heated to 135˚C under N_2 flow until a transparent liquid was obtained. Upon cooling the solution solidified and the solid was removed from the flask. Excess isobutyric acid was removed via vacuum drying at 100˚C, 30 in Hg. Direct ceramic yield

could not be determined due to ZnO sublimation, therefore theoretical CY (34%) was used instead. Yield of ZnB precursor reaction was 54%, while purity was determined to be 88%.

3.3.1.4 Copper Isobutyrate (CuB) {Cu[$O_2CCH_2(CH_3)_2$]$_2$}

[(CuO), 87.6 g, 1.1 mol] was reacted with [CH_3CH_2COOH, 300 mL, 3.3 mol] at a molar ratio of 1:3, in a 500 mL three neck round bottom flask using a distillation setup. The solution was stirred using a magnetic stir bar and heated to 135˚C under N_2 flow. A solid product was obtained during heating, which was then removed from the flask. Ceramic yield of the collected precursor was determined by TGA to be 25.6%, lower than the theoretical CY 33%. This discrepancy is attributed to excess, unreacted isobutyric acid. Yield of CuB precursor reaction was 86%, while purity was determined to be 78%.

3.3.1.5 Cobalt Propionate (CoP) [Co($O_2CCH_2CH_3$)$_2$]

[($CoCO_3$•H_2O), 43 g, 0.4 mol] was reacted with [CH_3COOH, 100 mL, 1.3 mol] at a molar ratio of 1:4, in a 250 mL three neck round bottom flask using a distillation setup. The solution was stirred using a magnetic stir bar and heated to 140˚C under N_2 flow. After 24 h [$(CH_3CH_2CO)_2O$, 52 mL, 0.4 mol] was added to the solution and stirring continued. Upon cooling, the solution crystalized and the solid was removed from the flask. Ceramic yield of the collected precursor was determined by TGA to be 27%, lower than the theoretical CY 36%. This discrepancy is attributed to excess, unreacted propionic acid. Yield of CoP precursor reaction was 74%, while purity was determined to be 78%.

3.3.2 Nanopowder Synthesis

A series of LF-FSP NPs was synthesized with base compositions of $(XNiMnFeTi)_3O_4$ where X = Co, Cu, and/or Zn. Selected amounts of Co, Cu, Zn, Ni, Mn, Fe, and/or Ti-containing

precursors were dissolved in EtOH following molar ratios of respective oxide decomposition products as shown in Table 3.2. Precursors were adjusted based on metal content in the predicted metal oxide decomposition product, as shown in Table 3.2 below. Added EtOH dilutes the precursor solution to a 3 wt.% CY solution. The total EtOH solution amounts for CoNMFT, CuNMFT, and ZnNMFT were 2, 1.5, and 1.5 L, respectively. Triethanolamine (TEA) was added to each solution as a solubility aid (50 mL). Using the LF-FSP process, the precursor solution was aerosolized with O_2 gas, ignited using CH_4/O_2 torches, and collected downstream via electrostatic precipitator (ESP), as described elsewhere [50,51,53,57–60].

Table 3.2: HEO Precursors Molar Ratios and Quantities Dissolved in EtOH and triethanolamine.

HEO	CoP		CuB		ZnB		NiB		MnB		FeB		TiG	
	g	mol	g	mol	g	mol	g	mol	g	mol	g	mol	g	mol
CoNMFT	28.0	0.14	-	-	-	-	33.7	0.14	26.8	0.12	36.8	0.16	71.5	0.21
CuNMFT	-	-	21.7	0.11	-	-	23.6	0.11	18.7	0.09	25.7	0.10	50.0	0.15
ZnNMFT	-	-	-	-	17.6	0.11	25.0	0.11	20.0	0.09	25.6	0.11	43.2	0.13

A supernatant solution was formed using collected ESP powder and 4 wt.% Bicine via ultrasonication. The solution was decanted after 3 h to remove unwanted, undispersed material. The resulting solution was heated under N_2 at 80˚C to remove EtOH.

3.3.3 Materials Characterization

X-Ray Diffraction (XRD) was performed (SmartLab XRD, Rigaku, Japan) operating at 40kV and 45mA with a scan rate of 8º 2Θ min^{-1} and step size of 0.01 2Θ in Bragg-Brentano geometry. Lattice parameters were calculated using Rietveld refinement using target phase $ZnFe_2O_4$, PDF: 01-089-7412.

Three-dimensional unit cell visualization, Graphical Abstract, was performed using VESTA 3 [64].

Additional characterization techniques and conditions can be found detailed in Chapter 2.3.

3.3.4 Electrochemical Characterization and Sample Preparation

The HEO NPs were coated with a conductive carbon coating. Typically, 1 g of dispersed NP is mixed with 10 wt.% anhydrous glucose via mortar and pestle, then pressed into a pellet (10 ksi/ 30 s) and placed into an alumina crucible. Pellets are heated using a tube furnace to 500˚C/30 min/Ar with heating and cooling rates of 2˚C and 3˚C/min, respectively. The resulting, calcined pellet is then ground using a mortar and pestle for 5 min before electrochemical characterization. Slurries were prepared using the mass ratio of 75: 15: 10 for AAM: carbon: binder, respectively. Conductive carbon used was C65 (Timcal). A dual binder system was used in a mass ratio of 2:1 for carboxymethyl cellulose (CMC): styrene-butadiene rubber (SBR, 40 wt.% solids). Dry materials were mixed via mortar and pestle before ball-milling in deionized water, DIW for 24 h. After ball milling, additional DIW was added and further mixing was done via SpeedMixer (1250 rpm, 5 min). Finally, styrene-butadiene rubber (40% solids solution, SBR) was added and mixed again via SpeedMixer (1250 rpm, 5 min).

The finished slurry was cast on Cu foil (9 μm; MSE Supplies) with a wet gap of 200 μm, and dried in ambient conditions at 60˚C followed by vacuum drying overnight at 85˚C. For coin cell testing, 14 mm diameter anodes were punched out using a handheld punch. Each anode was pressed in Carver uniaxial press at 3 ksi/30 s/50 °C between two 50 μm mylar sheets. Li metal foil (750 μm, Sigma Aldrich) was scraped clean of oxide and punched to 16 mm diameter. Celgard 2400 separators, 25 μm, from MTI were used for all samples. MTI 2032 size coin cell components made from SS304 were used. Baseline electrolyte used was 60 μL 1.2M $LiPF_6$ in 2/4/4 blend by volume EC/DMC/EMC (Soulbrain MI). All coin cells were assembled in an Ar-filled glovebox (Labstar Pro, MBraun, Stratham, NH, United States).

All coin cell cycling was performed using BioLogic battery cyclers from 0.01 to 3 V at room temperature unless otherwise stated. Galvanostatic cycling with potential limitation (GCPL) was used to determine material capacity. Constant current, constant voltage (CCCV) charging was used with a C/20 CV cutoff step, where 1C = 500 mAh g^{-1}. All potentials are given vs. Li/Li^+ unless otherwise stated. Rates study included charging current densities of 50 (5 cycles), 100 (5 cycles), and 250 mA g^{-1} for remaining cycles. Discharge current densities included 5 cycles of 50, 100, 250, 500, 1000, 2500 mA g^{-1} and extended cycling at 250 mA g^{-1}.

3.4 Results and Discussion

In the following sections, we first characterize the HEO NPs via phase and compositional analysis using XRD and ICP-MS. Second, we assess material morphology via SEM/EDS, PSA, and BET followed by spectroscopy studies via FTIR and XPS.

Thereafter, we explore their electrochemical behavior via cyclic voltammetry (CV), and GCPL. In conclusion, a basic economic assessment of the materials in this study is presented and compared with previous works in literature as well as industry.

3.4.1 Material Characterization

3.4.1.1 Phase and Composition

Figure 3.3 XRD studies on the synthesized HEO NPs show a single phase, matching the target spinel phase $ZnFe_2O_4$ (PDF: 01-089-7412). The target phase was selected based on previously reported compositionally complex spinel oxides [12]. The retention of a single phase indicates that the selected TMs Co, Cu, and Zn are interchangeable without any major structural consequences. This points to the wide compositional landscape available to H/MEO materials. Calculated lattice

parameter and corresponding unit cell volume from Rietveld analysis are shown in Table 3.3 below.

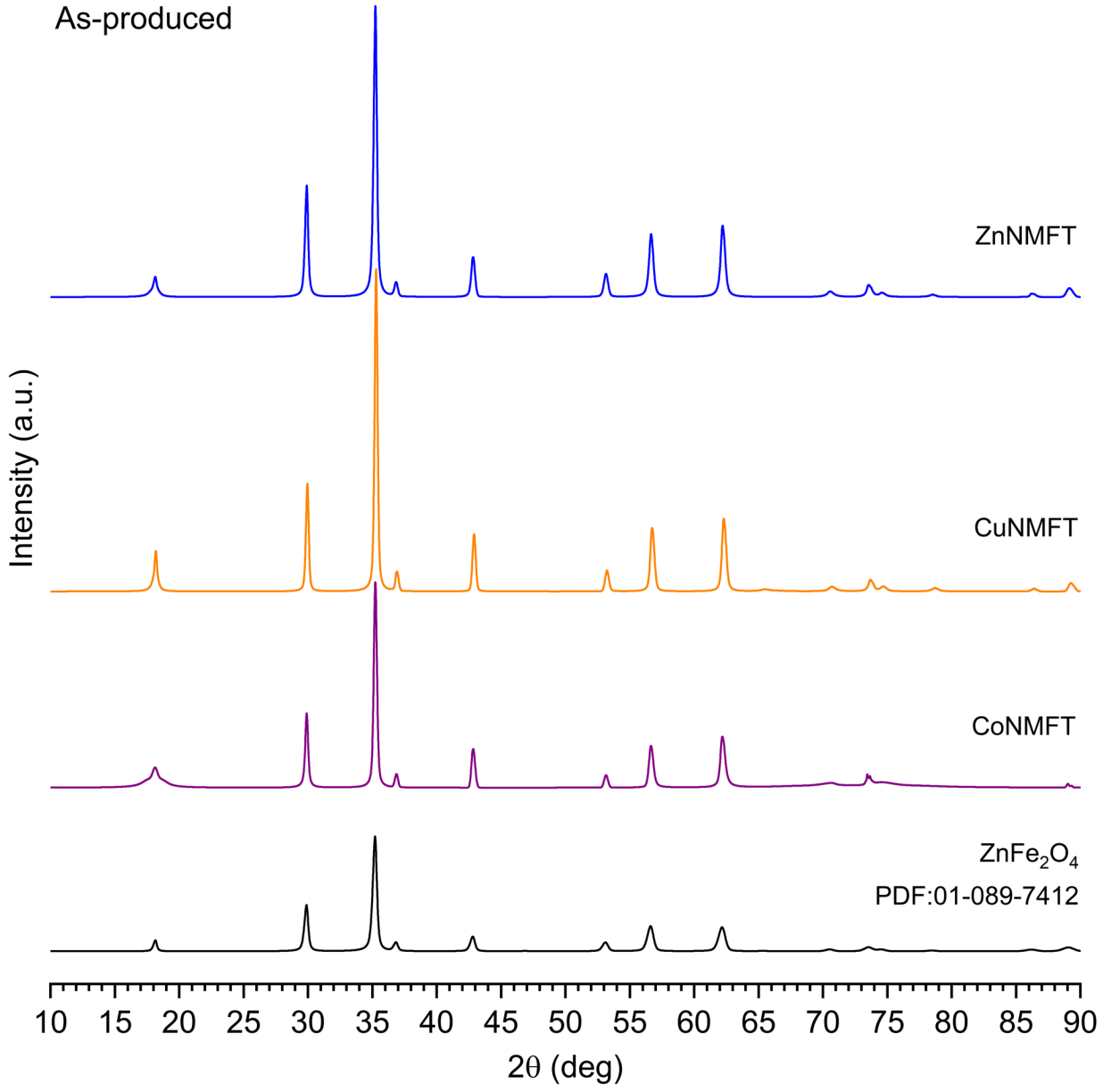

Figure 3.3: XRD studies of as-produced HEOs compared to target phase $ZnFe_2O_4$ (PDF:01-089-7412).

While the target phase was achieved, the chemical composition of each material is important to consider for electrochemical application. To this end, ICP-MS studies were performed on the

as-produced materials. Results showed good agreement between target and measured compositions.

Table 3.3: Summary of ICP-MS and XRD results for synthesized HEOs.

Sample	ICP-MS (rel. mol)							Rietveld Refinement		
	Co	Cu	Zn	Ni	Mn	Fe	Ti	α (Å)	α^3 (Å^{-3})	ρ (g cm^{-3})
CoNMFT	0.23	-	-	0.21	0.20	0.15	0.21	8.42579	598.2	5.11
CuNMFT	-	0.22	-	0.19	0.18	0.20	0.20	8.42477	598.0	5.14
ZnNMFT	-	-	0.24	0.19	0.18	0.20	0.20	8.43712	600.6	5.23

3.4.1.2 Morphology

Morphology is an important consideration for choosing AAMs for electrochemical application. Previous studies have demonstrated improved performance from nano-scale AAMs when compared to micron-scale AAMs, for both H/MEOs and other conversion-type materials [3,12,17].

SEM and EDS studies of the synthesized HEOs show similar morphologies and elemental distributions independent of composition. The observed homogeneity is in good agreement with the XRD studies such that there are no secondary phases observed.

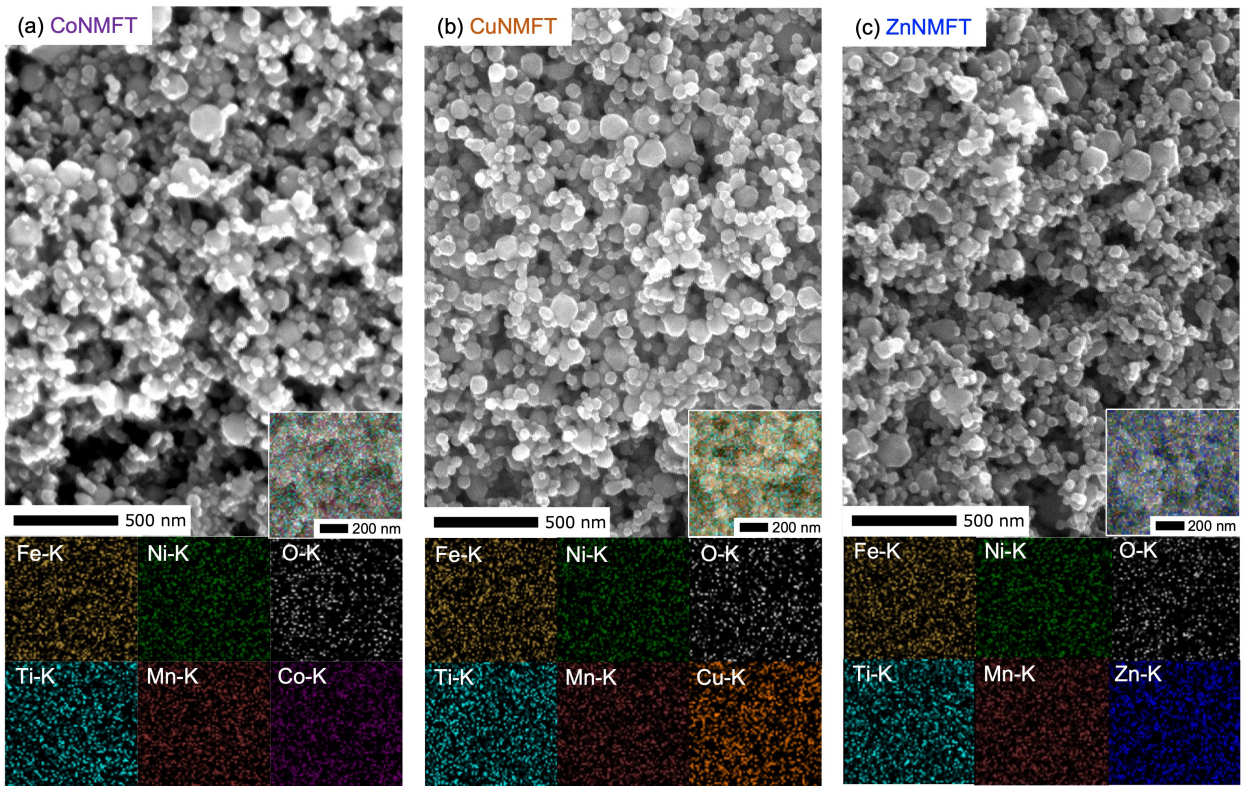

Figure 3.4: SEM and EDS mapping of (a) CoNMFT, (b) CuNMFT, and (c) ZnNMFT nanoparticles.

As produced HEO average particle sizes (APSs) and specific surface areas (SSAs) were analyzed via PSA and BET. APSs for the synthesized NP primary particles were between 65 and 90 nm via PSA. Additionally, BET SSAs were between 18 and 23 m^2 g^{-1}. D_{BET} was calculated from BET and crystallographic data using Equation 8.

$$D_{BET} = \frac{6000}{\rho_{theoretical} * SSA_{BET}} \tag{8}$$

Where D_{BET} is the particle diameter [nm], $\rho_{theoretical}$ is the theoretical density (g cm^{-3}) and SSA_{BET} is calculated SSA from BET (m^2 g^{-1}). Equation (2) is most accurate for spherical, non-agglomerated particles. The corresponding APSs increase but remain nanoscale. Table 3.4 and Figure 3.5 provide graphical results and a summary of PSA and BET results.

Table 3.4: Specific Surface Areas and calculated APS from BET and PSA.

HEO	SSA via BET (m^2 g^{-1})	APS via BET (nm)	Mean APS via PSA (nm)
CoNMFT	20.0 ± 0.4	55	79
CuNMFT	18.7 ± 0.3	60	89

ZnNMFT	23.0 ± 0.5	50	65

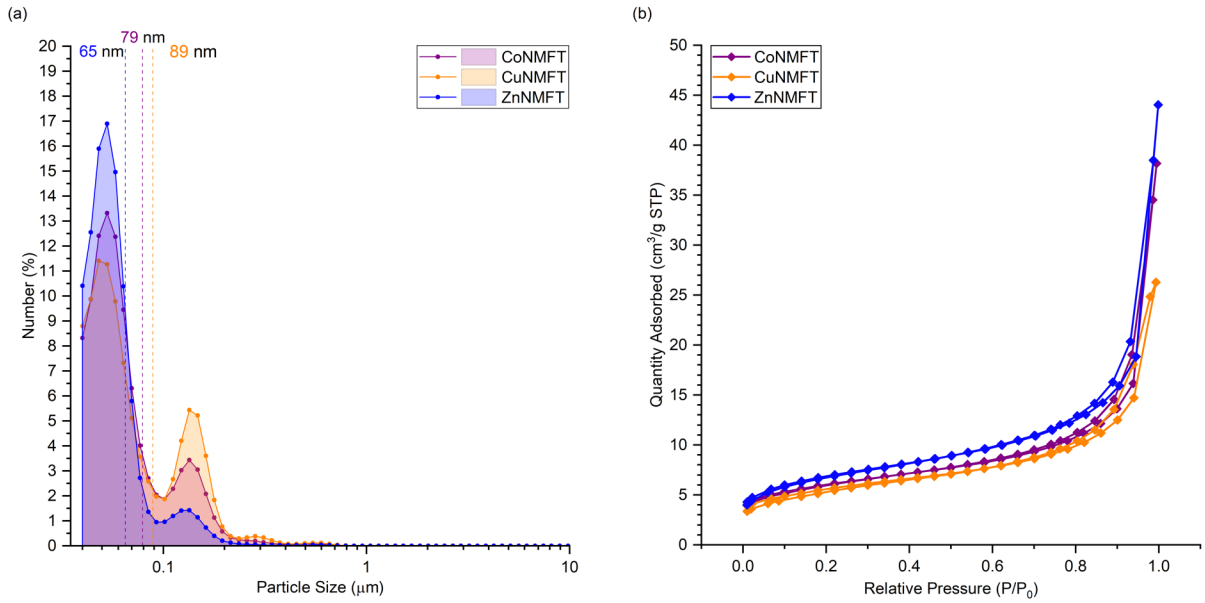

Figure 3.5: (a) PSA and (b) BET studies of as-produced HEO NPs.

3.4.1.3 Spectroscopy

While XRD can provide important structural information, additional understanding can be gained by decreasing the measurement length scale. With a target of a homogenous, single-phase material, characterization at different length scales should be in agreement [8]. To this end, both FTIR and XPS techniques were used to evaluate elemental distribution and bonding environments.

Typical FTIR metal-oxygen bond stretching (n) vibrations present below 1000 cm^{-1}. All synthesized HEOs show the same absorbance bands with small differences in relative amplitude and no evidence of organic bonds (Figure 3.12). Additionally, FTIR studies on a representative sample with added glucose before and after heating show the presence of glucose nO-H and nC-H between 3500 and 3200 cm^{-1} as well as nC-O 1200 to 800 cm^{-1} that disappear on heating to 500˚C/0.5 h/Ar (Figure 3.12). The amount of remaining C was confirmed via TGA-DTA to be ~3% after heating, see Figure 3.13.

The core-level XPS spectra of the corresponding elements are illustrated in Figure 3.6 for (CoNMFT), Figure 3.7 (CuNMFT), and Figure 3.8 (ZnNMFT). Summaries of Ni, Mn, Fe, and Ti binding energies and deconvoluted peak ratios can be found in Table 3.5, while an analogous summary for Co, Cu, Zn, and O can be found in Table 3.6. Typically, the average valency for a given element can be estimated by the ratio of different peak areas corresponding to unique valence states. The ratios of peak areas are listed for each element for each material in Table 3.5 and Table 3.6.

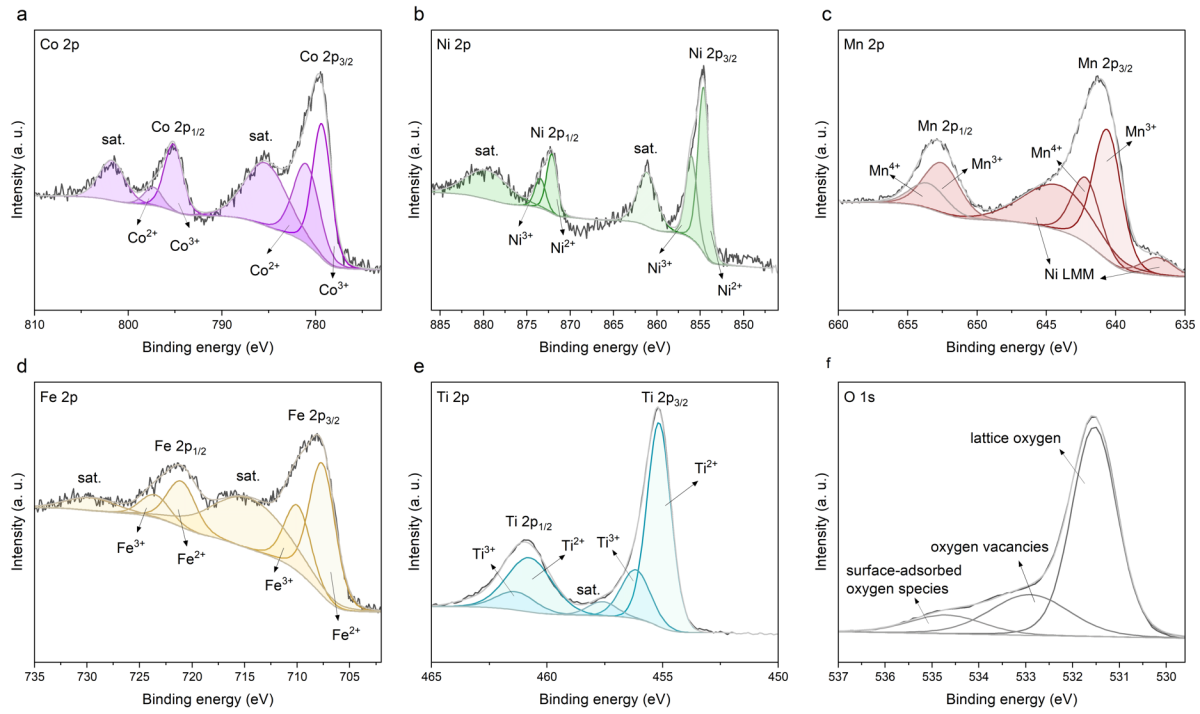

Figure 3.6: (a) Co 2p, (b) Ni 2p, (c) Mn 2p, (d) Fe 2p, (e) Ti 2p, and (f) O 1s XPS spectra for CoNMFT.

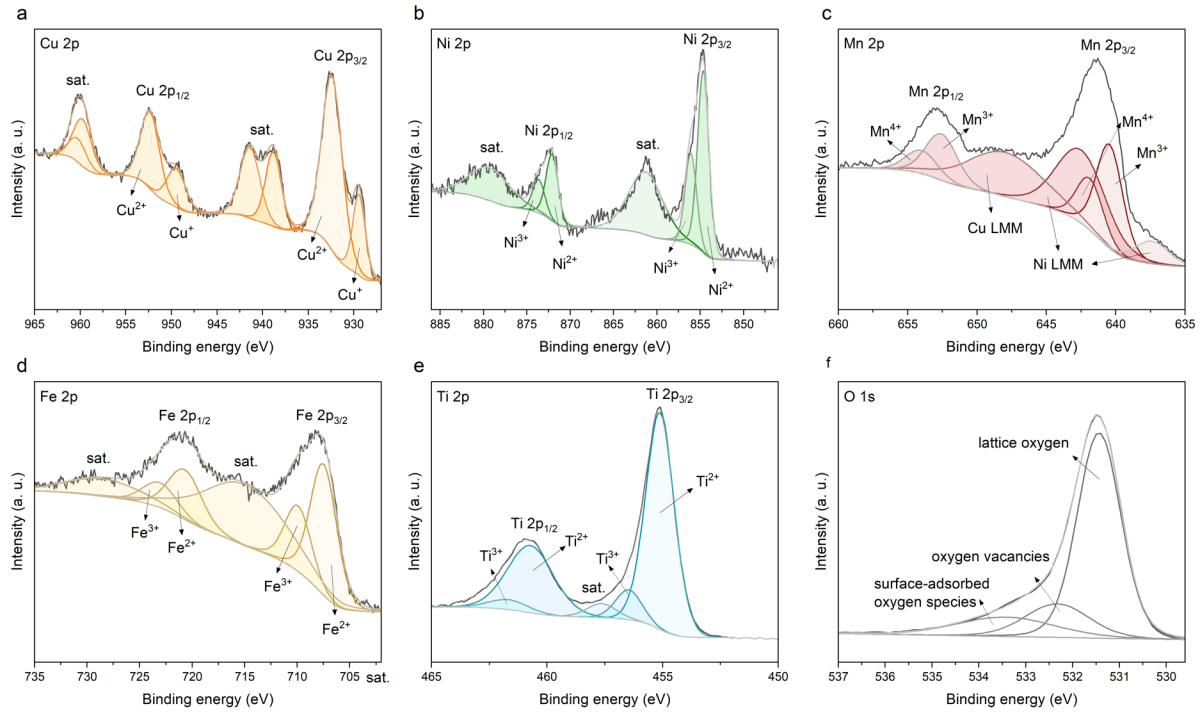

Figure 3.7: (a) Cu 2p, (b) Ni 2p, (c) Mn 2p, (d) Fe 2p, (e) Ti 2p, and (f) O 1s XPS spectra for CuNMFT.

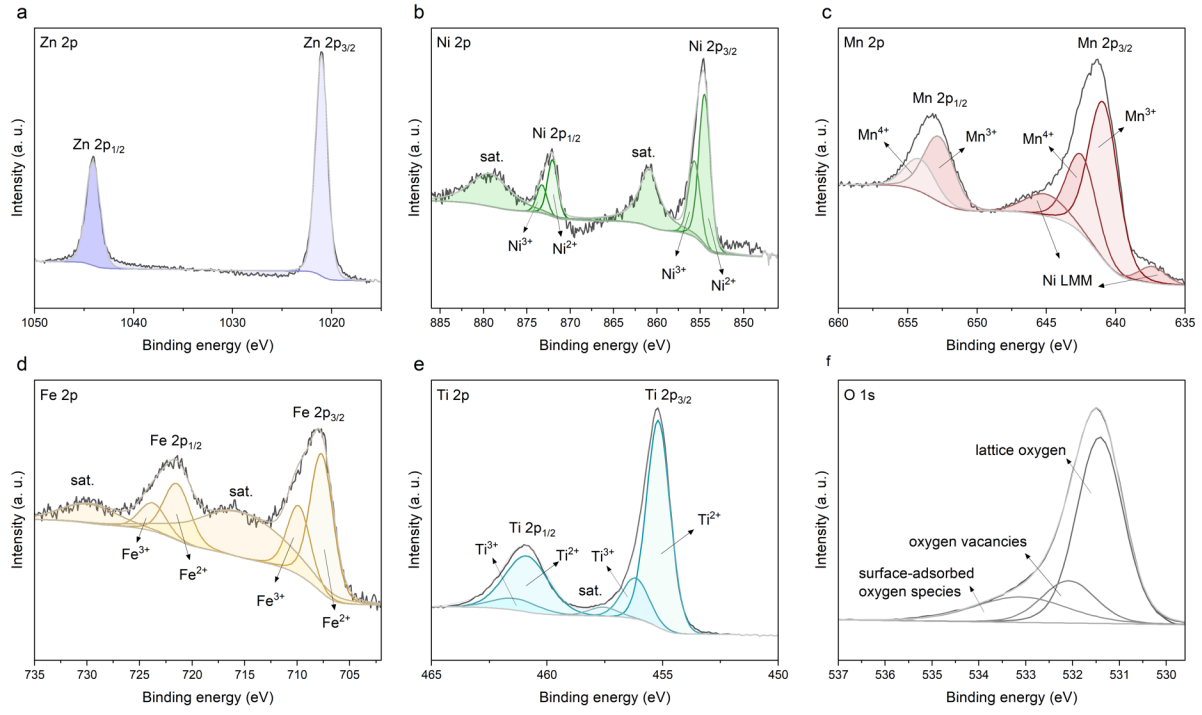

Figure 3.8: (a) Zn 2p, (b) Ni 2p, (c) Mn 2p, (d) Fe 2p, (e) Ti 2p, and (f) O 1s XPS spectra for ZnNMFT.

The Ni 2p XPS spectra show two spin–orbit peaks at 854.6 eV for Ni $2p_{3/2}$ and 872.2 eV for Ni $2p_{1/2}$. Deconvolution of Ni $2p_{3/2}$ demonstrates two peaks at ~854 eV and ~856 eV ascribed to Ni^{2+} and Ni^{3+}, respectively. Two high-binding-energy satellite peaks are observed at 861.1 eV (Ni $2p_{3/2}$) and 879.6 eV (Ni $2p_{1/2}$) [65,66]. The average Ni valence state was 2.2+, 2.3+, and 2.5+ for Co-, Cu-, and ZnNMFT, respectively.

The Mn $2p_{3/2}$ and Mn $2p_{1/2}$ peaks centered at 641.3 and 652.9 eV, where the Mn $2p_{3/2}$ is deconvoluted into Mn^{3+} at ~640 and Mn^{4+} at ~642 eV [67]. The peaks at 644.1 and 636.9 eV are overlapping areas with Ni Auger lines [68]. The impact of the Auger peaks from Cu is also observed in CuNMFT [69]. The average Mn valence state was 3.3+ for all samples.

In the Fe 2p spectra, the peak centered at 708.2 eV is assigned to Fe $2p_{3/2}$ and that at 728.1 eV is for Fe $2p_{1/2}$. Fe^{2+} and Fe^{3+} can be fitted at ~707 and ~709 eV, respectively. Two satellite peaks belonging to Fe $2p_{3/2}$ and Fe $2p_{1/2}$ are at 713.2 and 729.7 eV, respectively [66,70]. The average Fe valence state was 2.4+, 2.4+, and 2.3+ for Co-, Cu-, and ZnNMFT, respectively.

The Ti 2p spectra exhibit major spin-orbit lines Ti $2p_{3/2}$ at 455.2 eV and Ti $2p_{1/2}$ at 460.8 eV. Spectral fitting of the Ti $2p_{3/2}$ peaks indicates Ti^{2+} at ~455.1 eV, Ti^{3+} at ~456 eV, and a weak peak of Ti^{4+} at ~457.6 eV [71]. The average Ti valence state was 2.2+, 2.1+, and 2.2+ for Co-, Cu-, and ZnNMFT, respectively.

Table 3.5: XPS results for Ni, Mn, Fe, and Ti in synthesized HEO samples.

Sample		Ni		Mn		Fe		Ti	
		Ni^{2+}	Ni^{3+}	Mn^{3+}	Mn^{4+}	Fe^{2+}	Fe^{3+}	Ti^{2+}	Ti^{3+}
CoNMFT	eV	854.60	856.01	640.6	642.15	707.6	709.96	455.19	456.50
	Atom%	73.0	26.0	66.7	33.3	58	42	80.8	19.2
CuNMFT	eV	854.64	856.07	640.45	641.87	707.48	709.92	455.12	456.60
	Atom%	71.8	28.2	66.7	33.3	59.9	40.1	86.7	13.3
ZnNMFT	eV	854.49	855.67	640.89	642.47	707.67	709.86	455.19	456.30
	Atom%	49.9	50.1	66.7	33.3	67.1	32.9	84.9	15.1

The O 1s spectra deconvolution reveals three peaks at ~531, ~532, and ~533 eV ascribed to lattice oxygen (O_L, M−O in metal oxide), oxygen vacancies (Ov), and chemisorbed oxygen species O_C, respectively [23,41]. It has been reported that oxygen vacancy-rich HEO is beneficial for facilitating electron transport and enhancing electrochemical performance [41].

In CoNMFT, the Co 2p spectra shows two major peaks at 779.5 and 795.3 eV, attributable to Co $2p_{3/2}$ and Co $2p_{1/2}$, respectively [66]. Two satellite peaks are at 784.9 and 801.6 eV. Curve-fitting of the Co $2p_{3/2}$ peak suggests Co^{2+} (779.33 eV) and Co^{3+} (780.9 eV) with a concentration ratio of 54.5/45.5 resulting in an average of $Co^{2.5+}$.

Cu 2p spectra for CuNMFT exhibit Cu $2p_{3/2}$ and Cu $2p_{1/2}$ peaks located at ~930.9 and ~951.1 eV, respectively [72]. The Cu $2p_{3/2}$ peak splits into 930.98 eV for Cu^{2+} (77.7 %) and 928.03 eV for Cu^{+} (22.3 %), resulting in an average of $Cu^{1.8+}$. The presence of intense satellites in the Cu 2p spectra originates from the presence of Cu^{2+} species [73].

The Zn 2p spectra of ZnNMFT reveal binding energies for Zn $2p_{3/2}$ at 1021.03 eV (64.99 %) and Zn $2p_{1/2}$ centered at 1044.1 eV (35.01 %). The binding energy difference of 23.1 eV is consistent with reported separated Zn $2p_{3/2}$ and Zn $2p_{1/2}$ main levels in ZnO [74,75].

Table 3.6: XPS results for Co, Cu, Zn, and O in synthesized HEO samples.

Sample		Co		Cu		Zn		O		
		Co^{2+}	Co^{3+}	Cu^{1+}	Cu^{2+}	Zn^{2+}	Zn^{2+}	O_L	O_V	O_C
CoNMFT	eV	779.33	790.90	-	-	-	-	531.54	532.91	534.7
	Atom%	54.5	45.5	-	-	-	-	67.4	22.8	9.8
CuNMFT	eV	-	-	928.03	930.98	-	-	531.44	532.33	533.43
	Atom%	-	-	22.3	77.7	-	-	68.8	16.6	14.6
ZnNMFT	eV	-	-	-	-	1021.03	1044.10	531.42	532.08	533.11
	Atom%	-	-	-	-	65.0	35.0	65.1	17.1	17.8

3.4.2 Electrochemical Characterization

3.4.2.1 Cyclic Voltammetry

CV studies were performed on as-produced HEOs from 0.01 to 3.00 V using a scan rate of 0.1 mV s^{-1} (Figure 3.9). Typical in conversion type anodes, there is a significant cathodic peak near below 0.5 V during the first scan, corresponding to the reduction of Co, Cu, Zn, Ni, Mn, and/or Fe to their respective metal states along with solid electrolyte interphase and Li_2O formation [12,26]. These processes are largely irreversible, as seen by the discrepancy between the magnitude of the cathodic and anodic peaks from the first and second scan. Focusing on the seminal ESO (MgZnNiCuCo)O, previous studies showed that Zn and a portion of Co will participate reversibly in redox reactions [76]. Additionally, Cu-containing samples show smaller initial peaks < 0.5 V with an additional peak at 1.1 V during the first scan compared to the Co- and Zn-containing samples. There is good agreement between this work and previous studies on the reduction peak corresponding to Cu^{2+} and Cu^{1+} between 1.2 and 1.0 V [77]. Additionally, there is evidence of reversible Ti redox from Ti^{3+} to Ti^{4+} back to Ti^{3+} at 1.7 V and 0.9 V, respectively, which is typically seen in $LiTi_2O_4$ [12].

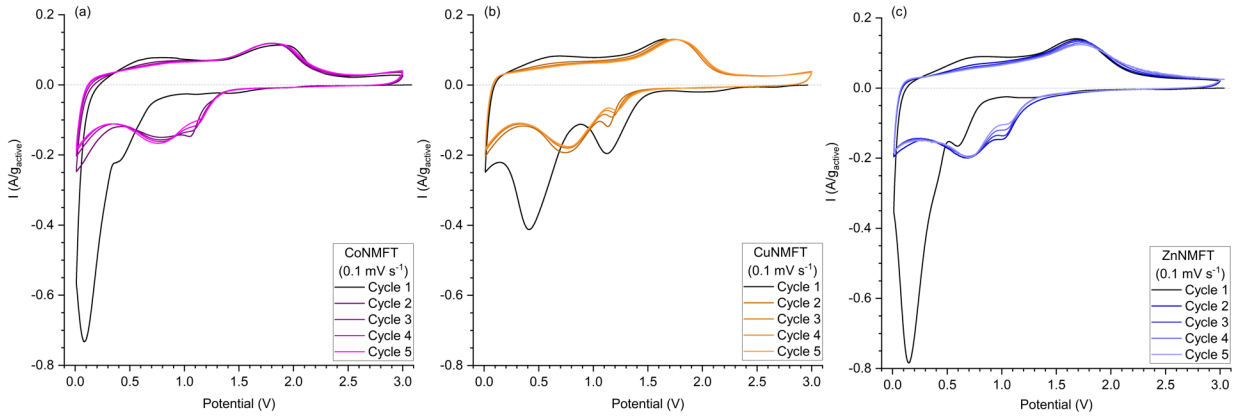

Figure 3.9: CV studies of (a) CoNMFT, (b) CuNMFT, and (c) ZnNMFT with scan rate of 0.1 mV s^{-1} from 0.01 to 3.00 V.

3.4.2.2 Galvanostatic Cycling with Potential Limitation (GCPL) – Rates Study

Synthesized HEOs were tested via GCPL with varying discharge rates between 0.01 and 3.00 V as described in Section 2.4. Half-cells were cycled with varying current densities for 30 cycles, as shown in Figure 3.10. As demonstrated during CV studies, CuNMFT show redox activity at a higher potential than either Zn- or CoNMFT during the initial cycle, resulting in a steeper potential capacity curve. ZnNMFT outperformed both Co- and Cu-containing HEOs with 480 mAh g^{-1} at 250 mA g^{-1} compared to 420 mAh g^{-1} (CoNMFT) and 390 mAh g^{-1} (CuNMFT). At 100, 250, 500, 1000, and 2500 mA g^{-1}, ZnNMFT showed discharge capacities of 555, 490, 440, 325, and 190 mAh g^{-1}.

All three materials show a small amount of capacity loss after five cycles at 2500 mA g^{-1}. After 2500 mA g^{-1}, ZnNMFT returned to 250 mA g^{-1} and after 3 cycles showed a discharge capacity of 470 mAh g^{-1}, which is 96% capacity retention after fast cycling. After fast cycling, CoNMFT and CuNMFT showed discharge capacities of 375 and 345 mAh g^{-1} respectively, which corresponds to 88% capacity retention for both materials, Figure 3.10. The increased capacity retention of ZnNMFT anodes after fast cycling is likely another consequence of the fully reversible de/alloying of Zn, as it can be expected that additional Co and Cu will irreversibly alloy beyond the first cycle, which would result in capacity loss. This observation is supported by CV curves, in which smaller current responses are seen in CoNMFT and CuNMFT anodes than in ZnNMFT anodes. This suggests that the amount of irreversibly alloyed metals may increase throughout early cycles, and these materials therefore present a lower capacity. Potential vs. capacity curves can be found in the insets of Figure 3.10 for the relevant cycles at 250 mA g^{-1}. While showing the lowest capacity, CuNMFT showed the best capacity retention after 30 cycles at 95%. CoNMFT and ZnNMFT showed 73 and 91% retention over the same period, respectively. It is worth noting that CoNMFT,

a composition previously synthesized in literature, showed lower capacity than ZnNMFT but a higher capacity than CuNMFT in initial cycling [9,11,37,38,73].

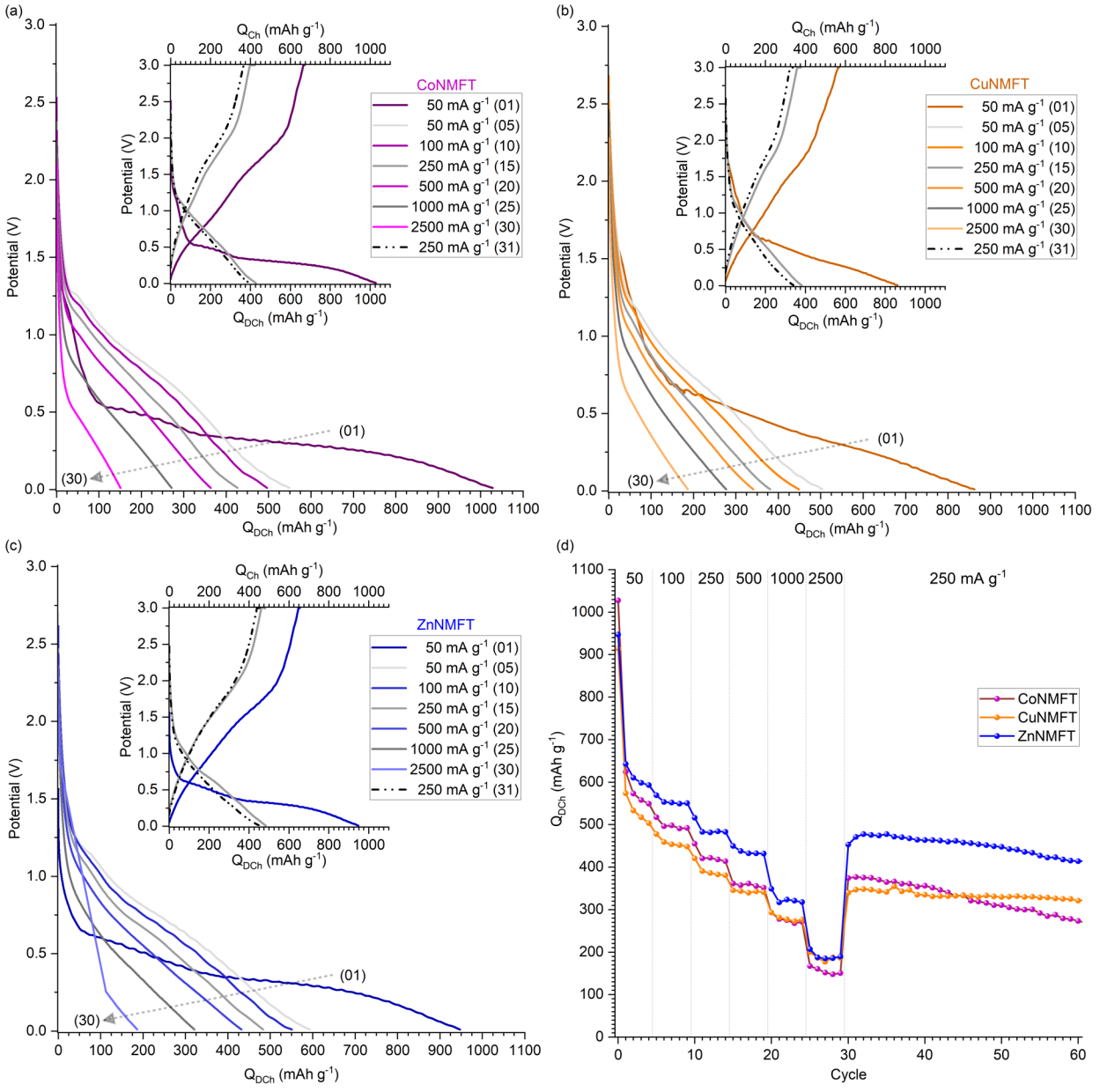

Figure 3.10: GCPL studies showing potential vs charge and discharge capacities curves for (a) CoNMFT, (b) CuNMFT, and (c) ZnNMFT. (d) Discharge capacities per cycle for all synthesized HEO materials during rates test.

Generally, Co-containing H/MEOs show good performance in literature. Zn has been shown to undergo fully reversible de/alloying reaction with Li – juxtaposed to Co which is reported to only partially participate in redox reactions [76]. The remaining non-particpating Co joins Cu in

the metal state after the initial conversion reaction [76]. In a previous study, Chen et al. [12] demonstrated the conversion of Ni, Co, Mn, and Fe with varying levels of reversibilty in the CoNMFT composition. In that study, Co showed nearly complete reduction but only oxidized to ~50% of the original valence state [12]. One could expect CoNMFT to show higher 1st discharge capacity from a conversion reaction compared to CuNMFT because Co is more likely in the trivalent state than Cu, and Co can participate in future redox reactions [12,76]. In this study, initial discharge reaction for CoNMFT is ~15% higher than CuNMFT (Figure 3.10).

An interesting effect of the different de/alloying behaviors of each metal is the impact of irreversible alloying on the electronic conductivity of anode materials. It can be expected that electron transfer will be a defining characteristic of anode performance during rapid cycling, therefore constituents that irreversibly alloy can be expected to provide additional conductivity which supports strong rate performance.

In CuNMFT anodes, where Cu is expected to fully alloy and remain metallic, anodes exhibit the strongest rate performance, overtaking CoNMFT at a discharge rate of 1000 mA g^{-1} and equaling ZnNMFT at 2500 mA g^{-1}. This behavior explains the initially low capacity, as Cu is unlikely to provide any reversible capacity, but instead provides an additional means of electron transport as well as a solid framework that supports rapid ΔV for redox-active constituents [76]. The rate performance of CoNMFT is consistent with this mechanism as well, where a fraction of Co irreversibly alloys, which explains why CoNMFT has superior rate performance to ZnNMFT, as Zn is not expected to remain metallic in any amount.

Further support for this interpretation can be seen in the first-cycle performance of each synthesized HEO sample. The difference between the first discharge and charge capacity can indicate redox reaction reversibility. An irreversible alloying reaction will provide capacity on first

discharge but will have little effect on the following charge. Conversely, a reversible reaction will also produce capacity during the ensuing charge. In ZnNMFT, there is 300 mAh g^{-1} difference between first dis/charge, as compared to 350 mAh g^{-1} in CuNMFT and CoNMFT. This follows results from previous studies of RS-1 anodes, which show a fully reversible de/alloying reaction of ZnO, a partially reversible reaction of CoO, and a fully irreversible reaction of Cu [76]. In terms of 1st cycle coulombic efficiency, ZnNMFT showed the most promising reversibility with 66.4%, while CoNMFT and CuNMFT showed similar results of 64.9 and 64.8%, respectively.

First cycle capacity is also in good agreement with XPS data, as the average oxidation state of Co is shown to be greater than that of Zn, which is greater than Cu. Upon first discharge, the same trend is observed in the corresponding HEO anodes, demonstrating that the first discharge is influenced by the alloying of Co, Cu, and Zn. Higher initial oxidation state should lead to higher discharge capacity as the components are reduced to near metallic states. This relationship can be observed in the present study as 1st cycle Q_{DCh} CoNMFT > ZnNMFT > CuNMFT.

One potential reason for the observed deviation in performance from literature is the difference in electrode mass loading. It is common practice to use low areal AAM loading for electrochemical studies, typically from 0.5 to 1.5 mg cm^{-2} [11,13,17,39,40]. The HEO electrodes in this study were 2.5-3.0 mg cm^{-2}. When cycled at 250 mA g^{-1}, the corresponding areal capacities for Zn-, Co-, and CuNMFT ranged from 1.35 to 1.05 mAh cm^{-2}. This range does not meet current industry requirements; however, it remains important to continue increasing areal loadings to meet industrial needs [78,79].

While areal loadings require continued improvement, H/MEOs can already compete with industrial materials in one critical area: volumetric capacity. Typically, in basic materials research focus is placed on gravimetric metrics such as gravimetric capacity; however, next generation

materials must reflect both mass and volume constraints in applications such as EVs. Gr has a theoretical density of 2.2 g cm^{-3}, while HEOs in this study have theoretical densities that range from 5.11 to 5.23 g cm^{-3}, see Table 3.3. Previous studies have demonstrated that H/MEO anode materials do not undergo severe volume changes on de/lithiation like other high capacity AAMs such as Si [3,12,28,30,32,40]. Given this low ΔV, we can estimate the volumetric capacity of synthesized HEOs using crystallographic densities. Gr has a theoretical volumetric capacity of 820 Ah L^{-1} compared to 2460 Ah L^{-1} for ZnNMFT.

3.4.2.3 Economic Analysis

To contextualize cycling results in terms of cost-effectiveness and material sourcing, an economic analysis of the precursor materials was conducted. Notably, this study neglects potential processing costs, which are expected to be relatively uniform across all HEOs, for the purpose of comparing solely between compositions. This analysis should not be treated as a definitive material cost, as it is solely a means of gauging the economic effects of compositional alterations. Further information about sourcing of prices can be found in Chapter 3.5.

As shown in Figure 3.11, economic analysis shows compelling evidence to discontinue the use of Co in HEO anodes. For the HEOs synthesized in this study, the price of Co metal is nearly twice that of any other metal. This figure is likely an underestimate of the true cost of Co usage, as it does not account for well-documented supply chain issues nor poor working conditions during the mining process. [80].

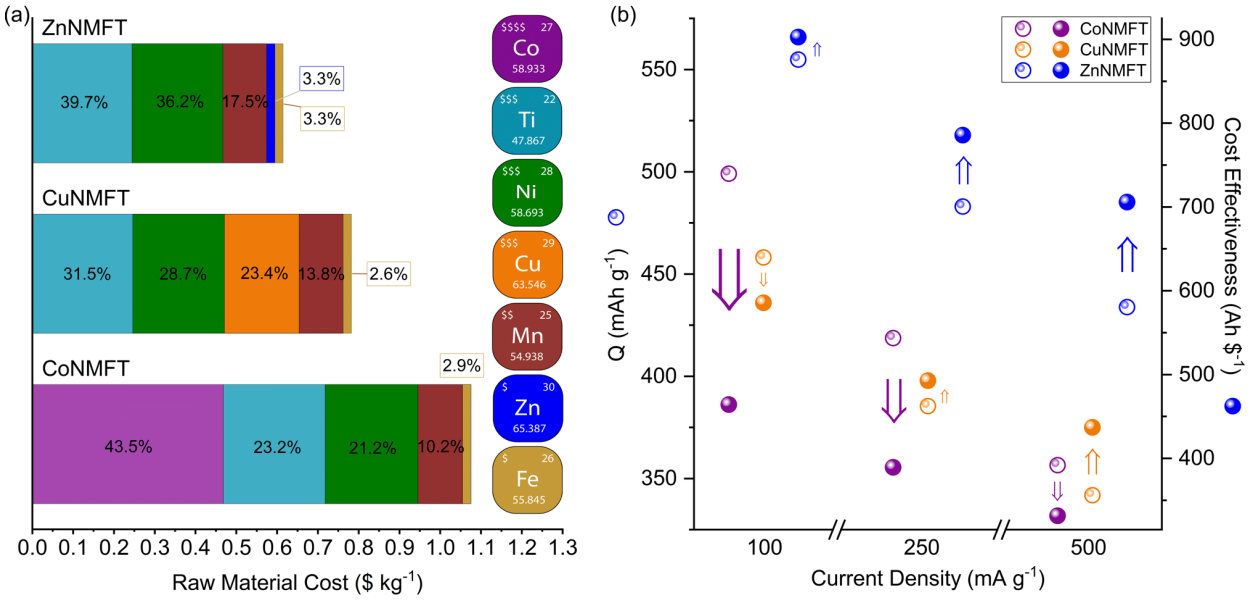

Figure 3.11: Contribution of constituent metals to HEO price (a) and cost effectiveness of synthesized HEO anodes (b). Points in (b) represent the average Q_{DCh} of each rate divided by material cost. Arrows in (b) indicate relative change in relative performance per cost vs performance.

This economic analysis pairs well with the electrochemical data, as ZnNMFT has the highest capacity of all studied compositions as well as the lowest cost, Figure 3.11. Given that Co has a cost 20x greater than that of Zn, the CoNMFT cost is 1.75x that of ZnNMFT. Paired with anode performance, ZnNMFT has more than double the cost effectiveness of CoNMFT at current densities of 250 and 500 mA g^{-1}, showing that the economic benefit of a Zn for Co substitution does not come at the expense of lesser electrochemical performance.

The effectiveness of Zn in HEO anodes represents an important step towards the practicality of industrializing this new family of anodes. By avoiding the use of Co, we can avoid many of the sourcing issues present in the development of high energy density cathodes [80]. Given the compositional flexibility offered by these HEO systems, the ZnNMFT system can be further altered to meet more specific goals, especially reducing cost by doping in Ni or Ti sites, which currently represent the most expensive precursor materials. Additionally, the LF-FSP synthesis

method is favorable for increasing synthesis scale, as a kinetic product can be obtained in a continuous process.

3.5 Conclusions

We report the synthesis and characterization of three HEO nanoparticle systems for use as next generation AAMs. Previous H/MEO studies rely on Co and/or Cr for high performance; however, for safety and cost issues this is not ideal for large scale application. To this end, two novel compositions were produced, replacing Co $(CoNiMnFeTi)_3O_4$ with Zn $(ZnNiMnFeTi)_3O_4$ and Cu $(CuNiMnFeTi)_3O_4$. The distinction between HEO and MEO is calculated based on entropy metric via the sublattice model due to the two cationic sublattices in the spinel structure. XRD and SEM/EDX results indicate a single phase ($Fd\bar{3}m$) was maintained with uniform elemental distribution for each synthesized HEO independent of composition. A decrease in performance was expected by replacing Co in favor of Zn/Cu; however, galvanostatic cycling results show improved performance for Zn-containing HEO vs. analogous Co- and Cu-containing HEOs. ZnNMFT showed gravimetric capacity improvement over industry standard Gr (470 mAh g_{HEO}^{-1} vs. 372 mAh g_{Gr}^{-1}), there is a larger gain in volumetric capacity (2460 mAh cm_{HEO}^{-3} vs. 820 mAh cm_{Gr}^{-3}) due to high density of spinel HEOs (>5 g cm^{-3}).

Cost also plays a significant role alongside performance for large scale application. The individual constituents within H/MEOs can come from a large compositional landscape, such that design choices can be made by prioritizing economic factors. To this end, a brief economic analysis was introduced showcasing the effect of exchanging high cost for lower cost materials on both the raw materials price, but also factoring in respective performance. ZnNMFT showed improvement over CoNMFT in capacity per cost by 2x. We believe that economic considerations should be at

the forefront of HEO design choices, in addition to classic considerations such as performance and longevity.

3.5.1 Acknowledgements

The authors acknowledge support from a DMR NSF Grant No. DMR-1926199 and a generous gift from Mercedes-Benz Research & Development North America (MBRDNA) for this work. The authors acknowledge the financial support of the University of Michigan College of Engineering and technical support from the Michigan Center for Materials Characterization.

Additionally, the authors appreciate the technical support from Van Vlack lab for materials characterization (Dr. Sahar Farjami, Dr. Ying Qi) and Michigan Elemental Analysis Lab (MEAL) for ICP-MS measurements (Dr. Angela Dial). The authors also wish to acknowledge and thank Dr. Eleni Temeche, Erik D. Flaspohler and Marie C. Taylor for their contributions.

3.6 Appendix

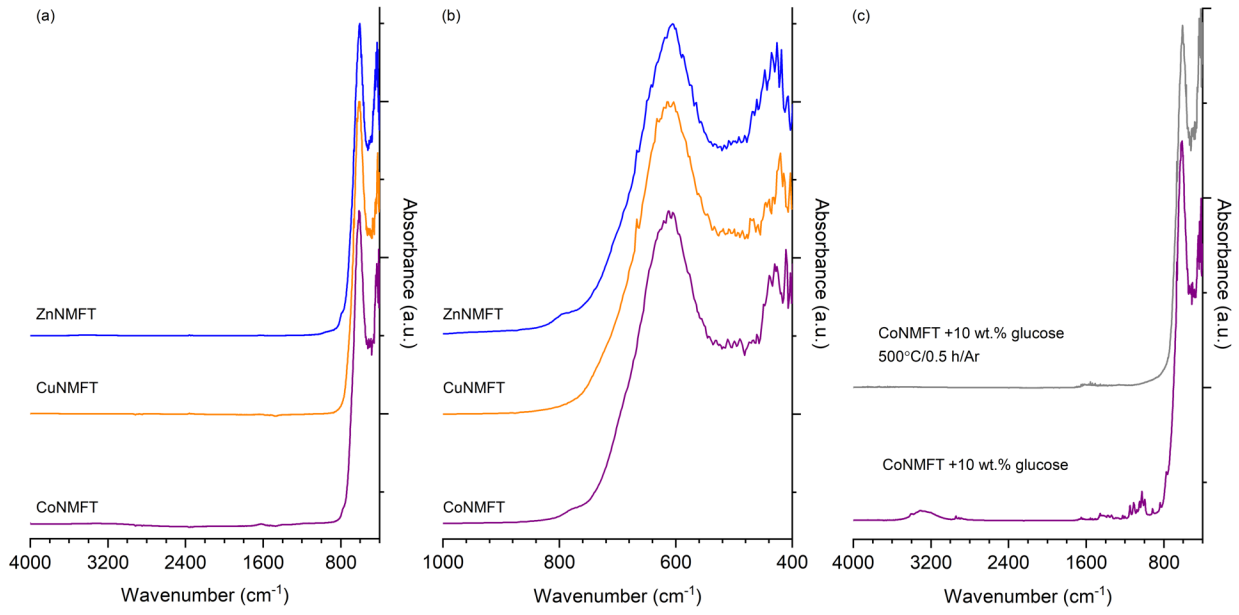

Figure 3.12: FTIR studies of (a,b) as-produced HEOs and (c) HEOs with carbon coating before and after heating.

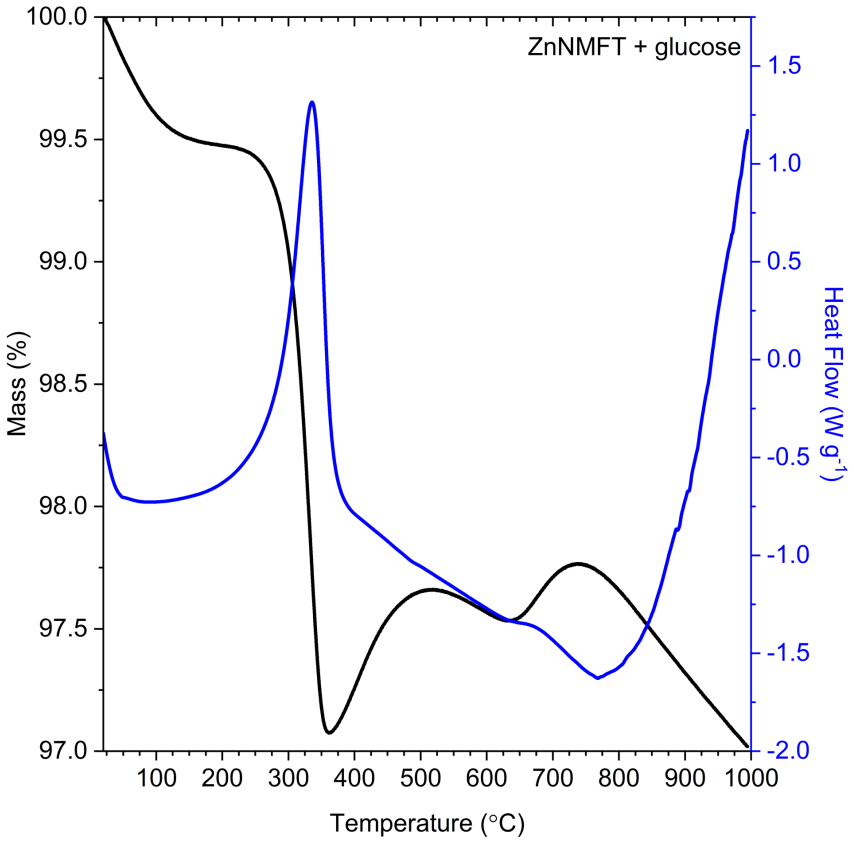

Figure 3.13: TGA-DTA of ZnNMFT sample with glucose heated in air with ramp rate of 5˚C min^{-1}.

Reported prices of Ni, Co, Cu, Zn, and Mn are for high-purity (> 99%) metals. Due to a lack of market data, Fe and Ti are instead given as high-purity Fe_2O_3 and anatase TiO_2, respectively. Both of these metals are present in all studied compositions, therefore this change is not expected to significantly alter the comparative analysis of xNMFT compositions. Prices sourced from the London Metal Exchange (LME) and Statistica represent a 12-month average from May 2022 to April 2023, and prices from the Shanghai Metals Market (SMM) represent the average price from April 2023, as 12-month averages were unavailable.

Table 3.7: Prices of publicly-traded mineral resources used for comparative cost analysis.

Metal	Ni	Co	Cu	Zn	Mn	Fe (Fe_2O_3)	Ti (TiO_2)
USD/kg	4.14	8.49	3.12	0.34	2.13	0.13	3.34
USD/mol	0.243	0.500	0.20	0.022	0.117	0.022	0.266
Source	[81]	[81]	[81]	[81]	[81]	[81]	[82]

References

[1] T.G. Brandt, A.R. Tuokkola, M. Yu, R.M. Laine, Liquid-feed flame spray pyrolysis enabled synthesis of Co- and Cr-free, high-entropy spinel oxides as Li-ion anodes, Chemical Engineering Journal 474 (2023) 145495. https://doi.org/10.1016/j.cej.2023.145495.

[2] J.B. Goodenough, Y. Kim, Challenges for rechargeable Li batteries, Chemistry of Materials 22 (2010) 587–603. https://doi.org/10.1021/cm901452z.

[3] X. Zhao, V.P. Lehto, Challenges and prospects of nanosized silicon anodes in lithium-ion batteries, Nanotechnology 32 (2021). https://doi.org/10.1088/1361-6528/abb850.

[4] R. Mo, X. Tan, F. Li, R. Tao, J. Xu, D. Kong, Z. Wang, B. Xu, X. Wang, C. Wang, J. Li, Y. Peng, Y. Lu, Tin-graphene tubes as anodes for lithium-ion batteries with high volumetric and gravimetric energy densities, Nat Commun 11 (2020) 1–11. https://doi.org/10.1038/s41467-020-14859-z.

[5] C.M. Rost, E. Sachet, T. Borman, A. Moballegh, E.C. Dickey, D. Hou, J.L. Jones, S. Curtarolo, J.P. Maria, Entropy-stabilized oxides, Nat Commun 6 (2015). https://doi.org/10.1038/ncomms9485.

[6] J.W. Gibbs, A Method of Geometrical Representation of the Thermodynamic Properties of Substances by Means of Surfaces, Transactions of the Connecticut Academy of Arts and Sciences (1873) 382–404.

[7] B.L. Musicó, D. Gilbert, T.Z. Ward, K. Page, E. George, J. Yan, D. Mandrus, V. Keppens, The emergent field of high entropy oxides: Design, prospects, challenges, and opportunities for tailoring material properties, APL Mater 8 (2020). https://doi.org/10.1063/5.0003149.

[8] O.F. Dippo, K.S. Vecchio, A universal configurational entropy metric for high-entropy materials, Scr Mater 201 (2021) 113974. https://doi.org/10.1016/j.scriptamat.2021.113974.

[9] M. Brahlek, M. Gazda, V. Keppens, A.R. Mazza, S.J. McCormack, A. Mielewczyk-Gryń, B. Musico, K. Page, C.M. Rost, S.B. Sinnott, C. Toher, T.Z. Ward, A. Yamamoto, What is in a name: Defining “high entropy” oxides, APL Mater 10 (2022). https://doi.org/10.1063/5.0122727.

[10] G.D. Price, S.L. Price, J.K. Burdett, The factors influencing cation site-preferences in spinels a new mendelyevian approach, Phys Chem Miner 8 (1982) 69–76. https://doi.org/10.1007/BF00309016.

[11] A. Sarkar, L. Velasco, D. Wang, Q. Wang, G. Talasila, L. de Biasi, C. Kübel, T. Brezesinski, S.S. Bhattacharya, H. Hahn, B. Breitung, High entropy oxides for reversible energy storage, Nat Commun 9 (2018). https://doi.org/10.1038/s41467-018-05774-5.

[12] T.Y. Chen, S.Y. Wang, C.H. Kuo, S.C. Huang, M.H. Lin, C.H. Li, H.Y.T. Chen, C.C. Wang, Y.F. Liao, C.C. Lin, Y.M. Chang, J.W. Yeh, S.J. Lin, T.Y. Chen, H.Y. Chen, In operando synchrotron X-ray studies of a novel spinel $(Ni_{0.2}Co_{0.2}Mn_{0.2}Fe_{0.2}Ti_{0.2})_3O_4$ high-entropy oxide for energy storage applications, J Mater Chem A Mater 8 (2020) 21756–21770. https://doi.org/10.1039/d0ta06455f.

[13] Q. Wang, A. Sarkar, Z. Li, Y. Lu, L. Velasco, S.S. Bhattacharya, T. Brezesinski, H. Hahn, B. Breitung, High entropy oxides as anode material for Li-ion battery applications: A practical approach, Electrochem Commun 100 (2019) 121–125. https://doi.org/10.1016/j.elecom.2019.02.001.

[14] M. Fracchia, M. Coduri, M. Manzoli, P. Ghigna, U.A. Tamburini, Is configurational entropy the main stabilizing term in rock-salt $Mg_{0.2}Co_{0.2}Ni_{0.2}Cu_{0.2}Zn_{0.2}O$ high entropy oxide?, Nat Commun 13 (2022) 1–4. https://doi.org/10.1038/s41467-022-30674-0.

[15] E. Lökçü, Ç. Toparli, M. Anik, Electrochemical Performance of $(MgCoNiZn)_{1-x}Li_xO$ High-Entropy Oxides in Lithium-Ion Batteries, ACS Appl Mater Interfaces 12 (2020) 23860–23866. https://doi.org/10.1021/acsami.0c03562.

[16] P. Ghigna, L. Airoldi, M. Fracchia, D. Callegari, U. Anselmi-Tamburini, P. D'angelo, N. Pianta, R. Ruffo, G. Cibin, D.O. De Souza, E. Quartarone, Lithiation Mechanism in High-Entropy Oxides as Anode Materials for Li-Ion Batteries: An Operando XAS Study, ACS Appl Mater Interfaces 12 (2020) 50344–50354. https://doi.org/10.1021/acsami.0c13161.

[17] N. Qiu, H. Chen, Z. Yang, S. Sun, Y. Wang, Y. Cui, A high entropy oxide $(Mg_{0.2}Co_{0.2}Ni_{0.2}Cu_{0.2}Zn_{0.2}O)$ with superior lithium storage performance, J Alloys Compd 777 (2019) 767–774. https://doi.org/10.1016/j.jallcom.2018.11.049.

[18] B. Xiao, G. Wu, T. Wang, Z. Wei, Z. Xie, Y. Sui, J. Qi, F. Wei, X. Zhang, L.B. Tang, J.C. Zheng, Enhanced Li-Ion Diffusion and Cycling Stability of Ni-Free High-Entropy Spinel Oxide Anodes with High-Concentration Oxygen Vacancies, ACS Appl Mater Interfaces 15 (2023) 2792–2803. https://doi.org/10.1021/acsami.2c12374.

[19] M. Wentker, M. Greenwood, M.C. Asaba, J. Leker, A raw material criticality and environmental impact assessment of state-of-the-art and post-lithium-ion cathode technologies, J Energy Storage 26 (2019) 101022. https://doi.org/10.1016/j.est.2019.101022.

[20] M. Wentker, M. Greenwood, J. Leker, A bottom-up approach to lithium-ion battery cost modeling with a focus on cathode active materials, Energies (Basel) 12 (2019) 1–18. https://doi.org/10.3390/en12030504.

[21] J. Zhao, X. Yang, Y. Huang, F. Du, Y. Zeng, Entropy Stabilization Effect and Oxygen Vacancies Enabling Spinel Oxide Highly Reversible Lithium-Ion Storage, ACS Appl Mater Interfaces 13 (2021) 58674–58681. https://doi.org/10.1021/acsami.1c18362.

[22] Z. Sun, Y. Zhao, C. Sun, Q. Ni, C. Wang, H. Jin, High entropy spinel-structure oxide for electrochemical application, Chemical Engineering Journal 431 (2022) 133448. https://doi.org/10.1016/j.cej.2021.133448.

[23] T.X. Nguyen, J. Patra, J.K. Chang, J.M. Ting, High entropy spinel oxide nanoparticles for superior lithiation-delithiation performance, J Mater Chem A Mater 8 (2020) 18963–18973. https://doi.org/10.1039/d0ta04844e.

[24] T.X. Nguyen, J. Patra, C.C. Tsai, W.Y. Xuan, H.Y.T. Chen, M.S. Dyer, O. Clemens, J. Li, S.B. Majumder, J.K. Chang, J.M. Ting, Secondary-Phase-Induced Charge–Discharge Performance Enhancement of Co-Free High Entropy Spinel Oxide Electrodes for Li-Ion Batteries, Adv Funct Mater (2023). https://doi.org/10.1002/adfm.202300509.

[25] B. Petrovičovà, W. Xu, M.G. Musolino, F. Pantò, S. Patanè, N. Pinna, S. Santangelo, C. Triolo, High-Entropy Spinel Oxides Produced via Sol-Gel and Electrospinning and Their Evaluation as Anodes in Li-Ion Batteries, Applied Sciences (Switzerland) 12 (2022). https://doi.org/10.3390/app12125965.

[26] X.F. Luo, J. Patra, W.T. Chuang, T.X. Nguyen, J.M. Ting, J. Li, C.W. Pao, J.K. Chang, Charge–Discharge Mechanism of High-Entropy Co-Free Spinel Oxide Toward Li+ Storage Examined Using Operando Quick-Scanning X-Ray Absorption Spectroscopy, Advanced Science 9 (2022) 1–12. https://doi.org/10.1002/advs.202201219.

[27] B. Xiao, G. Wu, T. Wang, Z. Wei, Y. Sui, B. Shen, J. Qi, F. Wei, J. Zheng, High-entropy oxides as advanced anode materials for long-life lithium-ion Batteries, Nano Energy 95 (2022) 106962. https://doi.org/10.1016/j.nanoen.2022.106962.

[28] D. Csík, D. Zalka, K. Saksl, D. Capková, R. Džunda, Four-component high entropy spinel oxide as anode material in lithium-ion batteries with excellent cyclability, J Phys Conf Ser 2382 (2022). https://doi.org/10.1088/1742-6596/2382/1/012003.

[29] J. Patra, T.X. Nguyen, C.C. Tsai, O. Clemens, J. Li, P. Pal, W.K. Chan, C.H. Lee, H.Y.T. Chen, J.M. Ting, J.K. Chang, Effects of Elemental Modulation on Phase Purity and Electrochemical Properties of Co-free High-Entropy Spinel Oxide Anodes for Lithium-Ion Batteries, Adv Funct Mater 32 (2022). https://doi.org/10.1002/adfm.202110992.

[30] M. Moździerz, K. Świerczek, J. Dąbrowa, M. Gajewska, A. Hanc, Z. Feng, J. Cieślak, M. Kądziołka-Gaweł, J. Płotek, M. Marzec, A. Kulka, High-Entropy $Sn_{0.8}(Co_{0.2}Mg_{0.2}Mn_{0.2}Ni_{0.2}Zn_{0.2})_{2.2}O_4$ Conversion-Alloying Anode Material for Li-Ion Cells: Altered Lithium Storage Mechanism, Activation of Mg, and Origins of the Improved Cycling Stability, ACS Appl Mater Interfaces 14 (2022) 42057–42070. https://doi.org/10.1021/acsami.2c11038.

[31] H. Minouei, N. Tsvetkov, M. Kheradmandfard, J. Han, D.E. Kim, S.I. Hong, Tuning the electrochemical performance of high-entropy oxide nanopowder for anode Li-ion storage via structural tailoring, J Power Sources 549 (2022) 232041. https://doi.org/10.1016/j.jpowsour.2022.232041.

[32] X. Yang, H. Wang, Y. Song, K. Liu, T. Huang, X. Wang, C. Zhang, J. Li, Low-Temperature Synthesis of a Porous High-Entropy Transition-Metal Oxide as an Anode for

High-Performance Lithium-Ion Batteries, ACS Appl Mater Interfaces 14 (2022) 26873–26881. https://doi.org/10.1021/acsami.2c07576.

[33] Y. Wang, H. Li, H. Liu, L. Yang, C. Zeng, Preparation and formation mechanism of Cr-free spinel-structured high entropy oxide $(MnFeCoNiCu)_3O_4$, Ceram Int 49 (2023) 1940–1946. https://doi.org/10.1016/j.ceramint.2022.09.159.

[34] B. Talluri, M.L. Aparna, N. Sreenivasulu, S.S. Bhattacharya, T. Thomas, High entropy spinel metal oxide $(CoCrFeMnNi)_3O_4$ nanoparticles as a high-performance supercapacitor electrode material, J Energy Storage 42 (2021) 103004. https://doi.org/10.1016/j.est.2021.103004.

[35] C. Liu, materials Electrochemical properties of four novel high-entropy spinel oxides used as lithium-ion battery anodes synthesized by the glycine-nitrate SCS method, J Mater Sci 58 (2023) 8005–8021. https://doi.org/10.1007/s10853-023-08498-0.

[36] K.H. Tian, C.Q. Duan, Q. Ma, X.L. Li, Z.Y. Wang, H.Y. Sun, S.H. Luo, D. Wang, Y.G. Liu, High-entropy chemistry stabilizing spinel oxide $(CoNiZnXMnLi)_3O_4$ (X = Fe, Cr) for high-performance anode of Li-ion batteries, Rare Metals 41 (2022) 1265–1275. https://doi.org/10.1007/s12598-021-01872-4.

[37] C.Q. Duan, K. Tian, X. Li, D. Wang, H. Sun, R. Zheng, Z. Wang, Y. Liu, New spinel high-entropy oxides $(FeCoNiCrMnXLi)_3O_4$ (X = Cu, Mg, Zn) as the anode material for lithium-ion batteries, Ceram Int 47 (2021) 32025–32032. https://doi.org/10.1016/j.ceramint.2021.08.091.

[38] H.Z. Xiang, H.X. Xie, Y.X. Chen, H. Zhang, A. Mao, C.H. Zheng, Porous spinel-type $(Al_{0.2}CoCrFeMnNi)_{0.58}O_{4-\delta}$ high-entropy oxide as a novel high-performance anode material for lithium-ion batteries, J Mater Sci 56 (2021) 8127–8142. https://doi.org/10.1007/s10853-021-05805-5.

[39] Y. Zheng, X. Wu, X. Lan, R. Hu, A Spinel $(FeNiCrMnMgAl)_3O_4$ High Entropy Oxide as a Cycling Stable Anode Material for Li-Ion Batteries, Processes 10 (2022). https://doi.org/10.3390/pr10010049.

[40] H. Chen, N. Qiu, B. Wu, Z. Yang, S. Sun, Y. Wang, A new spinel high-entropy oxide $(Mg_{0.2}Ti_{0.2}Zn_{0.2}Cu_{0.2}Fe_{0.2})_3O_4$ with fast reaction kinetics and excellent stability as an anode material for lithium ion batteries, RSC Adv 10 (2020) 9736–9744. https://doi.org/10.1039/d0ra00255k.

[41] D. Wang, S. Jiang, C. Duan, J. Mao, Y. Dong, K. Dong, Z. Wang, S. Luo, Y. Liu, X. Qi, Spinel-structured high entropy oxide $(FeCoNiCrMn)_3O_4$ as anode towards superior lithium storage performance, J Alloys Compd 844 (2020) 156158. https://doi.org/10.1016/j.jallcom.2020.156158.

[42] O.S. and H. Administration, 1910.1026 - Chromium (VI), 2019. https://www.osha.gov/laws-regs/regulations/standardnumber/1910/1910.1026.

[43] W. Li, S. Lee, A. Manthiram, High-Nickel NMA: A Cobalt-Free Alternative to NMC and NCA Cathodes for Lithium-Ion Batteries, Advanced Materials 32 (2020) 1–6. https://doi.org/10.1002/adma.202002718.

[44] Y. Kim, W.M. Seong, A. Manthiram, Cobalt-free, high-nickel layered oxide cathodes for lithium-ion batteries: Progress, challenges, and perspectives, Energy Storage Mater 34 (2021) 250–259. https://doi.org/10.1016/j.ensm.2020.09.020.

[45] S.Y. Wang, T.Y. Chen, C.H. Kuo, C.C. Lin, S.C. Huang, M.H. Lin, C.C. Wang, H.Y. Chen, Operando synchrotron transmission X-ray microscopy study on (Mg, Co, Ni, Cu, Zn)O high-entropy oxide anodes for lithium-ion batteries, Mater Chem Phys 274 (2021) 125105. https://doi.org/10.1016/j.matchemphys.2021.125105.

[46] D. Stenzel, B. Zhou, C. Okafor, M.V. Kante, L. Lin, G. Melinte, T. Bergfeldt, M. Botros, H. Hahn, B. Breitung, S. Schweidler, High-entropy spinel-structure oxides as oxygen evolution reaction electrocatalyst, Front Energy Res 10 (2022) 1–11. https://doi.org/10.3389/fenrg.2022.942314.

[47] A.H. Phakatkar, M.T. Saray, M.G. Rasul, L. V. Sorokina, T.G. Ritter, T. Shokuhfar, R. Shahbazian-Yassar, Ultrafast Synthesis of High Entropy Oxide Nanoparticles by Flame Spray Pyrolysis, Langmuir 37 (2021) 9059–9068. https://doi.org/10.1021/acs.langmuir.1c01105.

[48] A. Sarkar, R. Djenadic, N.J. Usharani, K.P. Sanghvi, V.S.K. Chakravadhanula, A.S. Gandhi, H. Hahn, S.S. Bhattacharya, Nanocrystalline multicomponent entropy stabilised transition metal oxides, J Eur Ceram Soc 37 (2017) 747–754. https://doi.org/10.1016/j.jeurceramsoc.2016.09.018.

[49] S. Kumar, J.A. Azurdia, R.M. Laine, Synthesis of $(MgO)_x(Fe_2O_3)_{1-x}$ nanoparticles via liquid feed flame spray pyrolysis. A non-stoichiometric spinel phase outside the normal phase diagram, Journal of Ceramic Processing Research 11 (2010) 517–522.

[50] E. Temeche, S. Indris, R.M. Laine, $LiAlO_2/LiAl_5O_8$ Membranes Derived from Flame-Synthesized Nanopowders as a Potential Electrolyte and Coating Material for All-Solid-State Batteries, ACS Appl Mater Interfaces 12 (2020) 46119–46131. https://doi.org/10.1021/acsami.0c13021.

[51] E. Yi, W. Wang, J. Kieffer, R.M. Laine, Flame made nanoparticles permit processing of dense, flexible, Li^+ conducting ceramic electrolyte thin films of cubic-$Li_7La_3Zr_2O_{12}$ (c-LLZO), J Mater Chem A Mater 4 (2016) 12947–12954. https://doi.org/10.1039/c6ta04492a.

[52] K. Saito, E. Yi, R.M. Laine, Y. Sugahara, Preparation of Nb-doped TiO_2 nanopowder by liquid-feed spray pyrolysis followed by ammonia annealing for tunable visible-light absorption and inhibition of photocatalytic activity, Ceram Int 46 (2020) 1314–1322. https://doi.org/10.1016/j.ceramint.2019.09.094.

[53] E. Yi, W. Wang, J. Kieffer, R.M. Laine, Key parameters governing the densification of cubic-$Li_7La_3Zr_2O_{12}$ Li^+ conductors, J Power Sources (2017). https://doi.org/10.1016/j.jpowsour.2017.03.126.

[54] M. Yu, T.G. Brandt, E. Temeche, R.M. Laine, Stabilizing High-Voltage Cathodes via Ball-Mill Coating with Flame-Made Nanopowder Electrolytes, ACS Appl Mater Interfaces 14 (2022) 49617–49632. https://doi.org/10.1021/acsami.2c09284.

[55] W. Wang, E. Yi, A.J. Fici, R.M. Laine, J. Kieffer, Lithium Ion Conducting Poly(ethylene oxide)-Based Solid Electrolytes Containing Active or Passive Ceramic Nanoparticles, Journal of Physical Chemistry C 121 (2017) 2563–2573. https://doi.org/10.1021/acs.jpcc.6b11136.

[56] S. Liu, C. Zhou, Y. Wang, W. Wang, Y. Pei, J. Kieffer, R.M. Laine, Ce-Substituted Nanograin $Na_3Zr_2Si_2PO_{12}$ Prepared by LF-FSP as Sodium-Ion Conductors, ACS Appl Mater Interfaces (2020). https://doi.org/10.1021/acsami.9b11995.

[57] E. Yi, W. Wang, S. Mohanty, J. Kieffer, R. Tamaki, R.M. Laine, Materials that can replace liquid electrolytes in Li batteries: Superionic conductivities in $Li_{1.7}Al_{0.3}Ti_{1.7}Si_{0.4}P_{2.6}O_{12}$. Processing combustion synthesized nanopowders to free standing thin films, J Power Sources 269 (2014) 577–588. https://doi.org/10.1016/j.jpowsour.2014.07.029.

[58] E. Temeche, E. Buch, X. Zhang, T. Brandt, A. Hintennach, R.M. Laine, Improved Electrochemical Properties of $Li_4Ti_5O_{12}$Nanopowders (NPs) via Addition of $LiAlO_2$and Li_6SiON Polymer Electrolytes, Derived from Agricultural Waste, ACS Appl Energy Mater 4 (2021) 1894–1905. https://doi.org/10.1021/acsaem.0c02994.

[59] E. Temeche, E. Yi, V. Keshishian, J. Kieffer, R.M. Laine, Liquid-feed flame spray pyrolysis derived nanopowders (NPs) as a route to electrically conducting calcium aluminate ($12Ca_{O.7}Al_2O_3$) films, J Eur Ceram Soc (2019). https://doi.org/10.1016/j.jeurceramsoc.2018.11.051.

[60] E. Yi, E. Temeche, R.M. Laine, Superionically conducting beta"-Al_2O_3 thin films processed using flame synthesized nanopowders, J Mater Chem A Mater 6 (2018) 12411–12419. https://doi.org/10.1039/c8ta02907e.

[61] K. Wegner, B. Schimmoeller, B. Thiebaut, C. Fernandez, T.N. Rao, Pilot plants for industrial nanoparticle production by flame spray pyrolysis, KONA Powder and Particle Journal 29 (2011) 251–265. https://doi.org/10.14356/kona.2011025.

[62] R. Strobel, S.E. Pratsinis, Flame aerosol synthesis of smart nanostructured materials, J Mater Chem 17 (2007) 4743–4756. https://doi.org/10.1039/b711652g.

[63] W.Y. Teoh, R. Amal, L. Mädler, Flame spray pyrolysis: An enabling technology for nanoparticles design and fabrication, Nanoscale 2 (2010) 1324–1347. https://doi.org/10.1039/c0nr00017e.

[64] K. Momma, F. Izumi, VESTA 3 for three-dimensional visualization of crystal, volumetric and morphology data, J Appl Crystallogr 44 (2011) 1272–1276.

[65] M.C. Biesinger, B.P. Payne, L.W.M. Lau, A. Gerson, R.S.C. Smart, X-ray photoelectron spectroscopic chemical state Quantification of mixed nickel metal, oxide and hydroxide systems, Surface and Interface Analysis 41 (2009) 324–332. https://doi.org/10.1002/sia.3026.

[66] M.C. Biesinger, B.P. Payne, A.P. Grosvenor, L.W.M. Lau, A.R. Gerson, R.S.C. Smart, Resolving surface chemical states in XPS analysis of first row transition metals, oxides and hydroxides: Cr, Mn, Fe, Co and Ni, Appl Surf Sci 257 (2011) 2717–2730. https://doi.org/10.1016/j.apsusc.2010.10.051.

[67] E.S. Ilton, J.E. Post, P.J. Heaney, F.T. Ling, S.N. Kerisit, XPS determination of Mn oxidation states in Mn (hydr)oxides, Appl Surf Sci 366 (2016) 475–485. https://doi.org/10.1016/j.apsusc.2015.12.159.
[68] M.C. Biesinger, L.W.M. Lau, A.R. Gerson, R.S.C. Smart, The role of the Auger parameter in XPS studies of nickel metal, halides and oxides, Physical Chemistry Chemical Physics 14 (2012) 2434–2442. https://doi.org/10.1039/c2cp22419d.
[69] L. Deng, F. Lin, Q. Yu, X. He, A. Liu, W. Shi, J. Feng, Improved ferromagnetic behavior and novel near-infrared photoluminescence in Mg/Mn-codoped CuCrO2 ceramics, J Mater Sci 51 (2016) 7491–7501. https://doi.org/10.1007/s10853-016-0028-z.
[70] A.P. Grosvenor, B.A. Kobe, M.C. Biesinger, N.S. McIntyre, Investigation of multiplet splitting of Fe 2p XPS spectra and bonding in iron compounds, Surface and Interface Analysis 36 (2004) 1564–1574. https://doi.org/10.1002/sia.1984.
[71] V. Natu, M. Benchakar, C. Canaff, A. Habrioux, S. Célérier, M.W. Barsoum, A critical analysis of the X-ray photoelectron spectra of Ti_3C_2Tz MXenes, Matter 4 (2021) 1224–1251. https://doi.org/10.1016/j.matt.2021.01.015.
[72] M.C. Biesinger, Advanced analysis of copper X-ray photoelectron spectra, Surface and Interface Analysis 49 (2017) 1325–1334. https://doi.org/10.1002/sia.6239.
[73] M.C. Biesinger, L.W.M. Lau, A.R. Gerson, R.S.C. Smart, Resolving surface chemical states in XPS analysis of first row transition metals, oxides and hydroxides: Sc, Ti, V, Cu and Zn, Appl Surf Sci 257 (2010) 887–898. https://doi.org/10.1016/j.apsusc.2010.07.086.
[74] E. Fazio, A.M. Mezzasalma, G. Mondio, T. Serafino, F. Barreca, F. Caridi, Optical and structural properties of pulsed laser ablation deposited ZnO thin film, Appl Surf Sci 257 (2011) 2298–2302. https://doi.org/10.1016/j.apsusc.2010.09.092.
[75] P. Sundara Venkatesh, S. Balakumar, K. Jeganathan, Post-annealing effects on the structural and optical properties of vertically aligned undoped ZnO nanorods grown by radio frequency magnetron sputtering, RSC Adv 4 (2014) 5030–5035. https://doi.org/10.1039/c3ra43639j.
[76] K. Wang, W. Hua, X. Huang, D. Stenzel, J. Wang, Z. Ding, Y. Cui, Q. Wang, H. Ehrenberg, B. Breitung, C. Kübel, X. Mu, Synergy of cations in high entropy oxide lithium ion battery anode, Nat Commun 14 (2023) 1–9. https://doi.org/10.1038/s41467-023-37034-6.
[77] C. Day, K. Greig, A. Massey, J. Peake, D. Crossley, R.A.W. Dryfe, Utilizing Cyclic Voltammetry to Understand the Energy Storage Mechanisms for Copper Oxide and its Graphene Oxide Hybrids as Lithium-Ion Battery Anodes, ChemSusChem 13 (2020) 1504–1516. https://doi.org/10.1002/cssc.201902784.
[78] V. Singh, S. Kuthe, N. V. Skorodumova, Electrode Fabrication Techniques for Li Ion Based Energy Storage System: A Review, Batteries 9 (2023). https://doi.org/10.3390/batteries9030184.

[79] Y. Kuang, C. Chen, D. Kirsch, L. Hu, Thick Electrode Batteries: Principles, Opportunities, and Challenges, Adv Energy Mater 9 (2019) 1–19. https://doi.org/10.1002/aenm.201901457.
[80] W.E. Gent, G.M. Busse, K.Z. House, The predicted persistence of cobalt in lithium-ion batteries, Nat Energy 2 (2022) 1132–1143. https://doi.org/10.1038/s41560-022-01129-z.
[81] London Metal Exchange (LME), (n.d.). https://www.lme.com.
[82] Shanghai Metals Market (SMM), (n.d.). https://www.metal.com.

Chapter 4 Nanocomposite Li- and Mn-rich Spinel Cathodes Characterized with a Green, Aqueous Binder System.

4.1 Summary

There is a growing need for alternatives to commercialized high-energy-density cathodes for Li-ion batteries with chemistries less dependent on Co and Ni and, in the past decade, particular attention has been placed on Li- and Mn- rich cathodes. Herein we report synthesis and characterization of Li- and Mn-rich cathode active materials (CAMs) with spinel-based nanocomposite structure having stoichiometries $Li_xMn_{1.5}Ni_{0.5}O_4$ (x=0.45-1.50) synthesized via liquid-feed flame spray pyrolysis. When cycled from 4.9 – 2.4 V, $Li_xMn_{1.5}Ni_{0.5}O_4$ (x=1.26, 1.50) exhibited energy densities greater than 1000 Wh kg_{CAM}^{-1} using a green, aqueous binder system. Increasing initial Li content results in larger 1st charge capacity, which can potentially serve as a Li donor to irreversible, Li-consuming solid electrolyte interphase formation in next generation anode active materials.

The study detailed in this chapter was primarily conducted by myself with specialized characterization performed by Dr. Kai Sun (HAADF-STEM), Dr. Sylvio Indris and Hang Li (^{7}Li NMR), and Andrew Tuokkola (PSA). The remaining authors – Prof. Richard M. Laine, Dr. Eleni Temeche, Dylan A. Edelman – contributed to this work via other mechanisms such as funding acquisition and manuscript revisions. This work is published in a journal article entitled "Nanocomposite Li- and Mn-rich Spinel Cathodes Characterized with a Green, Aqueous Binder System" in Chemical Engineering Journal, 2024, Vol 479C, page 147419 [1]. This text and figures in this chapter were adapted from that article by retained copyright of the author.

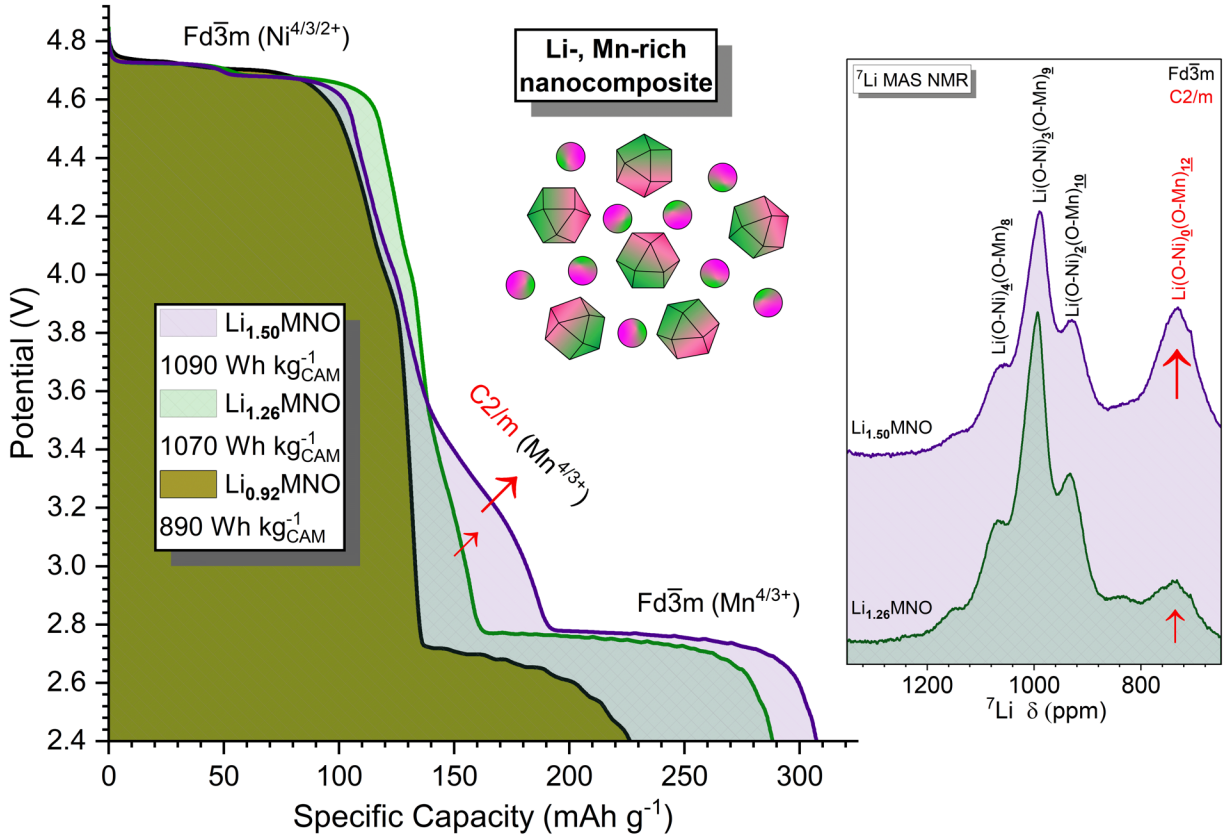

Figure 4.1: Graphical abstract showing potential vs. discharge capacity for Li_xMNO (x=0.92-1.50) and insert of ^7Li NMR results for $Li_{1.26}$ and $Li_{1.50}MNO$ showing the increase of Ni-free coordination sphere, indicating an increase in the monoclinic phase.

4.2 Introduction

Cathode active materials (CAMs) used in automotive Li-ion batteries have attracted extensive attention in global electrification due to high costs, typically the most expensive component in the cell, and unstable or insecure required supply chains [2–7]. These concerns are amplified by the growing need for commodity scale materials necessary to projected global vehicle electrification. Typically, battery electric vehicles (BEVs) target layered oxides with high energy density, greater

than 600 Wh kg_{CAM}^{-1}, such as lithium nickel manganese cobalt oxide (known as NMC xyz where x, y, and z are relative transition metal (TM) contents for $LiNi_xMn_yCo_zO_2$ compositions).

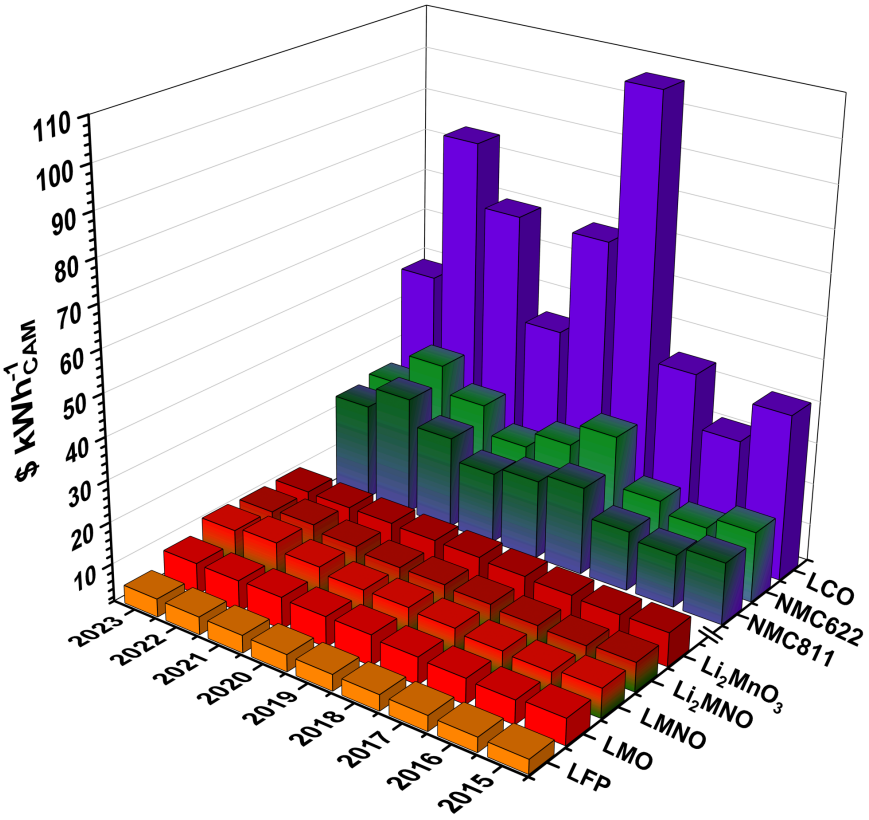

Figure 4.2: CAM pricing for Co-containing and Co-free cathodes over last nine years [3,8–10].

The practical cost of CAMs is a balance of raw material and processing costs ($ kg^{-1}) and energy storage (kWh kg^{-1}). Popular high-energy-density cathode materials for BEVs rely heavily on high Ni content, which subsequently results in projected supply chain strains, as illustrated in Figure 4.2. Alternately, polyanionic oxides like $LiFePO_4$ (LFP), or a combination of an NMC layered oxide with a spinel phase such as $LiMn_2O_4$ (s-LMO) can be used as a lower cost option with limited energy density (533 Wh $kg_{s\text{-}LMO}^{-1}$) [3,6]. Figure 4.2 illustrates past recent material costs for select CAMs, emphasizing the essential metals mentioned above and in Table 4.1 [3,8,9]. CAMs with high Ni and Co content typically experience increased price volatility compared to

Mn and Fe based chemistries. Despite the popularity of high Ni and Co containing cathode materials, projected supply chain and cost risks creates a need for alternate cathode chemistries outside of NMC.

The structural and electrochemical behavior of s-LMO and other Co-free cathode materials are presented in Table 4.1. s-LMO suffers from TM dissolution/migration (Mn^{2+}) but benefits from lower raw material costs due the absence of Ni and Co [3]. Select cell manufacturers use a blend of CAMs (NMC and s-LMO) to leverage the benefits and minimize the shortcomings of both materials, however; currently s-LMO is not the lone CAM in any production BEV [3,11]. Ni doping of s-LMO, $LiMn_{1.5}Ni_{0.5}O_4$, has been explored and is considered a viable production candidate due to increased redox potential (4.7 V vs. Li/ Li^+), and subsequent practical energy density (600 Wh kg_{CAM}^{-1} paired with Li metal anode) [12–16].

Table 4.1: Summary of select Co-free cathode materials [17,18].

Material	Abb.	C.S.	S.G.	Q_{theo} (Q_{exp}) [mAh g^{-1}]	UCV-LCV [V]	A.V. [V]	Energy [Wh kg^{-1}]	Ref.
$Li_1Mn_2O_4$	s-LMO	s	$Fd\bar{3}m$	147 (130)	4.9-3.5	4.1	533	[17]
$Li_1Mn_{1.5}Ni_{0.5}O_4$	s-LMNO	s	$P4_332$ $Fd\bar{3}m$	147 (130)	4.9-3.5	4.7	610	[12,17,19–21]
$Li_2Mn_{1.5}Ni_{0.5}O_4$	t-LMNO	t	$I4_1/amd$	195 (200)	4.9-2.4	4.0	800	[22,23]
Li_2MnO_3	m-LMO	m l	C2/m $R\bar{3}m$	458 (180)	5.0-2.0	3.8	684	[24]
Li_1FePO_4	LFP	o	P_{nma}	170 (160)	4.2-2.5	3.4	544	[17]

Several studies have assessed the structural and electrochemical effect of overlithiation on s-LMNO and similar Li accommodating structures [18,19,22,23,25]. A two-phase transition is known to occur when x>1 in Li_xMNO from spinel to tetragonal (t), such that empirically reported compositions of $Li_{1+x}MNO$ can instead be thought of as $(s\text{-}LMNO)_{1-0.5x}\cdot(t\text{-}LMNO)_{0.5x}$, henceforth abbreviated as st-LMNO [18,22,23,25,26]. This transition has been observed in samples prepared by both chemical and electrochemical lithiation [17,18,21,24,25]. It is important to note that most studies citing overlithiated LMNO composition report mixed phase st-LMNO [18,19,22,23,25].

st-LMNO shows similar redox activity to the base spinel within the typical s-LMNO cycling range (4.9 - 3.5 V vs Li/Li^+); however, distinct Mn redox activity is observed with LCVs below 3.5 V [18,19,22,23,25]. Typically, discharging s-LMNO below 3 V produces t-LMNO to accommodate the additional Li content past Li_1 [18]. Previous studies using st-LMNO cathodes in half-cell format demonstrated discharge capacities of 200-220 mAh g^{-1} when cycling between 4.9 and 2.4 V [18,19,22,23,25]. During charge, t-LMNO is delithiated first followed by s-LMNO. There is no significant redox contribution between the s-LMNO Ni redox and the t-LMNO Mn redox near 2.7 V, with the exception of a small Mn contribution near 4.0 V, resulting in a potential vs capacity curve with primarily horizontal and vertical features as opposed to sloping features [18]. The small Mn contribution near 4.0 V is a consequence of Mn^{3+} content, the result of oxygen vacancies, and can be used to quantify phase disorder [27–29].

Beyond s- and st-LMNO, Li_2MnO_3 (m-LMO) offers higher capacity and energy density than current BEV CAM materials. m-LMO benefits from theoretical two Li^+ extraction on charging (458 mAh g^{-1}). Experimentally the initial charge capacity is closer to 340 mAh g^{-1}; however, there is substantial irreversible capacity loss leading to a lower subsequent charge capacity (170 mAh g^{-1}) [30].The different redox behaviors in initial cycles have been studied extensively, and this irreversibility has been found to be a product of structural and electronic transformations, e. g. phase transformation from monoclinic to rock-salt and spinel structures [24,30,31]. The potential vs. capacity curves for the first cycle also differ in shape compared to subsequent cycles: initially shallow between 4.6 and 5.0 V vs. sloping between 3.0 and 5.0 V [23,29,30].

In addition to single phase CAMs, multiphase CAM composites such as m-LMO and s-LMNO [$xLi(Li_{1/3}Mn_{2/3})O_2 \cdot (1-x)LiMn_{1.5}Ni_{0.5}O_4$] have been explored [32]. Despite a high specific capacity (> 250 mAh g^{-1}), this phase suffers from commercialization barriers such as voltage decay along

with limited rate capability. Optimization of layered vs. spinel phase content can result in the m-LMO subphase stabilizing s-LMNO when cycled to an LCV of 2.4 V [31,32]. In the current work, the interplay of typically unstable m-LMNO acting to stabilize s-LMNO is explored.

A common failure mechanism for Mn-based cathode materials is Mn^{2+} dissolution into the electrolyte, an effect which is amplified by increased specific surface area (SSA). Newly formed Mn^{2+} dissolves easily in the electrolyte, effectively accelerating cell aging and reducing practical capacity [6,25,33–36]. Despite the disadvantages, increased SSAs in CAMs do offer benefits that require consideration [37]. Studies have found that the mechanism for strain release during (de)lithiation was influenced by the state of (de)lithiation and particle size [37–40]. s-LMNO particles with average particle sizes (APSs) < 1 μm were found to resist fracture during delithiation [39]. The higher specific surface area of nanoparticles can also be beneficial for improving kinetics of Li^+ (de)intercalation by decreasing the mean diffusion distance for Li^+ in the bulk. These effects should theoretically lead to higher capacity at higher C-rates and subsequently higher power [17,39,41,42].

s-LMNO has been synthesized by methods common to CAMs such as sol-gel, hydrothermal, spray pyrolysis, solution combustion, and co-precipitation synthesis methods [20,22,43–45]. The Laine group has used liquid feed flame spray pyrolysis (LF-FSP) to synthesize NPs realizing phase pure, unaggregated SE and anode nanoparticles [34,46–57]. LF-FSP has not been extensively explored as a synthesis method for CAMs with few examples in literature; however, other aerosol technologies such as FSP have been used to synthesize LFP, NMC, s-LMO, and $LiCoO_2$ [5,53,58–63]. Compared to FSP, LF-FSP offers the benefit of synthesis without HCl byproduct. Detailed LF-FSP procedures have been previously reported, while a basic schematic shown in Scheme 4.3 [34,46–52,54–56]. LF-FSP syntheses, at laboratory scales, can range from 10 to 300 g h^{-1}, while

commercial scale can synthesize nanopowder product on the order of kg h^{-1} in a continuous process [64–66]. LF-FSP offers the benefits of controlled morphology, phase purity, high yield, and relatively low cost while possible disadvantages include varying levels of crystallinity requiring additional powder calcination [46,55]. Due to the nature of high temperature synthesis followed by rapid quenching, LF-FSP can often access metastable, kinetically-driven phases not produced by standard calcination reactions [46–48,56].

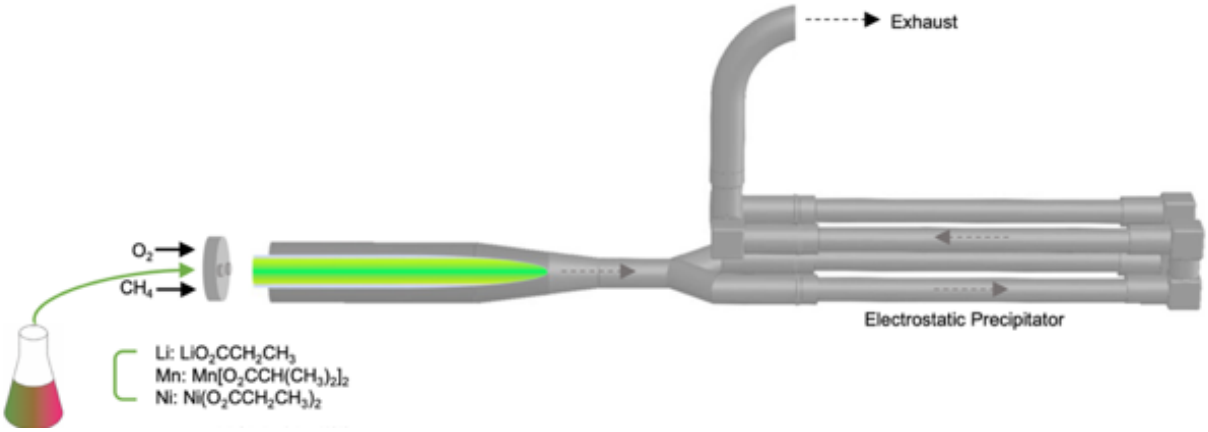

Scheme 4.3. Schematic of LF-FSP apparatus for s-LMNO synthesis.

In this work, we synthesized Li-, Mn-rich CAMs using LF-FSP with stoichiometries Li_xMNO with x = 0.45-1.50. As revealed via XRD, HAADF S/TEM, FTIR, and ^7Li NMR, initially amorphous and crystalline spinel phases transform to nanocomposites composed of spinel and monoclinic/layered phases post calcination (800ºC/6h/O_2). With increasing Li content, monoclinic phase content increases at the expense of the base spinel phase. Synthesized NPs showed a mixture of agglomerated, not aggregated spherical and faceted particle morphology with APSs 60-100 nm. After calcination (800ºC/6h/O_2) followed by ball milling, APSs for the processed NPs remained between 60-100 nm. In electrochemical testing, energy densities greater than 1000 Wh kg_{CAM}^{-1} (~300 mAh g^{-1}) were observed using a green, aqueous binder for $Li_{1.26}MNO$ and $Li_{1.50}MNO$ cycled

between 4.9 – 2.4 V. In addition, $Li_{0.92}MNO$ cycled in the typical window of 4.9 – 3.5 V resulted in 112 mAh g^{-1} after 50 cycles at 0.2C.

4.3 Materials and Methods

4.3.1 Precursor Synthesis

4.3.1.1 Lithium Propionate

Lithium hydroxide [($LiOH•H_2O$), 64 g, 1.5 mol] was reacted with propionic acid [CH_3CH_2COOH, 250 mL, 3.3 mol] at a molar ratio of 1:2.2 in a 500 mL three neck round bottom flask using a distillation setup under N_2 flow. The solution was stirred using a magnetic stir bar and heated to 130ºC under N_2 flow until a transparent liquid was obtained. Upon cooling $LiO_2CCH_2CH_3$ product was crystallized and vacuum dried at 100ºC to remove excess solvent. Experimental ceramic yield (CY_{exp}) of the precursor was 44.1%, compared to 46.2% theoretical CY (CY_{theo}). This discrepancy is attributed to a slight excess, unreacted propionic acid. Yield of the lithium propionate precursor reaction was 41%, while purity was determined to be 95%.

4.3.1.2 Manganese Isobutyrate

Manganese acetate tetrahydrate {[$Mn(OAc)_2•4H_2O$], 269.8 g, 1.1 mol} was reacted with isobutyric acid [$(CH_3)_2CHCOOH$, 300.0 mL, 3.3 mol] at a molar ratio of 1:3, in a 500 mL three neck round bottom flask using a distillation setup. The solution was stirred using a magnetic stir bar and heated to 135ºC under N_2 flow until a transparent liquid was obtained. Upon cooling the solution crystalized and the solid was removed from the flask. Excess isobutyric acid was removed via vacuum drying at 100ºC. CY_{exp} (34.7%) was higher than CY_{theo} (34.4%) and this difference is attributed to a combination of Mn^{3+} and Mn^{4+} decomposition products. Based on the mixed

decomposition products, yield of manganese isobutyrate was 45%, while purity was determined to be 98%.

4.3.2 Li_xMNO Synthesis

The series of NPs was synthesized via LF-FSP with base compositions of Li_xMNO with x ranging from 0.45-1.50. Select amounts of synthesized $LiO_2CCH_2CH_3$, $Mn[O_2CCH(CH_3)_2]_2$, and $Ni(O_2CCH_2CH_3)_2$ were dissolved in EtOH using molar ratio of respective oxide decomposition products. Precursors were adjusted based on metal content in the predicted metal oxide decomposition product, see Table 4.4. Excess Li-containing precursor was used as required in past syntheses of Li-containing materials using LF-FSP [47,48,50,51,53,54]. Dilution of the precursor solution to 3 wt.% CY was obtained by adjusting EtOH content. During LF-FSP synthesis, the precursor solution was aerosolized with O_2 gas, ignited using CH_4/O_2 torches, and collected downstream via electrostatic precipitator, as described elsewhere [47,48,50,53–56].

A supernatant solution was formed using collected ESP powder in EtOH and 3 wt.% PAA via ultrasonication. The solution was decanted after 3 h to remove unwanted, non-dispersed material. Dispersed NP was pressed into a pellet (10 ksi, 30 s) and placed into an alumina crucible. Pellets were heated using a tube furnace with conditions 800ºC/6 h/O_2 with heating and cooling rates of 5ºC min^{-1} and 3ºC min^{-1}, respectively. The resulting, calcined pellet was ground using a mortar and pestle for 5 min before further characterization.

4.3.3 Material Characterization

X-Ray Diffraction (XRD) was performed (SmartLab XRD, Rigaku, Japan) operating at 40kV and 45mA with a scan rate of 8º 2Θ min^{-1} and step size of 0.01 2Θ in Bragg-Brentano geometry.

Lattice parameters were calculated using Rietveld refinement using target phase $Li_1Mn_{1.5}Ni_{0.5}O_4$, PDF: 01-080-5507.

Thermogravimetric analysis (TGA) was run under air flow (60 mL min^{-1}) at ramp rate of 5ºC min^{-1} (SDT Q600, TA Instruments, Newcastle, DE, United States).

^{7}Li magic-angle spinning (MAS) nuclear magnetic resonance (NMR) spectroscopy was performed with a Bruker Avance neo 200 MHz spectrometer at a magnetic field of 4.7 T, corresponding to a resonance frequency of 77.8 MHz. Spinning was performed in 1.3 mm rotors at 55 kHz. Spectra were acquired with rotor-synchronized Hahn-echo pulse sequence using a π/2 pulse duration of 0.85 μs and a recycle delay of 60 s. Spectral intensities were normalized with respect to the sample mass and the number of scans. High resolution high-angle annular dark-field (HAADF) scanning transmission electron microscopy (S/TEM) studies were performed using Thermo Fisher Spectra 300 Probe-Corrected S/TEM.

Additional characterization techniques and conditions can be found detailed in Chapter 2.3.

4.3.4 Electrochemical Characterization

In typical slurry preparation, conductive carbon source was Super C65 (SSA ~65 m^2 g^{-1}) and binder was sodium carboxymethyl cellulose (CMC). Typical electrode composition for electrochemical testing was CAM/C65/CMC in mass ratio of 82.5/10/7.5, respectively. Slurry preparation began with mixing of CAM, Super C65, and CMC via mortar and pestle for ~2 min or until appearance was homogenous. DI water was added to a 20 mL glass vial, then dry material was added along with 3.0 g of 3 mm Æ YSZ beads. The mixture was ball milled for 2 d using a low intensity tumbler (20 rpm), and then briefly mixed using a Speedmixer twice for 150 s @ 1250 rpm (DAC 150.1 FVZ-K 230V, Hauschild Speedmixer, Inc, USA). The slurry was then transferred to carbon-coated aluminum foil (MTI, 18 μm Al, 1 μm C) and cast using a doctor blade with a

typical wet gap of 200 μm without agglomerates. The foil was dried at 50ºC until solvent was visibly removed, and then vacuum dried overnight at 90ºC. Additional samples were prepared using polyvinylidene difluoride (PVDF) (Solvay Solef 5130) in n-methyl-2-pyrrolidone (NMP, anhydrous) binder system following a similar procedure outlined previously. Baseline electrolyte used was 60 μL 1.2M $LiPF_6$ in EC/DMC/EMC, 2/4/4 blend by volume, with the addition of 0.02M lithium bis(oxalate)borate (LiBOB) (Soulbrain MI). All coin cells were assembled in a glovebox (Labstar Pro, MBraun, Stratham, NH, United States). For electrochemical testing, 12 mm diameter cathodes were punched out using a handheld punch. Typical areal loading was between 2.5 – 3.0 mg_{CAM} cm^{-2}, which corresponds to areal capacity of between 0.3 – 0.4 and 0.5 – 0.6 mAh cm^{-2} for LCVs of 3.5 and 2.4 V, respectively. Each cathode was pressed using a Carver uniaxial press at 4.5 ksi/1 min/55°C between two 50 μm mylar sheets. Li metal foil (750 μm, Sigma Aldrich) was scraped clean of oxide and punched to 16 mm diameter. Celgard 2400 separator (MTI, 25 μm) was used in all samples. MTI 2032 size coin cell components made from SS304 were used, except for AlF_3 coated caps (cathode side). These caps were used to avoid high voltage corrosion above 4.5 V Li/Li^+ [19].

All coin cell cycling was performed using BioLogic BTS battery cyclers with upper cutoff voltage (UCV) of 4.9 V and LCV of 3.5 or 2.4 V. The cycling windows using LCVs of 3.5 and 2.4 V are referred to as standard window (SW) and expanded window (EW). Tests were performed at room temperature (23°C). The 1C value used to calculate C-rates was based on theoretical capacities found in the literature of s-LMNO, 147 mAh g^{-1} [25,43]. Constant current, constant voltage (CCCV) charging was used with a C/20 CV cutoff step limited to 20 min. All potentials are given vs. Li/Li^+ unless otherwise stated. Typically, C-rates for galvanostatic cycling were 0.1C,

0.2C, and 0.1C for cycles 1-2, 3-52, and 53-57 respectively. Charge (Ch) and discharge (DCh) capacities are further abbreviated as Q_{Ch} and Q_{DCh}, respectively.

4.4 Results and Discussion

In the following sections, we first characterize as-produced and calcined Li_xMNO structure and morphologies by SEM/EDX, PSA, BET, XRD, HAADF S/TEM, and ICP-MS. In the second section we discuss additional material characterization via spectroscopy techniques FTIR and ^7Li MAS NMR for detailed structural and phase analysis. Finally, we investigate electrochemical behavior and properties of calcined NPs via cyclic voltammetry (CV), galvanostatic cycling, and dV dQ^{-1} using LCVs of 3.5 and 2.4 V.

4.4.1 Structure and Morphology

Typically, LF-FSP NP synthesis results in controlled morphology, which can be observed in this study [34,46–48,56]. NP imaging via SEM in addition to SSA analysis was performed to elucidate particle morphology. XRD and HAADF S/TEM studies aided in phase identification with ICP-MS and EDX confirming elemental content and relative distribution, respectively.

EDX elemental mapping shows uniform Ni, Mn, and O distribution across the NP surfaces (Figure 4.4), and particle morphology is representative of synthesized samples in this study, independent of Li content (additional SEM see Figure 4.11). As-produced NPs showed both spherical and cuboctahedron, or truncated octahedron, morphologies. In the case of calcined powders, there is expected particle growth due to increased surface energies (Figure 4.12).

As-produced material was tested for SSAs via BET method and calcined materials were tested via PSA after ball milling: particle size distributions are shown in Figure 4.4 while a summary of numerical data can be found in the Table 4.5. PSA number statistics show mean and median

particle size for $Li_{0.92\text{-}1.50}MNO$ of 63-102 and 61-64 nm, respectively. Similar APS values are observed in samples before and after ball milling, showing that there is no major APS reduction via ball milling during slurry preparation.

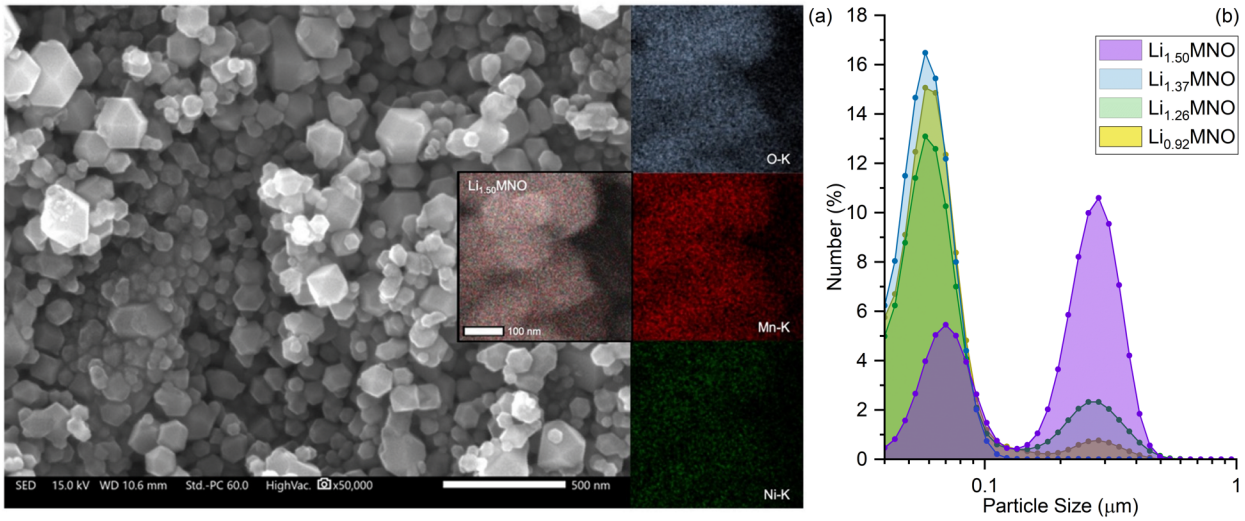

Figure 4.4: Morphology of as-produced $Li_{1.50}MNO$ sample via (a) SEM imaging and EDX elemental mapping and (b) PSA particle size distribution of calcined, ball milled Li_xMNO samples.

As-produced NPs display SSAs of 11-15 $m^2\ g^{-1}$ from BET calculations. The as-produced NPs show an inverse relation between SSA and Li content. There is good agreement between APSs from as-produced BET data and calcined PSA data, APSs, showing no significant particle size growth as a result of calcination (Figure 4.13). Calculated APSs for the as-produced materials range from 90-110 nm, with measured BET data shown in Figure 4.14.

While surface elemental composition can be determined from EDX, it is equally important to understand bulk material composition. As such, ICP-MS was performed on as-produced and calcined materials, with average results shown in Table 4.2. A linear relationship can be observed between the ratio of Li:TM in the precursor solution and the measured ICP ratio, shown in Figure 4.15.

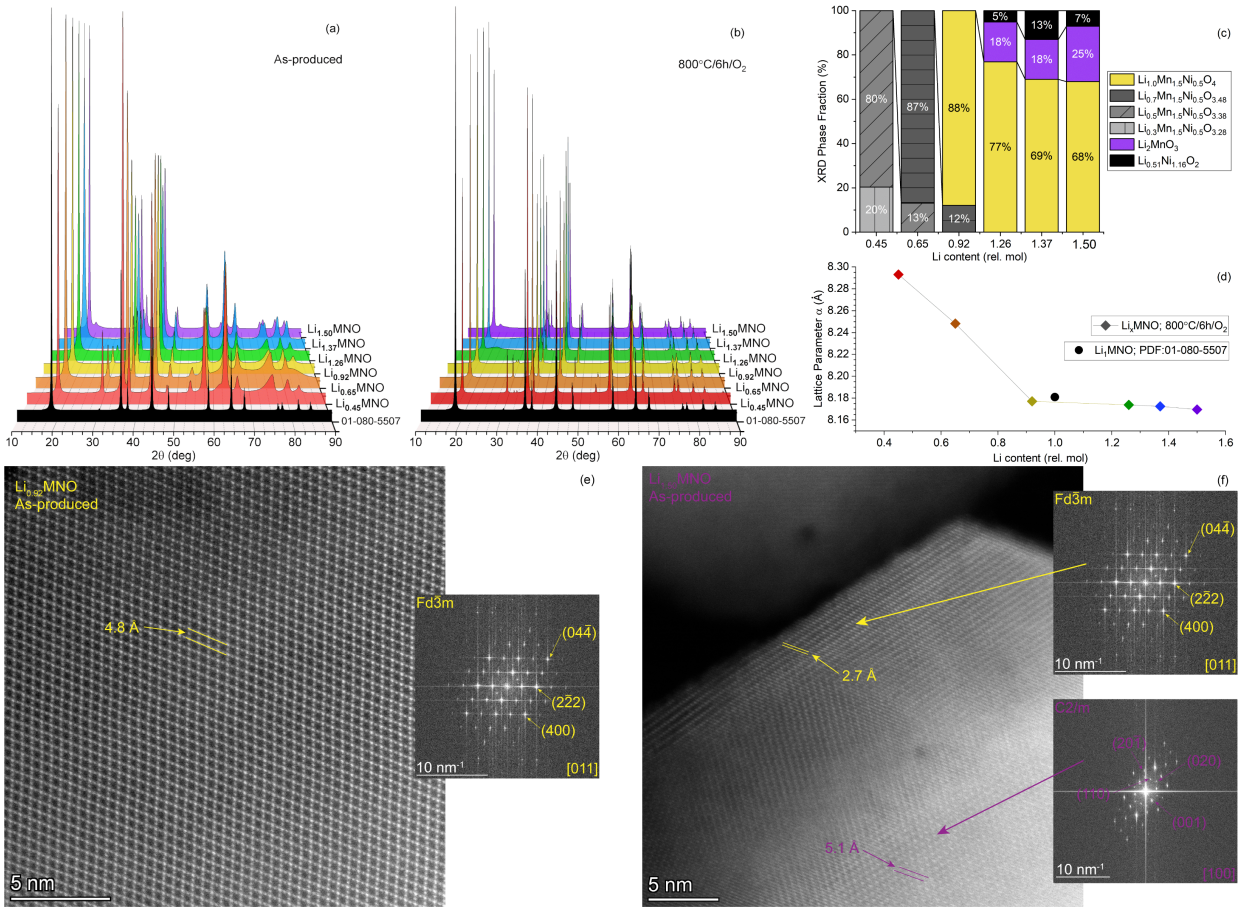

Figure 4.5: XRD studies for (a) as-produced and (b) calcined Li_xMNO NPs. (c) Phase fraction calculation from Rietveld refinement for calcined Li_xMNO NPs. (d) Rietveld refinement results for lattice parameter vs. ICP-MS Li content compared to Li_1MNO, $Fd\bar{3}m$. High resolution HAADF-S/TEM images of (e) $Li_{0.92}MNO$ and (f) $Li_{1.50}MNO$ with corresponding FFTs showing spinel (white text) and monoclinic (purple text) phases.

Table 4.2: Summarized ICP-MS results for ratios of Li, Mn, and Ni content for heated Li_xMNO NPs. Italicized values are basis for normalization.

Sample	Li (rel. mol)	Mn (rel. mol)	Ni (rel. mol)
$Li_{0.45}MNO$	0.45 ±0.04	*1.50*	0.50 ±0.01
$Li_{0.65}MNO$	0.65 ±0.02	*1.50*	0.52 ±0.01
$Li_{0.92}MNO$	0.92 ±0.03	*1.50*	0.50 ±0.01
$Li_{1.26}MNO$	1.26 ±0.02	*1.50*	0.50 ±0.01
$Li_{1.37}MNO$	1.37 ±0.01	*1.50*	0.51 ±0.01
$Li_{1.50}MNO$	1.50 ±0.04	*1.50*	0.48 ±0.01

XRD studies of as-produced (Figure 4.5a) and calcined (Figure 4.5b) Li_xMNO NPs show general phase agreement with the disordered s-LMNO phase (SG: 227, $Fd\bar{3}m$, PDF: 01-080-5507).

As-produced $Li_{0.45\text{-}1.26}MNO$ samples show good phase agreement with disordered s-LMNO, with an additional peak near 31º 2Θ corresponding to the (220) direction in underlithiated phases shown in Figure 4.16. The extraneous peak is likely due to atypical TM occupation of the 8a site, which is a result of underlithiation in the disordered spinel phase that scales inversely with increased Li content [38,67]. As-produced $Li_{1.50}MNO$ also shows a small reflection at 21º 2θ corresponding to m-LMO (SG: 12, C2/m, PDF: 01-078-5048). Detailed peak comparisons for as-produced NPs vs. matching phases are found in Figure 4.16. Further comparison between the as-produced NPs and calcined NPs are shown in Figure 4.17.

Observation of an underlithiated spinel phase, even in materials with more than Li_1 per formula unit as obtained via ICP-MS, is evidence of an amorphous, Li-containing phase in the as-produced material. Due to amorphous phase content, determination of phase fractions in as-produced NPs was not pursued via Rietveld refinement. Typically, materials with x>1 Li_xMNO show a secondary, tetragonal phase t-LMNO (SG: 141, $I4_1/amd$); however, as-produced and calcined Li_xMNO samples do not show t-LMNO content. [18,19,22,23]. The results of excess Li content via ICP-MS in conjunction with the absence of t-LMNO phase via XRD support the existence of a secondary, Li-containing phase. Among the possible candidates for the secondary phase(s) are m-LMO and a lithium nickel oxide (LNO) such as $Li_{0.51}Ni_{1.16}O_2$ (SG: 166, $R\bar{3}m$, PDF: 01-088-1607). Since ICP-MS results show a constant 3:1 atomic ratio of Mn:Ni in all synthesized samples, any secondary phase with high Mn content is most likely accompanied by an additional Ni-containing phase. Lithium nickel oxide is known to form alongside s-LMNO when calcining above 750 ºC [16,68].

Additionally, there is a significant shift to higher 2θ coincident with increased Li content which corresponds to a decrease in the unit cell size, as highlighted in Figure 4.5b and Figure 4.5d.

Rietveld refinement of the lattice parameter(s) was performed for each Li_xMNO NP sample using $Fd\bar{3}m$ s-LMNO as the target phase (PDF:01-080-5507). There is a clear relationship between increasing Li content and decreasing lattice parameter (Figure 4.5d). The NP sample closest to stoichiometric s-LMNO ($Li_{0.92}MNO$) shows a lattice parameter closest to the expected value for the disordered phase $Fd\bar{3}m$ (8.181 Å). With the addition of Li^+ into the structure, there is a subsequent partial transformation of Mn to lower valency, i.e. Mn^{4+} (0.535 Å ion radius) to Mn^{3+} (0.645 Å ion radius) to maintain charge neutrality [69]. This idea also qualitatively applies to underlithiated samples, such that low Li^+ content leads to increased Mn^{4+} content, resulting in a larger unit cell [21,42,68–70]. Estimation of phase fraction from Rietveld refinement is shown in Figure 4.5c, which shows the trend of increased Li content with increased m-LMO phase accompanied by LNO. These phase fractions are in agreement with the TM ratio for Mn and Ni. Additional Rietveld refinement results can be found in Table 4.6.

HAADF-S/TEM studies reveal the primary phases found in $Li_{0.92}MNO$ (Figure 4.5e) and $Li_{1.50}MNO$ (Figure 4.5f). $Li_{0.92}MNO$ showed typical interplanar spacing (4.8 Å) when viewed from the [011] direction, while the corresponding FFT is in good agreement with expected diffraction spots for (400), $(2\bar{2}2)$, and $(04\bar{4})$ crystallographic planes for $Fd\bar{3}m$ spinel. The overlithiated sample shows both C2/m and $Fd\bar{3}m$ phases, as shown by FFT indexing in Figure 4.5f. Similar to $Li_{0.92}MNO$, the interplanar spacing observed for the C2/m phase is larger than expected (5.1 vs 4.9 Å) in the [100] direction.

4.4.2 Spectroscopy Studies

In previous studies, spectroscopic techniques such as FTIR (Figure 4.6a) and ^7Li MAS NMR (Figure 4.6b,c) have been used to determine local bonding conditions and valency with mixed metal oxides such as s-LMNO [20,70,71].

FTIR has been used to distinguish ordered and disordered s-LMNO phases via relative magnitude of absorption bands. Kunduraci et al. [20] determined the 589 and 624 cm^{-1} intensities can be used to quantify the order/disorder of the sample [20,44]. These absorption bands are identified in Figure 4.6a as $\clubsuit_{N1}$ and $\clubsuit_{M1}$, respectively. Additional stretching bands for Ni-O and Mn-O are shown as $\clubsuit_{N2}$ and $\clubsuit_{M2}$, respectively, summarized in Table 4.7. When this ratio ($\clubsuit_{N1}$: $\clubsuit_{M1}$ intensity) is >1, the material is typically ordered whereas if the ratio is <1, the phase is disordered [20,44]. As-produced and calcined NPs show disordered structure based on FTIR, values shown in Table 4.8. Bands observed in as-produced samples are considerably less defined than in the calcined counterparts, attributed to an amorphous phase. Additional FTIRs can be found in Figure 4.18.

To further evaluate local bonding conditions within the synthesized Li_xMNO NP samples, ^7Li MAS NMR studies were conducted with the primary goals of further examination of Li-O-TM coordination spheres and identifying Li-containing secondary phases [70,72–74]. The chemical shifts observed in disordered s-LMNO are the result of paramagnetic shifts and broadening attributed to bond delocalization of unpaired electron densities from metal orbitals into the Li sites [70,72]. The magnitude of the chemical shift is dependent on the composition of the first coordination sphere, typically containing 12 TMs connected to Li via Li-O-TM bonding configuration. Stoichiometric, ordered LMNO spinel contains a ratio of 1:3 Ni:Mn such that the first coordination sphere for a completely ordered arrangement has a composition of $Li(O\text{-}Ni^{2+})_3(O\text{-}Mn^{4+})_9$. When all Mn is initially tetravalent, this primary signal occurs near 1000 ppm, shown in Figure 4.6c as peak C.

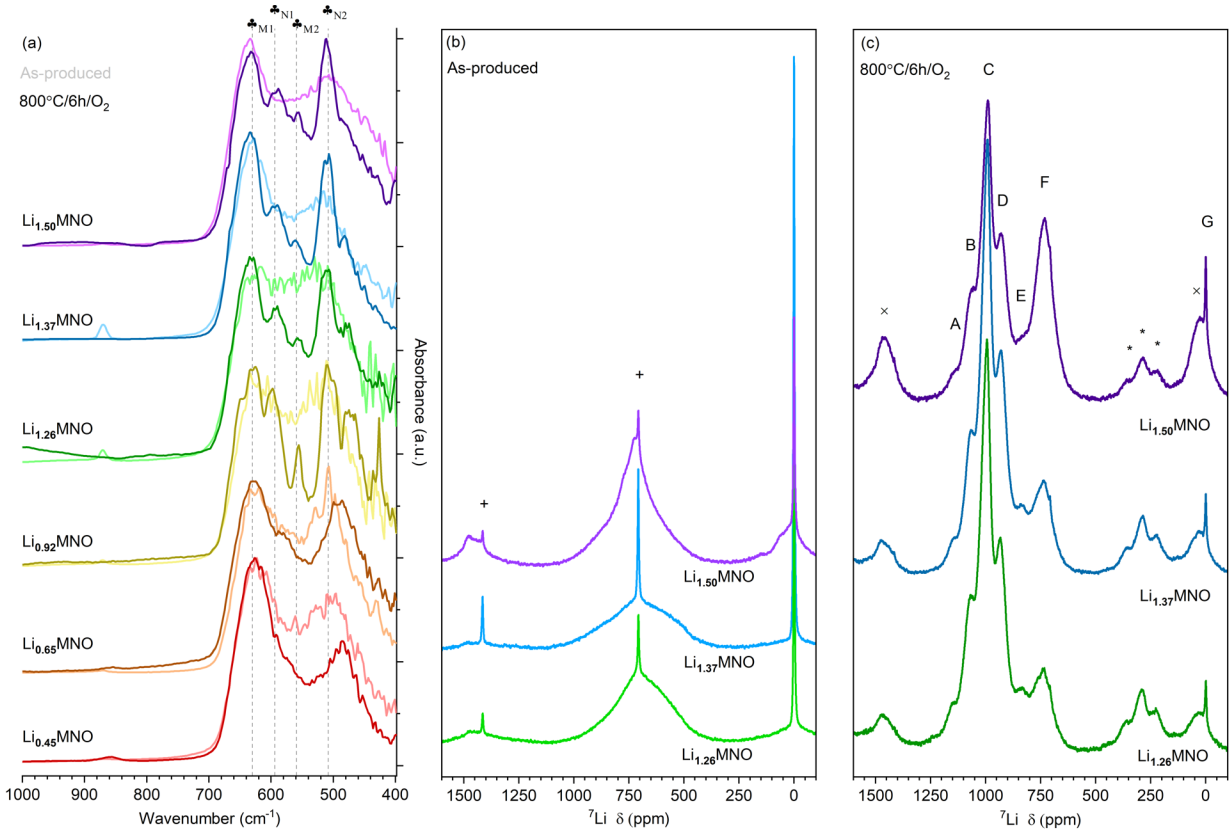

Figure 4.6: (a) FTIR of as-produced and calcined Li_xMNO samples. In (a), ♣N1, ♣N2, ♣M1 and ♣M2 indicate typical Ni-O and Mn-O bands. ^7Li NMR data of (b) as-produced and (c) calcined overlithiated Li_xMNO samples. In (c), the spinning sidebands of the diamagnetic phase around 0 ppm are labeled with "+". In (d), isotropic peaks A to E correspond to the different Ni/Mn environments in the first TM-O coordination shells of s-LMNO, and their spinning sidebands are labeled with "*". The isotropic peak (F) located at 773 ppm is ascribed to m-LMO and "×" is used to denote two spinning sidebands of this peak. The diamagnetic phase labeled with G appears at around 0 ppm.

Peaks observed in the range 1200-800 ppm (peaks A to E) reveal the presence of multiple Ni/Mn ratios on the 16d sites around the Li 8a site, while the peak close to 1000 ppm (peak C) with the highest intensity represents the most probable environment (9Mn/3Ni) and the peaks on the left and right side of this peak represent environments with more and less Ni, respectively [70,73,74]. Overall, the pattern of intensities of these peaks reveals the presence of a fully disordered arrangement of Ni/Mn on the 16d site, in agreement with the $Fd\bar{3}m$ symmetry observed with XRD and FTIR [70,73]. Increased crystallinity is expected as a result of high temperature calcination (800ºC/6h/O_2), therefore more defined Li environments in calcined samples (Figure 4.6c) are expected in comparison to the as-produced samples (Figure 4.6b). For the calcined

samples, there is increasing peak intensity near 773 ppm, peak F in Figure 4.6c, corresponding to a Ni-free coordination shell. The relative intensity of the peak F increases with increasing Li content. While these chemical shifts are typically not assigned to ordered or disordered s-LMNO, there is good agreement with typical chemical shifts seen in Li-TM compounds such as m-LMO [70,73,75]. As expected, the amount of this Li-rich phase increases with increasing overall Li content. Full ^{7}Li NMR spectra for $Li_{1.50\text{-}1.26}MNO$ samples can be found in Figure 4.19.

Primary characteristic of the as-produced NPs is a broad peak in the ~1000 to 400 ppm range. There is one defined peak near 720 ppm that can be assigned to either m-LMO or LNO phases [70,73]. Additionally, there is a significant signal near 0 ppm corresponding to diamagnetic Li-containing compounds such as Li_2CO_3 [71,72,76]. Note in the as-produced materials, FTIR also shows evidence of Li_2CO_3 at high Li-content. Li_2CO_3 content based on the area under the 0 ppm peak also shows a trend of lower concentration in calcined NPs (0.93%, 0.76%, 1.13% for $Li_{1.26}MNO$, $Li_{1.37}MNO$, $Li_{1.50}MNO$) compared to as-produced NPs (9.76%, 16.79%, 5.60% for $Li_{1.26}MNO$, $Li_{1.37}MNO$, $Li_{1.50}MNO$), in good agreement with FTIR. In theory, TGA-DTA of the as-produced NPs should be able to indicate the presence of Li_2CO_3 as it melts at 723ºC; however, in practice this temperature overlaps with known oxygen loss in LMNO above 700ºC and therefore the processes are difficult to deconvolute from each other, Figure 4.20 [44,77]. Independent of this analysis, it can be concluded that the observed spectra for the as-produced NPs are remarkably different from the calcined counterparts - revealing considerable amorphous phase content or spinels with very poor crystallinity in the as-produced samples.

4.4.3 Electrochemical Characterization

To further explore the calcined Li_xMNO NPs, electrochemical studies were performed using two different voltage windows. Typical cycling parameters are shown in Table **1** for s-LMNO.

Independent of x in Li_xMNO-type composition materials, the bulk of observed capacity is attributed to $Ni^{2+/4+}$ above 3.5 V, with additional Mn contribution shown as a shoulder near 4.0 V, varying on the level of disorder ($Mn^{3+/4+}$) [23]. Galvanostatic cycling was performed using UCV of 4.9 V (Figure 4.7a) and LCVs of 2.4 V (Figure 4.7b-e) and 3.5 V (inserts in Figure 4.7c-e). Materials with increased Li content displayed higher charge and discharge capacities (2.4 V). Galvanostatic cycling results for both LCVs are summarized in Figure 4.8. Redox activity is visualized in Figure 4.9 via potential per capacity color density plots combined with $dV\ dQ^{-1}$. Finally, Figure 4.10 features a comparison of industry standard binder to aqueous CMC.

4.4.3.1 Typical Cycling Window (SW, LCV=3.5V)

Stoichiometric and overlithiated samples display discharge capacity curves typical for s-LMNO, with the bulk of the capacity originating from $Ni^{4+/2+}$ redox activity. Potential vs capacity curves for $Li_{0.45}MNO$ and $Li_{0.65}MNO$ do not show typical flat Ni redox activity; however, there is a sloping voltage profile indicating gradual reduction/oxidation of Mn dominant environments [24,30,31,78,79]. This difference between redox processes can also be seen in CV studies, Figure 4.21.

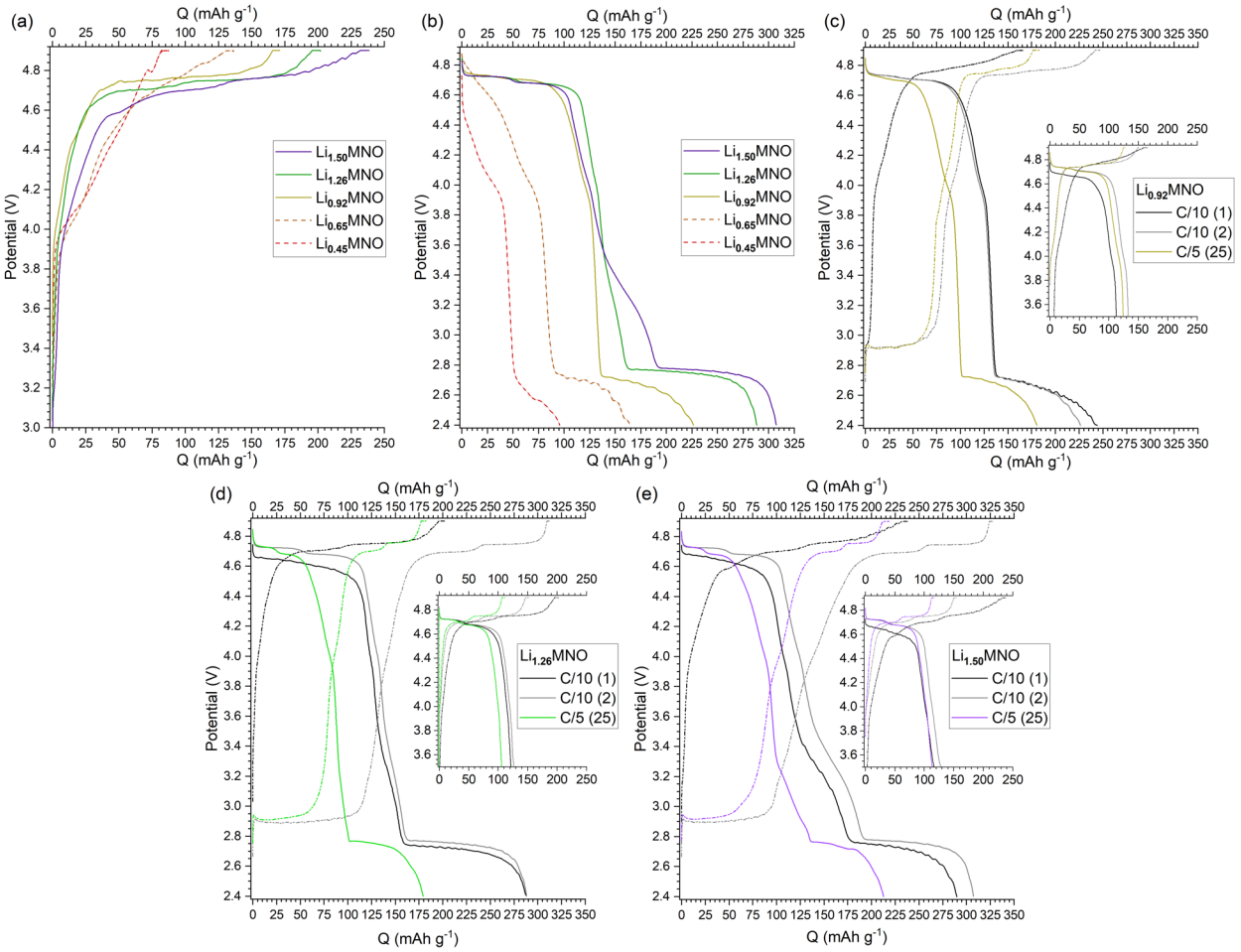

Figure 4.7: (a) Potential vs cycle 1 charge and (b) cycle 2 discharge capacity at C-rate of 0.1C with UCV-LCV of 4.9 – 2.4 V using CMC binder. Potential vs specific capacity curves for (c) $Li_{0.92}MNO$, (d) $Li_{1.26}MNO$, and (e) $Li_{1.50}MNO$ when cycled with LCV of 2.4 V using CMC binder. Inserts are NP sample cycled with LCV of 3.5 V.

Among samples with Li contents greater than 0.65, there is a correlation between increased charge capacity with increased Li content. This trend is highlighted in Figure 4.7a. Initial charge capacities for $Li_{1.26}MNO$ and $Li_{1.50}MNO$ are 205±6, and 235±3 mAh g^{-1} at 0.1C (14.7 mA g^{-1}), respectively. This result is contradictory to st-LMNO phase materials that typically display near identical 1st charge behavior above 4.5 V independent of initial Li concentration, or x in $(s\text{-}LMNO)_{1-0.5x}\cdot(t\text{-}LMNO)_{0.5x}$ compositions [23]. Typically, st-LMNO as a starting material first undergoes delithiation of the t-LMNO phase near 2.8 V, followed by typical s-LMNO delithiation

[18,19,22,23,25]. The difference in 1st cycle charge behavior indicates the presence of phases other than s- or st-LMNO.

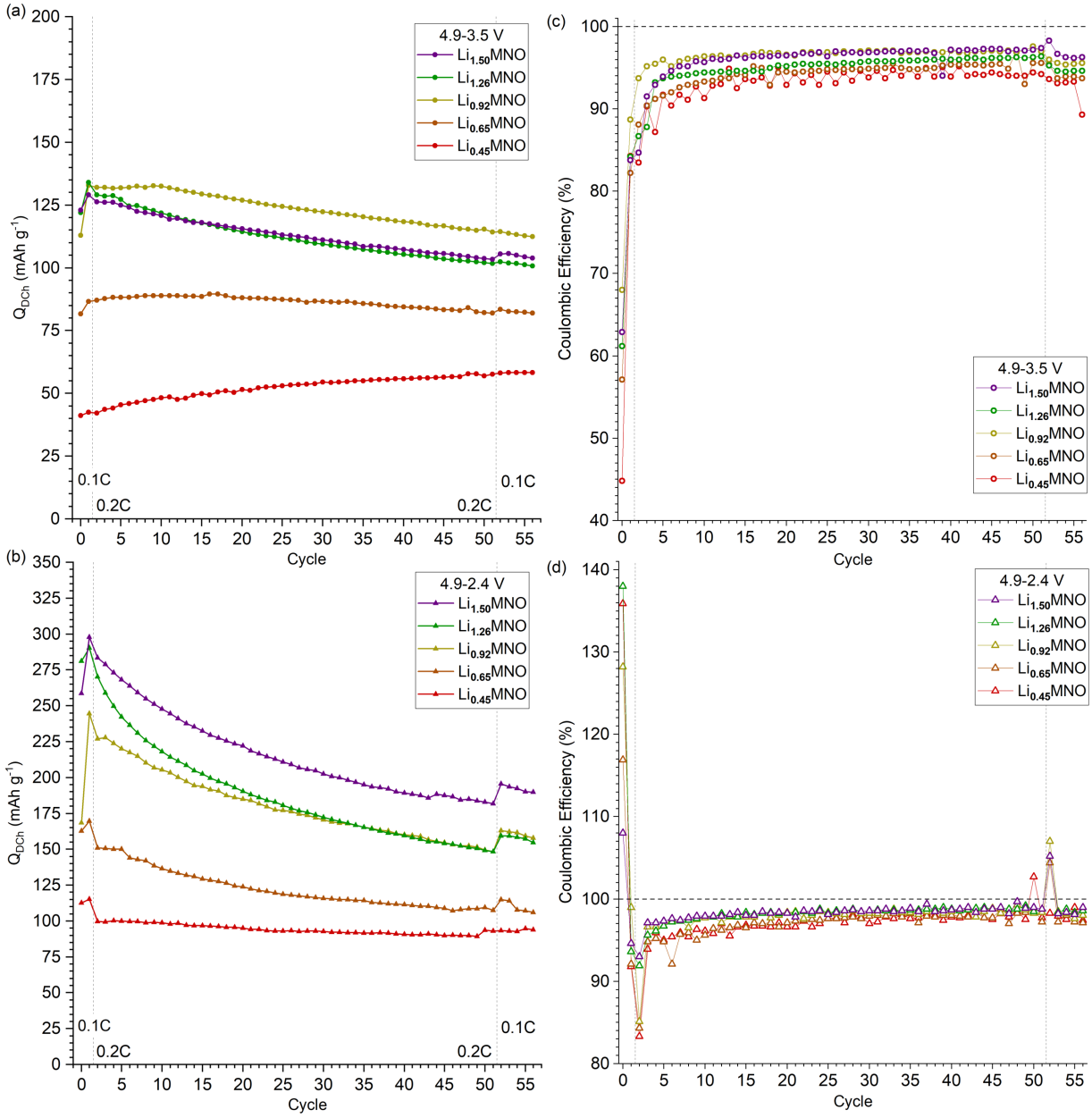

Figure 4.8: Capacity vs cycle for Li_xMNO materials with LCV of (a) 3.5 V and (b) 2.4 V using CMC binder. Coulombic efficiency per cycle for LCV of (c) 3.5 and (d) 2.4 V. Vertical dashed lines indicate C-rate change from 0.1C to 0.2C at cycle 2 and back to 0.1C at cycle 52. Horizontal dashed line indicates 100% coulombic efficiency.

Observed discharge redox plateaus occur at lower voltages than expected (4.55-4.6 vs. 4.7 V) when Li content increases from $Li_{0.92}$ to $Li_{1.50}$, which is most likely related to increases in the Mn-

rich phase (m-LMO). From published electrochemical data available for possible secondary phases presented in Table 4.1, m-LMO seems to be the likely candidate for the deviations from expected behavior in the initial capacity curves for Li_xMNO [75,79,80]. Initial charge capacity for m-LMO starts accumulating at lower potential (4.55-4.6 V) than s-LMNO, and this shoulder is observed in $Li_{1.50}MNO$. A more sloping profile is observed above 4.7 V for $Li_{1.50}MNO$, similar to m-LMO [18,19,22–24,30,31]. Additionally, the first cycle charge capacity (236-208 mAh/g) is irreversible after the first cycle – similar to the activation seen in m-LMO [24,30,31,79].

A portion of the excess charge capacity carries over to subsequent cycles but is not observed over time, resulting in lower coulombic efficiencies (CE) during initial cycles (Figure 4.8c,d). Phase fraction for each capacity contributing phase can be calculated based on the first charge capacity, assuming theoretical values for s-LMNO (147 mAh g^{-1}) and m-LMO (350 mAh g^{-1}). Based on 1st charge capacity, phase fraction ratio s-LMNO:m-LMO for $Li_{1.26}MNO$ and $Li_{1.50}MNO$ was calculated to 71:29 and 57:43, respectively.

4.4.3.2 Expanded Cycling Window (EW, LCV=2.4V)

Additional $Mn^{3+/4+}$ redox activity is accessible by widening the electrochemical window to a lower LCV (2.4 V) [18]. The increase in capacity is observed via a well-defined redox plateau near 2.7 V [18,19,22,23,25]. The LCV can be lowered further to 1.5 V for further Mn redox; however, there are additional phase transitions at higher Li content which result in impractical capacity retention, in addition to system issues such as instability with high-voltage electrolytes and incompatibility with system level BEV power electronics and thus this is not studied here [18,19,22]. In addition to high first charge capacity observed in Li_xMNO NPs, lowering the LCV to 2.4 V reveals discharge capacities up to 300 mAh g^{-1}, higher than the expected value of 200-

220 mAh g^{-1}, with an unexpected capacity curve shape – see Figure 4.7b-e [18,19,22,23,26]. Additional cycling data for $Li_{0.45}$ and $Li_{0.65}$MNO can be found in Figure 4.22.

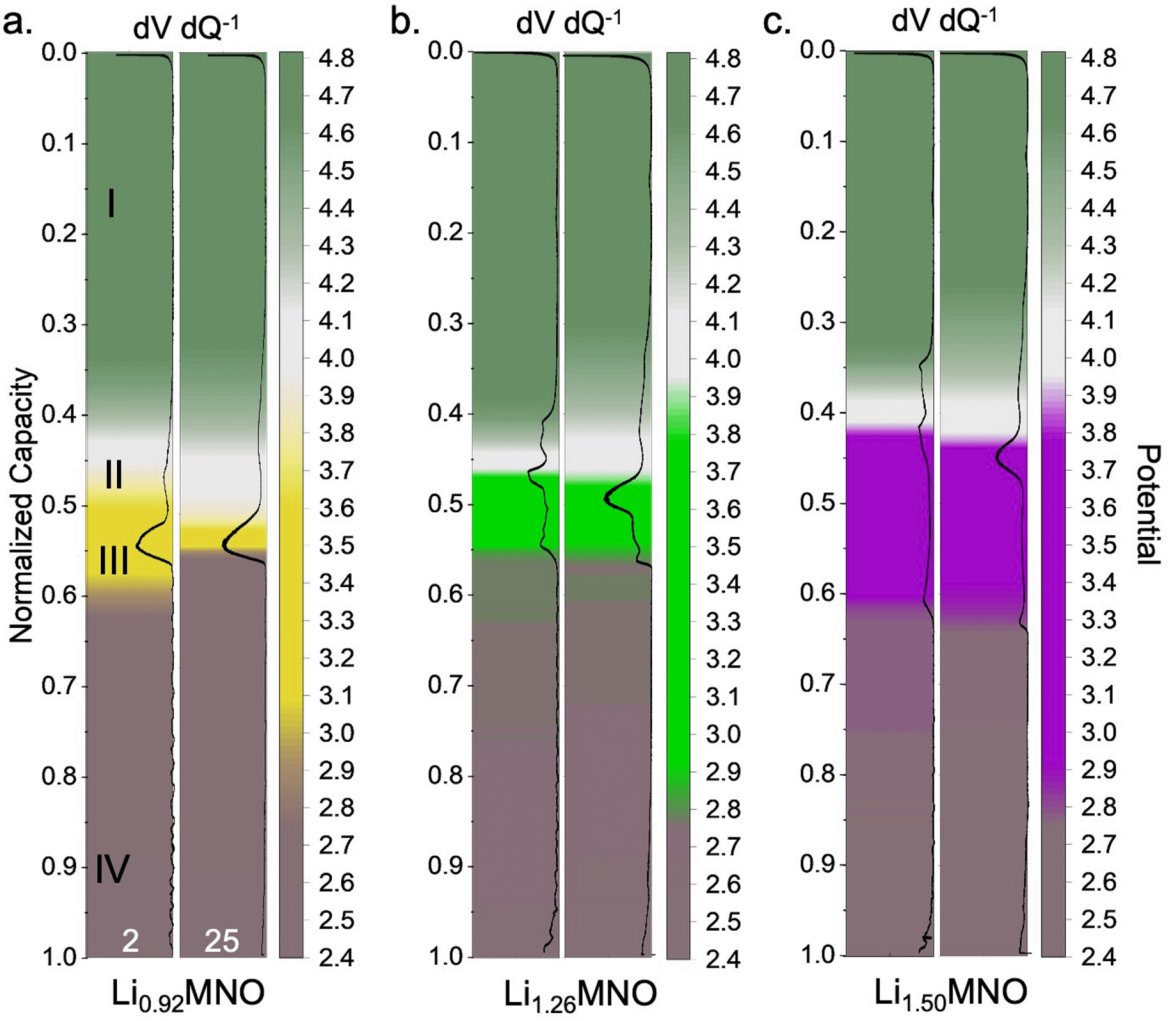

Figure 4.9: Potential per capacity color density plot for cycles 2 and 25 with overlaid dV dQ^{-1} plots emphasizing the intermediate potential range for (a) $Li_{0.92}$MNO, (b) $Li_{1.26}$MNO, and (c) $Li_{1.50}$MNO.

dV dQ^{-1} plots are often used to visualize features of the voltage curve in greater detail. Zero and nonzero regions in dV dQ^{-1} correspond to plateaus and slopes in the voltage curve, respectively, and can show at what state of charge certain phase changes and/or redox couples are active. Potential per capacity regions are visualized in Figure 4.9 with dV dQ^{-1} results (cycle 2, 0.1C; cycle 25, 0.2C) shown overlayed onto the voltage-capacity color density plots. In Figure

4.9a, the colored regions are labeled as I-IV where redox region I (green) is $Ni^{4+/3+}$, region II (white) is $Mn^{4+/3+}$ associated with spinel structure, region III (sample color) corresponds to the intermediate voltage region where significant redox does not typically occur, and finally region IV (grey) is additional $Mn^{4+/3+}$ associated with spinel/tetragonal phases. The inflection of colors corresponds to peaks observed in the dV dQ^{-1} plots. The intermediate potential region between redox activity near 4.0 V and 2.7 V should not reveal any significant capacity for s-LMNO/t-LMNO materials; however, there is a clear increase in the intermediate region with increasing initial lithium content with $Li_{1.50}$MNO showing ~ 25% of discharge capacity in this intermediate region compared to ~10% for $Li_{1.26}$MNO and $Li_{0.92}$MNO. The intermediate redox region increasing in magnitude with increasing Li content is further evidence of a secondary, Mn-rich phase. Additionally, the capacity heat maps for $Li_{1.26}$MNO and $Li_{1.50}$MNO do not show major change after 25 cycles. In contrast, $Li_{0.92}$MNO shows significant decrease in region III after 25 cycles, which is typical of s/st-LMNO material. Voltage decay is a serious issue for Li-rich oxides such as m-LMO [75,81]. The average discharge potential of the overlithiated materials were compared to $Li_{0.92}$MNO using 2.4 and 3.5 V LCV, Figure 4.23. There is minimal observed voltage decay within the SW (<0.3%) and EW (<3%) after 50 cycles at 0.2C. It is expected to observe higher rates of voltage decay for materials with higher amounts of m-LMO; however, the electrochemical data suggests that the presence of m-LMO in the CAM NPs does not significantly contribute to voltage decay.

4.4.3.3 CMC vs. PVDF Binder Systems

The electrochemical studies discussed thus far use water-processable CMC binder. Currently, PVDF remains the industry standard binder for cathode development; however, the hazards of required NMP solvent have been well documented [81–91]. PVDF has persisted as the industry

standard due to broad CAM compatibility and electrochemical stability. There is growing concern over the use of NMP in large scale battery manufacturing, such that governing bodies in North America and Europe have placed strict restrictions on use due to unreasonable risk for commercial use of NMP [89,90]. Water-based binder systems using guar gum, cellulose, alginate are being considered as green, safe alternatives to PVDF-NMP systems. CMC is often used as the AAM binder in a dual binder system with styrene butadiene rubber (SBR) and recent studies that show the utility of CMC as high-voltage cathode binder in single or dual-binder systems [81–84,86–88].

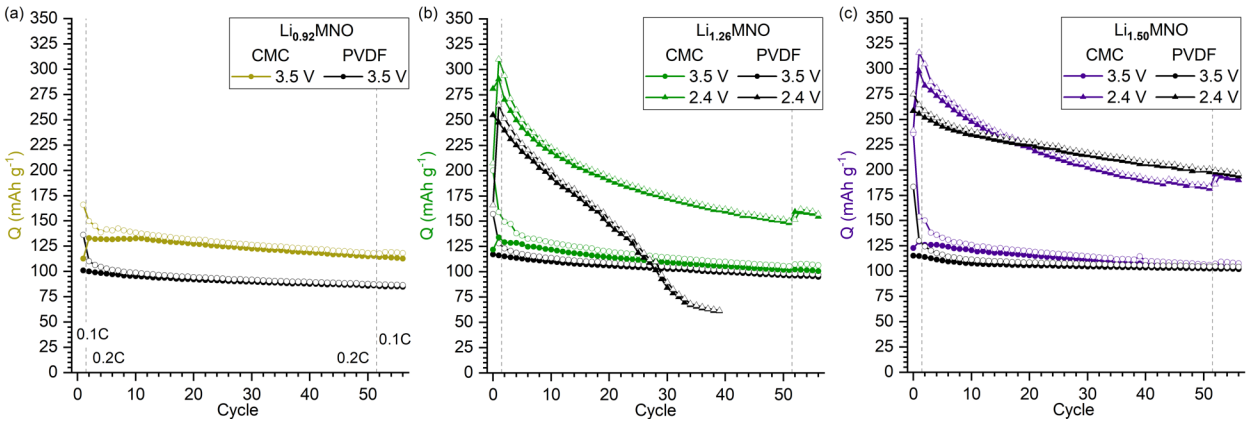

Figure 4.10: CMC vs PVDF studies for (a) $Li_{0.92}MNO$, (b) $Li_{1.26}MNO$, and (c) $Li_{1.50}MNO$. Vertical dashed lines indicate C-rate change from 0.1C to 0.2C at cycle 2 and back to 0.1C at cycle 52. Open and closed markers represent Q_{Ch} and Q_{DCh}, respectively.

Overlithiated materials highlighted in this study were also evaluated using a traditional PVDF in NMP binder system using the same relative CAM, C65, and binder electrode composition. Overall, cells containing PVDF showed similar redox behavior and cycling performance compared to cells with CMC, shown in Figure 4.10. This data shows that the same trends observed in CMC-based electrodes are also shown in traditional PVDF-based electrodes, and deviations from expected results should not be solely placed on the green binder system. All samples show higher capacity for cells using CMC binder over PVDF which follows previously reported studies [82,83,85,87,88]. Of note, there is higher observed CE in PVDF cells with similar capacity retention compared to CMC cells. One possible reason for this change is strictly due to the CMC

binder, where there is possible irreversible Na^+ diffusion out of the binder [88]. Typically, higher charge capacity and lower first cycle CEs are observed in samples with CMC compared to PVDF [82,83,86–88,92]. While improvements in discharge capacity and capacity retention at the lab scale are noteworthy, doing so with a potential next generation binder system points to this material system being a candidate for large-scale manufacturing.

Beyond the cathode, state-of-the-art anode active materials (AAMs) pose many issues for cells used for BEV application. Instead of Li metal in a typical research-level coin cell, there is a limited Li inventory supplied by the cathode in full cell format. Typically, high capacity AAMs suffer from low first cycle CE and irreversible capacity loss [93]. The low first cycle CE depletes Li inventory, consequently lowering the available Li inventory for reversible cycling. An important example of this phenomenon is Si-containing anodes that offer ~3x capacity compared to graphite but suffer low first cycle CE [93]. Li donors have been studied as coatings on either electrode but present manufacturing challenges. One solution to combat Li inventory loss is to use an "overlithiated" cathode, such that the cathode contains more Li content than is required for reversible cycling. The additional Li can be donated to irreversible, Li-consuming processes such as the formation of SEI layer on the anode [18,25]. CAMs with high Li content are needed in commercially viable cells. An overlithiated, Li donating cathode also has the potential to allow for higher N/P ratios in full cell assembly.

4.5 Conclusions

There is a growing need for alternative high energy density cathode chemistries away from NMC-type materials. Compositional focus should be high Mn and low Ni content for cost and future supply chain considerations while maximizing energy density. Herein we report synthesis

and characterization of mixed phase Li-, Mn-rich CAMs with maximum energy density greater than 1000 Wh kg^{-1} using a green, aqueous binder system, cycling data summarized in Table 4.3.

Table 4.3: Summary of Li_xMNO performance (cycle 2 @ 0.1C).

Sample	Cycle 1 Q_{Ch} (mAh g^{-1})	Cycle 2 Q_{DCh} (mAh g^{-1})		Cycle 2 DCh ED (Wh kg^{-1})		C/5 Q_{DCh} @ 50 cycles (%)	
	4.9 V	SW	EW	SW	EW	SW	EW
$Li_{0.45}MNO$	91	42	115	180	348	136	94
$Li_{0.65}MNO$	142	87	169	370	573	94	71
$Li_{0.92}MNO$	155	132	244	600	890	87	67
$Li_{1.26}MNO$	208	130	292	584	1070	79	55
$Li_{1.50}MNO$	236	129	300	578	1090	82	64

Increasing initial Li content results in larger 1st charge capacity, which has the potential to serve as Li donor in irreversible, Li-consuming SEI formation in next generation AAMs, as well as anode-free cells. Further optimization of the CAMs in this study is required to further validate candidacy for use in large scale manufacturing. One area that requires improvement is the capacity retention in the extended cycling window to 2.4 V. While $Li_{1.50}MNO$ and $Li_{1.26}MNO$ show initial energy densities greater than 1000 Wh kg^{-1}, capacity retention is poor after 50 cycles at 64% and 55%, respectively, when using LCV of 2.4 V.

4.5.1 Acknowledgements

The authors acknowledge support from a DMR NSF Grant No. DMR-1926199 and a generous gift from Mercedes-Benz Research & Development North America (MBRDNA) for this work. The authors acknowledge the financial support of the University of Michigan College of Engineering and technical support from the Michigan Center for Materials Characterization. Additionally, the authors appreciate the technical support from University of Michigan Battery Lab for battery cell testing (Dr. Greg Less), Van Vlack lab for materials characterization (Dr. Sahar Farjami, Dr. Ying Qi), Michigan Center for Materials Characterization for advanced materials characterization, and Michigan Elemental Analysis Lab (MEAL) for ICP-MS measurements (Dr.

Angela Dial). The authors also wish to acknowledge and thank undergraduate students Erik D. Flaspohler, Joseph Shangraw, Jaime Minarro-May, and Charlie Cappelletti for their contributions.

4.6 Appendix

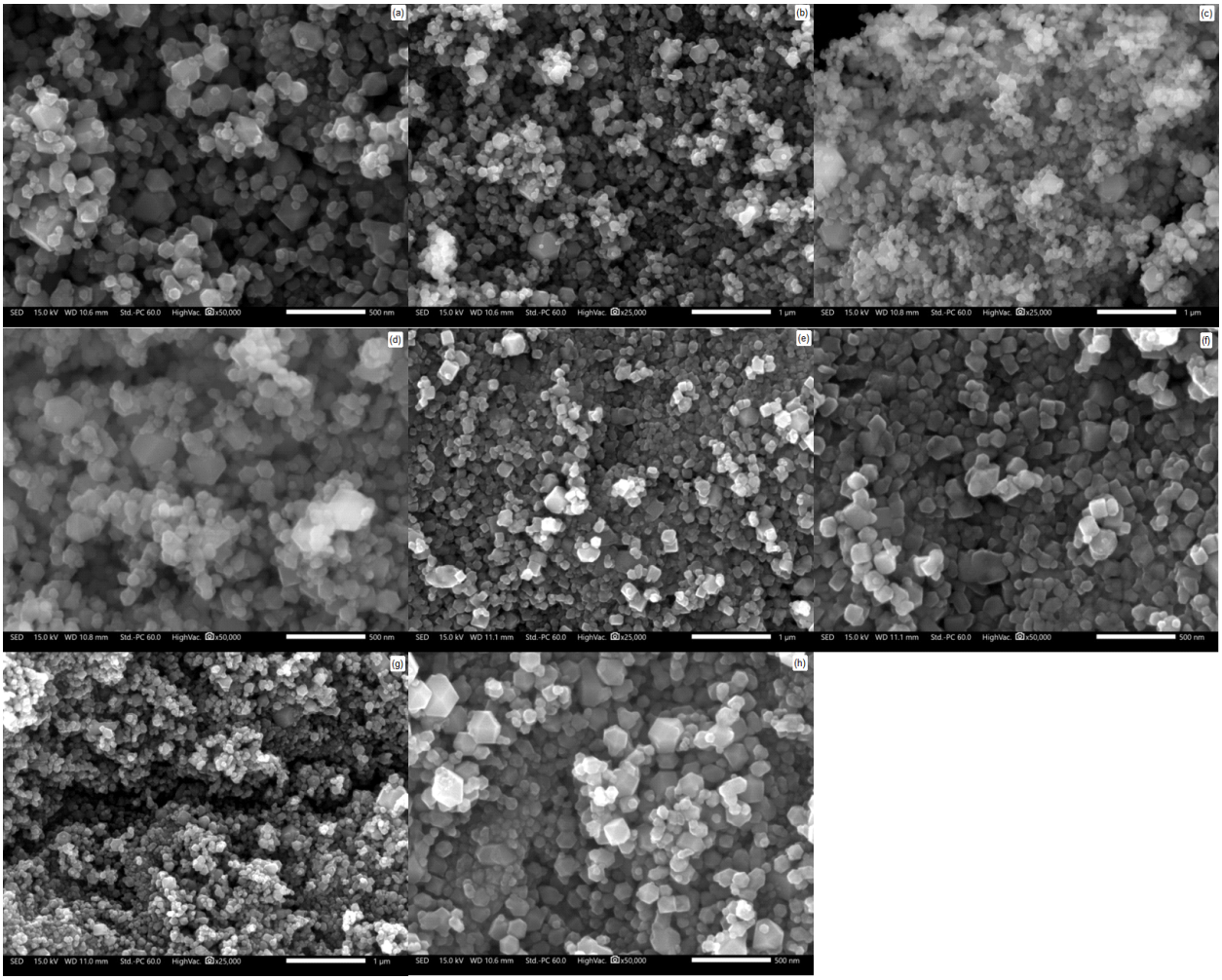

Figure 4.11: SEM of as-produced $Li_{0.92}MNO$ (a,b), $Li_{1.26}MNO$ (c,d), $Li_{1.37}MNO$ (e,f), and $Li_{1.50}MNO$ (g,h).

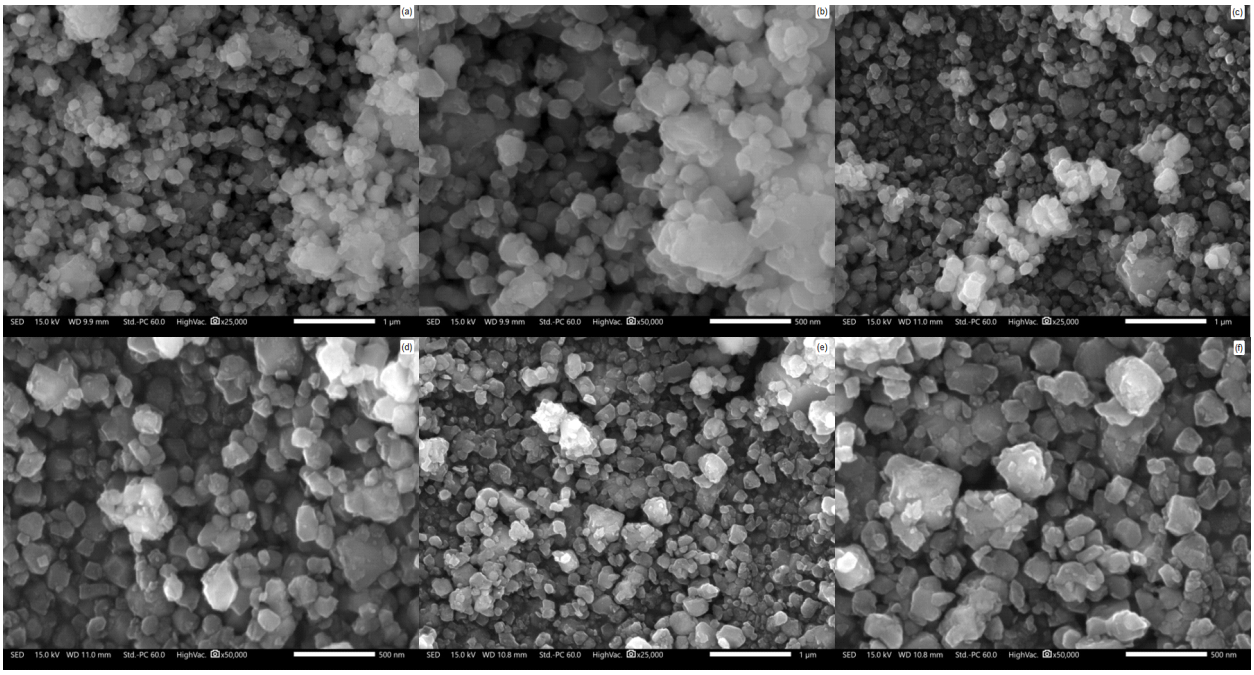

Figure 4.12: SEM of calcined (800ºC/6h/O_2) after mortar and pestle for $Li_{0.92}MNO$ (a,b), $Li_{1.26}MNO$ (c,d), and $Li_{1.50}MNO$ (e,f).

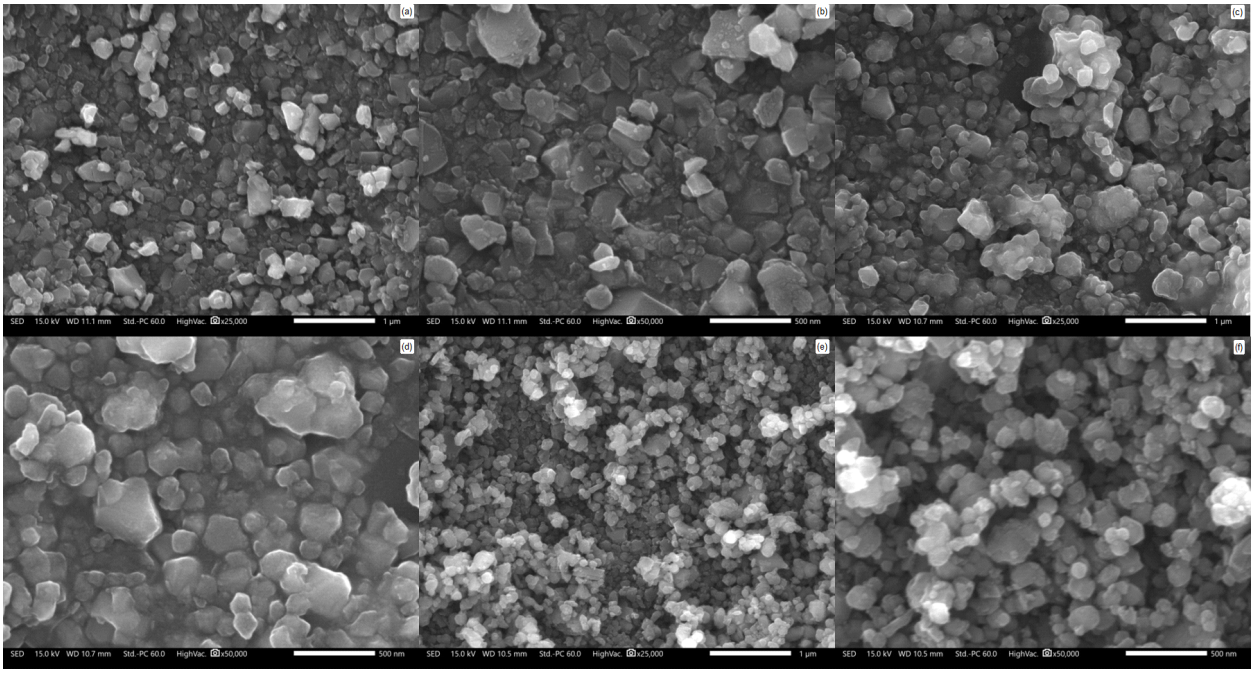

Figure 4.13: SEM of calcined (800ºC/6h/O_2) after ball milling for $Li_{0.92}MNO$ (a,b), $Li_{1.26}MNO$ (c,d), and $Li_{1.50}MNO$ (e,f).

BET results of as-produced $Li_{1+x}MNO$ NPs have SSAs of 11-15 $m^2\ g^{-1}$. APS was calculated from BET data using Equation 9:

$$D_{BET}[nm] = \frac{6000}{\rho_{theoretical} * SSA_{BET}} \quad (9)$$

D_{BET} is the particle diameter [nm], $\rho_{theoretical}$ is the theoretical density and SSA_{BET} is self-evident. Equation (3) is most accurate for spherical, non-agglomerated particles. The corresponding APSs increased but remain nanoscale. The disordered phase has a crystallographic density of 4.434 g cm^{-3}.

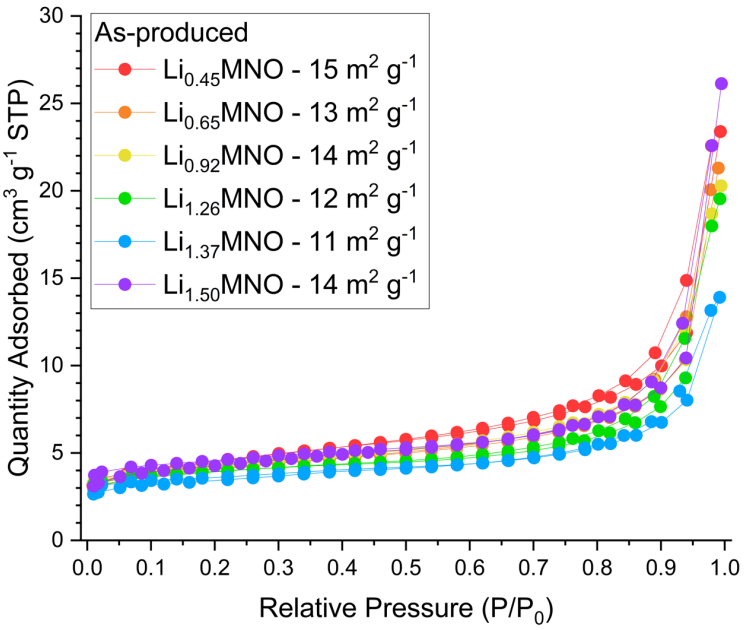

Figure 4.14: BET of as-produced Li_xMNO NPs.

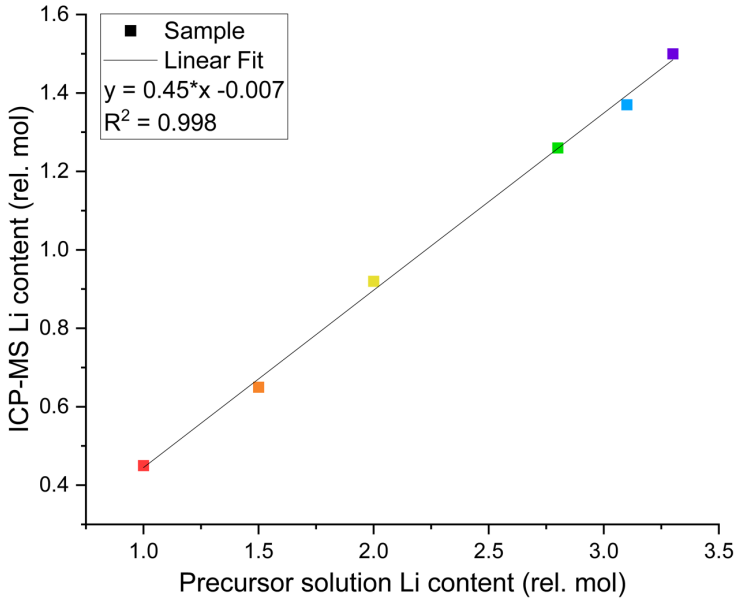

Figure 4.15: The relationship between amount of Li-precursor and measured Li content.

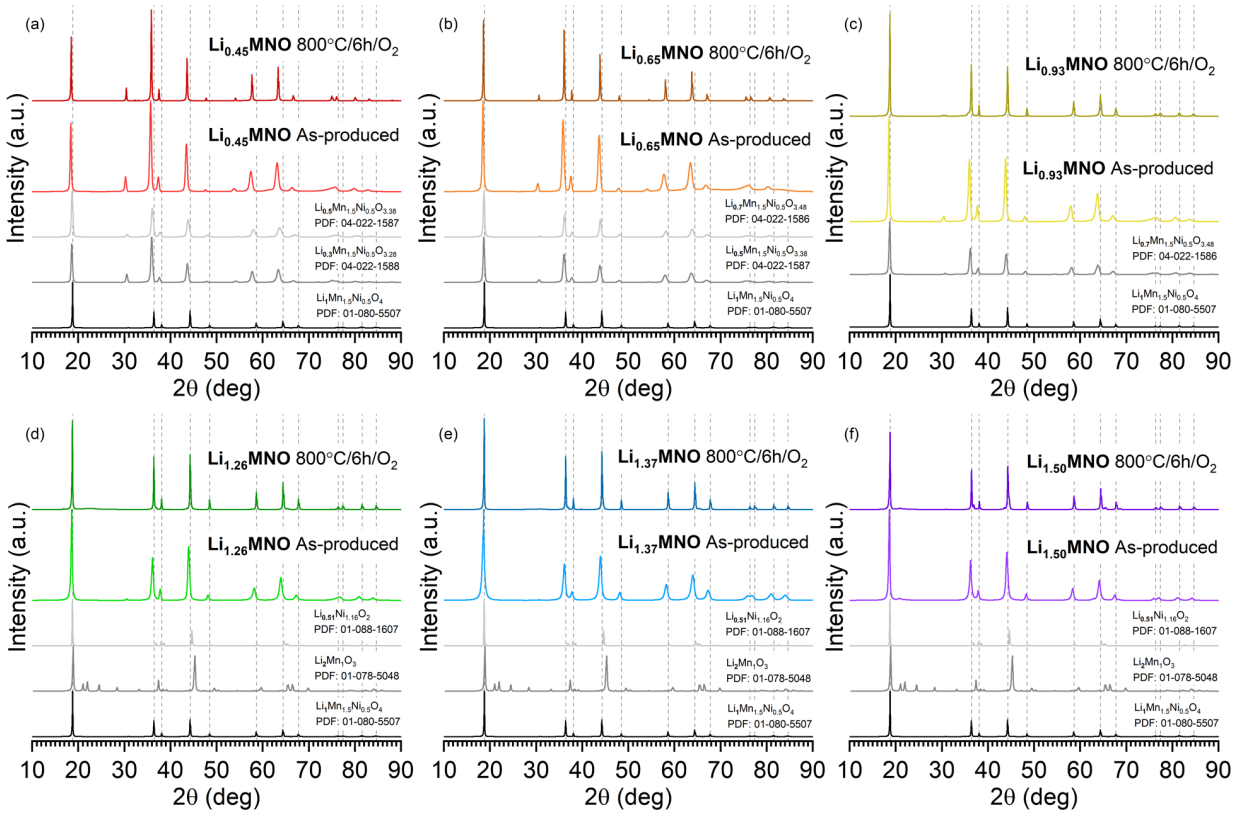

Figure 4.16: XRD studies of Li_xMNO (x=0.45-1.50) with target phases.

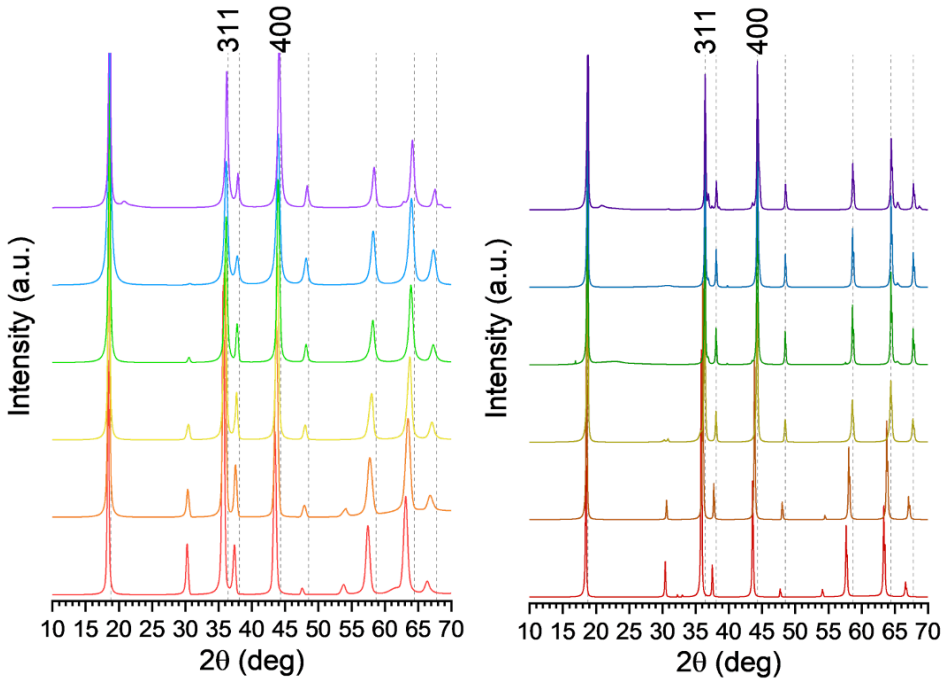

Figure 4.17: XRD studies of Li_xMNO (x=0.45-1.50) without target phases.

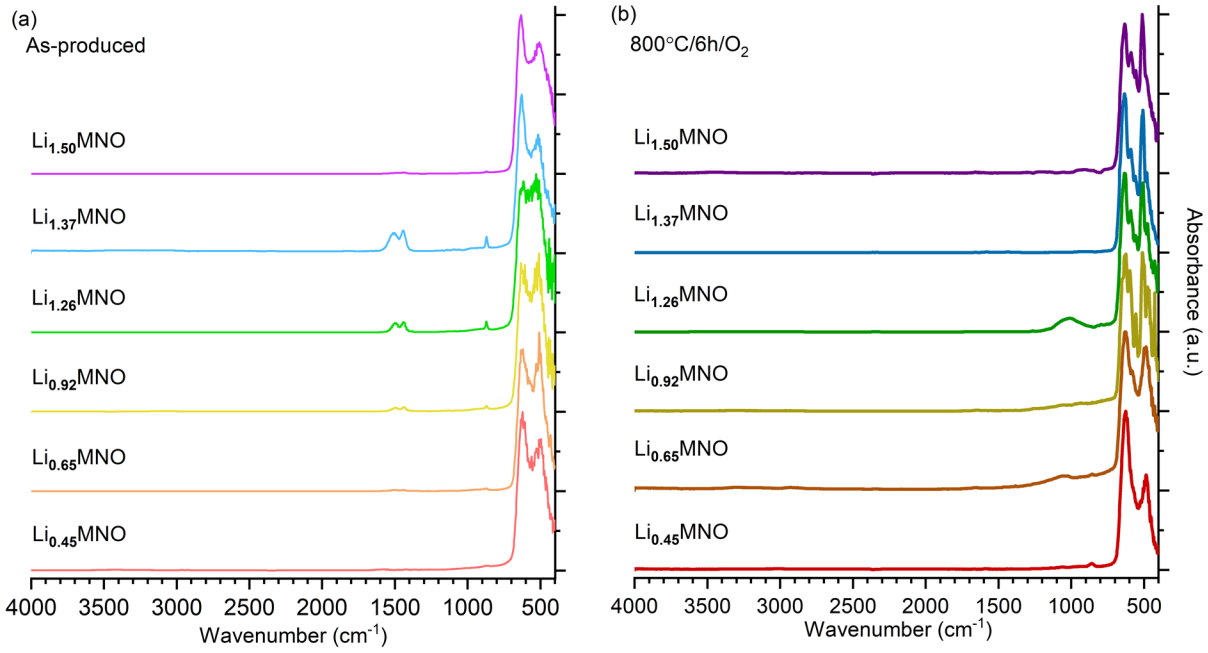

Figure 4.18: FTIR of as-produced (a) and calcined 800˚C/6h/O_2 (b) $Li_{1+x}MNO$ NPs from 400 to 4000 cm^{-1}.

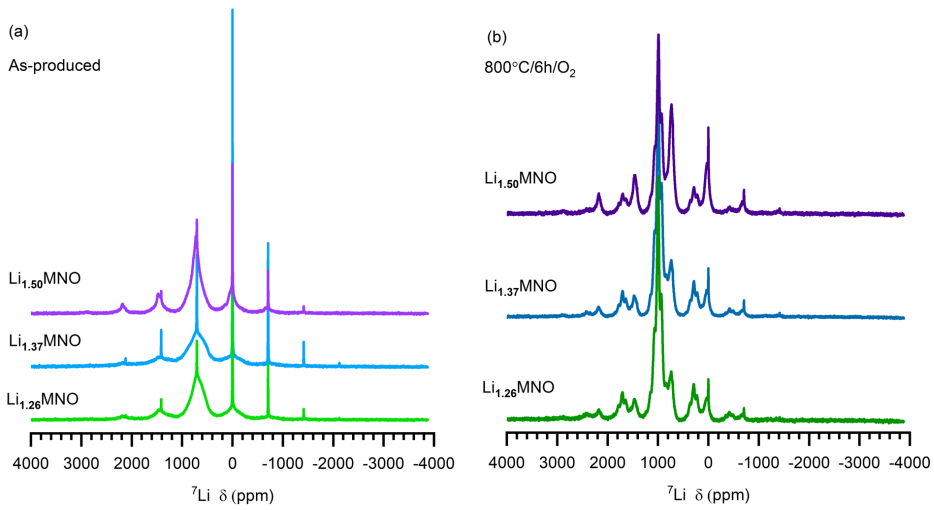

Figure 4.19: ^{7}Li NMR studies on as-produced (a) and calcined (b) $Li_{1.26}$, $Li_{1.37}$, and $Li_{1.50}$MNO NPs.

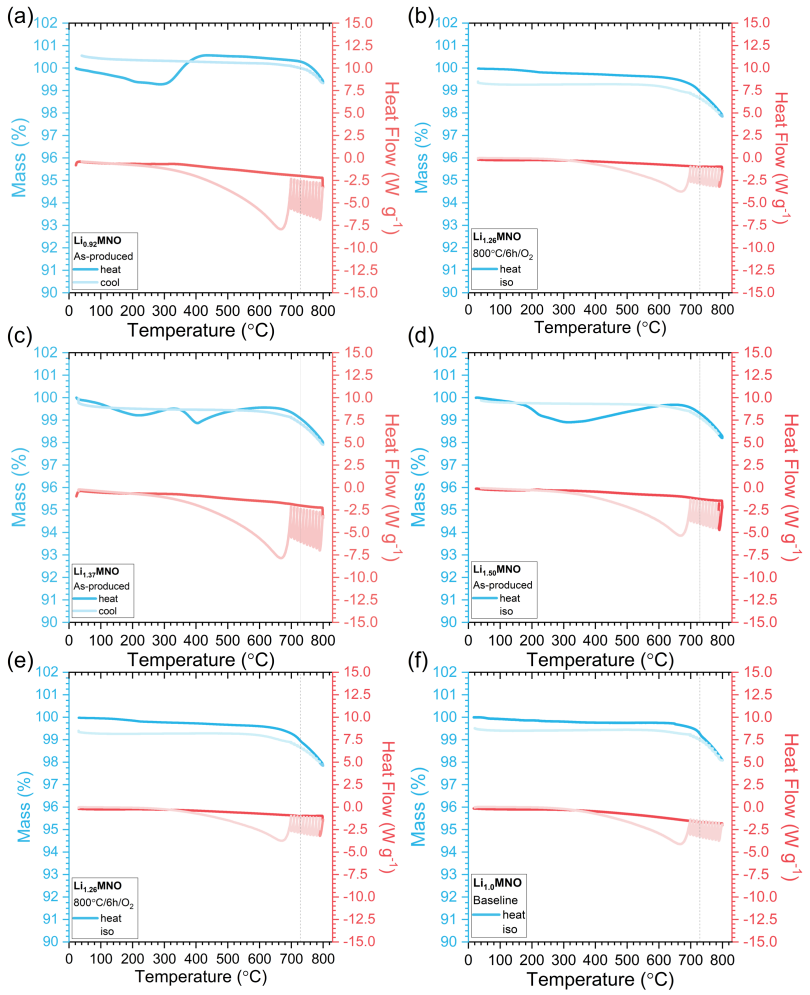

Figure 4.20: TGA-DTA studies for AP $Li_{0.93}$MNO (a), $Li_{1.26}$MNO (b), AP $Li_{1.37}$MNO (c), AP $Li_{1.50}$MNO (d), heated $Li_{1.26}$MNO (e), and Baseline (f). Vertical dashed line shown for T_m of Li_2CO_3.

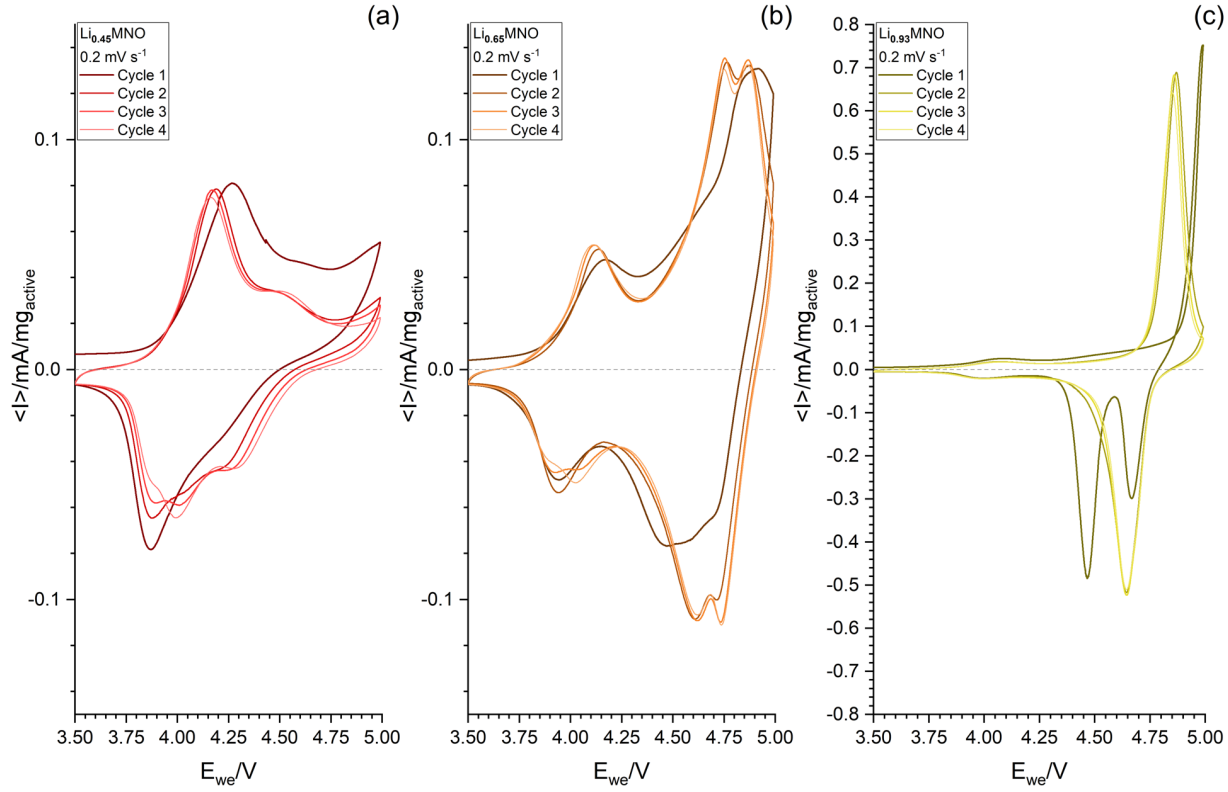

Figure 4.21: CV studies for $Li_{0.45}$ (a), $Li_{0.65}$ (a), and $Li_{0.92}MNO$ (c).

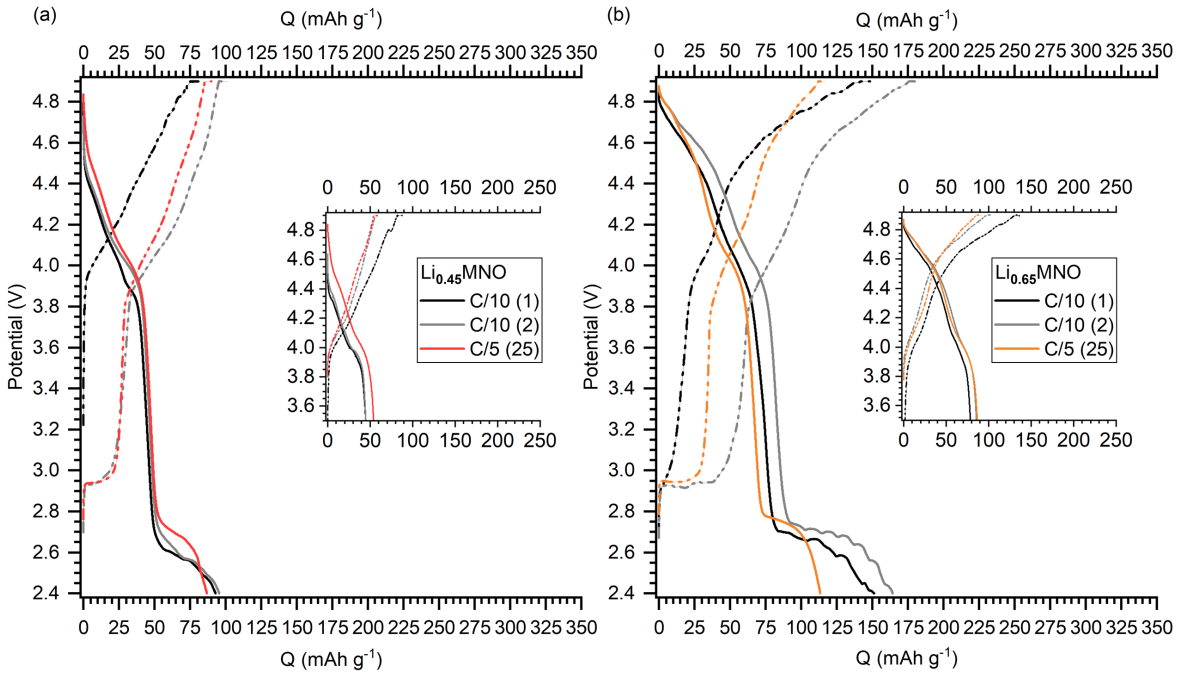

Figure 4.22: GCPL studies for $Li_{0.45}$ (a) and $Li_{0.65}MNO$ (b).

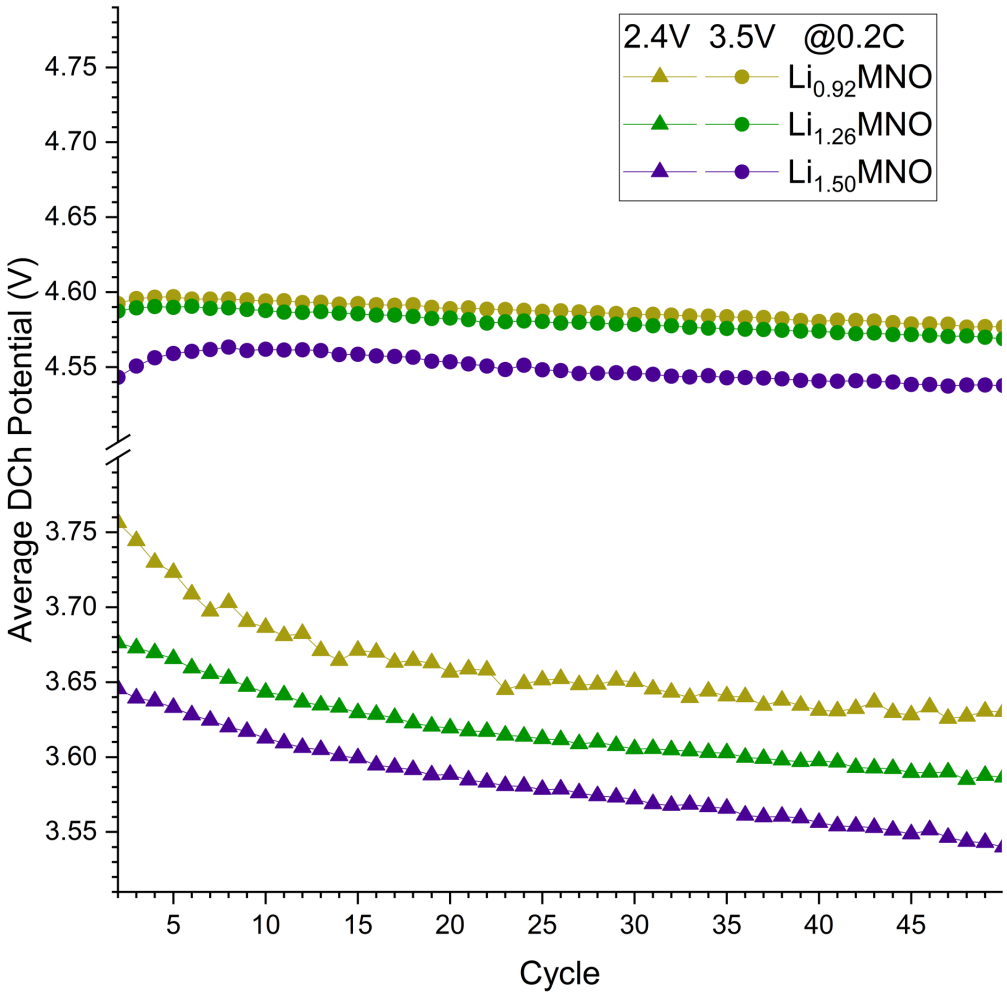

Figure 4.23: Average discharge potential for $Li_{0.92}$, $Li_{1.26}$, $Li_{1.50}$MNO NPs with LCV of 3.5 and 2.4 V.

Table 4.4: LMNO Precursors Molar Ratios and Quantities Dissolved in EtOH.

Sample	Lithium propionate $LiO_2CCH_2CH_3$			Manganese isobutyrate $Mn[O_2CCH(CH_3)_2]_2$			Nickel isobutyrate $Ni[O_2CCH(CH_3)_2]_2$		
	Molar ratio	g	mol	Molar ratio	g	mol	Molar ratio	g	mol
$Li_{0.45}$MNO	1	10.7	0.13	1.5	108.6	0.55	0.5	45.6	0.23
$Li_{0.65}$MNO	1.5	15.8	0.20	1.5	108.6	0.55	0.5	45.6	0.23
$Li_{0.92}$MNO	2	20.7	0.26	1.5	108.6	0.55	0.5	45.6	0.23
$Li_{1.26}$MNO	2.8	29.0	0.36	1.5	108.6	0.55	0.5	45.6	0.23
$Li_{1.37}$MNO	3.1	34.5	0.43	1.5	112.5	0.57	0.5	47.2	0.24
$Li_{1.50}$MNO	3.3	36.7	0.46	1.5	112.5	0.57	0.5	47.2	0.24

Table 4.5: PSA results.

Composition	d10 (μm)	d25 (μm)	d50 (μm)	d75 (μm)	d90 (μm)	d99 (μm)	mean (μm)	mode (μm)
$Li_{0.92}$MNO	0.046	0.054	0.064	0.076	0.094	0.347	0.077	0.061
$Li_{1.26}$MNO	0.047	0.055	0.066	0.084	0.264	0.424	0.102	0.061
$Li_{1.37}$MNO	0.046	0.052	0.061	0.071	0.082	0.102	0.063	0.061
$Li_{1.50}$MNO	0.046	0.053	0.062	0.074	0.088	0.273	0.070	0.063

Table 4.6: Results of Rietveld refinement (AP: as-produced NPs).

Material	Heat Treatment	Crystalline Phase	Space Group (Phase %)	Crystallinity (%)	*a* (Å)	R_{wp}	R_p	R_e	S	C^2
$Li_{0.45}$ MNO	AP	$Li_1Mn_{1.5}Ni_{0.5}O_4$	$Fd\bar{3}m$	8.7	8.3095	6.74	4.00	1.55	4.36	18.97
	800˚C	$Li_{0.3}Mn_{1.5}Ni_{0.5}O_{3.28}$ $Li_{0.5}Mn_{1.5}Ni_{0.5}O_{3.38}$	$Fd\bar{3}m$ (20) $Fd\bar{3}m$ (80)	99.8	8.2938	2.67	2.11	2.03	1.31	1.72
$Li_{0.65}$ MNO	AP	$Li_1Mn_{1.5}Ni_{0.5}O_4$	$Fd\bar{3}m$	99.9	8.3238	5.23	3.34	1.54	3.40	11.56
	800˚C	$Li_{0.5}Mn_{1.5}Ni_{0.5}O_{3.38}$ $Li_{0.7}Mn_{1.5}Ni_{0.5}O_{3.48}$	$Fd\bar{3}m$ (13) $Fd\bar{3}m$ (87)	99.9	8.2482	4.36	3.04	2.00	2.17	4.75
$Li_{0.92}$ MNO	AP	$Li_1Mn_{1.5}Ni_{0.5}O_4$	$Fd\bar{3}m$	99.9	8.2339	4.04	2.67	1.54	2.62	6.89
	800˚C	$Li_{0.7}Mn_{1.5}Ni_{0.5}O_{3.48}$ $Li_1Mn_{1.5}Ni_{0.5}O_4$	$Fd\bar{3}m$ (12) $Fd\bar{3}m$ (88)	99.6	8.1779	3.10	2.36	2.00	1.55	2.39
$Li_{1.26}$ MNO	AP	$Li_1Mn_{1.5}Ni_{0.5}O_4$	$Fd\bar{3}m$	99.9	8.2178	3.65	2.61	1.54	2.36	5.58
	800˚C	$Li_1Mn_{1.5}Ni_{0.5}O_4$ Li_2MnO_3 $Li_{0.51}Ni_{1.16}O_2$	$Fd\bar{3}m$ (77) C2/m (18) R3m (5)	99.7	8.1749	3.45	2.60	2.04	1.69	2.85
$Li_{1.37}$ MNO	AP	$Li_1Mn_{1.5}Ni_{0.5}O_4$	$Fd\bar{3}m$	85.5	8.2127	4.43	2.90	2.00	2.21	4.90
	800˚C	$Li_1Mn_{1.5}Ni_{0.5}O_4$ Li_2MnO_3 $Li_{0.51}Ni_{1.16}O_2$	$Fd\bar{3}m$ (69) C2/m (18) R3m (13)	99.9	8.1726	3.58	2.57	2.03	1.76	3.10
$Li_{1.50}$ MNO	AP	$Li_1Mn_{1.5}Ni_{0.5}O_4$	$Fd\bar{3}m$	96.7	8.2048	3.18	2.30	1.60	1.99	3.94
	800˚C	$Li_1Mn_{1.5}Ni_{0.5}O_4$ Li_2MnO_3 $Li_{0.51}Ni_{1.16}O_2$	$Fd\bar{3}m$ (68) C2/m (25) R3m (7)	99.7	8.1716	2.91	2.24	2.07	1.40	1.97

Table 4.7: Characteristic LMNO FTIR absorption bands [94,95].

Bond Type	Wavenumber (cm^{-1})	Symbol in Figure **4a,b**
Mn-O stretch	619-624	$\clubsuit_{M1}$
Mn-O stretch	557-559	$\clubsuit_{M2}$
Ni^{2+}-O stretch	588-594	$\clubsuit_{N1}$
Ni^{2+}-O stretch	496-500	$\clubsuit_{N2}$

Table 4.8: Disorder approximation via FTIR.

Material	Processing	♣$_{N1}$ Absorbance (a.u.)	♣$_{M1}$ Absorbance (a.u.)	♣$_{N1}$:♣$_{M1}$
$Li_{0.45}MNO$	As-produced	0.770	0.976	0.79
	800˚C	0.630	0.982	0.64
$Li_{0.65}MNO$	As-produced	0.770	0.896	0.86
	800˚C	0.760	0.992	0.77
$Li_{0.92}MNO$	As-produced	0.775	0.891	0.87
	800˚C	0.815	0.978	0.83
$Li_{1.26}MNO$	As-produced	0.872	0.952	0.92
	800˚C	0.764	0.917	0.83
$Li_{1.37}MNO$	As-produced	0.655	0.895	0.73
	800˚C	0.643	0.902	0.71
$Li_{1.50}MNO$	As-produced	0.704	0.926	0.76
	800˚C	0.752	0.934	0.81

References

[1] T.G. Brandt, E. Temeche, A.R. Tuokkola, H. Li, S. Indris, D.A. Edelman, K. Sun, R.M. Laine, A. Materials, D.A. Edelman, R.M. Laine, Nanocomposite Li- and Mn-Rich Spinel Cathodes Characterized with a Green, Aqueous Binder System, Chemical Engineering Journal 479C (2024) 147419. https://doi.org/https://doi.org/10.1016/j.cej.2023.147419.

[2] R.M. Salgado, F. Danzi, J.E. Oliveira, A. El-Azab, P.P. Camanho, M.H. Braga, The latest trends in electric vehicles batteries, Molecules 26 (2021) 1–41. https://doi.org/10.3390/molecules26113188.

[3] M.S.E. Houache, C.H. Yim, Z. Karkar, Y. Abu-Lebdeh, On the Current and Future Outlook of Battery Chemistries for Electric Vehicles—Mini Review, Batteries 8 (2022). https://doi.org/10.3390/batteries8070070.

[4] Y. Miao, P. Hynan, A. Von Jouanne, A. Yokochi, Current li-ion battery technologies in electric vehicles and opportunities for advancements, Energies (Basel) 12 (2019) 1–20. https://doi.org/10.3390/en12061074.

[5] G. Zang, J. Zhang, S. Xu, Y. Xing, Techno-economic analysis of cathode material production using flame-assisted spray pyrolysis, Energy 218 (2021) 119504. https://doi.org/10.1016/j.energy.2020.119504.

[6] M. Wentker, M. Greenwood, J. Leker, A bottom-up approach to lithium-ion battery cost modeling with a focus on cathode active materials, Energies (Basel) 12 (2019) 1–18. https://doi.org/10.3390/en12030504.

[7] M. Wentker, M. Greenwood, M.C. Asaba, J. Leker, A raw material criticality and environmental impact assessment of state-of-the-art and post-lithium-ion cathode technologies, J Energy Storage 26 (2019) 101022. https://doi.org/10.1016/j.est.2019.101022.

[8] W.E. Gent, G.M. Busse, K.Z. House, The predicted persistence of cobalt in lithium-ion batteries, Nat Energy 2 (2022). https://doi.org/10.1038/s41560-022-01129-z.

[9] J. Rumble, ed., CRC Handbook of Chemistry and Physics, 101st ed., CRC Press, 2020.

[10] W. Li, Y.G. Cho, W. Yao, Y. Li, A. Cronk, R. Shimizu, M.A. Schroeder, Y. Fu, F. Zou, V. Battaglia, A. Manthiram, M. Zhang, Y.S. Meng, Enabling high areal capacity for Co-free high voltage spinel materials in next-generation Li-ion batteries, J Power Sources 473 (2020) 228579. https://doi.org/10.1016/j.jpowsour.2020.228579.

[11] D. Andre, S.J. Kim, P. Lamp, S.F. Lux, F. Maglia, O. Paschos, B. Stiaszny, Future generations of cathode materials: An automotive industry perspective, J Mater Chem A Mater 3 (2015) 6709–6732. https://doi.org/10.1039/c5ta00361j.

[12] G. Liu, Y. Du, W. Liu, L. Wen, Study on the action mechanism of doping transitional elements in spinel $LiNi_{0.5}Mn_{1.5}O_4$, Electrochim Acta 209 (2016) 308–314. https://doi.org/10.1016/j.electacta.2016.05.073.

[13] T.A. Arunkumar, A. Manthiram, Influence of chromium doping on the electrochemical performance of the 5 v spinel cathode $LiMn_{1.5}Ni_{0.5}O_4$, Electrochim Acta 50 (2005) 5568–5572. https://doi.org/10.1016/j.electacta.2005.03.033.

[14] Y. Chen, Y. Sun, X. Huang, Origin of the Ni/Mn ordering in high-voltage spinel $LiNi_{0.5}Mn_{1.5}O_4$: The role of oxygen vacancies and cation doping, Comput Mater Sci 115 (2016) 109–116. https://doi.org/10.1016/j.commatsci.2016.01.005.

[15] T. Kocak, L. Wu, J. Wang, U. Savaci, S. Turan, X. Zhang, The effect of vanadium doping on the cycling performance of $LiNi_{0.5}Mn_{1.5}O_4$ spinel cathode for high voltage lithium-ion batteries, Journal of Electroanalytical Chemistry 881 (2021) 114926. https://doi.org/10.1016/j.jelechem.2020.114926.

[16] J. Li, H. Wang, W. Dong, Z. Shi, W. Xie, H. Qiao, Q. Yu, M. Zhang, J. Hu, L. Yang, J. Hong, Phase Transition Dominated High-Rate Performances of the High Voltage $LiNi_{0.5}Mn_{1.5}O_4$ Cathode: Improvement on Structure Evolution and Ionic Diffusivity by Chromium Doping, Journal of Physical Chemistry C 122 (2018) 25229–25236. https://doi.org/10.1021/acs.jpcc.8b09054.

[17] N. Nitta, F. Wu, J. Lee, G.Y.-M. Today, U. 2015, Li-ion battery materials: present and future, Materials Today 18 (2015).

[18] M. Mancini, P. Axmann, G. Gabrielli, M. Kinyanjui, U. Kaiser, M. Wohlfahrt-Mehrens, A High-Voltage and High-Capacity $Li_{1+x}Ni_{0.5}Mn_{1.5}O_4$ Cathode Material: From Synthesis to Full Lithium-Ion Cells, ChemSusChem 9 (2016) 1843–1849. https://doi.org/10.1002/cssc.201600365.

[19] M. Mancini, G. Gabrielli, P. Axmann, M. Wohlfahrt-Mehrens, Electrochemical Performance and Phase Transitions between 1.5 and 4.9 V of Highly-Ordered $LiNi_{0.5}Mn_{1.5}O_4$ with Tailored Morphology: Influence of the Lithiation Method , J Electrochem Soc 164 (2017) A6229–A6235. https://doi.org/10.1149/2.0291701jes.

[20] M. Kunduraci, G.G. Amatucci, Synthesis and Characterization of Nanostructured 4.7 V $Li_xNi_{0.5}Mn_{1.5}O_4$ Spinels for High-Power Lithium-Ion Batteries, J Electrochem Soc 153 (2006) A1345. https://doi.org/10.1149/1.2198110.

[21] S. Dalavi, M. Xu, B. Knight, B.L. Lucht, Effect of added LiBOB on high voltage ($LiNi_{0.5}Mn_{1.5}O_4$) spinel cathodes, Electrochemical and Solid-State Letters 15 (2012) 1–5. https://doi.org/10.1149/2.015202esl.

[22] J. Betz, L. Nowak, J.P. Brinkmann, P. Bärmann, M. Diehl, M. Winter, T. Placke, R. Schmuch, Understanding the impact of calcination time of high-voltage spinel $Li_{1+x}Ni_{0.5}Mn_{1.5}O_4$ on structure and electrochemical behavior, Electrochim Acta 325 (2019). https://doi.org/10.1016/j.electacta.2019.134901.

[23] J. Betz, L. Nowak, M. Winter, T. Placke, R. Schmuch, An Approach for Pre-Lithiation of $Li_{1+x}Ni_{0.5}Mn_{1.5}O_4$ Cathodes Mitigating Active Lithium Loss , J Electrochem Soc 166 (2019) A3531–A3538. https://doi.org/10.1149/2.1221914jes.

[24] R. Wang, X. He, L. He, F. Wang, R. Xiao, L. Gu, H. Li, L. Chen, Atomic structure of Li_2MnO_3 after partial delithiation and re-lithiation, Adv Energy Mater 3 (2013) 1358–1367. https://doi.org/10.1002/aenm.201200842.

[25] G. Gabrielli, M. Marinaro, M. Mancini, P. Axmann, M. Wohlfahrt-Mehrens, A new approach for compensating the irreversible capacity loss of high-energy Si/C|$LiNi_{0.5}Mn_{1.5}O_4$ lithium-ion batteries, J Power Sources 351 (2017) 35–44. https://doi.org/10.1016/j.jpowsour.2017.03.051.

[26] O.A. Drozhzhin, A.M. Alekseeva, V.A. Shevchenko, D. Chernyshov, A.M. Abakumov, E. V. Antipov, Phase transitions in the "spinel-layered" $Li_{1+x}Ni_{0.5}Mn_{1.5}O_4$ (x = 0, 0.5, 1) cathodes upon (de)lithiation studied with operando synchrotron x-ray powder diffraction, Nanomaterials 11 (2021) 1–12. https://doi.org/10.3390/nano11061368.

[27] J. Xiao, X. Chen, P. V. Sushko, M.L. Sushko, L. Kovarik, J. Feng, Z. Deng, J. Zheng, G.L. Graff, Z. Nie, D. Choi, J. Liu, J.G. Zhang, M.S. Whittingham, High-performance $LiNi_{0.5}Mn_{1.5}O_4$ Spinel controlled by Mn^{3+} concentration and site disorder, Advanced Materials 24 (2012) 2109–2116. https://doi.org/10.1002/adma.201104767.

[28] R. Amin, I. Belharouk, Part I: Electronic and ionic transport properties of the ordered and disordered $LiNi_{0.5}Mn_{1.5}O_4$ spinel cathode, J Power Sources 348 (2017) 311–317. https://doi.org/10.1016/j.jpowsour.2017.02.071.

[29] J. Yang, X. Han, X. Zhang, F. Cheng, J. Chen, Spinel $LiNi_{0.5}Mn_{1.5}O_4$ cathode for rechargeable lithiumion batteries: Nano vs micro, ordered phase (P4332) vs disordered phase ($Fd\bar{3}m$), Nano Res 6 (2013) 679–687. https://doi.org/10.1007/s12274-013-0343-5.

[30] P.J. Phillips, J. Bareño, Y. Li, D.P. Abraham, R.F. Klie, On the Localized Nature of the Structural Transformations of Li_2MnO_3 Following Electrochemical Cycling, Adv Energy Mater 5 (2015) 1–12. https://doi.org/10.1002/aenm.201501252.

[31] X. Dong, Y. Xu, S. Yan, S. Mao, L. Xiong, X. Sun, Towards low-cost, high energy density Li_2MnO_3 cathode materials, J Mater Chem A Mater 3 (2015) 670–679. https://doi.org/10.1039/c4ta02924k.

[32] P.K. Nayak, E. Levi, J. Grinblat, M. Levi, B. Markovsky, N. Munichandraiah, Y.K. Sun, D. Aurbach, High-Capacity Layered-Spinel Cathodes for Li-Ion Batteries, ChemSusChem 9 (2016) 2404–2413. https://doi.org/10.1002/cssc.201600576.

[33] R. Benedek, Role of Disproportionation in the Dissolution of Mn from Lithium Manganate Spinel, Journal of Physical Chemistry C 121 (2017) 22049–22053. https://doi.org/10.1021/acs.jpcc.7b05940.

[34] M. Yu, T.G. Brandt, E. Temeche, R.M. Laine, Stabilizing High-Voltage Cathodes via Ball-Mill Coating with Flame-Made Nanopowder Electrolytes, ACS Appl Mater Interfaces 14 (2022) 49617–49632. https://doi.org/10.1021/acsami.2c09284.

[35] X. Fan, C. Wang, High-voltage liquid electrolytes for Li batteries: Progress and perspectives, Chem Soc Rev 50 (2021) 10486–10566. https://doi.org/10.1039/d1cs00450f.
[36] S. Zhang, N.S. Andreas, R. Li, N. Zhang, C. Sun, D. Lu, T. Gao, L. Chen, X. Fan, Mitigating irreversible capacity loss for higher-energy lithium batteries, Energy Storage Mater 48 (2022) 44–73. https://doi.org/10.1016/j.ensm.2022.03.004.
[37] S.W. Lee, H.W. Lee, I. Ryu, W.D. Nix, H. Gao, Y. Cui, Kinetics and fracture resistance of lithiated silicon nanostructure pairs controlled by their mechanical interaction, Nat Commun 6 (2015) 1–7. https://doi.org/10.1038/ncomms8533.
[38] S. Kuppan, A. Jarry, R. Kostecki, G. Chen, A study of room temperature $Li_xNi_{0.5}Mn_{1.5}O_4$ solid solutions, Sci Rep 5 (2015) 1–11. https://doi.org/10.1038/srep08027.
[39] S. Kuppan, Y. Xu, Y. Liu, G. Chen, Phase transformation mechanism in lithium manganese nickel oxide revealed by single-crystal hard X-ray microscopy, Nat Commun 8 (2017). https://doi.org/10.1038/ncomms14309.
[40] G.T. Park, D.R. Yoon, U.H. Kim, B. Namkoong, J. Lee, M.M. Wang, A.C. Lee, X.W. Gu, W.C. Chueh, C.S. Yoon, Y.K. Sun, Ultrafine-grained Ni-rich layered cathode for advanced Li-ion batteries, Energy Environ Sci 14 (2021) 6616–6626. https://doi.org/10.1039/d1ee02898g.
[41] Q. Tian, Z. Zhang, L. Yang, Y. Xiang, Improving the lithium storage properties of $Li_4Ti_5O_{12}$ anodes by facile two-phase formation and nanostructure engineering strategy, J Alloys Compd 705 (2017) 638–644. https://doi.org/10.1016/j.jallcom.2017.02.175.
[42] C. Julien, A. Mauger, K. Zaghib, H. Groult, Optimization of layered cathode materials for lithium-ion batteries, Materials 9 (2016). https://doi.org/10.3390/MA9070595.
[43] P. Axmann, G. Gabrielli, M. Wohlfahrt-Mehrens, Tailoring high-voltage and high-performance $LiNi_{0.5}Mn_{1.5}O_4$ cathode material for high energy lithium-ion batteries, J Power Sources 301 (2016) 151–159. https://doi.org/10.1016/j.jpowsour.2015.10.010.
[44] H. Duncan, B. Hai, M. Leskes, C.P. Grey, G. Chen, Relationships between Mn^{3+} content, structural ordering, phase transformation, and kinetic properties in $LiNi_xMn_{2-x}O_4$ cathode materials, Chemistry of Materials 26 (2014) 5374–5382. https://doi.org/10.1021/cm502607v.
[45] J. Feng, Z. Huang, C. Guo, N.A. Chernova, S. Upreti, M.S. Whittingham, An organic coprecipitation route to synthesize high voltage $LiNi_{0.5}Mn_{1.5}O_4$, ACS Appl Mater Interfaces 5 (2013) 10227–10232. https://doi.org/10.1021/am4029526.
[46] S. Kumar, J.A. Azurdia, R.M. Laine, Synthesis of $(MgO)_x(Fe2O3)_{1-x}$ nanoparticles via liquid feed flame spray pyrolysis. A non-stoichiometric spinel phase outside the normal phase diagram, Journal of Ceramic Processing Research 11 (2010) 517–522.
[47] E. Temeche, S. Indris, R.M. Laine, $LiAlO_2/LiAl_5O_8$ Membranes Derived from Flame-Synthesized Nanopowders as a Potential Electrolyte and Coating Material for All-Solid-State Batteries, ACS Appl Mater Interfaces 12 (2020) 46119–46131. https://doi.org/10.1021/acsami.0c13021.

[48] E. Yi, W. Wang, J. Kieffer, R.M. Laine, Flame made nanoparticles permit processing of dense, flexible, Li^+ conducting ceramic electrolyte thin films of cubic- $Li_7La_3Zr_2O_{12}$ (c-LLZO), J Mater Chem A Mater 4 (2016) 12947–12954. https://doi.org/10.1039/c6ta04492a.

[49] K. Saito, E. Yi, R.M. Laine, Y. Sugahara, Preparation of Nb-doped TiO2 nanopowder by liquid-feed spray pyrolysis followed by ammonia annealing for tunable visible-light absorption and inhibition of photocatalytic activity, Ceram Int 46 (2020) 1314–1322. https://doi.org/10.1016/j.ceramint.2019.09.094.

[50] E. Yi, W. Wang, J. Kieffer, R.M. Laine, Key parameters governing the densification of cubic- $Li_7La_3Zr_2O_{12}$ Li^+ conductors, J Power Sources (2017). https://doi.org/10.1016/j.jpowsour.2017.03.126.

[51] W. Wang, E. Yi, A.J. Fici, R.M. Laine, J. Kieffer, Lithium Ion Conducting Poly(ethylene oxide)-Based Solid Electrolytes Containing Active or Passive Ceramic Nanoparticles, Journal of Physical Chemistry C 121 (2017) 2563–2573. https://doi.org/10.1021/acs.jpcc.6b11136.

[52] S. Liu, C. Zhou, Y. Wang, W. Wang, Y. Pei, J. Kieffer, R.M. Laine, Ce-Substituted Nanograin $Na_3Zr_2Si_2PO_{12}$ Prepared by LF-FSP as Sodium-Ion Conductors, ACS Appl Mater Interfaces (2020). https://doi.org/10.1021/acsami.9b11995.

[53] E. Yi, W. Wang, S. Mohanty, J. Kieffer, R. Tamaki, R.M. Laine, Materials that can replace liquid electrolytes in Li batteries: Superionic conductivities in $Li_{1.7}Al_{0.3}Ti_{1.7}Si_{0.4}P_{2.6}O_{12}$. Processing combustion synthesized nanopowders to free standing thin films, J Power Sources 269 (2014) 577–588. https://doi.org/10.1016/j.jpowsour.2014.07.029.

[54] E. Temeche, E. Buch, X. Zhang, T. Brandt, A. Hintennach, R.M. Laine, Improved Electrochemical Properties of $Li_4Ti_5O_{12}$Nanopowders (NPs) via Addition of $LiAlO_2$and Li_6SiON Polymer Electrolytes, Derived from Agricultural Waste, ACS Appl Energy Mater 4 (2021) 1894–1905. https://doi.org/10.1021/acsaem.0c02994.

[55] E. Temeche, E. Yi, V. Keshishian, J. Kieffer, R.M. Laine, Liquid-feed flame spray pyrolysis derived nanopowders (NPs) as a route to electrically conducting calcium aluminate ($12CaO.7Al_2O_3$) films, J Eur Ceram Soc (2019). https://doi.org/10.1016/j.jeurceramsoc.2018.11.051.

[56] E. Yi, E. Temeche, R.M. Laine, Superionically conducting beta"-Al_2O_3 thin films processed using flame synthesized nanopowders, J Mater Chem A Mater 6 (2018) 12411–12419. https://doi.org/10.1039/c8ta02907e.

[57] T.G. Brandt, A.R. Tuokkola, M. Yu, R.M. Laine, Liquid-feed flame spray pyrolysis enabled synthesis of Co- and Cr-free, high-entropy spinel oxides as Li-ion anodes, Chemical Engineering Journal 474 (2023) 145495. https://doi.org/10.1016/j.cej.2023.145495.

[58] H. Mohammadi, M. Khosravi, S.M. Jafari, Lithium cobalt oxide as lithium ion battery cathode materials prepared by flame spray pyrolysis method, Analytical and Bioanalytical Electrochemistry 10 (2018) 1–17.

[59] O. Waser, R. Büchel, A. Hintennach, P. Novák, S.E. Pratsinis, Continuous flame aerosol synthesis of carbon-coated nano-$LiFePO_4$ for Li-ion batteries, J Aerosol Sci 42 (2011) 657–667. https://doi.org/10.1016/j.jaerosci.2011.06.003.

[60] N.A. Hamid, S. Wennig, S. Hardt, A. Heinzel, C. Schulz, H. Wiggers, High-capacity cathodes for lithium-ion batteries from nanostructured $LiFePO_4$ synthesized by highly-flexible and scalable flame spray pyrolysis, J Power Sources 216 (2012) 76–83. https://doi.org/10.1016/j.jpowsour.2012.05.047.

[61] J. Zhang, S. Xu, K.I. Hamad, A.M. Jasim, Y. Xing, High retention rate NCA cathode powders from spray drying and flame assisted spray pyrolysis using glycerol as the solvent, Powder Technol 363 (2020) 1–6. https://doi.org/10.1016/j.powtec.2019.12.057.

[62] X. Zhang, H. Zheng, V. Battaglia, R.L. Axelbaum, Electrochemical performance of spinel $LiMn_2O_4$ cathode materials made by flame-assisted spray technology, J Power Sources 196 (2011) 3640–3645. https://doi.org/10.1016/j.jpowsour.2010.07.008.

[63] Y. Liang, K. Ku, Y. Lin, L. Yu, J. Wen, E. Lee, J. Libera, J. Lu, Process Engineering to Increase the Layered Phase Concentration in the Immediate Products of Flame Spray Pyrolysis, ACS Appl Mater Interfaces 13 (2021) 26915–26923. https://doi.org/10.1021/acsami.1c03930.

[64] R. Strobel, S.E. Pratsinis, Flame aerosol synthesis of smart nanostructured materials, J Mater Chem 17 (2007) 4743–4756. https://doi.org/10.1039/b711652g.

[65] W.Y. Teoh, R. Amal, L. Mädler, Flame spray pyrolysis: An enabling technology for nanoparticles design and fabrication, Nanoscale 2 (2010) 1324–1347. https://doi.org/10.1039/c0nr00017e.

[66] K. Wegner, B. Schimmoeller, B. Thiebaut, C. Fernandez, T.N. Rao, Pilot plants for industrial nanoparticle production by flame spray pyrolysis, KONA Powder and Particle Journal 29 (2011) 251–265. https://doi.org/10.14356/kona.2011025.

[67] H.W. Choi, S.J. Kim, Y.H. Rim, Y.S. Yang, Effect of Lithium Deficiency on Lithium-Ion Battery Cathode $Li_xNi_{0.5}Mn_{1.5}O_4$, Journal of Physical Chemistry C 119 (2015) 27192–27199. https://doi.org/10.1021/acs.jpcc.5b06501.

[68] G. Lim, D. Shin, K.H. Chae, M.K. Cho, C. Kim, S.S. Sohn, M. Lee, J. Hong, Regulating Dynamic Electrochemical Interface of $LiNi_{0.5}Mn_{1.5}O_4$ Spinel Cathode for Realizing Simultaneous Mn and Ni Redox in Rechargeable Lithium Batteries, Adv Energy Mater 12 (2022). https://doi.org/10.1002/aenm.202202049.

[69] C.P. Shih, M. Krajewski, P. Hasin, C.H. Chen, C.Y. Lee, J.Y. Lin, Spray-drying synthesis of fluorine-doped $LiNi_{0.5}Mn_{1.5}O_4$ as high-voltage cathodes for lithium-ion batteries, J Alloys Compd 932 (2023) 167641. https://doi.org/10.1016/j.jallcom.2022.167641.

[70] C.P. Grey, N. Dupré, NMR studies of cathode materials for lithium-ion rechargeable batteries, Chem Rev 104 (2004) 4493–4512. https://doi.org/10.1021/cr020734p.

[71] K. Shimoda, M. Murakami, H. Komatsu, H. Arai, Y. Uchimoto, Z. Ogumi, Delithiation/lithiation behavior of $LiNi_{0.5}Mn_{1.5}O_4$ studied by in situ and ex situ 6,7Li

NMR spectroscopy, Journal of Physical Chemistry C 119 (2015) 13472–13480. https://doi.org/10.1021/acs.jpcc.5b03273.

[72] M. Fehse, N. Etxebarria, L. Otaegui, M. Cabello, S. Mart, M. Angeles, I. Monterrubio, C.F. Elkjær, O. Fabelo, N.A. Enkubari, J. Miguel, M. Casas-cabanas, M. Reynaud, Influence of Transition-Metal Order on the Reaction Mechanism of LNMO Cathode Spinel : An Operando X - ray Absorption Spectroscopy Study, (2022). https://doi.org/10.1021/acs.chemmater.2c01360.

[73] J. Cabana, F.O. Omenya, N.A. Chernova, D. Zeng, M.S. Whittingham, C.P. Grey, Composition-Structure Relationships in the Li-Ion Battery Electrode Material $LiNi_{0.5}Mn_{1.5}O_4$, Chemistry of Materials 24 (2012) 2952–2964.

[74] M. Yavuz, N. Kiziltas-Yavuz, A. Bhaskar, M. Scheuermann, S. Indris, F. Fauth, M. Knapp, H. Ehrenberg, Influence of iron on the structural evolution of $LiNi_{0.4}Fe_{0.2}Mn_{1.4}O_4$ during electrochemical cycling investigated by in situ powder diffraction and spectroscopic methods, Z Anorg Allg Chem 640 (2014) 3118–3126. https://doi.org/10.1002/zaac.201400247.

[75] W. Hua, S. Wang, M. Knapp, S.J. Leake, A. Senyshyn, C. Richter, M. Yavuz, J.R. Binder, C.P. Grey, H. Ehrenberg, S. Indris, B. Schwarz, Structural insights into the formation and voltage degradation of lithium- and manganese-rich layered oxides, Nat Commun 10 (2019) 1–11. https://doi.org/10.1038/s41467-019-13240-z.

[76] J. Lee, N. Dupre, M. Avdeev, B. Kang, Understanding the cation ordering transition in high-voltage spinel $LiNi_{0.5}Mn_{1.5}O_4$ by doping Li instead of Ni, Sci Rep 7 (2017) 1–12. https://doi.org/10.1038/s41598-017-07139-2.

[77] H.W. Choi, S.J. Kim, M.Y. Jeong, S. Lee, Y.H. Rim, Y.S. Yang, Temperature-dependent oxygen behavior of $Li_xNi_{0.5}Mn_{1.5}O_4$ cathode material for lithium battery, APL Mater 4 (2016) 0–7. https://doi.org/10.1063/1.4968566.

[78] L. Lin, K. Qin, M. Li, Y. sheng Hu, H. Li, X. Huang, L. Chen, L. Suo, Spinel-related $Li_2Ni_{0.5}Mn_{1.5}O_4$ cathode for 5-V anode-free lithium metal batteries, Energy Storage Mater 45 (2022) 821–827. https://doi.org/10.1016/j.ensm.2021.12.036.

[79] Y. Hao, W. Liu, Q. Zhang, X. Wang, H. Yang, L. Kou, Z. Tian, L. Shao, H. Maleki Kheimeh Sari, J. Wang, H. Shan, X. Li, Optimized activation of Li_2MnO_3 effectively boosting rate capability of $xLi_2MnO_3 \cdot (1\text{-}x)LiMO_2$ cathode, Nano Energy 88 (2021). https://doi.org/10.1016/j.nanoen.2021.106240.

[80] J. Zheng, S. Myeong, W. Cho, P. Yan, J. Xiao, C. Wang, J. Cho, J.G. Zhang, Li- and Mn-Rich Cathode Materials: Challenges to Commercialization, Adv Energy Mater 7 (2017). https://doi.org/10.1002/aenm.201601284.

[81] T. Zhang, J.T. Li, J. Liu, Y.P. Deng, Z.G. Wu, Z.W. Yin, D. Guo, L. Huang, S.G. Sun, Suppressing the voltage-fading of layered lithium-rich cathode materials via an aqueous binder for Li-ion batteries, Chemical Communications 52 (2016) 4683–4686. https://doi.org/10.1039/c5cc10534j.

[82] Z. Wang, N. Dupré, A.C. Gaillot, B. Lestriez, J.F. Martin, L. Daniel, S. Patoux, D. Guyomard, CMC as a binder in $LiNi_{0.4}Mn_{1.6}O_4$ 5 v cathodes and their electrochemical performance for Li-ion batteries, Electrochim Acta 62 (2012) 77–83. https://doi.org/10.1016/j.electacta.2011.11.094.

[83] G.D. Salian, J. Højberg, C. Fink Elkjær, Y. Tesfamhret, G. Hernández, M.J. Lacey, R. Younesi, Investigation of Water-Soluble Binders for $LiNi_{0.5}Mn_{1.5}O_4$-Based Full Cells, ChemistryOpen 11 (2022) 1–8. https://doi.org/10.1002/open.202200065.

[84] I. Doberdò, N. Löffler, N. Laszczynski, D. Cericola, N. Penazzi, S. Bodoardo, G.T. Kim, S. Passerini, Enabling aqueous binders for lithium battery cathodes - Carbon coating of aluminum current collector, J Power Sources 248 (2014) 1000–1006. https://doi.org/10.1016/j.jpowsour.2013.10.039.

[85] N. Yabuuchi, Y. Kinoshita, K. Misaki, T. Matsuyama, S. Komaba, Electrochemical Properties of $LiCoO_2$ Electrodes with Latex Binders on High-Voltage Exposure , J Electrochem Soc 162 (2015) A538–A544. https://doi.org/10.1149/2.0151504jes.

[86] A. Brilloni, F. Marchesini, F. Poli, E. Petri, F. Soavi, Performance Comparison of LMNO Cathodes Produced with Pullulan or PEDOT:PSS Water-Processable Binders, Energies (Basel) 15 (2022). https://doi.org/10.3390/en15072608.

[87] S. Hitomi, K. Kubota, T. Horiba, K. Hida, T. Matsuyama, H. Oji, S. Yasuno, S. Komaba, Application of Acrylic-Rubber-Based Latex Binder to High-Voltage Spinel Electrodes of Lithium-Ion Batteries, ChemElectroChem 6 (2019) 5070–5079. https://doi.org/10.1002/celc.201901227.

[88] T. Zhao, Y. Meng, R. Ji, F. Wu, L. Li, R. Chen, Maintaining structure and voltage stability of Li-rich cathode materials by green water-soluble binders containing Na+ ions, J Alloys Compd 811 (2019). https://doi.org/10.1016/j.jallcom.2019.152060.

[89] European Commission, Restrictions Roadmap under the Chemicals Strategy for Sustainability, 2022. https://ec.europa.eu/docsroom/documents/49734%0Ahttps://ec.europa.eu/docsroom/documents/38861.

[90] M. Freedhoff, n-Methylpyrrolidone (NMP); Revision to Toxic Substances Control Act (TSCA) Risk Determination; Notice of Availability, Fed Regist 87 (2022) 212–223. https://doi.org/10.4135/9781483346526.n193.

[91] F. Duffner, L. Mauler, M. Wentker, J. Leker, M. Winter, Large-scale automotive battery cell manufacturing: Analyzing strategic and operational effects on manufacturing costs, Int J Prod Econ 232 (2021) 107982. https://doi.org/10.1016/j.ijpe.2020.107982.

[92] S. Radloff, R.-G. Scurtu, M. Hölzle, M. Wohlfahrt-Mehrens, Applying Established Water-Based Binders to Aqueous Processing of $LiNi_{0.83}Co_{0.12}Mn_{0.05}O_2$ Positive Electrodes , J Electrochem Soc 168 (2021) 100506. https://doi.org/10.1149/1945-7111/ac2861.

[93] E. Arca, G.M. Veith, R. Satish, T. Lin, G. Teeter, R. Kostecki, Understanding the Origin of the Nonpassivating Behavior of Si-Based Anodes during the Initial Cycles, Journal of Physical Chemistry C 126 (2022) 14058–14066. https://doi.org/10.1021/acs.jpcc.2c02976.

[94] M. Kunduraci, G.G. Amatucci, Synthesis and Characterization of Nanostructured 4.7 V $Li_xNi_{0.5}Mn_{1.5}O_4$ Spinels for High-Power Lithium-Ion Batteries, J Electrochem Soc 153 (2006) A1345. https://doi.org/10.1149/1.2198110.

[95] H. Duncan, B. Hai, M. Leskes, C.P. Grey, G. Chen, Relationships between Mn^{3+} content, structural ordering, phase transformation, and kinetic properties in LiNixMn2-xO4 cathode materials, Chemistry of Materials 26 (2014) 5374–5382. https://doi.org/10.1021/cm502607v.

Chapter 5 Liquid-Feed Flame Spray Pyrolysis Enabled Synthesis of $Li(TM)PO_4$ (TM=Fe, Mn, Ni) Nanopowders via Metalloorganic Precursors as Li-Ion Cathodes.

5.1 Summary

A major driving force in both industry and academia mandates improving battery materials based both on performance and/or cost. Therefore, the use of abundant, inexpensive elements such as Fe and Mn, in lieu of Co and/or Ni, in high-throughput syntheses can maximize cost savings for cathodes and, subsequently, energy storage. To this end, we examine the electrochemical performance of LFP, a well-studied cathode material, and LFP-type materials synthesized using an alternative, scalable method – using metal carboxylate precursors via liquid feed-flame spray pyrolysis (LF-FSP).

Herein, we report the synthesis and characterization of four $LiTMPO_4$ (TM = Fe, Mn, and/or Ni) NPs with varying degrees of Fe substitution: $LiFePO_4$, $LiMn_{1/3}Fe_{2/3}PO_4$, $LiMn_{2/3}Fe_{1/3}PO_4$, and $LiNi_{1/3}Mn_{1/3}Fe_{1/3}PO_4$. All materials were characterized as to morphological, structural, and spectroscopic techniques revealing successful synthesis of target materials. All synthesized materials showed the target olivine phase Pnma via XRD with APS 100 nm via PSA. The as-produced materials are primarily amorphous per XRD and FTIR; however, the target crystalline phase is obtained after calcination at 700˚C. Electrochemical studies including CV and GCPL demonstrate typical capacity and retention over a range of C-rates from 0.1 to 1.0C. An increase in practical energy density was obtained with 1/3 Mn substitution ($LiMn_{1/3}Fe_{2/3}PO_4$) compared to LFP (491±9 vs 464±3 Wh kg^{-1} at 1.0C), while maintaining excellent capacity retention after 100 cycles (~96%).

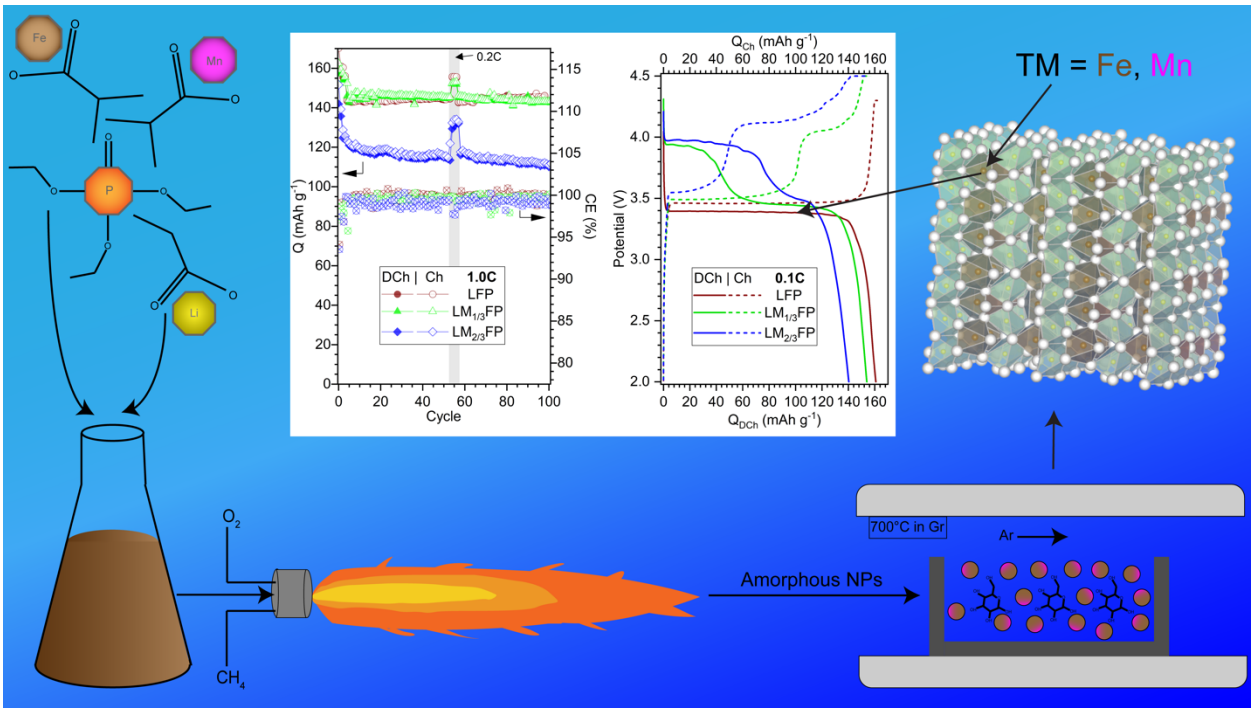

Figure 5.1: Graphical Abstract describing synthesis to characterization process for LMFP NPs.

5.2 Introduction

Lithium iron phosphate $Li_1Fe_1PO_4$ (LFP) is one of the foundational cathode materials for Li-ion batteries (LIBs) enabling global electrification due to desirable material and electrochemical properties. Alongside electrification, there is a global effort to reduce expensive (cost, resources, labor) minerals use in cathode active materials (CAMs), namely Co and Ni. In that regard, Co- and Ni-free CAMs are now attracting more attention due to their advantages reflected in the raw material costs and/or labor ethics compared to materials such as $LiCoO_2$ (LCO) and $LiNi_{0.6}Mn_{0.2}Co_{0.2}O_2$ (NMC622). Mn and Fe based cathodes are the primary target transition metals for low-cost LIB cathodes compared to Ni and Co [1,2]. When considering electrochemical performance, the effective cost difference between LFP and NMC622 or LCO – while highly dependent on a fluctuating global market – can be several orders of magnitude lower [2–5].

As a result of the atomic structure, polyanion phosphate cathodes benefit from stable de/lithiation due to strong P-O covalent bonding in addition to 1D Li diffusion channels [6–10]. LFP offers a specific capacity of 170 mAh g^{-1} competitive with other cathode materials such as NMC622 (~275 mAh g^{-1}); however, its relatively low redox potential (3.4 V vs. Li/Li^+) results in low energy density (≈580 Wh kg^{-1}) [6,9,10]. Substituting Fe with transition metal(s) (i.e. Mn) can increase average redox potentials, therefore increasing energy densities [6,9–15]. In particular, complete substitution for Fe, $LiMnPO_4$ (LMP), increases working potential to ~4.1 V vs. Li/Li^+ and has a theoretical energy density of 697 Wh kg^{-1} [6,9–15]. Introducing Ni in the CAM would further increase the working potential to 5.1 V vs. Li/Li^+, and complete substitution, $LiNiPO_4$, results in a high energy density of 800 Wh kg^{-1} [16].

However, LMP suffers from Jahn-Teller distortion promoted disproportionation of $2Mn^{3+}$ to Mn^{4+} and Mn^{2+} with subsequent Mn^{2+} dissolution, reducing practical capacity and stability [9,17]. Jahn-Teller distortion can result in the elongation of Mn-O bonds that edge share with PO_4 tetrahedrons, which results in an increase in activation energy of carrier migration [8,9,17]. Ultimately, the distorted Mn-O bonds reduce the intrinsic kinetic abilities of LMP. Additionally, there is significant volume change between the (de)lithiated states, ~10%, which results in cycling instability due to mechanical stresses in the cathode [18]. Partial Mn substitution in LFP can minimize LMP stability issues while increasing practical energy densities, all while maintaining a low cost profile. $LiMn_{1-x}Fe_xPO_4$ (LMFP) forms a solid solution for x=0-1 offering a wide range of compositions for any given set of target parameters such as energy density vs. cyclability. Both LFP (10^{-6} to 10^{-10} S cm^{-1}) and LMP (10^{-9} S cm^{-1}) suffer from poor electronic conductivity; typically alleviated via carbon coating [18–25].

Another important method of improving the conductivity of cathode materials is to decrease average particle sizes (APS) to nanoscale, i.e. nanopowders (NPs) [26–28]. Increased interfacial contact areas between active material and electrolyte provides more Li^+ diffusion pathways and potential for rapid Li^+ diffusion in (discharge) and out (charge) of the active material [29–32]. In principle, high specific surface areas (SSAs) should lead to superior charge transfer kinetics and shorter Li^+ diffusion paths on average. Characteristic migration times, for Li^+ within the interior of a cathode particle during intercalation, can be derived from Fick's law; Equation 10 [33]:

$$\tau = \frac{L^2}{4\pi D^*} \tag{10}$$

Here τ is the characteristic time (or Li^+ migration time), L is the diffusion length, and D^* is the diffusion coefficient of Li^+ in the host lattice. The decrease in characteristic time from micro- to nanoparticles can be as much as a factor of 10^6 [33]. Greater access to Li^+ should lead, in theory, to higher capacity at higher C-rates and subsequently higher power [33]. It is important to note that increased interfacial contact area between CAM and electrolyte will inevitably lead to increased SEI formation, which may negate some or all of the potential improvements anticipated using NP CAMs.

Ideal particle morphology will minimize the distance required for Li^+ diffusion, and with this consideration NPs are preferred over analogous micron-sized particles. LFP, LMFP, and LMP have been synthesized previously using common methods including coprecipitation, sol-gel and hydro/solvothermal processing, and solid-state reaction [6,7,17]. There are select examples of flame spray pyrolysis (FSP) synthesized cathode materials such as LFP; however, LF-FSP has not been explored extensively as a method for the synthesis of CAMs [34–38]. Detailed LF-FSP procedures have been reported previously [1,39–48]. In brief, LF-FSP offers the benefits of controlled morphology, phase purity, high yield, and relatively low cost while reaching kg h^{-1} in a

continuous, commercial scale process [41,48–51]. Compared to other aerosol technologies such as FSP, LF-FSP offers the benefit of synthesis without HCl byproduct [51].

Previous studies on NP syntheses via liquid-feed flame spray pyrolysis (LF-FSP) demonstrated phase pure, unaggregated oxide NPs (APS < 100 nm) with promising applications such as solid electrolytes, CAMs, and anode active materials [1,39–48,52,53]. Herein we report the synthesis and characterization of LFP-type materials by LF-FSP with varying ratios of Fe:Mn ($LiFePO_4$, $LiMn_{1/3}Fe_{2/3}PO_4$, and $LiMn_{2/3}Fe_{1/3}PO_4$) and with the addition of Ni ($LiNi_{1/3}Mn_{1/3}Fe_{1/3}PO_4$). Material characterization studies including morphological, structural, and spectroscopic techniques reveal successful syntheses of the target materials. Electrochemical performance of synthesized materials was demonstrated in half-cell format with varying C-rates. An increase in practical energy density was obtained with 1/3 Mn substitution ($LiMn_{1/3}Fe_{2/3}PO_4$) compared to LFP, 491±9 vs 464±3 Wh kg^{-1} at 1.0C, respectively.

5.3 Materials and Methods

5.3.1 Precursors

5.3.1.1 Iron Isobutyrate (FeB) {$Fe[O_2CCH(CH_3)_2]_2$}

{$[Fe(NO_3)_3 \bullet 9H_2O]$, 267 g, 0.66 mol} was reacted with $[(CH_3)_2CHCOOH$, 300 mL, 3.3 mol] at a molar ratio of 1:3, in a 500 mL three neck round bottom flask using a distillation setup. The solution was stirred using a magnetic stir bar and heated to 135˚C under N_2 flow until a solid product was obtained. The solid was then cooled and removed from the flask. Excess isobutyric acid was removed via vacuum drying at 100˚C, 30 in Hg. Ceramic yield of the collected precursor was determined by TGA to be 24.8%, lower than the theoretical CY 31%. This discrepancy is

attributed to excess, unreacted isobutyric acid. Yield of FeB precursor reaction was 38%, while purity was determined to be 80%.

5.3.1.2 Nickel Propionate

Nickel hydroxide {[$Ni(OH)_2$], 102 g, 1.1 mol} was reacted with propionic acid [CH_3CH_2COOH, 300 mL, 3.3 mol] at a molar ratio of 1:3, in a 500 mL three neck round bottom flask using a distillation setup. The solution was stirred using a magnetic stir bar and heated to 135ºC under N_2 flow until a transparent liquid was obtained. Upon cooling the solution crystalized and the solid was removed from the flask. CY_{exp} of the collected precursor was determined by TGA to be 33%, lower than CY_{theo} of 35%. This discrepancy is attributed to excess, unreacted propionic acid. Yield of nickel propionate precursor reaction was 69%, while purity was determined to be 94%.

5.3.2 Nanopowder Synthesis

A series of LF-FSP NPs was synthesized with base compositions of $Li(TM)PO_4$ where TM = Fe, Mn, and/or Ni. Selected amounts of Fe, Mn, and/or Ni -containing precursors were dissolved in EtOH following molar ratios of respective oxide decomposition products as shown in Table 5.1. Precursors were adjusted based on metal content in the predicted metal oxide decomposition product, as shown in Table 5.1 below. Added EtOH dilutes the precursor solution to a 3 wt.% CY solution. Triethanolamine (TEA) was added to each solution as a solubility aid (50 mL). Using the LF-FSP process, the precursor solution was aerosolized with O_2 gas, ignited using CH_4/O_2 torches, and collected downstream via electrostatic precipitator (ESP), as described elsewhere [39,40,42,44,46,48,52].

Table 5.1: LFP-type Material Precursors Quantities Dissolved in EtOH and triethanolamine.

Precursor	LFP	$LM_{1/3}FP$	$LN_{1/3}M_{1/3}FP$	$LM_{2/3}FP$
	g	g	g	g
LiP	22.2	22.2	35.3	22.2
TEP	54.5	54.7	80.7	54.7
MnB	-	23.2	33.6	46.4
FeB	92.0	52.9	39.3	26.5
NiB	-	-	33.1	-

A supernatant solution was formed using collected ESP powder and 4 wt.% PAA via ultrasonication. The solution was decanted a total of two times, first after 3 h and then an additional 12 h, to remove unwanted, undispersed material. The resulting solution was heated under N_2 at 80˚C to remove EtOH.

5.3.3 Materials Characterization

X-Ray Diffraction (XRD) was performed (SmartLab XRD, Rigaku, Japan) operating at 40kV and 45mA with a scan rate of 8º 2θ min^{-1} and step size of 0.01 2θ in Bragg-Brentano geometry. Lattice parameters were calculated using Rietveld refinement using target phase $LiFePO_4$; PDF:01-080-4036.

Brunauer–Emmett–Teller Analysis (BET) specific surface area (SSAs) analyses were performed on the as-shot and select heated NPs (ASAP 2020, Micromeritics Instruments Corp, Norcross, GA, United States). The powders were degassed at 200 °C/2h before nitrogen adsorption and desorption analysis was conducted.

Additional characterization techniques and conditions can be found detailed in Chapter 2.3.

5.3.4 Electrochemical Characterization and Sample Preparation

The LFP-type NPs were coated with a conductive carbon coating. Typically, 1 g of dispersed NP was mixed with 10 wt.% anhydrous glucose via mortar and pestle, then pressed into a pellet (10 ksi/ 30 s) and placed into a graphite crucible. Pellets are heated using a tube furnace to 700˚C/2

h/Ar with heating and cooling rates of 3˚C and 5˚C/min, respectively. The resulting, calcined pellet is then ground using a mortar and pestle for 5 min before electrochemical characterization. Slurries were prepared using the mass ratio of 85: 7.5: 7.5 for CAM: carbon: binder, respectively. Conductive carbon used was C65 (Timcal). A single binder system (PVDF, Solvay Solef 5130) was used as a 5 wt.% premix in anhydrous NMP. Dry materials were mixed via mortar and pestle before ball-milling with PVDF solution and additional NMP for 24 h. After ball milling, additional NMP was added and further mixing was done via SpeedMixer (1250 rpm, 2 min, 3 times).

The mixed slurry was then cast onto carbon-coated aluminum foil (MTI, 18 μm Al, 1 μm C) using a doctor blade with a typical wet gap of 400 μm without agglomerates. The foil was dried at 60ºC until solvent was visibly removed, and then vacuum dried overnight at 90ºC. For coin cell testing, 12 mm diameter anodes were punched out using a handheld punch. Each cathode was pressed in Carver uniaxial press at 2.5 ksi/30 s/55 °C between two 50 μm mylar sheets. Li metal foil (750 μm, Sigma Aldrich) was scraped clean of oxide and punched to 16 mm diameter. Celgard 2400 separators, 25 μm, from MTI were used for all samples. MTI 2032 size coin cell components made from SS304 were used. Baseline electrolyte used was 60 μL 1.2M $LiPF_6$ in 2/4/4 blend by volume EC/DMC/EMC with 10 wt.% FEC (Soulbrain MI). All coin cells were assembled in an Ar-filled glovebox (Labstar Pro, MBraun, Stratham, NH, United States).

All coin cell cycling was performed using BioLogic battery cyclers at room temperature with a lower cutoff voltage of 2.0 V with a composition-dependent upper cutoff voltage (UCV) of 4.3 (LFP), 4.5 (LMFP), or 5.0 and 5.4 V (LNMFP). Galvanostatic cycling with potential limitation (GCPL) was used to determine material capacity. Constant current, constant voltage (CCCV) charging was used with a C/20 CV cutoff step, where 1C = 170 (LFP and LMFP) or 141 (LNMFP)

mAh g^{-1}. All potentials are given vs. Li/Li^+ unless otherwise stated. Rates study included charge and discharge C-rates of 0.1C (2 cycles), 0.2C (2 cycles), and 0.2C or 1.0C for remaining cycles.

5.4 Results and Discussion

In the following sections, we first characterize the morphology of synthesized NPs materials via SEM/EDS, PSA, and BET followed by structural characterization via XRD. Second, we characterize chemical compositions and local structure via spectroscopy techniques including FTIR and XPS. Subsequently, electrochemical behavior is assessed via cyclic voltammetry (CV), galvanostatic cycling, potential limited (GCPL).

5.4.1 Material Characterization

5.4.1.1 Morphology

Particle morphology plays an important role in overall electrochemical performance, for both cathode and anode active materials [26,27,54,55]. Previous LF-FSP studies have shown uniform particle morphologies for as-produced NPs and the study presented here follows the trend [1,39,42,47]. A representative sample of SEM and EDS studies, Figure 5.2, provide evidence of uniform, spherical particle morphologies for as-produced materials with homogenous elemental distributions – independent of the overall material composition.

As-produced LFP-type NPs APSs were analyzed via PSA, Figure 5.2. All synthesized materials presented a unimodal distribution with APSs between 80 and 110 nm, Table 5.2. SSA can be calculated from PSA results assuming spherical particle morphology, an assumption which is supported by the particle morphology shown in SEM. [38,53].

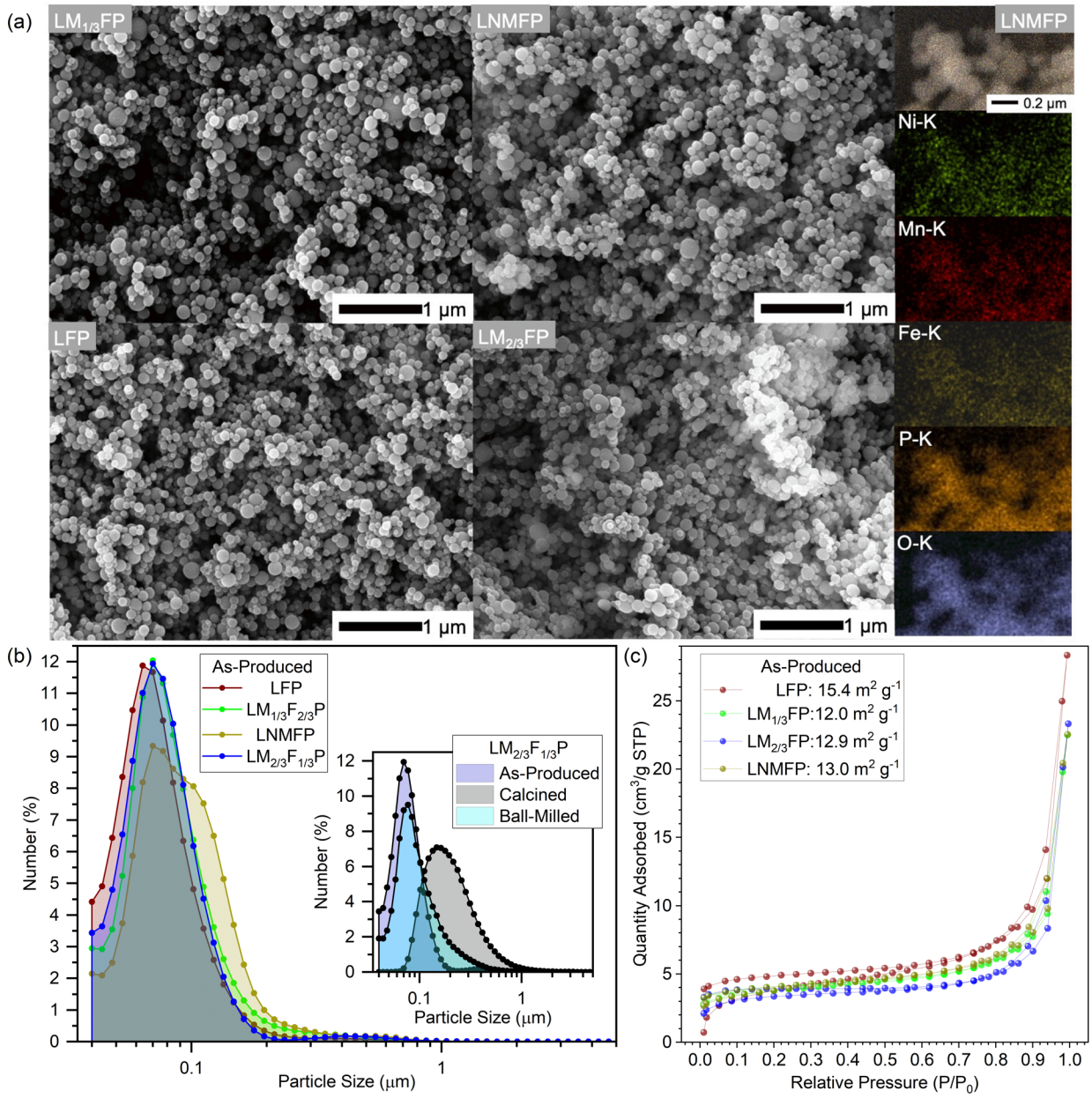

Figure 5.2: (a) SEM and EDS mapping a representative calcined LFP-type material, LNMFP. (b) PSA of as-produced NPs and heated sample. (c) BET of as-produced NPs.

The calculated SSA values are shown in Table 5.2. Additional PSA studies were performed on calcined $LM_{2/3}FP$ and calcined $LM_{2/3}FP$ after low-energy ball milling showing a relative increase and decrease in APS (270 vs. 117 nm). The additional PSA studies were performed to confirm the expected APS increase via calcination, and subsequent APS reduction via low-energy ball milling.

BET can be used as a primary method to determine SSAs of NPs. BET studies were performed with results shown in Figure 5.2 and Table 5.2, and are in good agreement with PSA.

Table 5.2: Atomic Composition from EDS with APS and SSA from PSA and BET for as-produced NP.

Material	Atomic Composition (mol%)				Mean APS via PSA (nm)	SSA via PSA (m^2 g^{-1})	SSA via BET (m^2 g^{-1})
	Li	Ni	Mn	Fe			
LFP	-	-	-	100	82	20	15
$LM_{1/3}FP$	-	-	33.0	67.0	95	17	12
LNMFP	-	33.6	35.8	30.6	108	15	13
$LM_{2/3}FP$	-	-	72	28	88	19	13

5.4.1.2 Structure and Spectroscopy

While XRD is commonly used as the standard for phase identification in crystalline materials; however, XRD is not particularly useful for amorphous materials. FTIR provides a useful alternative as it permits identification of local bonding order in materials and can aid in phase identification for amorphous materials. Coincidentally, XPS can be used to compare surface with bulk characteristics assessed via XRD and FTIR.

XRD reveals all as-produced compositions are amorphous with select low intensity reflections. After heating to 700˚C/6h/Ar with 10 wt.% anyhydrous glucose, the samples crystallize with the expected olivine phase(s), Figure 5.3. Olivine structured LFP-type materials fall into space group Pnma (or Pbnm depending on axis coordinates); $LiFePO_4$ PDF: 01-080-4036.

Mn-containing samples show shift to lower 2θ and higher unit cell volume in good agreement with the expected diffraction pattern for Mn-containing, lithiated phosphates ($LiMn_{0.7}Fe_{0.3}PO_4$; PDF:04-024-7794). Heating in a graphite crucible prevents unwanted oxidation and formation of secondary metal oxide phases. Calculated lattice parameters and the corresponding unit cell volumes from Rietveld analyses are shown in Table 5.3. All samples transform from amorphous to crystalline after calcination.

Table 5.3: Summary of Rietveld Refinement results for synthesized LFP-type NPs.

Material	Rietveld Refinement			
	a (Å)	*b* (Å)	*c* (Å)	Unit Cell Volume (Å^{-3})
LFP	10.341(8)	6.009(4)	4.692(4)	291.56
$LM_{1/3}FP$	10.390(2)	6.051(13)	4.685(8)	294.55
LNMFP	10.271(8)	5.998(5)	4.706(3)	289.92
$LM_{2/3}FP$	10.423(14)	6.077(14)	4.717(4)	298.78

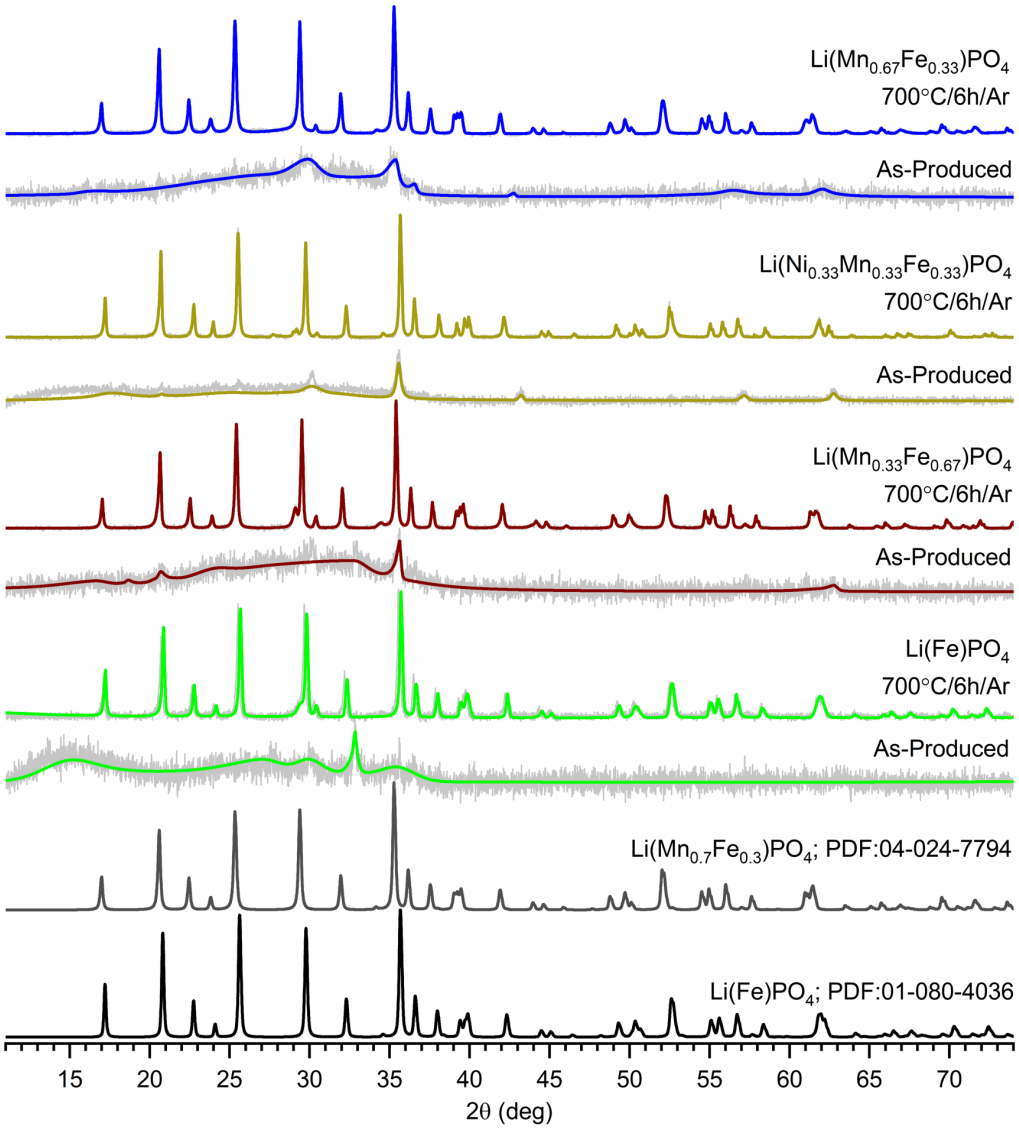

Figure 5.3: XRD studies of as-produced and calcined LFP-type materials.

Characteristic FTIR spectra for metal phosphate materials typically present below 1300 cm^{-1} [56]. Phosphate P-O stretching (n) and bending (d) appear typically between 1000-1150 cm^{-1} and

450-650 cm^{-1}, respectively, per Figure 5.4 [56]. All synthesized LFP-type materials show similar absorbance bands with small shifts to higher wavenumber for the substituted samples. As-produced materials are in good agreement with previous studies on vitreous LFP materials, and calcined materials show typical crystalline LFP features. The transformation from amorphous to crystalline phase is consistent with XRD.

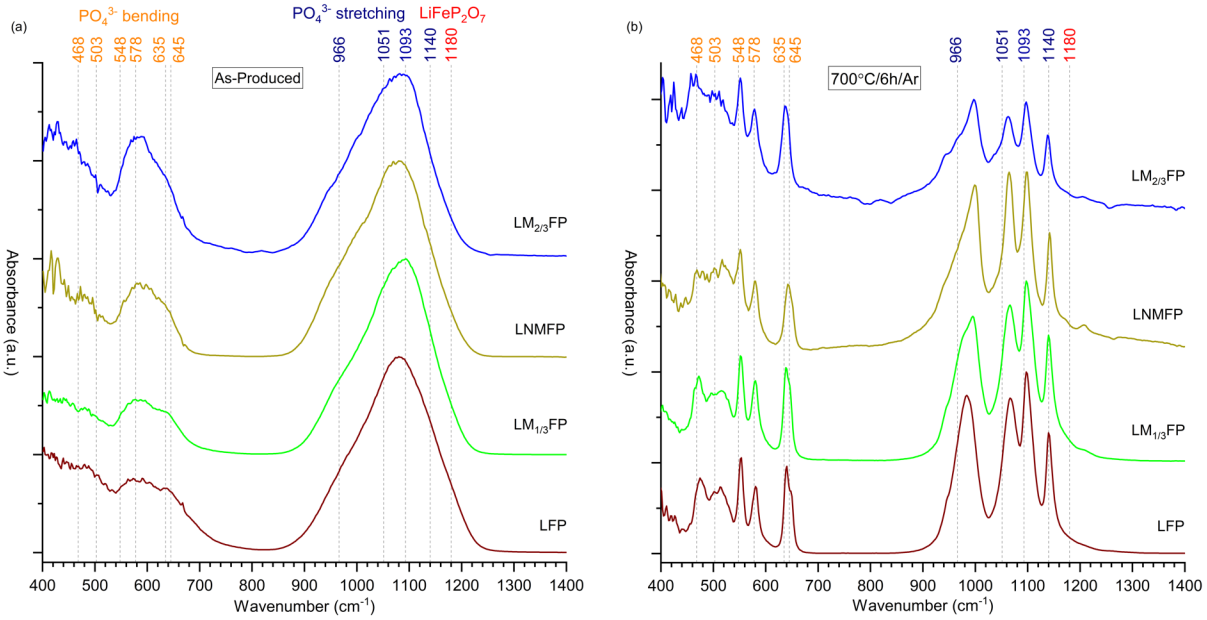

Figure 5.4: FTIR of (a) as-produced and (b) calcined LFP-type materials.

Figure 5.5 presents core-level XPS scans for LFP, $LM_{1/3}FP$, LNMFP, and $LM_{2/3}FP$. Figure 5.5 shows 2p scans for Ni, Mn, Fe, and P for all LFP-type materials and results are in good agreement with literature. Because XPS provides surface characterization, the carbon coating on heated materials prevents reliable measurement of the elemental metals, which are not abundant on particle surfaces. Li 1s spectra are not reported due to signals from Fe 3p, Mn 3p, Ni 3p, which are seen at binding energy levels of 50-60 eV, making analysis unreliable [57].

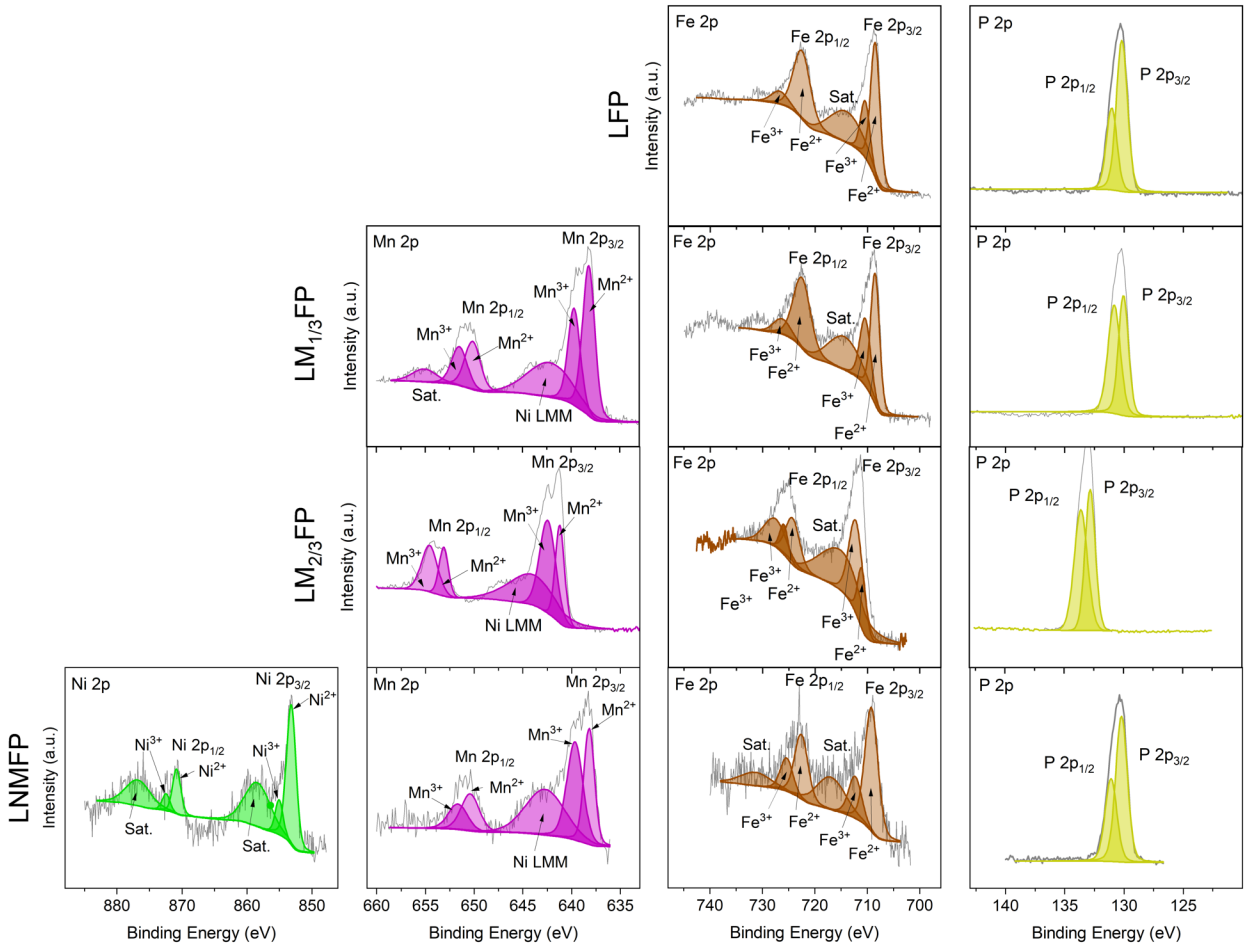

Figure 5.5: XPS core-level scans of as-produced LFP-type NPs for Ni, Mn, Fe, and P.

Ni 2p XPS spectra show two spin-orbit peaks at 853 and 870 eV for Ni $2p_{3/2}$ and Ni $2p_{1/2}$, respectively. High binding energy satellite peaks were observed at 858.7 and 876.8 eV for Ni $2p_{3/2}$ and Ni $2p_{1/2}$, respectively [58,59]. Average oxidation states of Ni in each composition are shown in Table 5.4.

Mn 2p XPS spectra show two spin-orbit peaks at 640 and 651 eV for Mn $2p_{3/2}$ and Mn $2p_{1/2}$, respectively [60]. Auger peaks from Ni are seen in LNMFP. Average oxidation states of Mn in each composition are shown in Table 5.4.

Fe 2p XPS spectra show two spin-orbit peaks at 710 and 723 eV for Fe $2p_{3/2}$ and Fe $2p_{1/2}$, respectively. A high binding energy satellite peak was observed at 715 eV for Fe $2p_{3/2}$ [59,61]. Average oxidation states of Fe in each composition are shown in Table 5.4.

P 2p XPS spectra show a peak at 130 eV for P $2p_{3/2}$. These spectra were deconvoluted into two peaks, corresponding to P-O and P=O, which are both expected in the structure of an LFP-type material [62]. Further details can be found in Table 5.4.

Table 5.4: Deconvolution of XPS spectra showing transition metal oxidation states in LFP-type materials.

Material		Ni		Mn		Fe		P	
		Ni^{2+}	Ni^{3+}	Mn^{2+}	Mn^{3+}	Fe^{2+}	Fe^{3+}	P-O	P=O
LFP	eV	-	-	-	-	708.5	710.5	130	131
	Atom%	-	-	-	-	70	30	66	34
	Oxidation	-		-		**2.3+**		-	
$LM_{1/3}FP$	eV	-	-	638	640	708.5	710.5	130	131
	Atom%	-	-	61	39	61	39	47	53
	Oxidation	-		**2.4+**		**2.4+**		-	
$LM_{2/3}FP$	eV	-	-	641	642	711	713	130	131
	Atom%	-	-	62	38	46	54	46	54
	Oxidation	-		**2.4+**		**2.5+**		-	
LNMFP	eV	853	855	638	640	709	712	130	131
	Atom%	80	20	44	56	74	26	64	36
	Oxidation	**2.2+**		**2.6+**		**2.3+**		-	

In the deconvolution of C 1s spectra, the main peaks detected were C-O bonding at 286 eV, C-C bonding in sp^2 coordination at 284 eV, and C-C bonding in sp^3 coordination at 283 eV [62–64]. The shift of C-C bonding is additional evidence of the successful carbon coating via glucose decomposition through calcination at 700˚C.

In the deconvolution of O 1s spectra, the main peaks detected were standard oxygen in the LFP lattice at 528 eV, C-O bonding at 530 eV, and C=O bonding at 533 eV [62].

5.4.2 Electrochemical Characterization

5.4.2.1 Cyclic Voltammetry (CV)

CV studies provide relative redox potentials and magnitudes for the synthesized NPs for 4 cycles using a scan rate of 0.2 mV s^{-1}, Figure 5.6. NPs containing Mn were cycled between 2-4.5 V to allow for full Mn redox, while LFP was cycled to 4.2 V. As expected, LFP and $LM_{1/3}FP$/$LM_{2/3}FP$ showed 1 and 2 primary redox processes, respectively. The magnitude of the current response for Fe and Mn is proportional to the relative composition, i.e. increasing at 4.2 V as Mn content increases in Figure 5.6 compared to Figure 5.6 for $LM_{2/3}FP$ and $LM_{1/3}FP$, respectively.

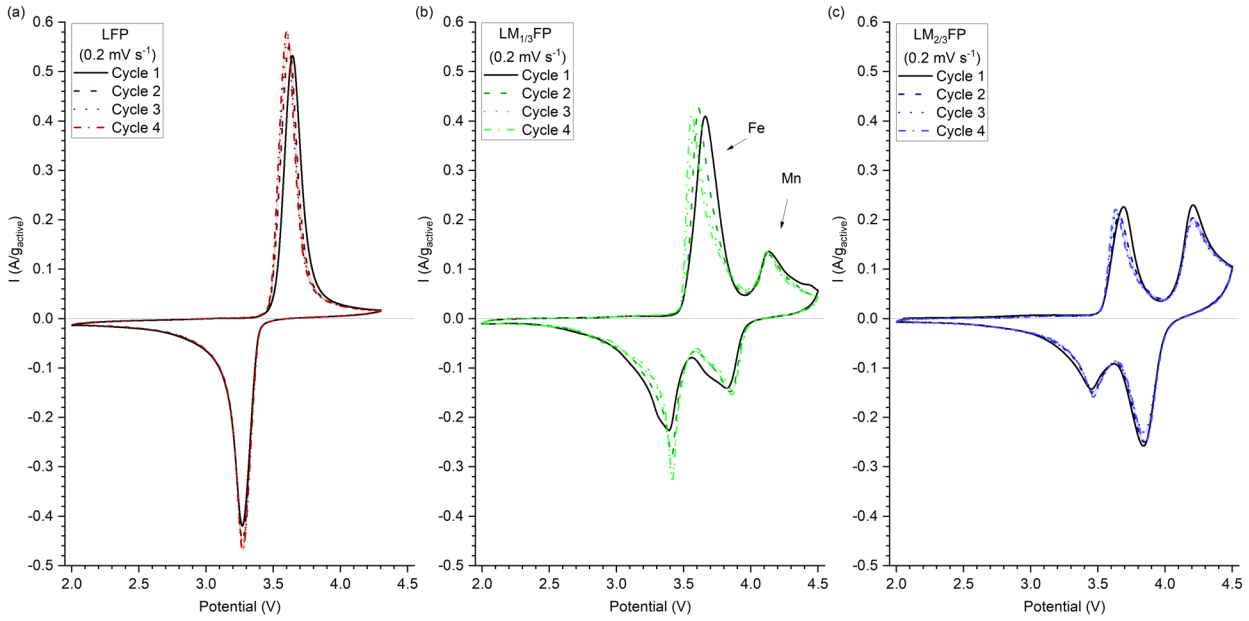

Figure 5.6: CV studies of (a) LFP, (b) $LM_{1/3}FP$, and (c) $LM_{2/3}FP$ materials.

5.4.2.2 Galvanostatic Cycling with Potential Limitation (GCPL)

Calcined LFP (3.4 V vs. Li/Li^+) and LMFP (3.4 and 4.0 V vs. Li/Li^+) NPs display typical electrochemical behavior with targeted redox plateau(s). Potential vs. specific capacity at different C-rates is shown in Figure 5.7. As Mn content increases, there is a decrease in available capacity at elevated C-rates. As stated in the Introduction, this is expected due to the Jahn–Teller distortion originated from the differences in Fe-O and Mn-O bonding, specifically the elongation of Mn-O,

when adjacent to PO_4 tetrahedron, which hinders the charge/discharge kinetics [18,25]. Both LFP and $LM_{1/3}FP$ showed good capacity retention at varying C-rates with 155±2(145±1) and 150±2(145±3) mAh g^{-1} at 0.2(1.0)C, while $LM_{2/3}FP$ showed lower capacity with 125±2(122±2) mAh g^{-1} at 0.2(1.0)C. Both $LM_{1/3}FP$ and $LM_{2/3}FP$ show a preferential decrease in Mn vs. Fe redox activity when using a discharge rate of 1.0C. This is further evidence of the reduced kinetics of Mn compared to Fe within LMFP.

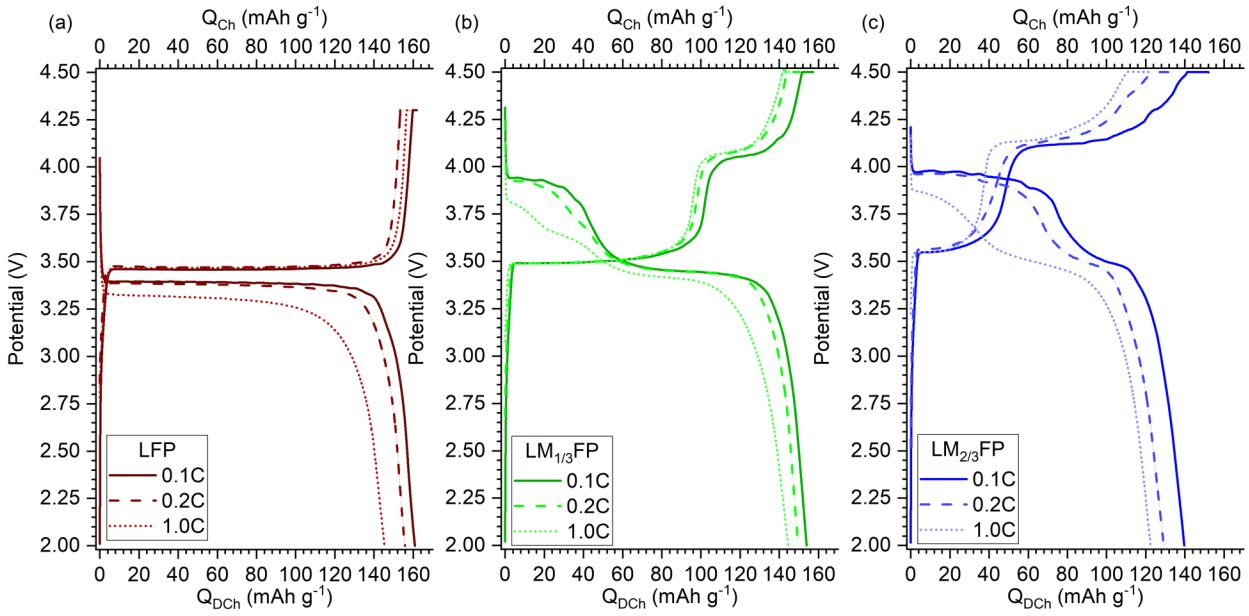

Figure 5.7: Potential vs. specific capacity at different C-rates for LFP (a), $LM_{1/3}FP$ (b), and $LM_{2/3}FP$ (c).

Additional GCPL studies were performed on the calcined NPs using discharge C-rates of 0.2 and 1.0C. After two cycles at 0.1C, all materials showed good cycling stability with respect to capacity retention, see Figure 5.8. After 50 cycles at 0.2C, each cathode was tested at 1.0C for 5 cycles, and returned back to 0.2C. The fast discharge cycles are denoted in Figure 5.8 with a gray highlight. After the fast discharge period, all materials returned to previously observed capacities at 0.2C. This capacity retention shows the structural stabililty at higher C-rates. If the faster C-rates resulted in structural degradation, one would expect to observe decreased capacity when returning to slower C-rate – or an increase in the rate of capacity degradation. Neither of these

possible cases are observed in Figure 5.8. In the 1.0C GCPL studies, a similar capacity check was performed after 50 cycles at 0.2C (gray highlighted in Figure 5.8). A similar relationship is observed in that the capacity returns to the previous value after the 0.2 C cycles.

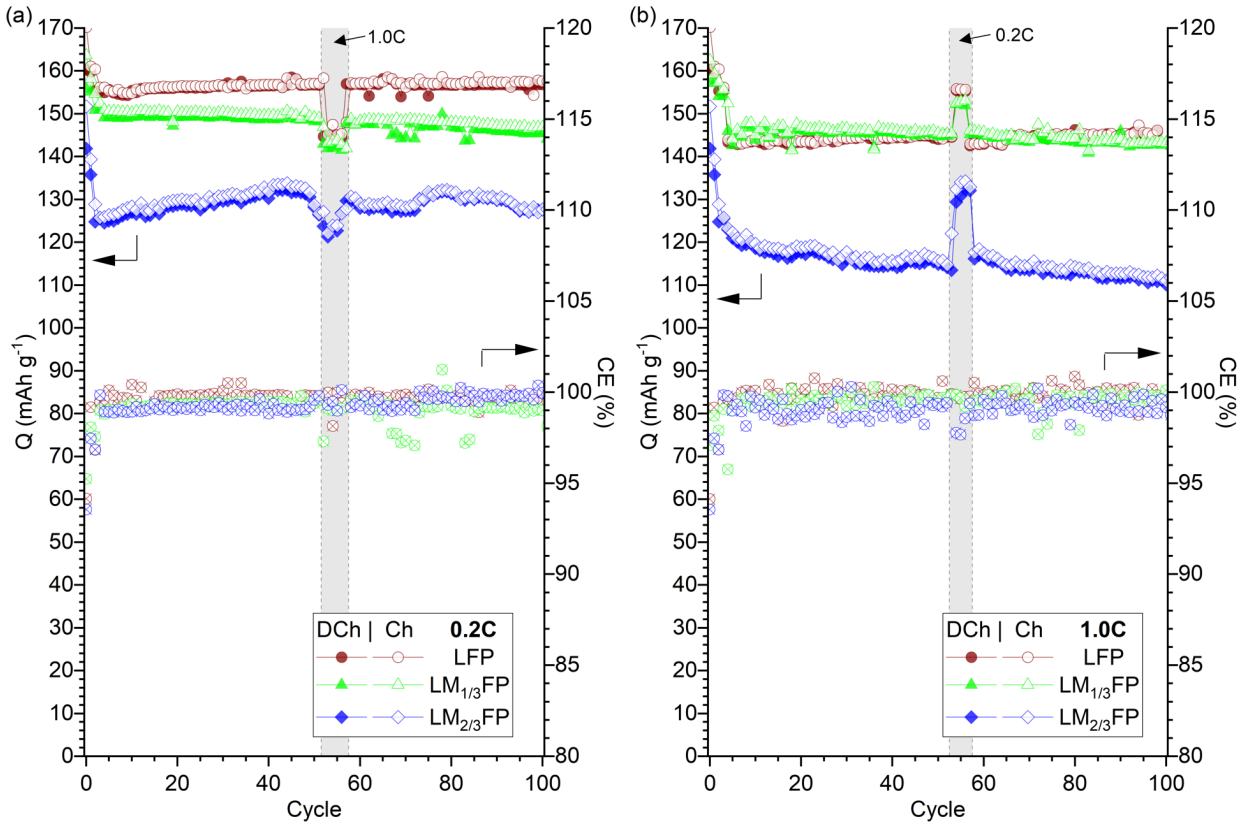

Figure 5.8: GCPL cycling study of LFP-type NPs using discharge C-rates of 0.2C (a) and 1.0C (b).

Additionally, Ni redox activity in the olivine structure is typically observed above 5.0 V, which is outside the cycling window for either LFP or LMFP. CV studies were performed on calcined LNMFP samples up to 5.0 V, shown in Figure 5.9, demonstrating Fe and Mn redox activity; however, very little if any Ni redox activity is observed. With this consideration, two UCVs were tested via GCPL, 5.0 and 5.4 V, to investigate the high-voltage cycling performance of LNMFP. The theoretical capacity for LNMFP is reduced to 141 mAh g^{-1} due to the Ni component. In both cases, the observed capacity falls short of the expected capacity, ~100 and ~80 mAh g^{-1} using a UCV of 5.4 and 5.0 V, respectively. Previous studies cite increased structural degradation for most

Ni phosphates vs Mn and Fe derivatives [16,65]. Increased capacity degradation can be observed for both UCVs in Figure 5.8 compared to LFP and LMFP materials. It is important to note that the liquid electrolyte in this study is not optimized for high voltage operation, and improved cycling results for LNMFP could be obtained with electrolyte optimization; however, this type of optimization is outside the scope of this study. The poor performance of LNMFP is further evidence that high Ni is not an ideal solution for optimal performance in the case of polyanion cathodes.

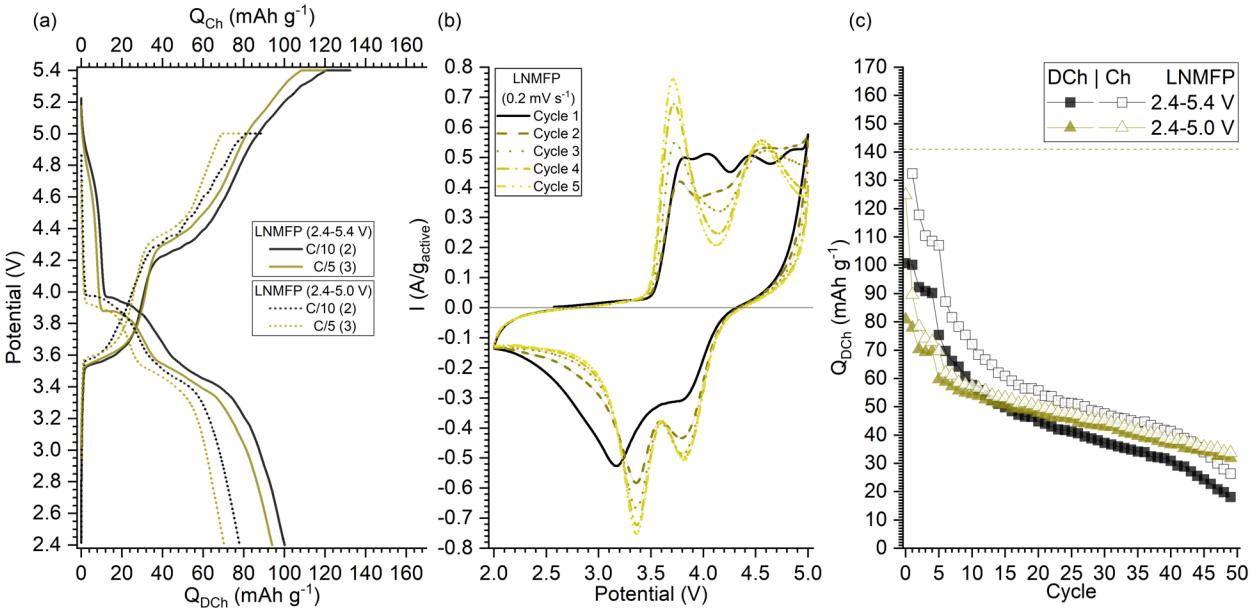

Figure 5.9: GCPL and CV studies of LNMFP.

5.5 Conclusions

Driven by the push in academia and industry alike to improve battery materials on performance and/or cost bases, we examine LFP and LFP-type materials synthesized using an alternative method – from metal carboxylate precursors via LF-FSP. On a cost bases, it remains vital to carefully select compositions based on raw material cost and anticipated electrochemical properties. The use of abundant, inexpensive elements such as Fe and Mn in high-throughput

syntheses can maximize cost savings. LF-FSP used in this work offers a scalable method for LFP-type NPs for use in low-cost LIBs.

In this study we report the synthesis and ensuing characterization of four LFP-type NPs: $LiFePO_4$, $LiMn_{1/3}Fe_{2/3}PO_4$, $LiMn_{2/3}Fe_{1/3}PO_4$, and $LiNi_{1/3}Mn_{1/3}Fe_{1/3}PO_4$. All synthesized materials showed the target olivine phase Pnma via XRD with APS below 100 nm via PSA. The as-produced material displayed primarily amorphous characteristics via XRD and FTIR; however, the target crystalline phase was achieved after calcination at 700˚C. Electrochemical studies including CV and GCPL demonstrate typical capacity and retention over a range of C-rates from 0.1 to 1.0C as shown in Table **5**. An improvement in discharge energy density can be achieved via 1/3 Mn substitution, $LiMn_{1/3}Fe_{2/3}PO_4$, while maintaining excellent capacity retention (96±2%). By establishing LF-FSP as a via synthesis route for high performance LFP and LFP-type NPs, further studies can be performed to evaluate additional compositions and doping schemes.

Table 5.5: Summary of LFP-type NP electrochemical performance.

Material	Specific Capacity [mAh g^{-1}]			Energy Density [Wh kg^{-1}]			Capacity Retention [%]	
	0.1C	0.2C	1C	0.1C	0.2C	1C	0.2C	1C
LFP	160±2	155±2	145±1	534±7	512±7	464±3	101±1	102±2
$LM_{1/3}FP$	155±1	150±2	145±3	544±4	524±7	491±9	96±1	96±2
$LN_{1/3}M_{1/3}FP$	100±5	92±5	-	360±20	330±20	-	43±3	-
$LM_{2/3}FP$	139±1	125±2	122±2	510±4	452±7	421±7	101±2	88±2

5.5.1 Acknowledgements

The authors acknowledge support from a DMR NSF Grant No. DMR-1926199 and a generous gift from Mercedes-Benz Research & Development North America (MBRDNA) for this work. The authors acknowledge the financial support of the University of Michigan College of Engineering and technical support from the Michigan Center for Materials Characterization. Additionally, the authors appreciate the technical support from Van Vlack lab for materials characterization (Dr. Sahar Farjami, Dr. Ying Qi). The authors also wish to acknowledge and thank Dr. Eleni Temeche, Erik D. Flaspohler and Marie C. Taylor for their contributions.

References

[1] M. Yu, T.G. Brandt, E. Temeche, R.M. Laine, Stabilizing High-Voltage Cathodes via Ball-Mill Coating with Flame-Made Nanopowder Electrolytes, ACS Appl Mater Interfaces 14 (2022) 49617–49632. https://doi.org/10.1021/acsami.2c09284.

[2] M. Wentker, M. Greenwood, J. Leker, A bottom-up approach to lithium-ion battery cost modeling with a focus on cathode active materials, Energies (Basel) 12 (2019) 1–18. https://doi.org/10.3390/en12030504.

[3] M. Wentker, M. Greenwood, M.C. Asaba, J. Leker, A raw material criticality and environmental impact assessment of state-of-the-art and post-lithium-ion cathode technologies, J Energy Storage 26 (2019) 101022. https://doi.org/10.1016/j.est.2019.101022.

[4] J.T. Frith, M.J. Lacey, U. Ulissi, A non-academic perspective on the future of lithium-based batteries, Nat Commun 14 (2023). https://doi.org/10.1038/s41467-023-35933-2.

[5] M.S.E. Houache, C.H. Yim, Z. Karkar, Y. Abu-Lebdeh, On the Current and Future Outlook of Battery Chemistries for Electric Vehicles—Mini Review, Batteries 8 (2022). https://doi.org/10.3390/batteries8070070.

[6] A. Mauger, C.M. Julien, Olivine positive electrodes for li-ion batteries: Status and perspectives, Batteries 4 (2018). https://doi.org/10.3390/batteries4030039.

[7] C.M. Julien, A. Mauger, J. Trottier, K. Zaghib, P. Hovington, H. Groult, Olivine-based blended compounds as positive electrodes for lithium batteries, Inorganics (Basel) 4 (2016). https://doi.org/10.3390/inorganics4020017.

[8] D. Di Lecce, J. Hassoun, Lithium Transport Properties in $LiMn_{1\alpha}Fe_{\alpha}PO_4$ Olivine Cathodes, Journal of Physical Chemistry C 119 (2015) 20855–20863. https://doi.org/10.1021/acs.jpcc.5b06727.

[9] L. Yang, W. Deng, W. Xu, Y. Tian, A. Wang, B. Wang, G. Zou, H. Hou, W. Deng, X. Ji, Olivine $LiMn_xFe_{1-x}PO_4$ cathode materials for lithium ion batteries: restricted factors of rate performances, J Mater Chem A Mater 9 (2021) 14214–14232. https://doi.org/10.1039/d1ta01526e.

[10] N. Tolganbek, Y. Yerkinbekova, S. Kalybekkyzy, Z. Bakenov, A. Mentbayeva, Current state of high voltage olivine structured $LiMPO_4$ cathode materials for energy storage applications: A review, J Alloys Compd 882 (2021) 160774. https://doi.org/10.1016/j.jallcom.2021.160774.

[11] Y. Liu, Y.J. Gu, J.L. Deng, G.Y. Luo, F.Z. Wu, Y. Mai, X.Y. Dai, J.Q. Li, Effect of doped Mn on improving the electrochemical performance of $LiFePO_4$, Journal of Materials

Science: Materials in Electronics 31 (2020) 2887–2894. https://doi.org/10.1007/s10854-019-02833-5.

[12] J. Li, M. Xiang, Y. Wang, J. Wu, H. Zhao, H. Liu, Effects of adhesives on the electrochemical performance of monodisperse $LiMn_{0.8}Fe_{0.2}PO_4$/C microspheres as cathode materials for high power lithium-ion batteries, J Mater Chem A Mater 5 (2017) 7952–7960. https://doi.org/10.1039/c7ta00104e.

[13] K. Wu, G. Hu, K. Du, Z. Peng, Y. Cao, Synthesis and characterization of high-rate $LiMn_{1/3}Fe_{2/3}PO_4$/C composite using nano-$MnFe_2O_4$ as precursor, Mater Lett 152 (2015) 217–219. https://doi.org/10.1016/j.matlet.2015.03.133.

[14] A.B. Muñoz-García, B. Tirri, I. Capone, A. Matic, M. Pavone, S. Brutti, Structural evolution of disordered $LiCo_{1/3}Fe_{1/3}Mn_{1/3}PO_4$ in lithium batteries uncovered, J Mater Chem A Mater 8 (2020) 19641–19653. https://doi.org/10.1039/d0ta05350c.

[15] N. Meethong, Y.H. Kao, S.A. Speakman, Y.M. Chiang, Aliovalent substitutions in olivine lithium iron phosphate and impact on structure and properties, Adv Funct Mater 19 (2009) 1060–1070. https://doi.org/10.1002/adfm.200801617.

[16] M.H. Nasir, N.K. Janjua, J. Santoki, Electrochemical Performance of Carbon Modified $LiNiPO_4$ as Li-Ion Battery Cathode: A Combined Experimental and Theoretical Study, J Electrochem Soc 167 (2020) 130526. https://doi.org/10.1149/1945-7111/abb83d.

[17] J. Ling, C. Karuppiah, S.G. Krishnan, M. V. Reddy, I.I. Misnon, M.H. Ab Rahim, C.C. Yang, R. Jose, Phosphate Polyanion Materials as High-Voltage Lithium-Ion Battery Cathode: A Review, Energy and Fuels 35 (2021) 10428–10450. https://doi.org/10.1021/acs.energyfuels.1c01102.

[18] K. Saravanan, V. Ramar, P. Balaya, J.J. Vittal, $Li(Mn_xFe_{1-x})PO_4$/C (x = 0.5, 0.75 and 1) nanoplates for lithium storage application, J Mater Chem 21 (2011) 14925–14935. https://doi.org/10.1039/c1jm11541c.

[19] B. Ramasubramanian, S. Sundarrajan, V. Chellappan, M. V. Reddy, S. Ramakrishna, K. Zaghib, Recent Development in Carbon-$LiFePO_4$ Cathodes for Lithium-Ion Batteries: A Mini Review, Batteries 8 (2022) 1–25. https://doi.org/10.3390/batteries8100133.

[20] R. Kashi, M. Khosravi, M. Mollazadeh, Effect of carbon precursor on electrochemical performance of $LiFePO_4$-C nano composite synthesized by ultrasonic spray pyrolysis as cathode active material for Li ion battery, Mater Chem Phys 203 (2018) 319–332. https://doi.org/10.1016/j.matchemphys.2017.10.021.

[21] W. Jiang, M. Wu, F. Liu, J. Yang, T. Feng, Variation of carbon coatings on the electrochemical performance of $LiFePO_4$ cathodes for lithium ionic batteries, RSC Adv 7 (2017) 44296–44302. https://doi.org/10.1039/c7ra08062j.

[22] F. Krumeich, O. Waser, S.E. Pratsinis, Thermal annealing dynamics of carbon-coated $LiFePO_4$ nanoparticles studied by in-situ analysis, J Solid State Chem 242 (2016) 96–102. https://doi.org/10.1016/j.jssc.2016.07.002.

[23] Z. wei Xiao, Y. jie Zhang, G. rong Hu, Effect of different carbon precursors on properties of $LiFePO_4$/C, J Cent South Univ 22 (2015) 4507–4514. https://doi.org/10.1007/s11771-015-2999-3.

[24] L.T.N. Huynh, H.H.A. Nguyen, T.T.D. Tran, T.T.T. Nguyen, T.M.A. Nguyen, T.H. La, V.M. Tran, L.P. Le, Electrode composite $LiFePO_4$@carbon: Structure and electrochemical performances, J Nanomater 2019 (2019). https://doi.org/10.1155/2019/2464920.

[25] H. Yang, C. Fu, Y. Sun, L. Wang, T. Liu, Fe-doped $LiMnPO_4$@C nanofibers with high Li-ion diffusion coefficient, Carbon N Y 158 (2020) 102–109. https://doi.org/10.1016/j.carbon.2019.11.067.

[26] W. Ren, H. Chen, R. Qiao, Y. Lin, F. Pan, In situ probing of interfacial kinetics for studying the electrochemical properties of active nano/micro-particles and the state of Li-ion batteries, J Mater Chem A Mater 5 (2017) 22598–22606. https://doi.org/10.1039/c7ta07332a.

[27] J. Yi, C. Wang, Y. Xia, Comparison of thermal stability between micro- and nano-sized materials for lithium-ion batteries, Electrochem Commun 33 (2013) 115–118. https://doi.org/10.1016/j.elecom.2013.04.015.

[28] X. mei GUAN, G. jun LI, C. yang LI, R. ming REN, Synthesis of porous nano/micro structured $LiFePO_4$/C cathode materials for lithium-ion batteries by spray-drying method, Transactions of Nonferrous Metals Society of China (English Edition) 27 (2017) 141–147. https://doi.org/10.1016/S1003-6326(17)60016-5.

[29] M. Wentker, M. Greenwood, J. Leker, A bottom-up approach to lithium-ion battery cost modeling with a focus on cathode active materials, Energies (Basel) 12 (2019) 1–18. https://doi.org/10.3390/en12030504.

[30] S. Kuppan, Y. Xu, Y. Liu, G. Chen, Phase transformation mechanism in lithium manganese nickel oxide revealed by single-crystal hard X-ray microscopy, Nat Commun 8 (2017). https://doi.org/10.1038/ncomms14309.

[31] N. Nitta, F. Wu, J. Lee, G. Yushin, Li-ion battery materials: present and future, Materials Today 18 (2015). https://doi.org/10.1016/j.mattod.2014.10.040

[32] Q. Tian, Z. Zhang, L. Yang, Y. Xiang, Improving the lithium storage properties of $Li_4Ti_5O_{12}$ anodes by facile two-phase formation and nanostructure engineering strategy, J Alloys Compd 705 (2017) 638–644. https://doi.org/10.1016/j.jallcom.2017.02.175.

[33] C. Julien, A. Mauger, K. Zaghib, H. Groult, Optimization of layered cathode materials for lithium-ion batteries, Materials 9 (2016). https://doi.org/10.3390/MA9070595.

[34] G. Zang, J. Zhang, S. Xu, Y. Xing, Techno-economic analysis of cathode material production using flame-assisted spray pyrolysis, Energy 218 (2021) 119504. https://doi.org/10.1016/j.energy.2020.119504.

[35] X. Zhang, H. Zheng, V. Battaglia, R.L. Axelbaum, Electrochemical performance of spinel $LiMn_2O_4$ cathode materials made by flame-assisted spray technology, J Power Sources 196 (2011) 3640–3645. https://doi.org/10.1016/j.jpowsour.2010.07.008.

[36] O. Waser, R. Büchel, A. Hintennach, P. Novák, S.E. Pratsinis, Continuous flame aerosol synthesis of carbon-coated nano-$LiFePO_4$ for Li-ion batteries, J Aerosol Sci 42 (2011) 657–667. https://doi.org/10.1016/j.jaerosci.2011.06.003.

[37] N.A. Hamid, S. Wennig, S. Hardt, A. Heinzel, C. Schulz, H. Wiggers, High-capacity cathodes for lithium-ion batteries from nanostructured $LiFePO_4$ synthesized by highly-flexible and scalable flame spray pyrolysis, J Power Sources 216 (2012) 76–83. https://doi.org/10.1016/j.jpowsour.2012.05.047.

[38] T.G. Brandt, E. Temeche, A.R. Tuokkola, H. Li, S. Indris, D.A. Edelman, K. Sun, R.M. Laine, A. Materials, D.A. Edelman, R.M. Laine, Nanocomposite Li- and Mn-Rich Spinel Cathodes Characterized with a Green, Aqueous Binder System, Chemical Engineering Journal 479C (2024) 147419. https://doi.org/https://doi.org/10.1016/j.cej.2023.147419.

[39] E. Yi, E. Temeche, R.M. Laine, Superionically conducting beta"-Al_2O_3 thin films processed using flame synthesized nanopowders, J Mater Chem A Mater 6 (2018) 12411–12419. https://doi.org/10.1039/c8ta02907e.

[40] E. Temeche, S. Indris, R.M. Laine, $LiAlO_2$/$LiAl_5O_8$ Membranes Derived from Flame-Synthesized Nanopowders as a Potential Electrolyte and Coating Material for All-Solid-State Batteries, ACS Appl Mater Interfaces 12 (2020) 46119–46131. https://doi.org/10.1021/acsami.0c13021.

[41] S. Kumar, J.A. Azurdia, R.M. Laine, Synthesis of $(MgO)_x(Fe_2O_3)_{1-x}$ nanoparticles via liquid feed flame spray pyrolysis. A non-stoichiometric spinel phase outside the normal phase diagram, Journal of Ceramic Processing Research 11 (2010) 517–522.

[42] E. Yi, W. Wang, J. Kieffer, R.M. Laine, Flame made nanoparticles permit processing of dense, flexible, Li^+ conducting ceramic electrolyte thin films of cubic- $Li_7La_3Zr_2O_{12}$ (c-LLZO), J Mater Chem A Mater 4 (2016) 12947–12954. https://doi.org/10.1039/c6ta04492a.

[43] K. Saito, E. Yi, R.M. Laine, Y. Sugahara, Preparation of Nb-doped TiO_2 nanopowder by liquid-feed spray pyrolysis followed by ammonia annealing for tunable visible-light absorption and inhibition of photocatalytic activity, Ceram Int 46 (2020) 1314–1322. https://doi.org/10.1016/j.ceramint.2019.09.094.

[44] E. Yi, W. Wang, J. Kieffer, R.M. Laine, Key parameters governing the densification of cubic- $Li_7La_3Zr_2O_{12}$ Li^+ conductors, J Power Sources (2017). https://doi.org/10.1016/j.jpowsour.2017.03.126.

[45] W. Wang, E. Yi, A.J. Fici, R.M. Laine, J. Kieffer, Lithium Ion Conducting Poly(ethylene oxide)-Based Solid Electrolytes Containing Active or Passive Ceramic Nanoparticles, Journal of Physical Chemistry C 121 (2017) 2563–2573. https://doi.org/10.1021/acs.jpcc.6b11136.

[46] E. Temeche, E. Buch, X. Zhang, T. Brandt, A. Hintennach, R.M. Laine, Improved Electrochemical Properties of $Li_4Ti_5O_{12}$ Nanopowders (NPs) via Addition of $LiAlO_2$ and Li_6SiON Polymer Electrolytes, Derived from Agricultural Waste, ACS Appl Energy Mater 4 (2021) 1894–1905. https://doi.org/10.1021/acsaem.0c02994.

[47] S. Liu, C. Zhou, Y. Wang, W. Wang, Y. Pei, J. Kieffer, R.M. Laine, Ce-Substituted Nanograin $Na_3Zr_2Si_2PO_{12}$ Prepared by LF-FSP as Sodium-Ion Conductors, ACS Appl Mater Interfaces (2020). https://doi.org/10.1021/acsami.9b11995.

[48] E. Temeche, E. Yi, V. Keshishian, J. Kieffer, R.M. Laine, Liquid-feed flame spray pyrolysis derived nanopowders (NPs) as a route to electrically conducting calcium aluminate ($12CaO.7Al_2O_3$) films, J Eur Ceram Soc (2019). https://doi.org/10.1016/j.jeurceramsoc.2018.11.051.

[49] R. Strobel, S.E. Pratsinis, Flame aerosol synthesis of smart nanostructured materials, J Mater Chem 17 (2007) 4743–4756. https://doi.org/10.1039/b711652g.

[50] W.Y. Teoh, R. Amal, L. Mädler, Flame spray pyrolysis: An enabling technology for nanoparticles design and fabrication, Nanoscale 2 (2010) 1324–1347. https://doi.org/10.1039/c0nr00017e.

[51] K. Wegner, B. Schimmoeller, B. Thiebaut, C. Fernandez, T.N. Rao, Pilot plants for industrial nanoparticle production by flame spray pyrolysis, KONA Powder and Particle Journal 29 (2011) 251–265. https://doi.org/10.14356/kona.2011025.

[52] E. Yi, W. Wang, S. Mohanty, J. Kieffer, R. Tamaki, R.M. Laine, Materials that can replace liquid electrolytes in Li batteries: Superionic conductivities in $Li_{1.7}Al_{0.3}Ti_{1.7}Si_{0.4}P_{2.6}O_{12}$. Processing combustion synthesized nanopowders to free standing thin films, J Power Sources 269 (2014) 577–588. https://doi.org/10.1016/j.jpowsour.2014.07.029.

[53] T.G. Brandt, A.R. Tuokkola, M. Yu, R.M. Laine, Liquid-feed flame spray pyrolysis enabled synthesis of Co- and Cr-free, high-entropy spinel oxides as Li-ion anodes, Chemical Engineering Journal 474 (2023) 145495. https://doi.org/10.1016/j.cej.2023.145495.

[54] M. Castle, G. Richardson, J.M. Foster, Understanding rapid charge and discharge in nano-structured lithium iron phosphate cathodes, Eur J Appl Math 33 (2021) 328–368. https://doi.org/10.1017/S0956792521000036.

[55] X. Zhao, V.P. Lehto, Challenges and prospects of nanosized silicon anodes in lithium-ion batteries, Nanotechnology 32 (2021). https://doi.org/10.1088/1361-6528/abb850.

[56] A. Ait Salah, P. Jozwiak, K. Zaghib, J. Garbarczyk, F. Gendron, A. Mauger, C.M. Julien, FTIR features of lithium-iron phosphates as electrode materials for rechargeable lithium batteries, Spectrochim Acta A Mol Biomol Spectrosc 65 (2006) 1007–1013. https://doi.org/10.1016/j.saa.2006.01.019.

[57] J. Moulder, Handbook of X-ray Photoelectron Spectroscopy: A Reference Book of Standard Spectra for Identification and Interpretation of XPS Data, 1992.

[58] M.C. Biesinger, B.P. Payne, L.W.M. Lau, A. Gerson, R.S.C. Smart, X-ray photoelectron spectroscopic chemical state Quantification of mixed nickel metal, oxide and hydroxide systems, Surface and Interface Analysis 41 (2009) 324–332. https://doi.org/10.1002/sia.3026.

[59] M.C. Biesinger, B.P. Payne, A.P. Grosvenor, L.W.M. Lau, A.R. Gerson, R.S.C. Smart, Resolving surface chemical states in XPS analysis of first row transition metals, oxides

and hydroxides: Cr, Mn, Fe, Co and Ni, Appl Surf Sci 257 (2011) 2717–2730. https://doi.org/10.1016/j.apsusc.2010.10.051.
[60] E.S. Ilton, J.E. Post, P.J. Heaney, F.T. Ling, S.N. Kerisit, XPS determination of Mn oxidation states in Mn (hydr)oxides, Appl Surf Sci 366 (2016) 475–485. https://doi.org/10.1016/j.apsusc.2015.12.159.
[61] A.P. Grosvenor, B.A. Kobe, M.C. Biesinger, N.S. McIntyre, Investigation of multiplet splitting of Fe 2p XPS spectra and bonding in iron compounds, Surface and Interface Analysis 36 (2004) 1564–1574. https://doi.org/10.1002/sia.1984.
[62] H. Lee, H.-S. Lim, X. Ren, L. Yu, M.H. Engelhard, K.S. Han, J. Lee, H.-T. Kim, J. Xiao, J. Liu, W. Xu, J.-G. Zhang, Detrimental Effects of Chemical Crossover from the Lithium Anode to Cathode in Rechargeable Lithium Metal Batteries, ACS Energy Lett 3 (2018) 2921–2930. https://doi.org/10.1021/acsenergylett.8b01819.
[63] R. Liu, J. Chen, Z. Li, Q. Ding, X. An, Y. Pan, Z. Zheng, M. Yang, D. Fu, Preparation of $LiFePO_4$/C Cathode Materials via a Green Synthesis Route for Lithium-Ion Battery Applications, Materials 11 (2018) 2251. https://doi.org/10.3390/ma11112251.
[64] W. Yang, Z. Wang, L. Chen, Y. Chen, L. Zhang, Y. Lin, J. Li, Z. Huang, Suppression of degradation for lithium iron phosphate cylindrical batteries by nano silicon surface modification, RSC Adv 7 (2017) 33680–33687. https://doi.org/10.1039/C7RA06027K.
[65] K. Kubaya, P. Taddesse, Mn^{2+}- and Fe^{2+}-doped $LiNiPO_4$ cathode materials: structural, electrical, dielectric, and electrochemical properties, Appl Phys A Mater Sci Process 128 (2022) 1–9. https://doi.org/10.1007/s00339-022-05767-8.

Chapter 6 Future Work

The studies presented in this work demonstrate LF-FSP as a novel and valuable synthesis method for LIB active materials. Some level of optimization was required in each study achieve the current findings. In most cases, further optimization can be performed to enhance resulting properties such as performance, composition, and/or cost. In addition to optimization studies of Li_xMNO, HEO, and LMFP, two areas of future work are high entropy phosphates and disordered rock salt (DRX) cathodes. DRX materials have the most promise for application as state-of-the-art cathodes for Li-ion batteries and should be prioritized in future work.

6.1 High Entropy Phosphates

Lithium iron phosphate $Li_1Fe_1PO_4$ (LFP) is one of the foundational cathode materials for Li-ion batteries leading to global electrification as discussed in Chapters 1 and 5. LFP benefits from stable de/lithiation as a result of strong P-O covalent bonding in addition to 1D Li diffusion channels [1]. The specific capacity of LFP (170 mAh g^{-1}) is competitive with other cathode materials; however, a relatively low redox potential (3.4 vs. Li/Li^+) results in a lower energy density (578 Wh kg^{-1}) [1].

Partial transition metal substitution for Fe (i.e. Mn) can increase redox potential, and therefore energy density [1–6]. Both LFP and LMFP suffer from poor electronic conductivity, which can be alleviated to some extent via carbon coating [7–12]. Additionally, transition metal doping (Zn, Ni, Mn, Cu, Mg, Ti) has been shown to improve electrochemical performance via structural

modification such as increasing Li diffusion channel size and/or improving electronic conductivity [2,13–20].

The number of dopants is usually limited to 1 or 2 in a typical LFP-type material study with low overall concentration (<10 %) [13,16]. One reason for this limitation is the difficulty in synthesizing a single phase due to enthalpy of mixing penalties. High entropy materials such as high entropy oxides (HEOs) have synthesized single phase material with many constituent elements by leveraging entropy-driven stabilization, outweighing the classical enthalpy penalizations [21–25]. High entropy materials, having configurational entropy > 1.5R, were first observed in metallic alloys, but have extended to oxides, carbides, nitrides, and phosphates [26–30].

In electrochemical applications, HEOs have recently gained traction in academia as a candidate for next generation Li-ion battery anode materials, as discussed in Chapters 1 and 3 [29,31]. There are select examples of high entropy cathode materials; however, most examples rely on either rare-earth, toxic, or expensive constituent elements [32–36]. While there are examples of high entropy phosphates, current examples are limited to catalytic or Na-ion battery applications [26–28,30]. To the best of our knowledge, there are no examples of high-entropy, lithiated transition metal phosphates (HEPs) for Li-ion cathode application.

The design of a high entropy, lithiated transition metal phosphates must begin with clarifying nomenclature and objectives. High-entropy materials can be defined by a variety of different methods, including the solid solution model (SS), the sublattice model (SL), and entropy metric (EM) [21,24,25,37]. The SS model relies on the assumption of a single lattice, while the SL model and EM can account for multiple lattices. Olivine structured materials, such as LFP have two cationic lattices for Li (M1) and Fe (M2) [20]. With consideration of only one lattice, a system

with high entropy exclusively on the M2 site might be considered compositionally complex. The functionality of LFP as a cathode material relies on unimpeded Li pathways such that the M1 lattice would ideally remain as Li only, while the M2 lattice would accommodate the selected transition metals. Varying entropy on a single site within a crystal structure was previously demonstrated for perovskite-type materials, in which atomic location can be controlled with elements of a similar molecular radius [38]. With the inclusion of additional constituent elements, there is an opportunity for advanced design control. Poor electronic conductivity has been well documented for Li-ion phosphate cathode materials, and this should be taken into design consideration when selecting constituent elements.

LF-FSP is the ideal synthesis tool to explore single phase HEPs due to the high degree of compositional control and rapid quenching that often results in kinetic phases not observed in other synthesis techniques. In a similar vein to HEOs as AAMs, the primary motivator for HEPs as CAMs would be to understand if there is any synergistic effect, resulting in improved performance.

6.2 DRX Cathodes

As vehicle electrification continues, more and more will be demanded from EVs especially concerning range and cost. High energy density CAMs were discussed in Chapters 1 and 4, but there is still room for improvement. One promising candidate is disordered rock salt (DRX) cathodes such as lithium manganese titanium oxide (LMTO), $Li_{1.2}Mn_{0.4}Ti_{0.4}O_2$. Unlike traditional layered metal oxides (LMOs) which are primarily constrained to Ni, Mn, and Co redox active centers, DRX-type cathodes can be based on Mn, Ni, V, Mo, Fe, and other earth abundant elements [39]. This diversity of usable, redox active transition metals can take pressure off of strained Co and Ni supply chains while still targeting high energy density (800 Wh kg^{-1}) [39,40]. Depending

on the selected redox active transition metals, specific capacity of DRX cathodes can range from 200-400 mAh g^{-1} [40].

Commonly, performance optimization of commercialized CAMs includes manipulation of the UCV, which in turn removes additional Li from the structure (e.g. NMC622 and 811) [41]. The extended removal of Li is paired with decreased stability of the layers and can lead to structural collapsing [39,40]. There is not a comparable process in DRX as the random cation distribution is believed to eliminate structural collapse and changes in interlayer spacing [39,40].

Rock salt structures were thought, before the discovery of DRX cathodes, to be electrochemically inactive due to the close packing and lack of clear Li diffusion pathways. It has been shown that HV cycling of CAMs can lead to irreversible, electrochemically inert rock salt phases on the surface [42–44]. Increasing the Li/metal ratio and cation disordering in the rock salt structure, can result in Li^+ diffusion– even delivering >300 mAh g^{-1} [42]. DRX materials are theorized to have low isotropic volume expansion on lithiation/delithiation, but this has not been studied extensively yet [39].

Unlike commercialized CAMs, DRX cathodes can also use irreversible and/or reversible oxygen redox activity. It has been shown recently that oxygen (O^{2-}) in the lattice can be oxidized to O^{x-} (where $0 < x < 2$), and results in two competing processes [39,45]. Unstable O^{x-} can disproportionate to O^{2-} (lattice oxygen) and O_2 gas [46]. The second process involves oxidized O^{x-} reduced back either to O^{2-} or O^{y-} (where $x < y < 2$). This alternative process results in reversible oxygen redox, which in turn results in vastly superior lithium storage over typical CAMs. Detailed studies of TM and oxygen redox activity in compositions like $Li_{1.2}Mn_{0.4}Ti_{0.4}O_2$ lay the groundwork for future studies on additional compositions.

References

[1] A. Mauger, C.M. Julien, Olivine positive electrodes for li-ion batteries: Status and perspectives, Batteries 4 (2018). https://doi.org/10.3390/batteries4030039.

[2] Y. Liu, Y.J. Gu, J.L. Deng, G.Y. Luo, F.Z. Wu, Y. Mai, X.Y. Dai, J.Q. Li, Effect of doped Mn on improving the electrochemical performance of $LiFePO_4$, Journal of Materials Science: Materials in Electronics 31 (2020) 2887–2894. https://doi.org/10.1007/s10854-019-02833-5.

[3] J. Li, M. Xiang, Y. Wang, J. Wu, H. Zhao, H. Liu, Effects of adhesives on the electrochemical performance of monodisperse $LiMn_{0.8}Fe_{0.2}PO_4$/C microspheres as cathode materials for high power lithium-ion batteries, J Mater Chem A Mater 5 (2017) 7952–7960. https://doi.org/10.1039/c7ta00104e.

[4] K. Wu, G. Hu, K. Du, Z. Peng, Y. Cao, Synthesis and characterization of high-rate $LiMn_{1/3}Fe_{2/3}PO_4$/C composite using nano-$MnFe_2O_4$ as precursor, Mater Lett 152 (2015) 217–219. https://doi.org/10.1016/j.matlet.2015.03.133.

[5] A.B. Muñoz-García, B. Tirri, I. Capone, A. Matic, M. Pavone, S. Brutti, Structural evolution of disordered $LiCo_{1/3}Fe_{1/3}Mn_{1/3}PO_4$ in lithium batteries uncovered, J Mater Chem A Mater 8 (2020) 19641–19653. https://doi.org/10.1039/d0ta05350c.

[6] L. Yang, W. Deng, W. Xu, Y. Tian, A. Wang, B. Wang, G. Zou, H. Hou, W. Deng, X. Ji, Olivine $LiMn_xFe_{1-x}PO_4$ cathode materials for lithium ion batteries: restricted factors of rate performances, J Mater Chem A Mater 9 (2021) 14214–14232. https://doi.org/10.1039/d1ta01526e.

[7] B. Ramasubramanian, S. Sundarrajan, V. Chellappan, M. V. Reddy, S. Ramakrishna, K. Zaghib, Recent Development in Carbon-$LiFePO_4$ Cathodes for Lithium-Ion Batteries: A Mini Review †, Batteries 8 (2022) 1–25. https://doi.org/10.3390/batteries8100133.

[8] R. Kashi, M. Khosravi, M. Mollazadeh, Effect of carbon precursor on electrochemical performance of $LiFePO_4$-C nano composite synthesized by ultrasonic spray pyrolysis as cathode active material for Li ion battery, Mater Chem Phys 203 (2018) 319–332. https://doi.org/10.1016/j.matchemphys.2017.10.021.

[9] W. Jiang, M. Wu, F. Liu, J. Yang, T. Feng, Variation of carbon coatings on the electrochemical performance of $LiFePO_4$ cathodes for lithium ionic batteries, RSC Adv 7 (2017) 44296–44302. https://doi.org/10.1039/c7ra08062j.

[10] F. Krumeich, O. Waser, S.E. Pratsinis, Thermal annealing dynamics of carbon-coated $LiFePO_4$ nanoparticles studied by in-situ analysis, J Solid State Chem 242 (2016) 96–102. https://doi.org/10.1016/j.jssc.2016.07.002.

[11] Z. wei Xiao, Y. jie Zhang, G. rong Hu, Effect of different carbon precursors on properties of $LiFePO_4$/C, J Cent South Univ 22 (2015) 4507–4514. https://doi.org/10.1007/s11771-015-2999-3.

[12] L.T.N. Huynh, H.H.A. Nguyen, T.T.D. Tran, T.T.T. Nguyen, T.M.A. Nguyen, T.H. La, V.M. Tran, L.P. Le, Electrode composite $LiFePO_4$@carbon: Structure and electrochemical performances, J Nanomater 2019 (2019). https://doi.org/10.1155/2019/2464920.
[13] S.P. Chen, D. Lv, J. Chen, Y.H. Zhang, F.N. Shi, Review on Defects and Modification Methods of $LiFePO_4$ Cathode Material for Lithium-Ion Batteries, Energy and Fuels 36 (2022) 1232–1251. https://doi.org/10.1021/acs.energyfuels.1c03757.
[14] K. Kubaya, P. Taddesse, Mn^{2+}- and Fe^{2+}-doped $LiNiPO_4$ cathode materials: structural, electrical, dielectric, and electrochemical properties, Appl Phys A Mater Sci Process 128 (2022) 1–9. https://doi.org/10.1007/s00339-022-05767-8.
[15] L. Wang, R. Wei, H. Zhang, K. Zhang, F. Liang, Y. Yao, Y. Li, B-Mg co-doping behavior of $LiFePO_4$ cathode material: balance of oxygen vacancy and enhancement of electrochemical performance, Ionics (Kiel) 28 (2022) 593–600. https://doi.org/10.1007/s11581-021-04349-7.
[16] N. Meethong, Y.H. Kao, S.A. Speakman, Y.M. Chiang, Aliovalent substitutions in olivine lithium iron phosphate and impact on structure and properties, Adv Funct Mater 19 (2009) 1060–1070. https://doi.org/10.1002/adfm.200801617.
[17] Y. Liu, Y.J. Gu, G.Y. Luo, Z.L. Chen, F.Z. Wu, X.Y. Dai, Y. Mai, J.Q. Li, Ni-doped $LiFePO_4$/C as high-performance cathode composites for Li-ion batteries, Ceram Int 46 (2020) 14857–14863. https://doi.org/10.1016/j.ceramint.2020.03.011.
[18] S.B. Lee, S.H. Cho, J.B. Heo, V. Aravindan, H.S. Kim, Y.S. Lee, Copper-substituted, lithium rich iron phosphate as cathode material for lithium secondary batteries, J Alloys Compd 488 (2009) 380–385. https://doi.org/10.1016/j.jallcom.2009.08.144.
[19] H. Liu, Q. Cao, L.J. Fu, C. Li, Y.P. Wu, H.Q. Wu, Doping effects of zinc on $LiFePO_4$ cathode material for lithium ion batteries, Electrochem Commun 8 (2006) 1553–1557. https://doi.org/10.1016/j.elecom.2006.07.014.
[20] Y. Ge, X. Yan, J. Liu, X. Zhang, J. Wang, X. He, R. Wang, H. Xie, An optimized Ni doped $LiFePO_4$/C nanocomposite with excellent rate performance, Electrochim Acta 55 (2010) 5886–5890. https://doi.org/10.1016/j.electacta.2010.05.040.
[21] S.J. McCormack, A. Navrotsky, Thermodynamics of high entropy oxides, Acta Mater 202 (2021) 1–21. https://doi.org/10.1016/j.actamat.2020.10.043.
[22] C.M. Rost, E. Sachet, T. Borman, A. Moballegh, E.C. Dickey, D. Hou, J.L. Jones, S. Curtarolo, J.P. Maria, Entropy-stabilized oxides, Nat Commun 6 (2015). https://doi.org/10.1038/ncomms9485.
[23] S.S. Aamlid, M. Oudah, J. Rottler, A.M. Hallas, Understanding the Role of Entropy in High Entropy Oxides, J Am Chem Soc (2022). https://doi.org/10.1021/jacs.2c11608.
[24] O.F. Dippo, K.S. Vecchio, A universal configurational entropy metric for high-entropy materials, Scr Mater 201 (2021) 113974. https://doi.org/10.1016/j.scriptamat.2021.113974.
[25] M. Brahlek, M. Gazda, V. Keppens, A.R. Mazza, S.J. McCormack, A. Mielewczyk-Gryń, B. Musico, K. Page, C.M. Rost, S.B. Sinnott, C. Toher, T.Z. Ward, A. Yamamoto, What is

in a name: Defining “high entropy” oxides, APL Mater 10 (2022). https://doi.org/10.1063/5.0122727.

[26] Z. Wang, X. Zhang, X. Wu, Y. Pan, H. Li, Y. Han, G. Xu, J. Chi, J. Lai, L. Wang, High-entropy phosphate/C hybrid nanosheets for efficient acidic hydrogen evolution reaction, Chemical Engineering Journal 437 (2022) 135375. https://doi.org/10.1016/j.cej.2022.135375.

[27] B. Wu, G. Hou, E. Kovalska, V. Mazanek, P. Marvan, L. Liao, L. Dekanovsky, D. Sedmidubsky, I. Marek, C. Hervoches, Z. Sofer, High-Entropy NASICON Phosphates ($Na_3M_2(PO_4)_3$ and $NaMPO_4O_x$, M = Ti, V, Mn, Cr, and Zr) for Sodium Electrochemistry, Inorg Chem 61 (2022) 4092–4101. https://doi.org/10.1021/acs.inorgchem.1c03861.

[28] H. Qiao, X. Wang, Q. Dong, H. Zheng, G. Chen, M. Hong, C.P. Yang, M. Wu, K. He, L. Hu, A high-entropy phosphate catalyst for oxygen evolution reaction, Nano Energy 86 (2021) 106029. https://doi.org/10.1016/j.nanoen.2021.106029.

[29] J.W. Sturman, E.A. Baranova, Y. Abu-Lebdeh, Review: High-Entropy Materials for Lithium-Ion Battery Electrodes, Front Energy Res 10 (2022) 1–15. https://doi.org/10.3389/fenrg.2022.862551.

[30] Z. Zhao, H. Chen, H. Xiang, F.Z. Dai, X. Wang, Z. Peng, Y. Zhou, $(La_{0.2}Ce_{0.2}Nd_{0.2}Sm_{0.2}Eu_{0.2})PO_4$: A high-entropy rare-earth phosphate monazite ceramic with low thermal conductivity and good compatibility with Al_2O_3, J Mater Sci Technol 35 (2019) 2892–2896. https://doi.org/10.1016/j.jmst.2019.08.012.

[31] T.G. Brandt, A.R. Tuokkola, M. Yu, R.M. Laine, Liquid-feed flame spray pyrolysis enabled synthesis of Co- and Cr-free, high-entropy spinel oxides as Li-ion anodes, Chemical Engineering Journal 474 (2023) 145495. https://doi.org/10.1016/j.cej.2023.145495.

[32] Q. Yang, G. Wang, H. Wu, B.A. Beshiwork, D. Tian, S. Zhu, Y. Yang, X. Lu, Y. Ding, Y. Ling, Y. Chen, B. Lin, A high-entropy perovskite cathode for solid oxide fuel cells, J Alloys Compd 872 (2021) 159633. https://doi.org/10.1016/j.jallcom.2021.159633.

[33] J. Sturman, C.-H. Yim, E.A. Baranova, Y. Abu-Lebdeh, Communication—Design of $LiNi_{0.2}Mn_{0.2}Co_{0.2}Fe_{0.2}Ti_{0.2}O_2$ as a High-Entropy Cathode for Lithium-Ion Batteries Guided by Machine Learning , J Electrochem Soc 168 (2021) 050541. https://doi.org/10.1149/1945-7111/ac00f4.

[34] Q. Zheng, Z. Ren, Y. Zhang, T. Qin, J. Qi, H. Jia, L. Jiang, L. Li, X. Liu, L. Chen, Surface Phase Conversion in a High-Entropy Layered Oxide Cathode Material, ACS Appl Mater Interfaces 15 (2023) 4643–4651. https://doi.org/10.1021/acsami.2c16194.

[35] S. Zhang, Z. Liu, L. Li, Y. Tang, S. Li, H. Huang, H. Zhang, Electrochemical activation strategies of a novel high entropy amorphous V-based cathode material for high-performance aqueous zinc-ion batteries, J Mater Chem A Mater 9 (2021) 18488–18497. https://doi.org/10.1039/d1ta05205e.

[36] Z. Shijie, L. Na, S. Liping, L. Qiang, H. Lihua, Z. Hui, A novel high-entropy cathode with the A_2BO_4-type structure for solid oxide fuel cells, J Alloys Compd 895 (2022). https://doi.org/10.1016/j.jallcom.2021.162548.

[37] A. Sarkar, B. Breitung, H. Hahn, High entropy oxides: The role of entropy, enthalpy and synergy, Scr Mater 187 (2020) 43–48. https://doi.org/10.1016/j.scriptamat.2020.05.019.

[38] A. Sarkar, R. Djenadic, D. Wang, C. Hein, R. Kautenburger, O. Clemens, H. Hahn, Rare earth and transition metal based entropy stabilised perovskite type oxides, J Eur Ceram Soc 38 (2018) 2318–2327. https://doi.org/10.1016/j.jeurceramsoc.2017.12.058.

[39] R.J. Clément, Z. Lun, G. Ceder, Cation-disordered rocksalt transition metal oxides and oxyfluorides for high energy lithium-ion cathodes, Energy Environ Sci 13 (2020) 345–373. https://doi.org/10.1039/c9ee02803j.

[40] D. Chen, J. Ahn, G. Chen, An Overview of Cation-Disordered Lithium-Excess Rocksalt Cathodes, ACS Energy Lett 6 (2021) 1358–1376. https://doi.org/10.1021/acsenergylett.1c00203.

[41] W. Li, S. Lee, A. Manthiram, High-Nickel NMA: A Cobalt-Free Alternative to NMC and NCA Cathodes for Lithium-Ion Batteries, Advanced Materials 32 (2020) 1–6. https://doi.org/10.1002/adma.202002718.

[42] A. Urban, J. Lee, G. Ceder, The configurational space of rocksalt-type oxides for high-capacity lithium battery electrodes, Adv Energy Mater 4 (2014). https://doi.org/10.1002/aenm.201400478.

[43] P. Stüble, V. Mereacre, H. Geßwein, J.R. Binder, On the Composition of $LiNi_{0.5}Mn_{1.5}O_4$ Cathode Active Materials , Adv Energy Mater 2203778 (2023) 2203778. https://doi.org/10.1002/aenm.202203778.

[44] G. Lim, D. Shin, K.H. Chae, M.K. Cho, C. Kim, S.S. Sohn, M. Lee, J. Hong, Regulating Dynamic Electrochemical Interface of $LiNi_{0.5}Mn_{1.5}O_4$ Spinel Cathode for Realizing Simultaneous Mn and Ni Redox in Rechargeable Lithium Batteries, Adv Energy Mater 12 (2022). https://doi.org/10.1002/aenm.202202049.

[45] K. Zhou, S. Zheng, H. Liu, C. Zhang, H. Gao, M. Luo, N. Xu, Y. Xiang, X. Liu, G. Zhong, Y. Yang, Elucidating and Mitigating the Degradation of Cationic-Anionic Redox Processes in $Li_{1.2}Mn_{0.4}Ti_{0.4}O_2$ Cation-Disordered Cathode Materials, ACS Appl Mater Interfaces (2019). https://doi.org/10.1021/acsami.9b16011.

[46] J. Lee, D.A. Kitchaev, D.H. Kwon, C.W. Lee, J.K. Papp, Y.S. Liu, Z. Lun, R.J. Clément, T. Shi, B.D. McCloskey, J. Guo, M. Balasubramanian, G. Ceder, Reversible Mn^{2+}/Mn^{4+} double redox in lithium-excess cathode materials, Nature 556 (2018) 185–190. https://doi.org/10.1038/s41586-018-0015-4.